

# REPORT DOCUMENTATION PAGE

AFRL-SR-AR-TR-05-  
0050

Public reporting burden for this collection of information is estimated to average 1 hour per response, including the time for reviewing instruction data needed, and completing and reviewing this collection of information. Send comments regarding this burden estimate or any other aspect of this burden to Department of Defense, Washington Headquarters Services, Directorate for Information Operations and Reports (0704-0188), 124302. Respondents should be aware that notwithstanding any other provision of law, no person shall be subject to any penalty for failing to con valid OMB control number. PLEASE DO NOT RETURN YOUR FORM TO THE ABOVE ADDRESS.

1. REPORT DATE (DD-MM-YYYY) 28 January 2005	2. REPORT TYPE Final Technical Report	3. DATES COVERED (From - To) 01 Nov 2002 - 31 Oct 2004		
4. TITLE AND SUBTITLE In Situ Evaluation of 3-D Woven Composite Structural Performance Using Fiber Optic Sensors.		5a. CONTRACT NUMBER F49620-03-C-0006		
		5b. GRANT NUMBER		
		5c. PROGRAM ELEMENT NUMBER		
		5d. PROJECT NUMBER		
		5e. TASK NUMBER		
		5f. WORK UNIT NUMBER		
7. PERFORMING ORGANIZATION NAME(S) AND ADDRESS(ES)		8. PERFORMING ORGANIZATION REPORT NUMBER 3		
Firm: 3TEX, Inc. 109 MacKenan Drive Cary, NC 27511	Research Institution: University of Dayton Research Institute, 300 College Park, Dayton, OH 45469			
9. SPONSORING / MONITORING AGENCY NAME(S) AND ADDRESS(ES) Department of the Air Force AF Office of Scientific Res. 4015 Wilson Blvd. Arlington, VA 22203-1954		10. SPONSOR/MONITOR'S ACRONYM(S) 20050322 408 DRT		
12. DISTRIBUTION / AVAILABILITY STATEMENT Distribution Statement A. Approved for public release; distribution is unlimited.				
13. SUPPLEMENTARY NOTES Prepared in cooperation with the subcontractor Luna Innovations, Inc., 2851 Commerce Street, Blacksburg, VA 24060				
14. ABSTRACT Report developed under STTR contract for topic AF 00T002 describes scientific approaches, engineering solutions and practical results of in situ strain monitoring in 3-D woven composite materials, their bonded and bolted joints using integrated networks of Bragg grating fiber optic sensors. A number of continuous optical fibers carrying hundreds of sensors were integrated into 3-D weaving process simultaneous with the host warp, fill and Z-yarns, and thus became an integral part of produced 3-D woven preform. The preform was then consolidated using VARTM process and provided experimental flat coupons for tensile and flexural testing. The same fiber optics instrumented material was used for fabrication of double-lap bonded and bolted joint elements, which were exposed to uniaxial tensile tests. Experimental results showed capability of the integrated fiber optic sensors to monitor internal strain fields and adequately respond to strain concentration caused by cutouts, bolts and overlap ends. Experimental strain field results obtained from integrated fiber optic sensors were compared with foil gage and Moiré interferometry data, as well as with finite element analysis results and showed good agreement. A practical cut and Polish method of connecting ends of integrated optical fibers to the data acquisition system was developed and validated.				
15. SUBJECT TERMS STTR Report; Composite Materials; Woven Fabrics; Fiber Optic Sensors; Health Monitoring				
16. SECURITY CLASSIFICATION OF: UNCLASSIFIED		17. LIMITATION OF ABSTRACT UNLIMITED	18. NUMBER OF PAGES 133	19a. NAME OF RESPONSIBLE PERSON Alexander E. Bogdanovich
a. REPORT Unclassified	b. ABSTRACT Unclassified	c. THIS PAGE Unclassified		19b. TELEPHONE NUMBER (include area code) 919-481-2500 ext. 113

**TABLE OF CONTENTS**

<b>1. OBJECTIVES.....</b>	<b>5</b>
<b>2. SUMMARY OF EFFORT.....</b>	<b>5</b>
<b>3. SIGNIFICANCE TO THE FIELD.....</b>	<b>6</b>
<b>4. PROJECT PARTNERS, THEIR EXPERTISE AND EXPERIENCE.....</b>	<b>7</b>
<b>5. ACCOMPLISHMENTS/NEW FINDINGS.....</b>	<b>7</b>
5.1. Research Highlights of Phase II, Year 1.....	7
5.2. Research Highlights of Phase II, Year 2.....	7
<b>6. BRIEFS ON TASKS AND ACCOMPLISHMENTS BY AREA.....</b>	<b>8</b>
6.1. Automation of the Sensor Insertion Process Into 3-D Woven Preforms.....	8
6.2. Fiber/Sensor Mapping.....	8
6.3. Development of CAP Method/Connector Combination.....	9
6.4. Manufacturing of Instrumented Specimens, Testing and Comparisons of Experimental Results.....	10
6.5. Sensitivity Analysis to Sensor Location and Orientation.....	10
<b>7. DETAILS OF EXPERIMENTAL WORK.....</b>	<b>10</b>
7.1. Fiber Optic Sensors and Equipment Provided by LUNA.....	10
7.2. 3Weave <sup>TM</sup> Automated Fiber Optic Integration Development.....	12
7.3. Sensor Challenges and Selection.....	15
7.4. Challenges of Fiber Optics Integration Into Weaving Processes.....	20
7.5. Fiber Optic Weaving Trials.....	22
7.6. Automated Weaving of DSS Sensing Fibers.....	27
7.7. Sensor Challenges/Lessons Learned.....	32
<b>8. TEST SAMPLE MANUFACTURE.....</b>	<b>32</b>
8.1. Fabric Preform Parameters.....	33

8.2. Composite Material Based on C-1025 Preform.....	33
8.3. Resin Infusion.....	34
8.4. Fabrication of Carbon Fiber Plates with Integrated DSS Fibers.....	34
8.5. Optical Sensor Mapping.....	35
9. FOUR-POINT BENDING TESTS.....	39
9.1. Data Acquisition.....	39
9.2. Experimental Samples and Test Procedures.....	39
9.3. Strain Monitoring Results in Four-Point Bending Tests.....	46
9.4. Summary and Conclusions from Bend Testing.....	57
10. DOUBLE-LAP BONDED JOINT WITH INTEGRATED SENSORS.....	57
10.1. Experimental Sample Configuration.....	57
10.2. Optical Sensor Location and Positions.....	59
10.3. Foil Strain Gage Location and Functionality.....	61
10.4. Test Procedure.....	62
10.5. Experimental Results Provided by Optical Sensors and Their Discussion.....	64
10.6. Double-Lap Bonded Joint with Moiré Grating.....	72
10.7. Nonlinearity/Damage Detection.....	83
10.8. Summary and Conclusions.....	86
11. DOUBLE-LAP BOLTED JOINT WITH INTEGRATED FBG SENSORS.....	87
11.1. Sample Configuration.....	87
11.2. Sensors, Instrumentation and Test Equipment.....	87
11.3. Test Procedure.....	88
11.4. Results of Double-Lap Bolted Joint Tests.....	90
12. ADDITIONAL TESTING AND MODELING OF 3Weave <sup>TM</sup> COMPOSITE MATERIAL.....	92

12.1. Objectives, Scope and Summary of Test Results.....	92
12.2. 3-D Modeling and Predictive Analysis of 3-D Woven Composite.....	93
12.3. Comparison of Theoretical and Experimental Results.....	97
<b>13. DEVELOPMENT OF CAP OPTICAL CONNECTION METHODS....</b>	<b>98</b>
13.1. Engineering Challenge.....	100
13.2. Literature Search on Fiber Optics Connectors.....	100
13.3. Polishing Technique.....	105
13.4. Fiber-Fiber Alignment Experiments.....	105
13.5. Fiber-Composite Alignment Experiments.....	108
13.6. Fiber-Composite Embedded EFPI Alignment Experiments.....	110
13.7. Cut and Polish Approach.....	117
13.8. Fiber-Composite Embedded Optical Fiber Cut and Polish Demonstration.....	120
13.9. Fiber-Composite Integrated DSS Cut And Polish Demonstration.....	121
13.10. Fiber-Composite Integrated DSS Panel Cut and Polish Attempt.....	123
<b>14. GENERAL CONCLUSIONS.....</b>	<b>125</b>
<b>15. PRACTICAL VALUE OF THE DEVELOPED METHODOLOGY...</b>	<b>126</b>
<b>16. REFERENCES.....</b>	<b>128</b>
<b>17. PERSONNEL SUPPORTED.....</b>	<b>131</b>
<b>18. PUBLICATIONS.....</b>	<b>131</b>
<b>19. INTERACTIONS/TRANSITIONS.....</b>	<b>132</b>
<b>20. NEW DISCOVERIES, INVENTIONS.....</b>	<b>133</b>
<b>21. HONORS/AWARDS.....</b>	<b>133</b>

## 1. OBJECTIVES

- Demonstrate automated weaving of optical fibers/sensor grids into 3-D textile preforms.
- Develop method/connector combination allowing reliable connection/reconnection to cut-exposed optical fibers by CAP method.
- Develop techniques for mapping of embedded sensor arrays.
- Produce optically instrumented open hole, bolted joint, and bonded joint specimens.
- Conduct testing of instrumented open hole, bolted joint, and bonded joint specimens and compare data with foil gage and Moiré interferometry results.
- Determine sensitivity of the embedded sensors to position and orientation with respect to open holes and bolts.
- Validate predictive analysis tools for 3-D woven composite materials and bonded joints by comparison with experimental strain data provided by integrated fiber optic sensors.

No changes were made to the objectives in the course of the project.

## 2. SUMMARY OF EFFORT

Research performed between 11/1/2002 and 10/31/2004 continued the development of experimental manufacturing methods for integrating fiber optic sensing systems into 3-D woven preforms and their composites, and functional validation of the sensing arrays. Composite panels with integrated arrays of Bragg grating fiber optic sensors were manufactured and used for producing experimental flat samples without holes and with drilled holes, samples of bonded joints and bolted joints. Extensive mechanical tests were performed on all aforementioned experimental samples, and data from optical sensing networks were compared to data obtained simultaneously from resistive foil gages, and Moiré interferometry strain sensing methods. Experimental data were also compared with theoretical displacement and strain values generated by 3-D modeling of composite specimens under test conditions. Integrated fiber optic sensing systems displayed strain distributions within, and along, individual fiber tows in the composite structures in real time, and clearly confirmed the anticipated effects of strain gradients near various stress risers. Results provided by integrated fiber optic sensing systems have revealed localized yield near stress risers prior to visible damage. A new method of making and repairing connections to optical fibers within composites, named Cut And Polish (CAP), has been demonstrated. The combined techniques of automated weaving of instrumented structural preforms, VARTM resin infusion, CAP connection, and real time display of internal strains is relevant to practical manufacture of smart materials and structures, which provide feedback for command, control, and in-situ health monitoring.

### KEYWORDS:

3-D Weaving, Textile Composites, Fiber Optics, Bragg Grating Sensors, Smart Materials, Mechanical Testing, Bonded Joints, Bolted Joints, Resin Infusion, Moiré Interferometry, 3-D Analysis.

### 3. SIGNIFICANCE TO THE FIELD

Manned, RPV, and UAV aircraft alike, depend on feedback systems to allow efficient flight control, damage assessment, and health monitoring (Figure). Disassembly necessary to access critical components in dense and layered airframes is considerable (Figure), and adds potential risk of mistakes in service. The cost of excessive periodic inspection, premature replacement, downtime, or catastrophic failures in use is expensive at best and tragic at worst. In-situ, real time strain and load monitoring can be performed in critical sites of the airframe indicating strain levels in different components. Damage location and extent can be detected. Flight and maneuvering adjustments can be made adaptively using sensor feedback. Vibration control and structural shape change can be accomplished using integrated actuators only with reliable feedback. Integration of secure and efficient communication systems within structures are possible by using the same manufacturing methods.

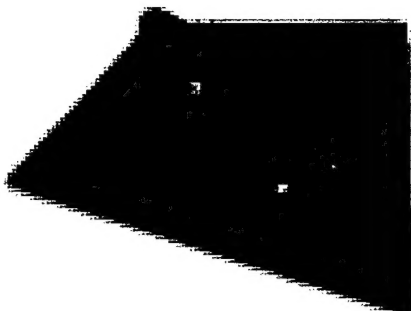


Figure 1. UAV's and RPV's require *feedback* from composite structural components exposed to in-service loading.

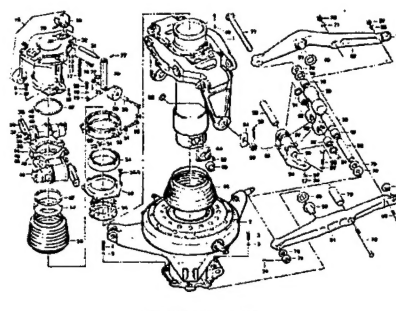


Figure 2. Replace/inspect tasks can entail extensive time/cost/risk.

In addition to the benefits of functionality mentioned above, data from such systems will drive the development and validation of critical 3-D structural analysis tools [1]. 3TEX has proposed the innovative approach of instrumenting 3-D textile reinforced composite materials and structures with sensors, actuators and/or other devices, systems or networks available in fibrous form, and making and repairing robust connection to the optical networks after manufacture of the parts. This novel technological approach enables for a low cost and practical manufacture of "smart" composite materials and structures. The approach includes:

- Gentle automated weaving of 3-D orthogonal preforms for composites with integrated devices, systems or networks, capitalizing on the straight fiber pathways of the preforms.
- Composite part manufacturing using various resin infusion methods which are safe for the functionality of integrated devices, systems or networks.
- Robust connection and reconnection techniques.
- Reliable data interrogation equipment and processing methods.

These considerations make the overall goal of automated production of preforms instrumented with sensors and other information systems and devices important to the mission, the objectives, and the future of the USAF.

## 4. PROJECT PARTNERS, THEIR EXPERTISE AND EXPERIENCE

This STTR research combined expertise and experience of three organizations:

- ◆ 3TEX, Inc. (3TEX) in 3-D weaving, composites fabrication using resin infusion methods, experimental characterization of composites, 3-D stress/strain and failure analysis.
- ◆ University of Dayton Research Institute (UDRI) in mechanical testing and composites characterization, sensor mapping, Moiré interferometry, 3-D modeling and analysis of composite structures.
- ◆ Luna Innovations, Inc. (LUNA) in fiber optic sensing systems, optical fiber connectors, Bragg grating sensors, data reduction equipment and methods.

The objectives that were set for Phase II were met on schedule. Listed below are specific accomplishments toward those objectives.

## 5. ACCOMPLISHMENTS/NEW FINDINGS

### 5.1. Research Highlights of Phase II, Year 1

- Demonstrated automated 3-D weaving of optical fibers integrated within warp, weft, and Z “host” fiber yarns.
- Achieved CAP (Cut And Polish) connection and reconnection to optical fibers in epoxy casting.
- Mapped positions of integrated Bragg grating sensor arrays using X-rays and metallic paint.
- Manufactured and tested in 4-point bending several 3-D woven carbon fiber/vinyl ester matrix specimens instrumented with hundreds of Bragg grating sensors. Mechanical tests were also performed on flat specimens with semi-circular cutouts to induce stress concentration.
- Demonstrated simultaneous measurement of internal strains at hundreds of points within bend specimens.
- Mapped the internal strain gradients within fiber architecture near the cutouts.

### 5.2. Research Highlights of Phase II, Year 2

- Performed fully automated integration of serial FBG sensing strands into warp, weft and Z directions simultaneously, in a planned grid formation appropriate for standardization.
- Manufactured and tested several 3-D woven carbon fiber/vinyl ester matrix specimens instrumented with hundreds of Bragg grating sensors. The specimens were made in form of standard tensile and bending coupons, double-lap bonded joint (which was also tested after drilling hole), and bolted lap joint (with two bolts).
- Compared test results for strains obtained from integrated Bragg grating arrays with external foil gauge data.
- Moiré interferometry results were obtained for bonded joint specimen and compared to optical sensor data. Integrated fiber optic sensors showed good correlation, even in the local regions of non-linear/inelastic response.

- Developed a Unit Cell level micro-mechanics model of the 3-D woven carbon/epoxy composite simulating the material studied in experimental work and applied the model to predict effective orthotropic elastic characteristics of composite using 3TEX in-house 3D MOSAIC code. Theoretical and experimental results were used to calibrate the Unit Cell model.
- Performed 3-D elastic analysis, using “Homogenized” and “Layered” models, of the 3-D woven carbon fiber composite under 4-point bending. Obtained transverse displacement and in-plane strain predictions were compared to experimental data provided by foil gages and integrated Bragg grating fiber optic sensors. Elastic properties used in the bending analysis were obtained by means of the micro-mechanics Unit Cell analysis mentioned above.
- Demonstrated CAP connections to large arrays of Bragg grating sensors at cut edges of composite samples.

## 6. BRIEFS ON TASKS AND ACCOMPLISHMENTS BY AREA

### 6.1. Automation of the Sensor Insertion Process Into 3-D Woven Preforms

The focus of this task was to successfully automate the integration of distributed strain sensing (DSS) optical fiber within woven composites.

In Year 1 of the Phase II program, 11 smooth and flexible SMF28 optical fibers were simultaneously, automatically, and continuously integrated into carbon fiber, glass, and aramid yarns and then into 3-D woven fabric separate paths. Fibers integrated along the warp (x) and fill (y) directions experience no bending and showed negligible losses within the preform, while optical fibers in the Z (through thickness) direction showed significant losses due to bending of the fibers.

In Year 2 of the Phase II program 21 FBG sensing fibers were integrated into a preform used for bonded joint specimens. These fibers allow for a 5X reduction in bending radius before light is lost over the baseline SMF28 commercial data/com fibers. 3 of these sensing fibers followed complex paths that turned 90 degrees from one axis to the other at least 8 times each. The tight bends did not prevent light beam transmission and interrogation around the corners. This result had implications for the automated integration of sensing fiber strands passing along z-axis, and the functionality of those strands in these configurations. Subsequently, 3 separate and continuous strands of FBG optical sensing fibers were automatically integrated into a 8mm thick carbon fiber preform in the warp, fill and Z yarns without damage. The fill-directional fibers were inserted in a regular 1cm grid pattern as is imagined for the production of standardized instrumented preforms. The 12" x 12" preform contained more than 800 gratings on just 3 strands.

### 6.2. Fiber/Sensor Mapping

In Phase I, it was demonstrated that X-rays could resolve both EFPI optical sensors and the optic strands integrated into a carbon/epoxy composite. DSS strands, though smaller, proved to be visible in radiographs as well. Mapping the exact positions of the Bragg gratings within

the DSS fibers themselves required increasing radio opacity artificially. Attempts by UDRI in Year 1 of Phase II using standard dye penetrant were unsuccessful due to the low viscosity and surface tension of the liquid. Further attempts at hand marking with metallic ink showed the fibers in X-rays. Automated application of this sort of ink may well provide a viable process long term, as well as eliminate uncertainty as to the position of the gratings.

Currently, ink jet printing of dashes onto the strands between the gratings of the fiber optic sensors in the draw tower during their manufacture visually marks the grating positions along the fibers. Grating position accuracy in this prototype was around  $\pm 5$  mm, but can be improved. Mapping of the gratings by X-ray may be enabled by modifying the ink jet printing process to use metal-doped ink, thereby automating the process. Ink jet heads and inks are commercially available to print radio-opaque patterns. This was not demonstrated to avoid interruption of standard process of the draw tower and FBG printing system at NASA LaRC used for this project. Application of the ink to the spaced between the gratings will leave the gratings themselves clean and suitable for formation of a strong bond.

### **6.3. Development of CAP Method/Connector Combination**

None of the mechanical test specimens produced in Phase I and Phase II used the new Cut And Polish (CAP) connector technology during mechanical testing. Instead, the leads dangled outside the preforms during resin infusion were fusion spliced into standard connectors. This is not suitable for a production environment. Fragile and expensive fiber optic sensors outside the fabric can be easily broken, thus rendering the sensors within the part ineffective. Success with the CAP technology cuts care of the delicate dangling leads from the process and allows repair and reconnection. Bare fibers, fibers in castings, sections of instrumented test specimens remaining intact after testing in other tasks of this program, as well as panels specifically designed with woven sensing grids were used to experiment with CAP to allow parallel development without risking test data.

During Phase I 3TEX demonstrated that Cartesian scanning and intensity monitoring could be used to home in on the cut end of an optical fiber. This method was demonstrated using simple laser source and detector set, and a milling machine as a 3-axis stage. This resulted in a coupling efficiency of 50% (3dB loss) by coarse alignment of two bare fibers. This scanning method was applied to later efforts with fine stages and embedded fibers. LUNA's work in Year 1 of the Phase II STTR on the proposed CAP method showed that connections could be made to fibers within epoxy castings.

In Year 2, LUNA successfully made CAP connections directly to the cut end of an optical fiber integrated in the composite, whereupon data was taken from an integrated EFPI sensor. Later experiments repeatedly demonstrated the successful CAP connection to integrated serial Brag grating arrays. Both the single end and through transmission methods were demonstrated, and sensors were successfully interrogated. In more than one case, a composite part was machined and polished at the site of a surface break in the DSS and connection was reestablished. This demonstrates that fiber lead preservation does not require to interrupt the normal composite manufacturing processes. The preforms may be cut, infused, trimmed, and finally the connection established after the part is complete.

## 6.4. Manufacturing of Instrumented Specimens, Testing and Comparisons of Experimental Results

At the end of Year 1, four test specimens had been instrumented with the FBG fiber optic sensors and tested using LUNA's Distributed Sensor System (DSS). The strain readings from 3 strands (30+ sensors carried by each of them) were displayed in real time during loading. Simple plots of data from "before" and "after" the addition of cutouts clearly showed not only increases in strains near the semi-circular cutouts, but also the internal strain gradients near the cut-outs.

In Year 2, two 3-D woven composite test specimens having integrated FBG fiber optic sensors were manufactured. In tensile tests of a bonded double-lap joint and a bolted double-lap joint, DSS equipment collected strain data from the sensors. Fiber optic sensor strain data taken during the bonded joint tests in particular, was compared to and correlated well with data collected simultaneously by Moiré interferometry and foil gauges. The DSS correctly registered non-linear areas of the bonded and bolted joint tests, as well as reproducing linear curves where the Moiré interferometry produced linear relations. In these tests, internal strains measured along 3 integrated optical fibers were displayed simultaneously, and in real time on monitors, and logged for analysis and plotting later.

## 6.5. Sensitivity Analysis to Sensor Location and Orientation

X-ray radiography showed that the sensing fibers wander slightly within the volume of the yarns into which of them was integrated. This allows only a 1mm corridor for the optical sensing fiber to deviate from its planned orientation. 100-200mm were typical distances over which this sort of wandering took place, which implies angles less than 1°. Data from the fiber optic sensors have been shown to be repeatable to within a 1% standard deviation. The effect of angular misalignment relative the fabric axes is, therefore, believed to be small. Sensor location relative to strain gradients, however, can be significant. Where the strains in question vary significantly across a single yarn diameter, as in the case of certain gratings within yarns located at the bondline, near a surface point load, or in a thin bending specimen, that sensor can be subjected to higher strains along with its surrounding structural host yarn. Certain consistent signature, like variations observed in data fields along a single fiber in bending specimens regardless of load, may well be indicative of this sensitivity. Those readings would be, in fact, highly believable. Smaller yarn sizes and more consistent integration of the sensing strands into the tows without any twist would limit those effects greatly. These "signature" patterns may also serve to uniquely identify parts and recognize yield, creep, or damage.

# 7. DETAILS OF EXPERIMENTAL WORK

## 7.1. Fiber Optic Sensors and Equipment Provided by LUNA

LUNA purchased and delivered to 3TEX a fusion splicer, cleaver, optical source and an optical power meter. Equipment details are provided below:

- **Power Meter:** OPM 4-2C. It is the lowest cost MM & SM power meter that allows you to set a reference measurement. It can be fitted with all the connector cap types. 9v power only. \$599 + FC adapter cap (p/n 8800-00-0200) is \$50.
- **Light Source:** OLS 2-1300-FC. It is a laser source with -10dBm output at 1310nm and is the lowest cost source that can be fitted with the FC connector. \$995 with FC interface.
- **Fusion splicer:** FSM-40SB (B = rear monitor) refurbished with a refurbished cleaver for \$6,000.

Upon delivery of the optical equipment, representatives from LUNA traveled to 3TEX to train their staff in the use of the fusion splicer, cleaver light source, and power meter. The tools and techniques were used to verify the survival and quantify the function of the optical fibers during and after weaving.

LUNA also delivered sections of DSS fiber 35m, 25m, and 9m for use by 3TEX. Individual gratings 5mm long were burned into the fiber on 10mm centers. The individual grating were continuous along the entire 35m length. All of the gratings cannot be interrogated at one time if the fiber is over 10 m. Although the gratings are nominally the same along the fiber, an unstrained room-temperature reflection of each grating has not been obtained. The average center wavelength of 187 gratings was  $1558.6 \text{ nm} \pm 0.1\text{nm}$ . This average value should not vary along the length of the fiber. A 0.1nm shift in the center wavelength roughly corresponds to 0.01% strain. The change in the center wavelength is a measure of the strain. While making a composite part strain and losses in the fiber will be introduced in each step of the process - including weaving, molding/curing, part machining and testing. The strain and losses in the DSS fiber should be tracked throughout the process.

The description sheet for the first 35m of DSS fiber is shown in Table 1. Macrobend losses are reported in dB/360° loop at a given radius. Through-the-thickness fibers integrated into 3-D woven fabric inevitably have high curvature bends on the top and bottom surface of the fabric. Losses resulting from such bends can be integrated over the length of the fiber.

Further on, power losses from small repetitive bends or microbends, as they are called, could occur as a result of weaving and preform compaction. Very tiny bends along the length of a single grating could locally change the grating period and, in essence, broaden the wavelength range reflected by that grating. Each of these effects, microbends and local grating changes, would add to the effects of macrobends.

Table 1. Description sheet for Luna DSS fiber.

Description sheet for DSS fiber			
Contractual and Administrative			
Shipping Address	Luna Innovations 2851 Commerce St. Blacksburg, VA 24060	Ship-to Address:	Don Wigent 3Tex Inc. 109 MacKenan Dr. Cary N.C. 27511

Phone Number	(540)552-5128		Ph. 919-481-2500
Fax number	(540)951-0760		Fax 919-481-6595
Contract Number	R00037		
Date of mfg	6/10/03	Date shipped	6/13/03
<b>Fiber Properties</b>			
<b>Optical properties</b>		<b>Physical properties</b>	
Numerical Aperture	0.2 ± 0.01	Length of fiber	35 m
Cutoff Wavelength	1290 nm ± 100 nm	Diam. of fiber	127 µm
Attenuation:	(dB)/(360° loop)*	Buffer type	Polyimide
1/2" radius	0.00	Buffer thickness	12 µm
1/4" radius	< 0.05	Fiber diameter	151 µm
1/8" radius	1.21 ± 0.1	Material descrip.	Ge-doped core
1/16" radius	6.0 ± 0.1	Tensile strength	>50 kpsi
<b>Grating Properties</b>			
Length	5 mm ± 1mm		
Spacing	1.0 cm		
Average center wavelength **	1558.6 nm ± 0.1 nm		
Reflection strength	≈0.02% per grating		
<b>Special Remarks or deviations:</b>			
*Measurement was made by wrapping one loop of fiber around an object with the stated radius and measuring the loss relative to no bend.			
** Reflected center wavelength was measured for 187 gratings. The average center wavelength is reported with an error that encompasses the measured variations.			
Certification:			

## 7.2. 3Weave™ Automated Fiber Optic Integration Development

In Year 1 of Phase II work, tests with SMF28 optical fibers demonstrated fully automated integration of plain single mode optical fibers into preforms during weaving. In year II, far more elaborate fabric patterns were automatically woven in using actual DSS sensing fibers.

Three-dimensional textile composites, i.e. those with fibers oriented in an organized fashion in three-dimensional space, have great potential for improving mechanical performance. Recent advances described in [2-5] and other publications have lead to a revolutionary, straight fiber multiple insertion process, referred here and henceforth as the 3Weave™ process. The 3Weave™ process is an automated method of producing net-shape fabric preforms which can be flat sheets of fabric, but also various cross-sectional shapes, including "I", "T", "Π", box, core, pile, etc. Some examples of application driven 3Weave™ preforms are shown in Figure 3. Importantly, various hybrid fabrics can be manufactured by combining fibers of different nature in the warp, fill and Z directions. Specifically, such fiber types as S-2 and E-glass, various carbon, various Kevlar®, Spectra®, stainless steel tows, and of now optical fibers have been successfully processed into 3Weave™ fabrics.

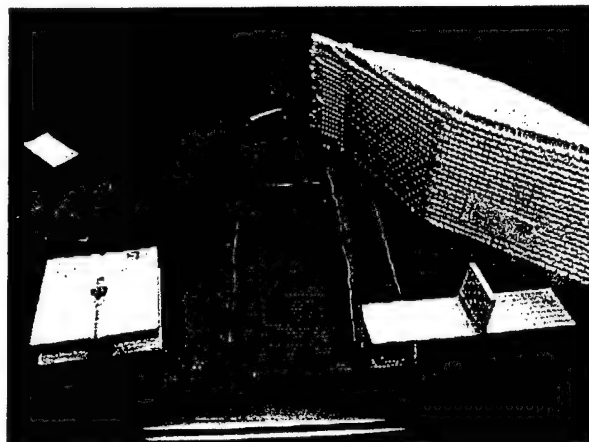


Figure 3. Examples of complex 3Weave™ preforms.

Weaving in general is defined as the formation of fabric by the "interlacing" of two sets of yarns, the warp and the weft. Weft yarn is inserted through an opening formed by deflecting some yarns up and some yarns down in a set of warp yarns. The essence of the patented 3Weave™ process [2] is that two or more weft yarns are simultaneously inserted from one or both sides, thus building full, multi layered, cross-sectional "slice" of 3-D fabric length with every cycle of the machine operation. In the 3Weave™ preforming process, a third set of yarns, called **Z-yarns**, ties the layers of non-interlaced warp and weft yarns into one fabric. A schematic illustration of this process is given in Figure 4.

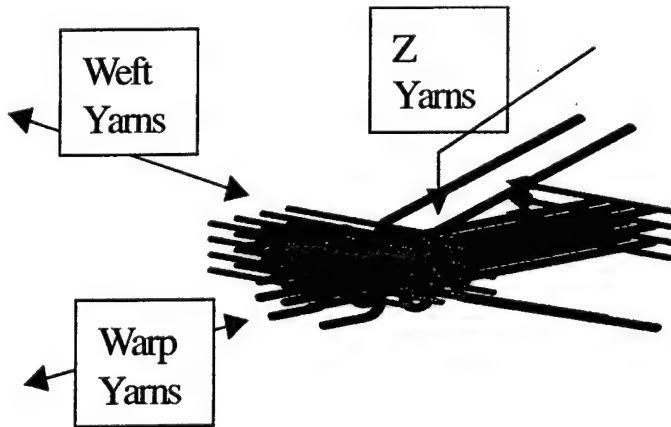


Figure 4. Illustration of the 3Weave™ multiple insertion process, showing straight yarns in two axes, which allows efficient light transmission via integrated optical fibers.

The resulting fiber architecture and the 3Weave™ manufacturing process itself are particularly suited to the integration of the optical fibers. It is illustrated by two model preforms in Figure 5. The idealized 3-D woven fabric models assume rectangular cross-sections of the yarns. Such assumption is validated by our experimental observations in the case of multi-filament yarns, see Figure 6.

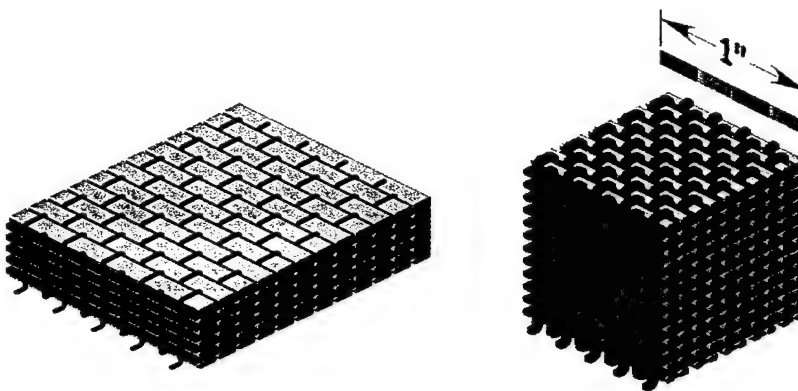


Figure 5. Models of a rather "thin" (left) and "thick" (right) 3Weave™ fabrics.

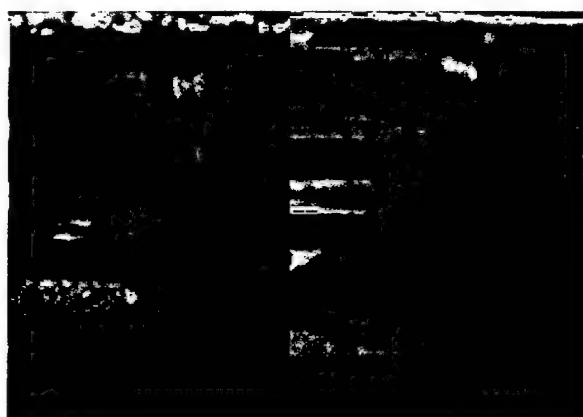


Figure 6. Fiber architecture of 3Weave™ after infusion.

The yarn paths in the schematic of Figure 5 run along the three Cartesian coordinates, with the Z-yarns taking a path essentially perpendicular to the fabric mid-plane inside the fabric, and parallel to the warp direction on the fabric surfaces. The radius to which an optical fiber within the Z yarns must bend is related to the size of the weft yarns as illustrated in Figure.

It is also worth noting that in the 3Weave™ process, individual warp yarn layers do not pass through heddles (wire suspended eyelets, see Figure 7), or forced to repeatedly pass between neighboring warp yarn layers as with 2-D weaving. Accordingly, weaving-induced fiber damage in this case is significantly reduced. These factors are extremely important in understanding why integrating optical fibers by the use of 3Weave™ process has significantly higher chance for success than doing the same with 2-D weaving on conventional looms.

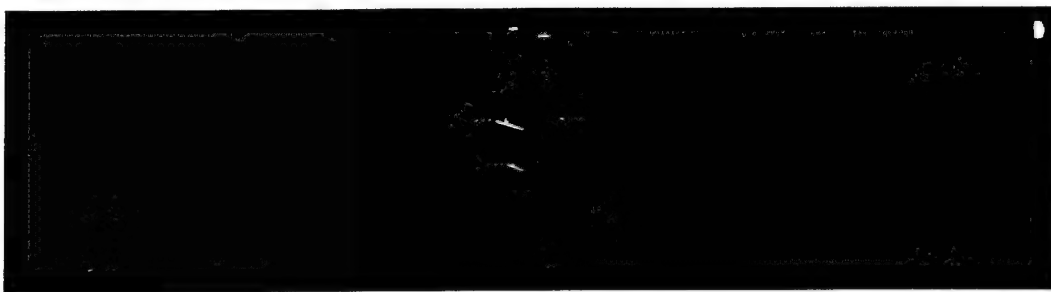


Figure 7. Heddles used to lift/lower Z yarns in looms.

Automated weaving machines, able to make materials and products on a commercial scale, rather than on a laboratory scale, has been accomplished using the 3Weave™ process and a new generation of machines designed and built at 3TEX. One such machine is shown in Figure 8. The 3Weave™ process is currently implemented on automated machines producing fabrics up to 183 cm (6 ft.) wide and over 5 cm (2 in.) thick.

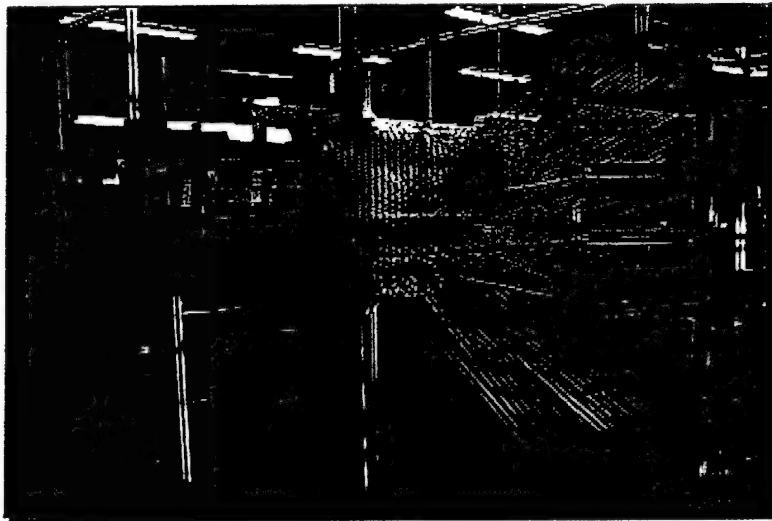


Figure 8. Photograph of industrial scale 3Weave™ weaving machine.

### 7.3. Sensor Challenges and Selection

A variety of challenges were experienced during Phase I effort. In particular, the EFPI (Extrinsic Fabry-Perot Interferometric) sensors chosen for Phase I placed reconciliation of desires for ease of application, versus pertinence and fidelity of data acquired slightly at odds. Some of the inherent features of the EFPI sensors provided advantages in obtaining high resolution of strain readings, but made the sensors more difficult to integrate in the weaving process. The increased diameter of the EFPI sensor head inherently provided a potential snag point, which can interfere with sharp corners. Heddle eyes, shown in Figure 9, which are used to lift the Z yarns into their square wave paths, posed a snag danger, if not successfully mitigated. The EFPI sensor has 3 basic elements, each of them affecting flexibility of the assembly. The body formed by the tube is rigid, whereas the optical fibers themselves are

substantially less rigid. Rigidity of the sensor bodies was anticipated to make routing of the sensor heads thorough the loom heddle eyes problematic. The capillary tube (or, more likely, the joint at lead entry) passing through a heddle eye, would be loaded in something similar to 3-point bending over the eye, see Figure 9, according to the shed angle and yarn tensions.

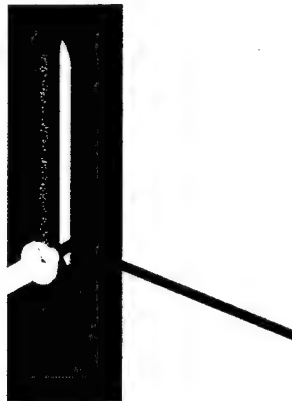


Figure 9. Detail of EFPI sensor/heddle interference.

However, weaving the EFPI sensors in the warp direction has been accomplished, with special manual care taken to position the sensors along the accompanying warp yarns. EFPI sensors were also placed in the weft direction in Phase I work, but that was done during pauses in weaving, because the EFPI sensors would be damaged during bending and sliding through the traditional rapier eyelets under tension, as illustrated in Figure 10. Besides, although the EFPI sensors may be serially multiplexed (daisy chained along the same fiber), only 8 or 10 EFPI sensors may be presently chained. This means that they can be placed only in a few specific locations within the preform. This requires special controlling means to register their warp-directional location.



Figure 10. Bending/Sliding through eyelet rapiers.

An intrinsic sensor type was chosen for Phase II work in the interest of efficient automation and technology transfer to the field. Intrinsic fiber optic sensors have sensing features fully

internal to the fiber itself. That means there are no outwardly physical features of the sensors within. Improved versions of some intrinsic sensor types, and standardized equipment to interrogate them have been brought to initial commercial availability. LUNA provided their manufactured DSS (Distributed Sensing System) fiber (shown in Figure 11) and demodulation system for use in this project. The only outward indication of the sensors within are the dark ink markings.

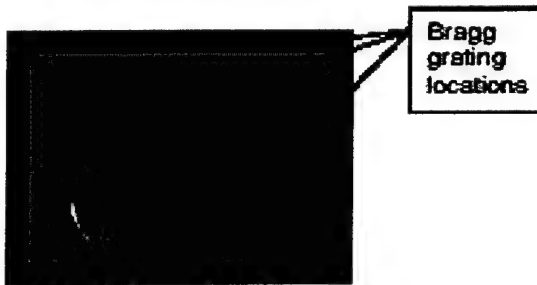


Figure 11. DSS fiber is flexible, has no edges to snag during weaving, and has numerous sensors carried by one fiber.

Changing to a serial Bragg grating type intrinsic sensor in Phase II eliminates the majority of the problems experienced with the EFPI type sensors. The DSS fibers are smooth and indistinguishable from the ordinary optical fiber types they are based on, and the relatively gentle 3Weave™ process does not attempt to crimp them. Sensors may be printed as frequently as one per cm or more, allowing one to map strain over an area with 1cm resolution. The resolution allows one to ignore the position along the fiber length in many applications. A plot of data from a grid of DSS sensing fiber on a plate is illustrated in Figure 12. Control of the DSS fibers position along their length is more difficult. This control exercise is analogous to feeding several striped ribbons through a pair of rollers, and ensuring that the stripes all line-up properly after some extended period of winding. The difficulty mounts with the length of production.

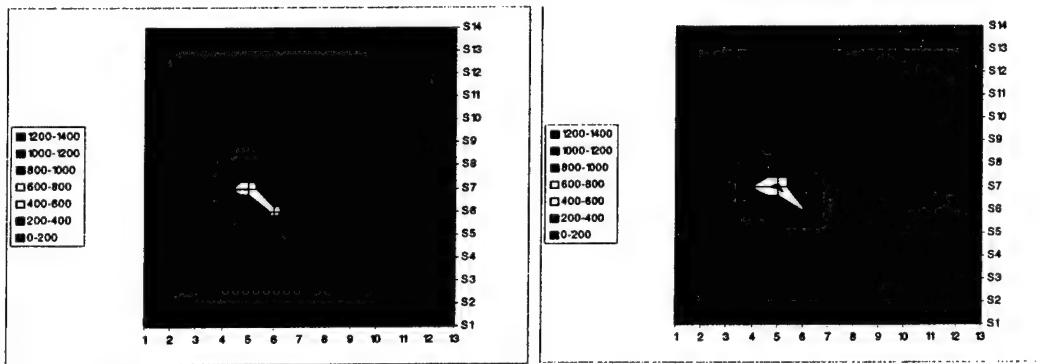


Figure 12. Mapped strain data from a panel instrumented with only four LUNA DSS fibers, clearly showed growth of a crack during testing in another, unrelated project.

FBG (Fiber Bragg Grating) optic sensors offer an advantage over other fiber optic sensor types in that a great many FBG sensor elements can be operated over a single optical fiber using a technique called fiber optic sensor multiplexing, see Figure 13. Fiber optic sensor multiplexing involves the use of fiber optic sensor network topologies that allow multiple sensors to be operated using the same instrumentation system. Although up to four EFPI strain sensors can be multiplexed, spectral interrogation FBG demodulation schemes can operate up to tens of FBGs per fiber, and coherence-based techniques such as that used by the LUNA's FBG DSS can operate up to hundreds of sensors along a single fiber.



Figure 13. Left - cabling for 450 foil gauges (1350 connections needed). Right – LUNA's sensing fiber with 750 sensors (only 1 connection is required).

The number of FBG sensors that a spectral interrogation system can operate is limited by system hardware, the full-scale strain range, and full-scale temperature range. The light source and/or detection scheme of the FBG spectral interrogation system will define the spectral range of the sensor system. Both strain and temperature will induce a spectral shift in the FBG response, so a wavelength "channel" is allocated for each of the sensors to accommodate the expected spectral shift, i.e., a spectral window of fixed spectral width. The number of channels that can be operated with a single spectral interrogation-based system is calculated by dividing the spectral range of the system by the spectral width that has been allocated.

Techniques used to operate FBG sensors include ratio-metric, spectral interrogation and coherence-based systems. Ratio-metric operation is the least robust measurement technique, though it provides a relatively low-cost system solution for making dynamic measurements using FBGs. The most commonly used interrogation scheme used to operate FBGs is spectral interrogation; the same scheme LUNA uses for its commercially available AFSS and Fiberscan systems. In spectral interrogation schemes, the spectral response of an optical fiber containing FBG sensors is measured. Spectral response is typically measured using either a broadband light source and spectrometer-based detection scheme or a simple photo detector with a scanning laser. Fixed-grating spectrometers, optical spectrum analyzers (OSAs) or scanning Fabry-Perot filters can be utilized in the former case.

For Phase II, a novel FBG sensor type for was considered as an alternative to EFPI sensors used in Phase I. This new sensor utilizing spectral interrogation demodulation scheme coupled with elliptical core fiber has been documented in [6]. The multi-axis FBG sensor technique uses elliptical core fiber and a specialized grating fabrication technique in an attempt to create an FBG sensor that allows strain measurement in the axial and transverse directions, i.e., an

attempt to decouple the inherent strain cross-sensitivity in FBGs. However, there is no commercially available strain gage instrumentation for the multi-axis sensor operation other than expensive optical spectrum analyzers, which only output is a wavelength information but not strain data.

Although attractive in theory, the multi-axis sensing technique faces serious practical challenges, such a stabilization of the FBG sensing fiber in the host structure, in order to determine the exact rotational state of a  $155 \mu\text{m}$  optical fiber after the sensor would be integrated in fabric preform and the preform infused with resin. Otherwise the direction in which strain is being measured is undetermined.

The DSS is based on a technique that has been reported in the literature [7,8]. The inventor of the DSS, Dr. Mark Froggat, formerly with NASA Langley, is now Chief Technology Officer for the Luna Innovations spin-off, Luna Technologies. At Luna Technologies, being headquartered in Blacksburg, VA, Dr. Froggat is developing the DSS for fiber optic communication instrumentation applications. Brooks Childers, previously with NASA Langley Research Center is a co-developer of the DSS, and he currently works for Luna Innovations, where he is commercializing the DSS unit for sensor applications. A representative application of the DSS and the unique measurement capabilities it provides have been demonstrated in an F-15 wing box strain mapping measurement application [9].

The main components of the LUNA's DSS system consist of a tunable laser, the optical network described, and a data acquisition system. It should be noted that other than the custom sensing fiber obtained from NASA Langley Research Center, this system was constructed of COTS hardware. The DSS can measure the wavelength of light reflected from literally thousands of low reflectivity FBG sensors distributed along single mode fibers. The wavelength of light (or spectrum) reflected from a FBG is influenced by the temperature and strain of the device to which it is attached. Consequently, FBG's attached to a device can be used to measure both the temperature and strain of the device. FBG's can also be used for a wider variety of sensing applications depending only upon the ingenuity of the user, e.g. for control of corrosion, hazardous gas concentration, pressure, etc. Figure 14 provides a side-by-side comparison of a DSS FBG and a conventional foil strain gage.

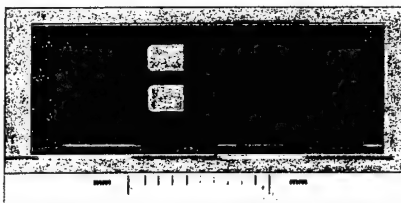


Figure 14. A side-by-side comparison of FBG array and a conventional foil gage. The black marks on the fiber show the locations of the Bragg gratings.

A useful feature of FBGs is that the measurement they provide is absolute. They are created by laser etching of a repetitive pattern in the core of the fiber. The light spectrum reflected from this pattern is fundamentally governed by the pattern's spacing. Therefore, if FBG's are attached to a material or structure early in its life cycle, they can monitor the residual stresses

induced by subsequent material processing, as well as the strain history over the life of the structure. This information can provide insight into the ultimate performance capability of a structure. Since optical fiber is made of glass, which is very strong for both tension and compression, the range of strains that can be measured is sufficient for most applications. It has also been shown that the pattern etching process does not affect the strength of the optical fiber, see [10,11], which is critical during weaving and infusion.

## 7.4. Challenges of Fiber Optics Integration Into Weaving Processes

The challenges presented by the integration of sensors into the weaving process, are also affected by those features of the weaving process that are inherent to the particular orientation of the desired sensor placement. Conventional 2-D weaving introduces substantial crimp, hence the name “warp” is natural for those fibers which are directed in the production direction. In contrast, the 3Weave™ process (schematically shown in Figure 4) provides inherently un-crimped geometry of the fabric. The importance of this feature of 3Weave™ process for the success of fiber optic sensor integration is very high.

### 7.4.1. Integration of Fiber Optics in Warp Direction

Warp fibers within 3Weave™ preforms are un-crimped and practically straight. They do not pass through heddles, and are not subjected to significant bending or tensile loads in the course of 3-D weaving. No significant barriers to warp-directional placement of optical fibers are apparent. Continuous supply of warp yarns from either creels or “beams” (cylindrical tubes) is commonly used in 3TEX fabric manufacturing, and appears to be quite adequate for the purpose of integrating optical fibers into the process.

With the EFPI type sensors used in Phase I, placement of the sensors in the warp locations within 3Weave™ preforms had two primary processing concerns. Those were survivability and location control. With regard to the survivability, the warp yarns are subject to far less force and deflection than the Z and weft yarns using the 3Weave™ process, and even the snag prone EFPI sensor heads can survive. The use of DSS fiber with multiplex sensors in Phase II alters the challenges in regards to their warp-directional placement. The spacing of the sensors at 1/cm allows continuous production. If only one or two, or even widely spaced sensors were used, then one would need to insure that the few integrated sensors are in exactly the right place. For example, an optical fiber may pass tangentially very close to a hole or bolt, but if a single sensor is used, it may be further down the fiber, and as such appears to be too remote for the function of monitoring the strain gradient. However, if the sensors are sufficiently frequent, then one or two of them will always be within 5mm of the point of interest. The resolution of the strain map, as set by the spacing of the Bragg gratings during manufacture, determines if registration control is needed or not. Thus, no attempt at registration of sensor strings along their length was made to date.

### 7.4.2. Integration of Fiber Optics in Fill Direction

In general, the fill (weft) directional yarns are also nearly straight (though their random waviness is, typically, more considerable than that of the respective warp yarns in the fabric).

More importantly, analogously to warp yarns, all fill yarns in 3Weave™ fabric are uncrimped. In some fabrics significant size loops are formed at the side edges, where the yarns turn back and forth across the preform, but the fiber bending radii there are controllable, and weft yarn placement is reasonably gentle, thus allowing automated placement of optical fibers integrated with the weft-directional yarns.

Weft yarns, and correspondingly, the weft (Y-direction) sensor assemblies and leads can be placed into manufactured fabric in two ways. The current method for placement of structural fibers exercised by 3TEX is by simultaneous pushing of several loops of weft yarn across, and between, the warp yarn layers by means of several rapiers with eyelets at the end of each rapiers. This allows for a continuous supply of weft yarns from bobbins and their continuous (uncut) placement across the width of the fabric. This approach seems best suited where passing the optical fibers through the eyelet is not a problem. Intrinsic sensor types seem to be the best option in this case, as no rigid sensor head is present to be subjected to the inherent bending, abrasion, and possible snags.

Weaving trials using the SMF28 optical fiber in the looped fashion showed no damage to the fibers, and very little signal attenuation within the fabric. Some attenuation is incurred in the loops at the edges of the fabric. The attenuation is dependent on whether the loop radius is above or below the transmission threshold radius for the fiber. These so-called "selvedge loops" can be increased or reduced to different sizes, and the size most suitable for the necessary light transmission can be chosen. However, such selvedge loop zones are usually cut away in the course of composite part manufacture. Thus, the problem of light attenuation caused by its travel through the weft selvedge loops is not a primary concern anyway.

#### **7.4.3. Integration of Fiber Optics in Z Direction**

The Z (through thickness) yarns in orthogonal 3-D weaves are "crimped", or bent over the respective weft yarns at the top and bottom surfaces of the fabric (see red yarns in Figure 4). Placement of sensors or leads commingled with the Z-yarns is, by far, the most challenging 3-D weaving task remaining, assuming that the sensor fibers are to be subjected to the current fiber treatment by machine in the course of Z-yarn placement. Trials have demonstrated automated weaving of optical fibers in the Z-axis when producing 3Weave™ fabric. These trials indicate that intrinsic sensor types, such as LUNA's DSS, will usually survive the Z-yarn treatment mechanically. Significant signal attenuation can occur if the bend radius in the Z-yarns approaches the transmission threshold radius of the optical fiber. LUNA's DSS fibers have numerical apertures that allow for tighter bends without leaking significant signal strength. This allows for their application within the Z-yarns of some 3Weave™ fabric structures, depending on the bend radii of the Z-yarns in the fabric.

#### **7.4.4. Weaving Effects on Optical Fibers**

By means of a simple collapsing loop test (illustrated in Figure 15), 830nm type wave guides used in Phase I were found to mechanically tolerate minimum radii at or below 2mm, while 1550nm SMF28 Acrylic, and LUNA DSS types used in Phase II tolerated 1.26mm and 1.2mm radii, respectively.

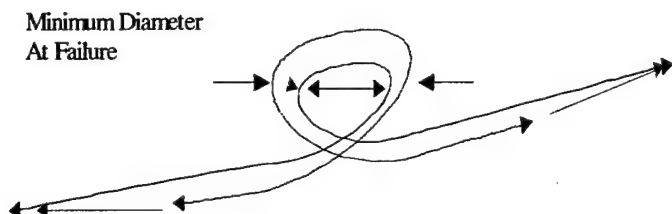


Figure 15. Collapsing loop test used to determine minimum bend radius.

Great care must be taken in the handling of the fibers. When bent to such small radii, they can become highly stressed. The transmission and sensing functions of the fiber take place within the innermost core at the center of the fiber, and as such under bending these functions are protected by their position at the neutral axis of the fiber. The 1.2mm radius of the DSS fiber is mechanically sufficient to allow weaving of the leads into the undulating Z pathways within many 3Weave™ preforms depending on the yarn and unit cell sizes involved.

Bends approaching and below threshold radii causes loss of light due to increasing reflection angles within the core. This can reduce the percentage of the signal remaining in the fiber core. The reduction on overall intensity makes signal to noise ratios increase, and impedes or precludes effective interrogation of the sensors in the fiber. Curves presented in Figure 16 illustrate the thresholds above, which transmission remains efficient in two fibers tested.

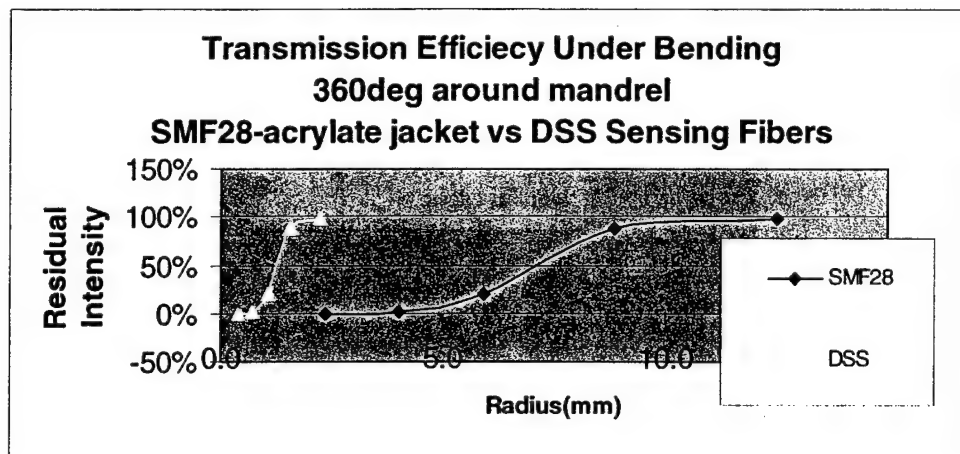


Figure 16. Effects of bending radius on transmission of 1550nm laser in optical fiber types.

## 7.5. Fiber Optic Weaving Trials

Weaving trials were performed by 3TEX in the first 9 months of Phase II and involved integration of standard SMF28 Single Mode acrylic coated optical fibers into preforms during weaving. These fibers were commingled with the "master" warp, weft and Z yarns, and in this way were integrated into the fabric in a fully automated fashion.

### 7.5.1. Conservation of Expensive DSS Fiber

Due to the high cost of DSS fiber, automated weaving has been pursued in steps. This included testing of the limits of the fiber types, selection of preform architecture to be used as the sensor carrier, and measuring live transmission during continuous weaving of the SMF28 optical fibers, on which the DSS fibers are based. Focus was on the safe and confident integration of the more expensive DSS fibers next. The SMF28 optical fibers (which are mechanically comparable to DSS fibers) have been integrated in a continuous, hands-free fashion within 3Weave™ preforms by machine, in the course of regular manufacturing early in Year 1. The effects of micro- and macro-bending on light transmission efficiencies were measured. Steps were taken to isolate various elements in the weaving systems and sensor systems for diagnosis. The SMF28 fibers used in those trials were found to require larger bend radii, transmitted less efficiently than the DSS fiber, and as such served as a conservative test dummy for the DSS fibers. The rationale was that any bending or loading that the less tolerant dummy fibers tolerate, should be easily survived by the DSS fibers.

### 7.5.2. Weaving of SMF 28 - Trial Experiments and Results

SMF28 1550 nm quartz based optical fiber with acrylate coating, was first integrated by 3TEX into two hybrid 3Weave™ preforms in the warp, weft, and Z directions (Figure 17). The placement of the fibers was performed simultaneously at up to 11 points. Placement was entirely hands free, continuous, and fully integrated into the 3Weave™ process. Minor, and commercially feasible adaptations to the existing, proprietary 3TEX weaving process were made to accommodate the special properties of the optical fibers being manipulated.

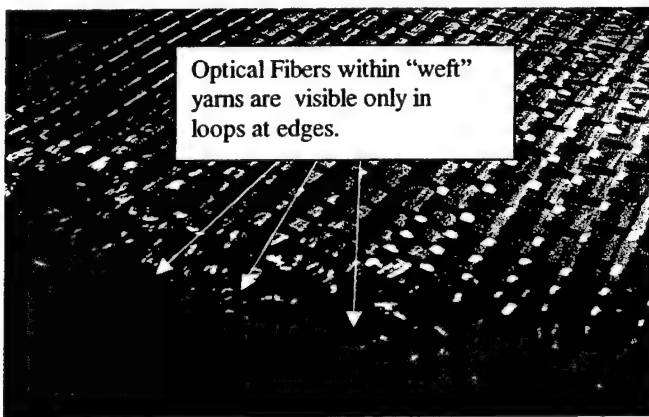


Figure 17. Hybrid preform with 11 separate continuous optical fibers integrated into the warp, weft, and Z- yarns.

Transmission efficiency was measured prior to and after winding from the fiber manufacturer's spools onto 3TEX's weaving specific bobbins. Tubes of 0.25mm diameter SMF28 acrylate coated optical fibers were loaded onto the normal fiber supply creels (spool racks) and drawn through all normal guide and tensioning systems along with Carbon, Aramid and Glass master fibers (see Figure 18). Each small "slave" optical fiber was commingled

with a larger master tow of structural fiber at some appropriate points in the weaving fiber guide systems.

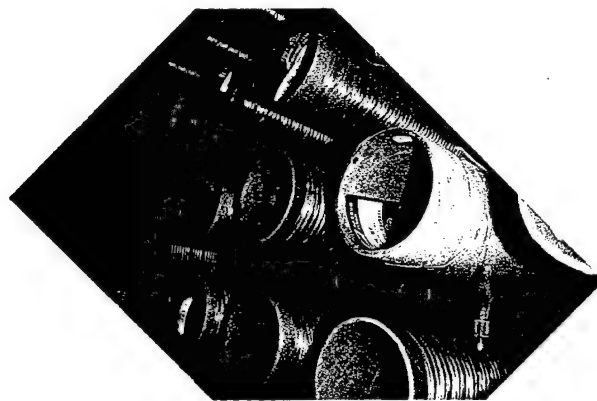


Figure 18. Connector on spool of optical fiber on creel.

Current 3Weave™ weaving machines utilize pushing rapiers, which push loops of weft yarn between the separated layers of warp yarns during weaving. This method uses a long needle having an eyelet at its tip to insert the continuous loops into the fabric as shown in Figure 10. This eliminates cutting the ends of weft yarns at the edge of the fabric, but requires the fibers to bend and slide through the eyelets at high speed during insertion. The EFPI sensors would not be suited for integration into the fabric in this way. However, this approach was used successfully to insert SMF28 optical fibers commingled with the host yarns. Simultaneous multiple insertion of the weft yarns by eyelet rapiers is realized in 3TEX machines.

***During weaving***, 1550nm laser light was passed through each optical fiber, along its path through entire weaving system (see Figure 19 and Figure 20). The signal attenuation was measured during changes to the process yielding various fabric geometries. Laser light was passed through optical fibers before, during, and after fabric formation, and attenuation effects on transmitted intensities were measured, documented, and related to fabric formation specifics. The pick density (weft yarn spacing, in picks/inch=ppi), and weft loop size were varied to test the effects of the resultant radii changes on transmission efficiencies (see Figure 21 and Figure 22). Connections were made at the optical supply packages, and at points beyond the fabric formation zone. This allowed transmission of light around the coils of the wound package, past the fiber supply contact points, through the weaving system, and through the fabric itself.

#### 7.5.3. Results of Weaving Trials

Gradual accumulation of any signal power losses due to micro-bending during weaving was monitored by means of a matched and calibrated 1550nm laser source and power meter. Calibration sequences allowed isolation of losses due uniquely to the supply and weaving systems from those associated to the fiber paths within the fabric preforms.

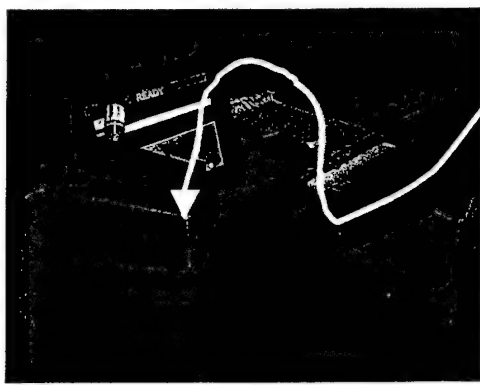


Figure 19. Meter detects transmission through entire spool, loom, and fabric.

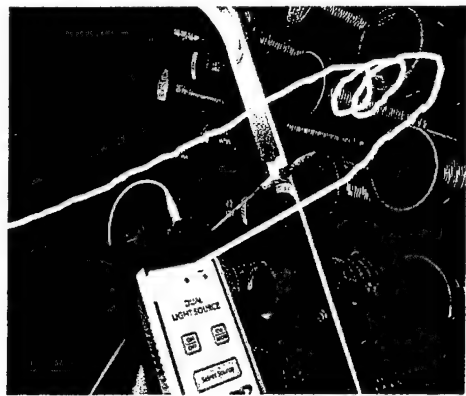


Figure 20. 1550nm laser light was transmitted into optical fibers at creel.

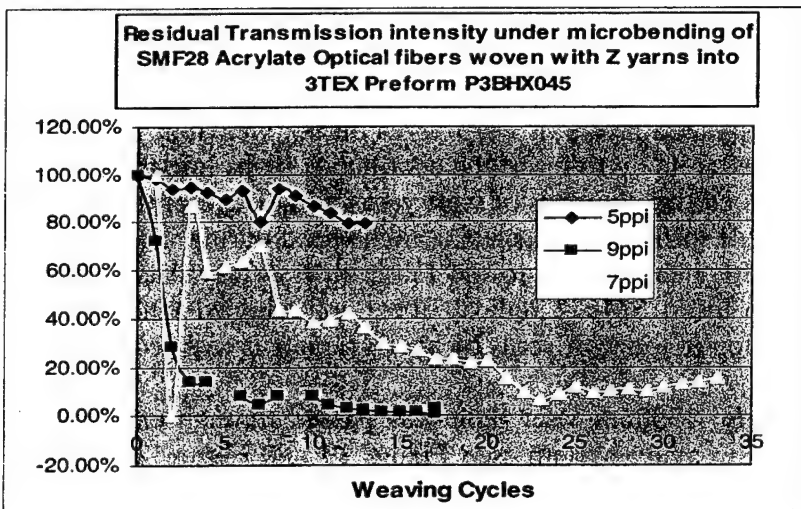


Figure 21. Effect of pick density on signal transmission during weaving by bends in Z-yarns.

Basic measurements were made to isolate the losses associated with the edge loops of the weft fibers versus those from within the fabric itself (the edges are usually trimmed before molding).

In the following section on mapping the fibers, the linearity of the warp and weft fibers can be clearly seen. Where the fiber must turn in a 3-D weave, such as in the Z-yarn, transmission losses mount with each weave cycle (pick). For comparison, a 2-D woven fabric has a sinusoidal crimp to both warp and weft yarns, and that would incur accumulating transmission losses caused by each individual undulation of the yarn path in both the X and Y axes. Forcing either yarn set in a 2-D woven straight to avoid crimp crimps the other even more and compromises the mechanical properties and symmetry of the composite as a result. In the 3-D orthogonal fabric, only the Z incurs losses, and the other two direction yarns are straight, and entirely normal.

Effective use of fiber optic sensors in the through thickness (Z) direction would need to address bending radius issues. Relative to the SMF28 acrylate optic fibers, the DSS poly-imide coated sensing fibers with a smaller 0.155mm diameter and a 4-5 fold improvement in minimum radius, were shown to have potential for improved performance. Further advancements may eliminate this barrier.

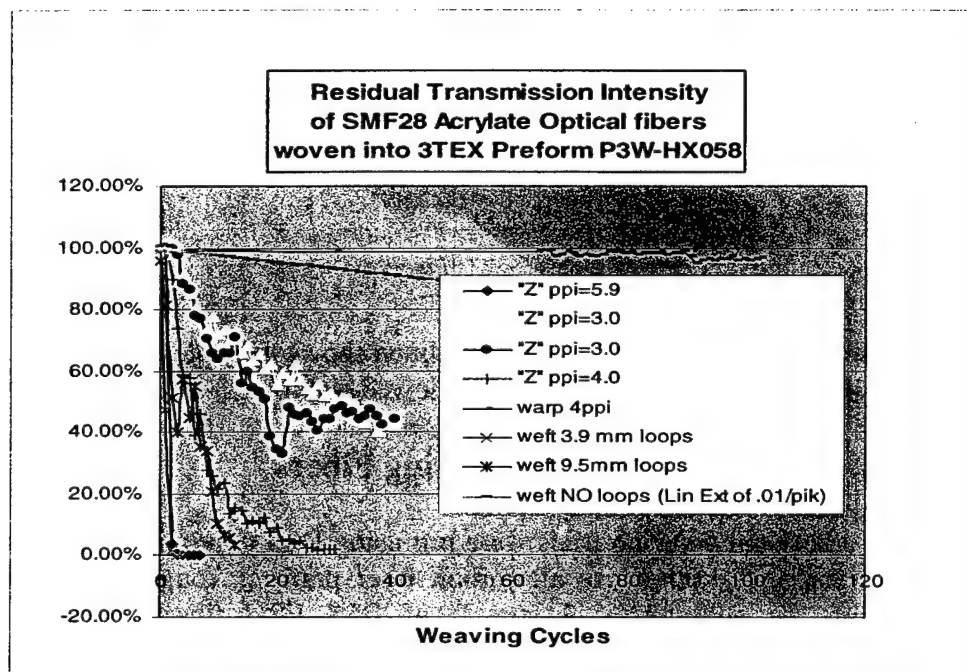


Figure 22. Transmission of 1550nm laser light through 3Weave™ preform during weaving.

Early in Year 2, two additional test specimens were manufactured. Every fiber optic strand in every test specimen provided sufficient optical signal to produce data for the tests. Of particular note is the fact that repeatable data was taken from select gratings along the Z yarns, considering that each of them made up to eight 90° turns along its pathways, despite the expected signal losses.

These three particular Bragg grating sensing fibers were placed into preforms used in bonded lap joint specimens. Interrogation of the many gratings along these sensing fibers, designated ZS1 and ZS2, revealed that some of the gratings registered strains consistently, while others registered highly inconsistent strain readings. The consistent gratings were found to have several bends between them and the DSS laser and interrogation system. This shows that the tight bends did not prevent transmission and interrogation around the corners. Those gratings, which registered inconsistent strains, were thought to have been located in tight bends, distorting the reflection planes, and so were difficult for the system to interpret. This result has implications for the automated integration of sensing fiber strands passing through the Z-axis, and the functionality of those strands in these configurations.

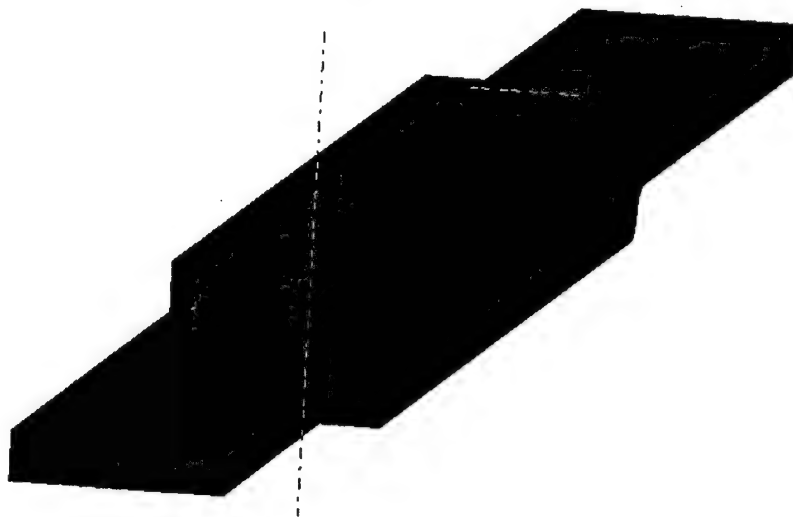


Figure 23. Schematic of double lap joint specimen shows multiple strands of DSS sensing fiber, including ZS1 and ZS2 which followed elaborate 3-axis circuitous path.

## 7.6. Automated Weaving of DSS Sensing Fibers

In late 2004 additional weaving trials were run using DSS polyimide coated fibers in the warp, weft, and Z yarns. An otherwise all carbon fiber preform, roughly 0.325 inches thick, was produced with the addition of 3 strands of DSS FBG fiber. These three strands were simultaneously integrated into the warp (X), weft (Y) and Z axes during weaving, each within its own carbon host yarn. The 3-D weaving machine used in these trials is shown in Figure 24.

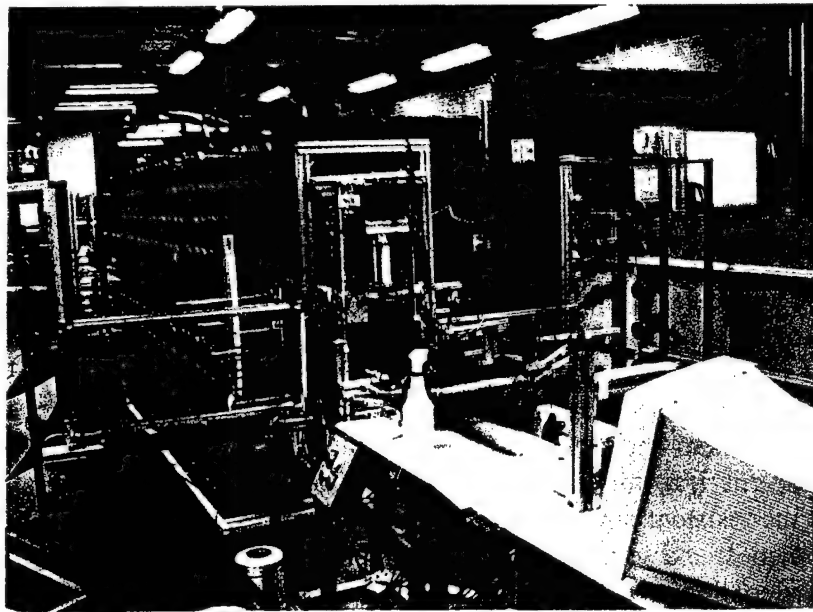


Figure 24. 3TEX 3-D weaving machine used for automated integration of DSS sensing type optical fibers into structural carbon fiber preform in X, Y, and Z axes simultaneously.

Optical fibers, both standard data/com type, and sensing types, were supplied to the loom from 3 inch diameter bobbins in the regular fashion. Each of the optical fibers merged with their host yarns by sharing the same guide eyelets, and heddles in the loom. These procedures are illustrated in Figure 25 and Figure 26.

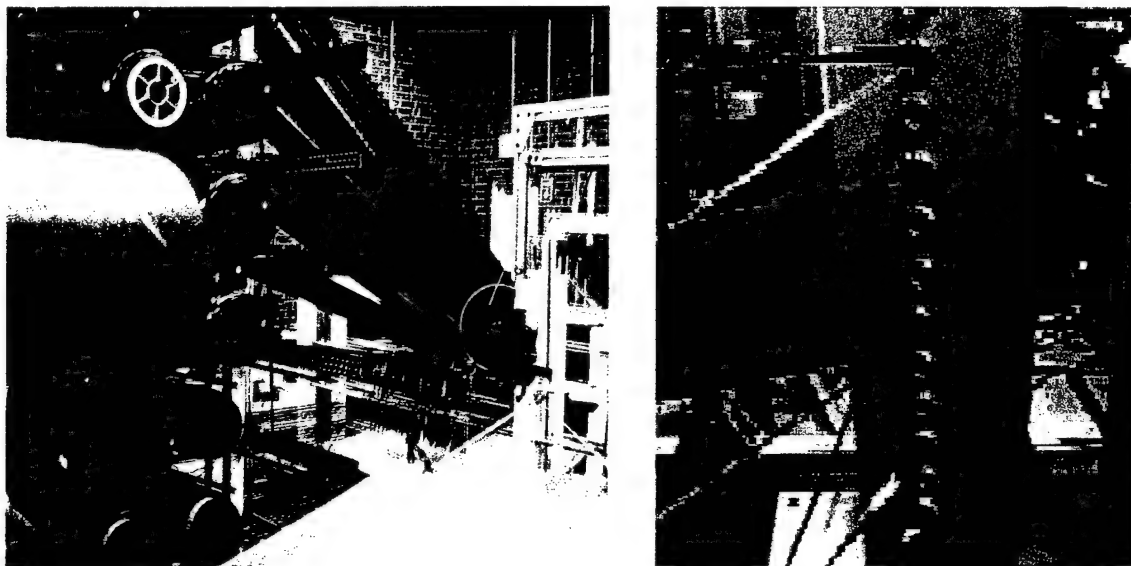


Figure 25. Optical fibers were wound onto standard bobbins, routed through independent tensioning systems, and then supplied to same eyelets as host yarns.



Figure 26. After being merged with a host yarn, the integrated pair passed through the eyelets of the rapiers in the case of the weft (Y) axis yarns.

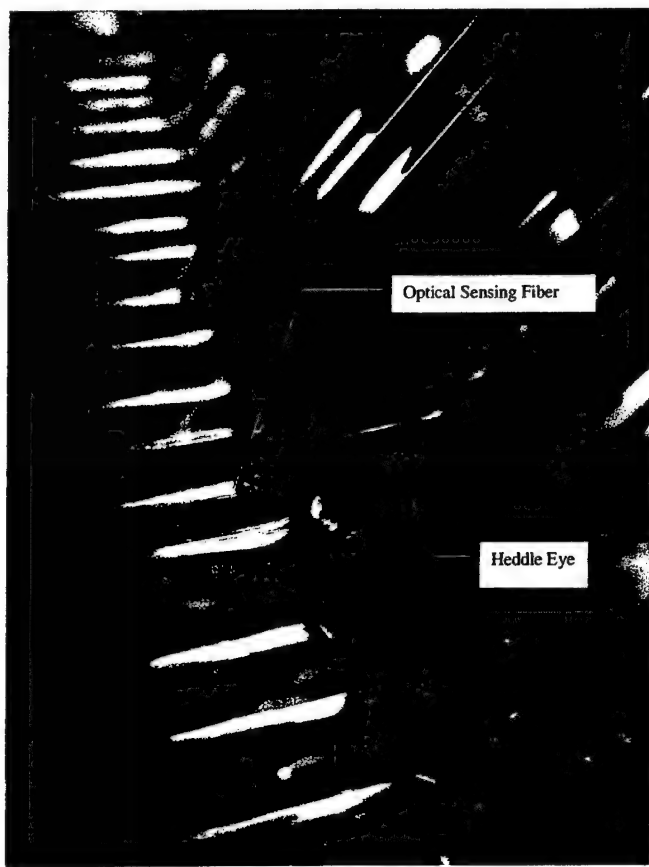


Figure 27. DSS fiber shows at edge of host carbon Z yarn while passing through special heddle eye during weaving.

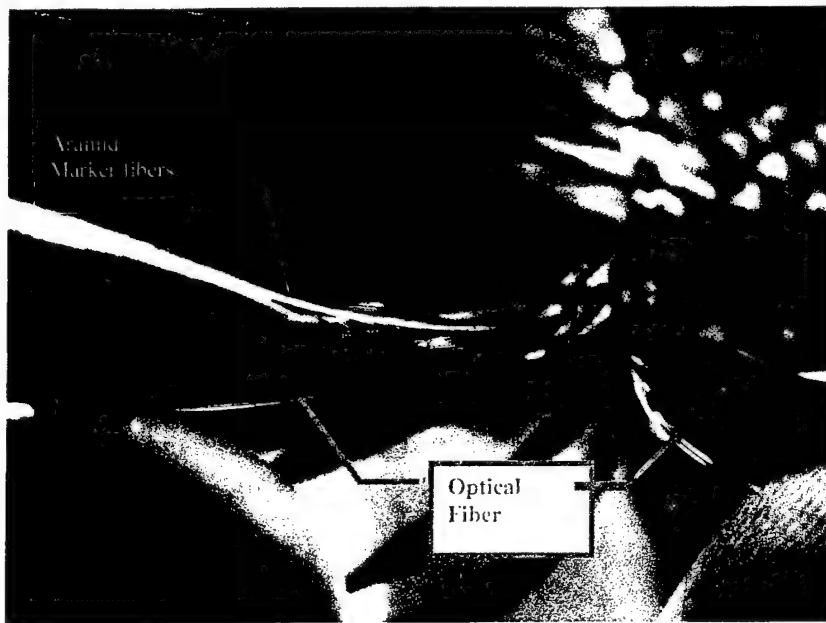


Figure 28. Optical fiber weft loops shown entering and re-emerging from edge of preform.

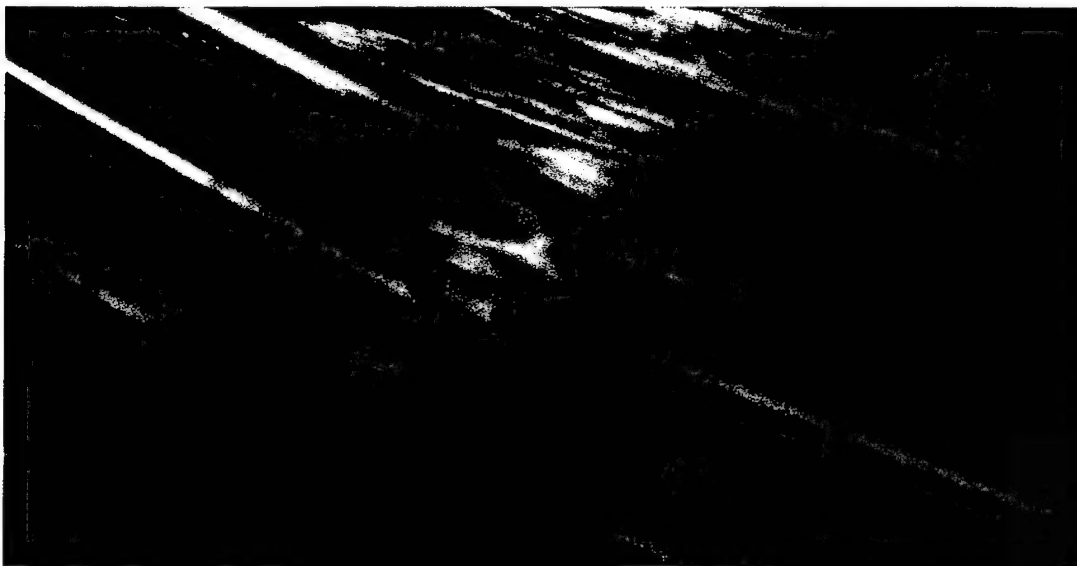


Figure 29. Yellow DSS fiber shows in Z yarn at fabric formation point (fell).

The loom re-inserted the weft yarn according to a preprogrammed schedule resulting in a periodic stripes of sensing fibers spaced arbitrarily at 1cm to match the spacing of the gratings along the fibers. One sensing strand was placed in the warp, and another was woven in with a standard host carbon Z yarn. Thin, yellow aramid yarns were added to the uppermost weft layer along with the sensor strands to serve as visual markers for the sensing strands hidden deep inside the preform.

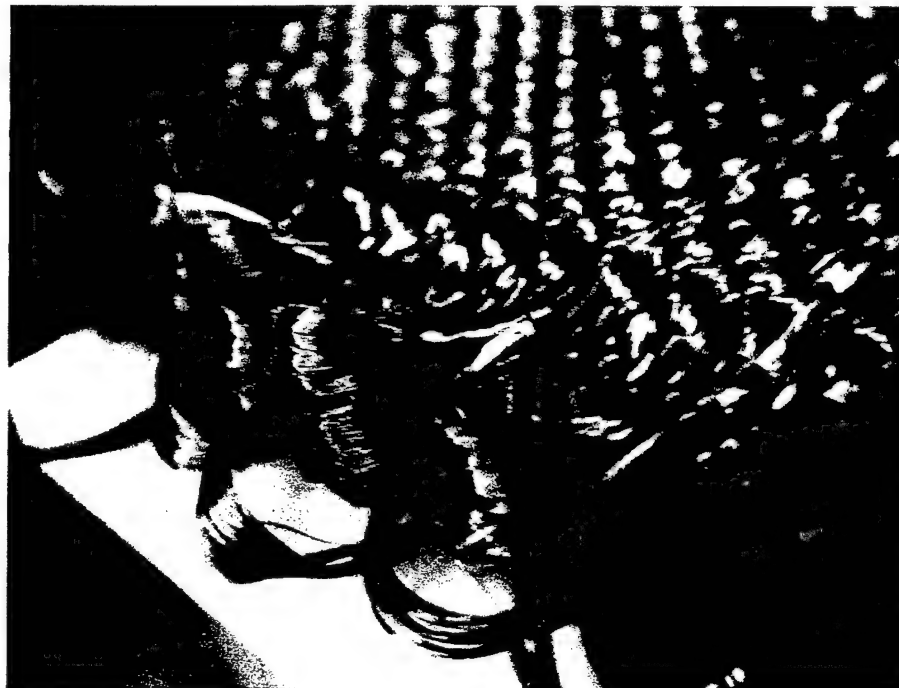


Figure 30. 1cm grid pattern is clearly marked by yellow aramid fibers at the surface.

The resultant preform had more than 800 gratings on 3 strands. This preform also had SMF28 fibers in various locations as might be done to provide a broad band data and communication channels for avionics. It is much like a standard preform might be produced.

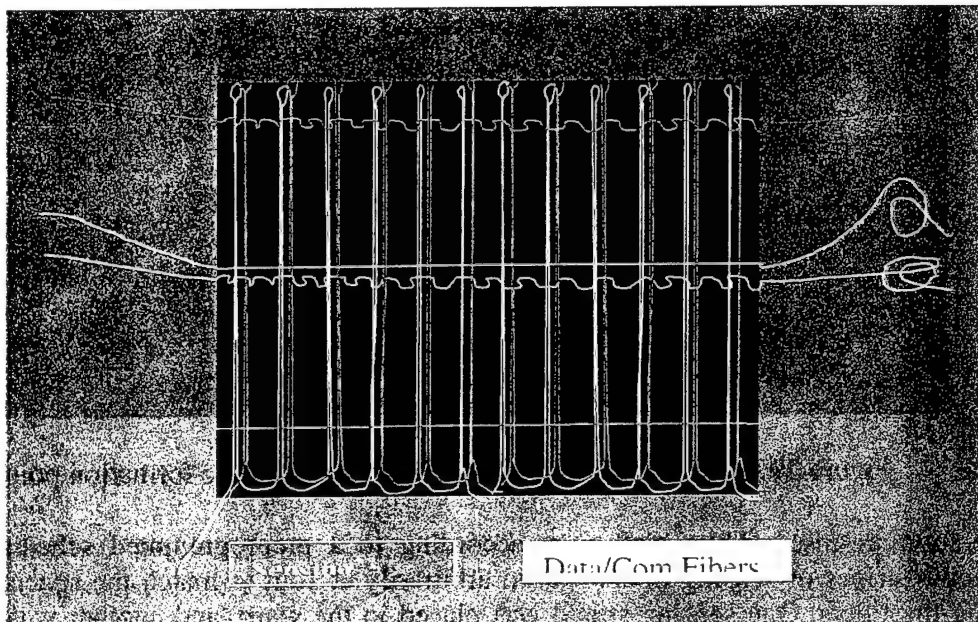


Figure 31. Loom software controlled grid pattern of sensing fiber and data/communication fiber.

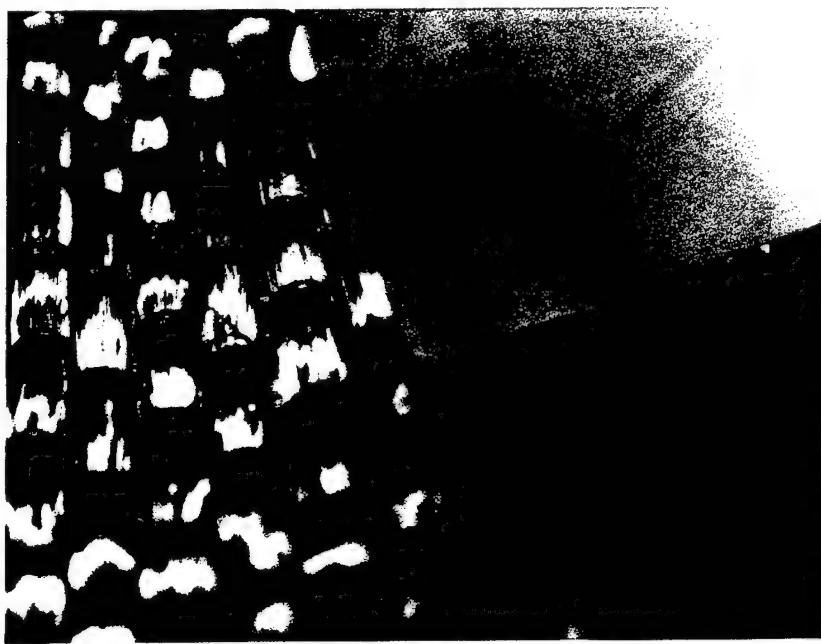


Figure 32. Z-axis sensing fiber shown at entry into preform.

## 7.7. Sensor Challenges/Lessons Learned

The Extrinsic Fabry-Perot Interferometric (EFPI) sensors chosen for Phase I [12] compromised ease of application to gain a data signal less cross-sensitive to changes in temperature and transverse strains. Limitations in the number of sensors locations available in the EFPI fiber and in the formability of the EFPI fiber itself, due to a larger diameter and increased stiffness, ultimately made the fiber Bragg grating (FBG) the preferred fiber optic type of sensor.

The use of serial Bragg grating type intrinsic sensors, such as FBG, in Phase II [13] eliminates the majority of the problems experienced when weaving with the EFPI type sensors. The FBG fibers are smooth and indistinguishable from the ordinary optical fiber types they are based on, and the relatively gentle 3Weave™ process [2,5] does not attempt to crimp them in the warp and weft directions. In the Z yarns, the undulations must be larger than the minimum transmission threshold bending radius to allow transmission.

A standardized grid pattern may be woven which would allow cutting of part preforms relative to the grid, and selection of the strand closest to the point of interest for interrogation. Automated weaving of instrumented preforms is practical as long as the cost of the sensing fiber is not prohibitive. Inclusion of SMF28 data/communications type fibers illustrates the ease of including networking functions in structural parts.

## 8. TEST SAMPLE MANUFACTURE

In Year 1 of Phase II, carbon fiber/vinyl-ester bend specimens, roughly 2 inch wide and 0.25 inch thick, were produced having 2-4 integrated sensing strands each. These were tested to failure in 4-point bending, and yielded valuable data. In Year 2 of Phase II, additional tests of double-lap bonded joint and double-lap bolted joint specimens were produced using the same composite materials/construction, as in Year 1. The same 3Weave™ C-1025 preform type was used previously for the 4-point bend test specimens. The panels from which the optically instrumented component parts for the bonded joints and bolted joints were cut, were produced by the same procedure and with the same matrix resin system as the bending specimens made in Year 1. The details of the preforms, matrix materials, resin infusion processes, and material properties are presented in later sections.

DSS fiber containing FBGs was integrated into selected yarns placed in the fill direction, as well as along several complex paths going in all three orthogonal directions of 3-D woven preform. FBG active grids measured 5mm in length with the centers spaced at 1cm intervals.

Each specimen had several multi-sensor fibers at various depths, locations across the width, as well as adhered in shallow grooves cut into the surface. Each lead had one sensor every 10mm. Each specimen therefore contained from tens to hundreds of integrated optical sensors. Thus, the data from these sensors provide a measurement of strain fields along the length (e.g., in fill direction of the fabric), along the width (e.g., in warp direction of the fabric), and through the thickness.

None of the specimens produced thus far in Phase I and Phase II used the new Cut And Polish (CAP) connector technology during mechanical testing. Instead, the leads dangled outside the preforms during resin infusion and were fusion spliced into standard connectors. While this is not suitable for a production environment, sections of instrumented test specimens, remaining intact after testing in other tasks of this program, were cut away and used to experiment with CAP to allow parallel development without risking test data.

## 8.1. Fabric Preform Parameters

Preform design selection for the bending tests was guided by goal of achieving a specimen suitable for easy testing and having acceptable sensor length to unit cell dimension ratios. For bending tests in particular, having several layers of yarns, in which sensors can be integrated, allows measurement of strain variation through the thickness at several levels. Strains on both compression and tension sides of the beam specimen were recorded. 3TEX manufactured preform type P3W-C1025-12 was used. The fiber and yarn types are listed in Table 2. There are 4 warp and 5 weft yarn layers in the fabric. The unit cell dimensions in the warp, weft and Z directions are 0.1 inch, 0.1 inch and 0.08 inch, respectively. Hence, the unit cell dimensions and the sensor length are nearly identical. Using this fiber preform allowed us to optimize the time and expenses incurred, and tied the resultant specimens to existing material property database.

Table 2. Preform Specifications for Specimens A-D.

### P3W-C1025 Nominal Preform Specifications.

Fiber Type	Warp (0°):	
Carbon PAN T700 24K , 1.1% Sizing, TORAY	Filling (90°):	
Carbon PAN T700 12K , 1.1% Sizing, TORAY	Z (Thickness):	
Carbon PAN T300 3K , 1% Sizing, TORAY	Measurement	Units
Nominal Architectural Parameters		
Width-end-to-end, We-e:	12	inch
Linear Weight,	59.17	oz/yd
Areal Weight	177.5	oz/yd <sup>2</sup>
Thickness, t:	0.25	inch
Warp (0°):	Weight	Fiber Vol.
	Fraction	Fraction
	43.20%	22.90%
Filling (90°):	52.30%	27.80%
Z (Thickness):	4.50%	2.40%
Total:	100.00%	53.20%

## 8.2. Composite Material Based on C-1025 Preform

3TEX manufactured preform type P3W-C1025-12, which was used in all Phase II mechanical test specimens. Pieces of flat preform are 12" wide and 0.236" thick. VARTM processing of this composite material is illustrated in Figure 1.



Figure 33. VARTM processing of 3-D woven composite panel with dangling optical leads.

After the composite specimens were manufactured, and uniaxial foil strain gages were mounted in the center of each facing of the specimen. The gages provided strain level measurements, as well as were used as comparison basis for tensile and compressive moduli determination. The gages were mounted using MBOND 200 adhesive after typical surface preparation (mild abrasive sanding, acetone wipe, MPREP-A, Neutralizer 5).

### 8.3. Resin Infusion

Practice in VARTM (Vacuum Assisted Resin Transfer Molding) manufacturing of composite panels based on 3-D woven performs with integrated optical fibers inside has been educational. There are certain challenges entailed in the resin infusion into 3-D woven fabric preform and composite consolidation cycle. With sensors integrated into the preform, the challenges are: deformation of the preform, simple handling of the preform with leads emerging, loads applied by atmospheric pressure outside vacuum bag, and need of protection of external leads from possible embedment. These challenges, largely related to the delicate nature of the dangling leads outside the preform, make an otherwise simple and cheap VARTM process a delicate and rather expensive procedure. In general, the leads can bear tension, but not bending. At the point where the optical fiber lead leaves the composite, it may just as well be clamped in a vise. If one merely lifted the vise straight up with the lead, it may, in fact, survive, but pulling sideways could readily snap the lead off. Pull on it, but do not bend it sharply at a point. Sensing fiber integrated within the preform is quite well protected by the structural fiber around it. CAP connections discussed later would eliminate, as anticipated, nearly all molding issues.

### 8.4. Fabrication of Carbon Fiber Plates with Integrated DSS Fibers

Up to 120 fiber optic Bragg grating sensors per specimen were integrated into 0.25 inch thick 3-D woven carbon fiber preform, which was then processed into composite panel using VARTM process. Subsequently, internally instrumented composite specimens were cut from the panel,

and mechanically tested in 4-point bending. 3TEX used VARTM to produce flexural specimens using 3TEX preforms with 2 or 4 lengths of DSS sensing fiber sensors integrated. In this section we briefly describe the developed processing approach. Derakane 470-300 vinyl ester resin was used (it was donated by Dow Chemical Corp.). This resin has provided competitive properties relative to a more expensive epoxy resins.

Table 3. Properties of Matrix in Bend Specimens "A"- "D".

Typical Room-Temperature Properties of Clear Castings Made with DERAKANE MOMENTUM 470 Resins <sup>(1)</sup>	
Tensile Strength, MPa/psi	85/12,500
Tensile Modulus, GPa/unit 10 <sup>5</sup> psi	3.6/5.2
Tensile Elongation, %	3.0-4.0
Flexural Strength, MPa/psi	130/19,00 0
Flexural Modulus, GPa/unit 10 <sup>5</sup> psi	3.8/5.5
Heat Distortion Temperature, °C (F°) at 1.82 MPa applied stress (at 264 psi applied stress)	150/300
Barcol Hardness	40

<sup>1</sup> Typical properties; not to be construed as specifications.

Table 4. Formulation of Derakane 470-300 resin used for Bend Specimens "A"- "D".

### DERAKANE\* 470-300

#### Typical Gel Times using methyl ethyl ketone peroxide

Temperature		10-20 minutes	20-40 minutes	40-60 minutes
15°-20°C	MEKP	2.00%	0.50%	1.00%
Cool 60s°F	Cobalt	0.30%	0.20%	0.20%
	DMA	0.10%	0.05%	0.05%
21°-26°C	MEKP	1.50%	0.50%	1.00%
Mild 70s°F	Cobalt	0.20%	0.15%	0.15%
	DMA	0.05%	0.05%	0.05%
27°-32°C	MEKP	2.00%	0.50%	1.00%
Warm 80s °F	Cobalt	0.20%	0.15%	0.15%
	DMA	0.05% <sup>1</sup>	0.05%	0.05%

<sup>1</sup> May be reduced or omitted at higher temperatures.

## 8.5. Optical Sensor Mapping

Radiographs made in Phase I clearly showed the capillary tubes in the EFPI sensor heads but poorly resolved the normal optical fiber leads themselves (Figure 34). The periodic Bragg

gratings within the LUNA's DSS sensing fiber are merely localized effects within standard optical fibers. They allow easier weaving, as they have no snag point or stress risers, but may not induce contrast in radiographs well, as was observed with the plain fibers themselves. Further, the position of the gratings along the length of the fibers would not be apparent even if the fibers were clearly visible. A marking method is thus desired.

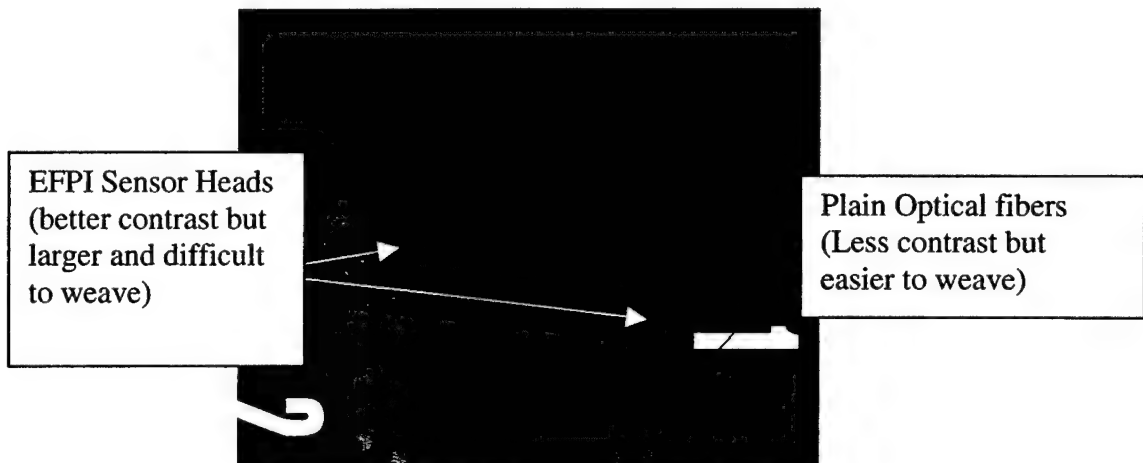


Figure 34. Radiograph from Phase I shows contrast of normal optical fibers versus EFPI sensor heads.

Bragg grating strain sensors are fabricated by burning gridlines into the surface of optical glass fibers. Because the active sensor area is the same diameter as the glass fiber lead, the lead and the sensor cannot be distinguished in an X-ray. Without some sort of marking, there is no way to detect (via X-ray) the location and orientation of the actual strain sensors. In this task, UDRI examined various ways of coating an optical fiber such that the Bragg grating could be differentiated from the optical fiber lead in an X-ray.

A number of issues exist with respect to coating the grating portion of the optical fiber. Any coating must be compatible with, and bond to, the surrounding material into which it is embedded. Without sufficient bonding, load will not be transferred to the sensor and the measured strain will be in error. The coating must be compatible with manufacturing equipment. The grating (sensor) portion of optical fiber cannot be seen visually; even with magnification the gratings are difficult to identify. As a result, coating of the gratings by hand is nearly impossible. The gratings must be marked by the manufacturing equipment that produces the gratings so that precise location of the grating is known. The X-ray-differentiating coating could then be applied during the creating of the gratings or in a secondary operation. The coating must be as thin as possible, otherwise the coating itself may produce a stress concentration that introduces error into the strain measurement. UDRI was able to identify several inexpensive coatings that provided sufficient contrast in an X-ray to differentiate between the marked sensor grating and optical fiber lead. Several vendors, whose equipment or secondary services may be able to apply the coating, were identified and contacted. However, none were able to provide marking or coating services without some degree of research and development. Because development of an

automated marking system was beyond the scope of the current project, the task was terminated at that point to initiate coupon fabrication and testing.

Figure 35 shows a comparison of optical fiber marked (coated) with silver-particle paint and silver-doped epoxy. A portion of gold-coated fiber provided by LUNA is also included. The X-ray in Figure 35 was taken through a piece of 3Weave™ approximately 0.340 inch thick using a 50kV source and 16 sec. exposure. Figure 35 shows the silver-doped epoxy to be impractical. The material is too viscous and the surface energy is too high, resulting in clumping. While the X-ray contrast is excellent, the epoxy mark would result in an unacceptable inclusion within the composite. The silver paint, when applied in a thin coating, results in good contrast while producing minimal clumping. A sample of this material was shipped to 3TEX for application to DSS fiber prior to weaving the 4-point bend samples.

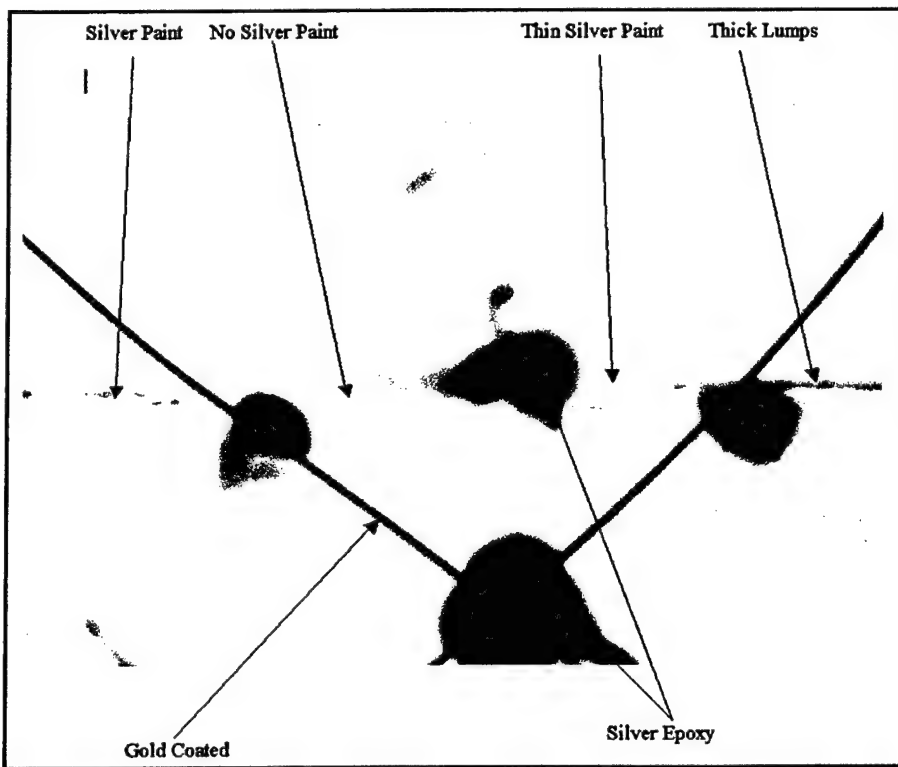


Figure 35. X-ray contrast comparison of various coatings.

#### Potential Coating Vendors

UDRI initiated a search for a commercial entity to apply markings on a production basis. UDRI contacted the following organizations:

- a. **Metal Technology of Indiana (MTI), Inc.**, Lebanon, IN
- b. **Fiberguide Industries**, Caldwell, ID. Fiberguide applied the gold coating to the optical fiber supplied to UDRI by LUNA.
- c. **The Powder Coating Institute**, Alexandria, VA. PCI is an industry-member group that promotes powder coating technology and provided contacts among coaters.
- d. **IBC Coatings Technologies, Inc.** Lebanon IN

Fiberguide's process is not suitable due to the high temperatures involved in coating with gold. IBC's process is much lower temperature and may prove suitable. If development work using Bragg grating technology continues, UDRI recommends contacting IBC to investigate a secondary process for marking. With simple inkjet technology, it should be possible to either mark the sensor areas directly with silver-based paint, or to mask the areas between sensors so that metallic-based markings can be applied to the sensors with a vapor deposition process.

UDRI demonstrated that X-ray with 25kV/5mA energy X-radiography could determine not only the location of the optical fibers within the composite, but also markings on the fiber to show the location of the gratings (sensors), as shown in Figure 36. In this case, the sensor was hand marked with a silver containing paint.

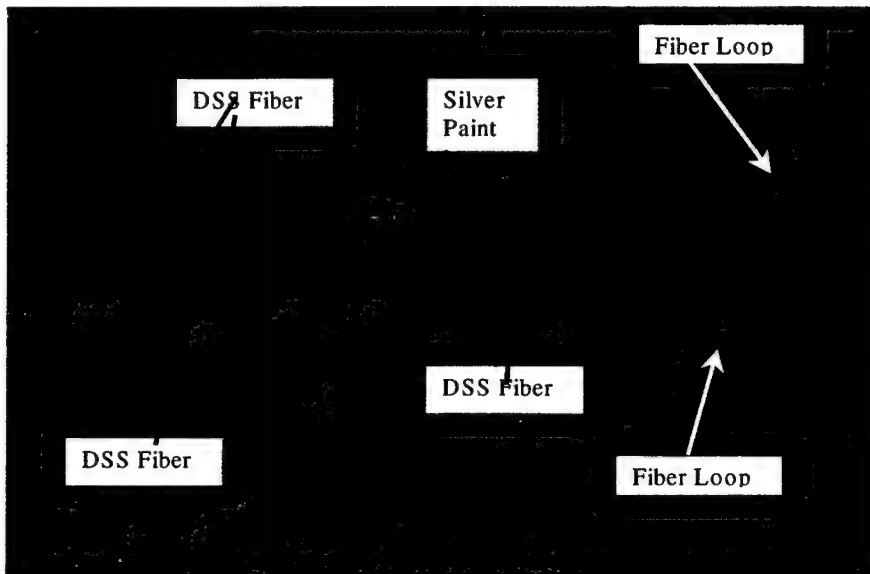


Figure 36. Specimen X-ray, normal view (right end enlarged).

The sensors in the LUNA's DSS fiber are periodic Bragg gratings internal to the fiber itself. For these fibers, the grating locations were marked with an inkjet printer as the fiber ran through the draw tower during production, but the ink was not visible to X-rays. Exact grating location on the fiber is therefore not visible to the eye or in a radiograph unless the part is marked during production.

However, Year 2 investigations into ink jet marking systems used to mark aircraft wiring harnesses, in the printing of conductive metallic circuits, and for radiograph marking systems have confirmed that the radio opaque inks may be applied in a controlled fashion to fine filaments in a continuous process. In the future, a metal-doped ink could be applied accurately and automatically through an inkjet printer during sensing fiber inline with drawing or grating printing processes.

All of the fiber locations in the bonded and bolted joint test specimens were X-rayed. Fiber locations were verified, but not real attempt was made to exactly determine the grating locations.

Sensor positions were ascertained using knowledge of the fiber location, data field symmetries, and grating spacing.

## 9. FOUR-POINT BENDING TESTS

Local arrays of 3-6 independent EFPI sensors were integrated into 3WEAVE™ preforms and composites in Phase I of this STTR [12]. In contrast, arrays of *hundreds* of Bragg grating sensors were placed in 4-point bending specimens in Year 1 of Phase II [13]. Simple plots of data from before and after the addition of cutouts to one of the bend specimens, clearly showed increases in strains nearer the semi-circular cutouts than farther away. This is indicative of a strain gradient around such stress riser. Details of the tests and data were reported in the testing and results sections of the Year 1 progress report.

In Year 2 of Phase II, strain data captured with optical fibers integrated in the adherents of a bonded joint and integrated in the middle plate of the bolted joint, showed internal strain gradients. For the bonded joint tests, the specimen was cycled to 1000 lb<sub>f</sub>, then a hole was drilled into the part and test loads were cycled to 2700 lb<sub>f</sub>. Data from optical fibers and Moiré interferometry patterns were compared. For the bolted joint tests, only optical fiber and resistive foil strain gauge data were taken.

### 9.1. Data Acquisition

LUNA personnel, using their DSS, had collected optical data at a rate of one scan per every 1-6 seconds (10-60 scans per minute). Microstrain data from the DSS and load data from the load cell were simultaneously displayed on video monitors and logged to text files. Text files were then imported into Microsoft® Excel for plotting. Strain gage signals were conditioned using Vishay 2210 Signal Conditioning Amplifiers. Analog output from the conditioners was logged via PC and recorded in text format. Foil strain gauge and load cell data were imported into Microsoft® Excel for manipulation and plotting.

In addition to the strain gage data, the PC recorded analog voltage from the DSS instrumentation's scan indicator. These data served as "markers" in the strain gage data file for optical data scans. The strain gage data in one file could then be correlated with the optical data collected by the DSS.

### 9.2. Experimental Samples and Test Procedures

This section summarizes 4-point bend testing of 3Weave™ samples with integrated fiber optic strain sensors. LUNA's DSS was used in the testing. It consists of discrete FBG sensors burned into a continuous optical fiber. The objective of the testing was to validate accurate strain data captured from the FBG sensors after the DSS fiber was integrated into a 3Weave™ preform and subjected to VARTM resin infusion process. Validation was accomplished through comparison of strain data to data collected from surface-mounted foil strain gages, accounting for location of the optical sensors with respect to the sample's neutral axis and individual fiber tows.

### 9.2.1. Sample Configuration

Four samples, labelled A-D, were prepared from 3Weave™ material with characteristics listed in Table 5.

Table 5. Four-point bending material specifications.

3Weave Style:	4.5 (4 Warp, 5 Weft)
Tow Size	3K
Nominal Unit Cell	Warp x-section (YZ plane): 0.0838 in. wide x 0.0246 in. tall Weft x-section (XZ Plane): 0.0817 in. wide x 0.0232 in. tall Z-Yarn x-section (YZ Plane): 0.0201 in wide x 0.0167 in wide
Nominal Fib. Vol.	48.7%
Nominal Length	12 in.
Nominal Wide	2.1 in.
Nominal Thickness	0.23 in.

A photograph of Sample D is shown in Figure 37. Dimensions of Samples A, C, and D were measured at locations shown in Figure 38. Detailed sample dimensions are given in Tables 6-8. Detailed dimensions for Sample B are not provided since acquisition of optical data was not successful during testing.

A uniaxial strain gage (active grid measuring 0.50 in. x 0.156 in.) was mounted in the center of each side of the samples. The gages provided strain measurement validation, as well as were used for comparison of tensile and compressive modulus values. The gages were mounted using MBOND 200 adhesive after typical surface preparation (mild abrasive sanding, acetone wipe, MPREP-A, Neutralizer 5). The location of the strain gage with respect to the dimension measurement locations is shown in Figure 38.



Figure 37. Example of 4-point bending sample (Sample D).

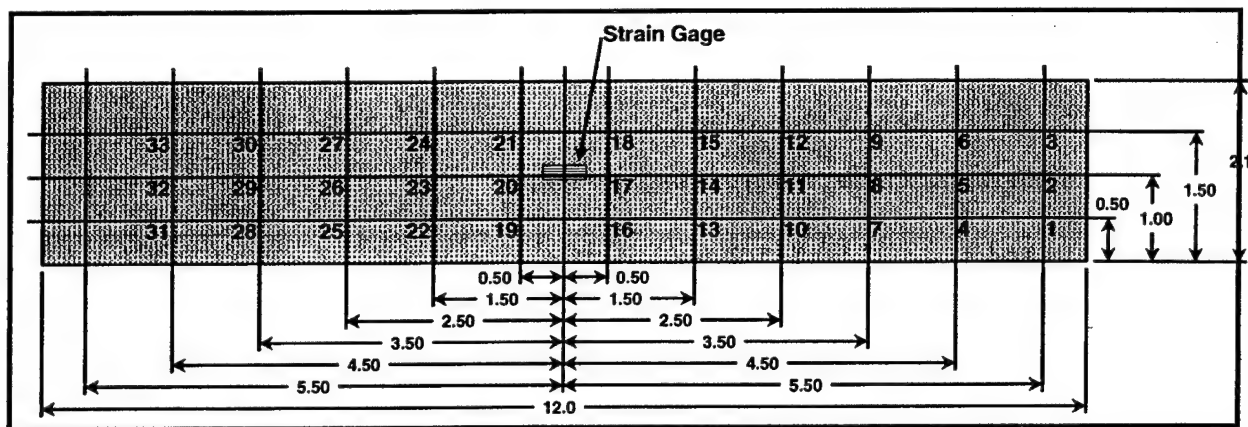


Figure 38. Locations for dimension measurements.

Table 6. Sample A Dimensions (inch).

Location	1	2	3	Width
Thickness	0.239	0.234	0.233	2.106
Location	4	5	6	Width
Thickness	0.232	0.232	0.229	2.111
Location	7	8	9	Width
Thickness	0.229	0.230	0.229	2.116
Location	10	11	12	Width
Thickness	0.231	0.241	0.230	2.120
Location	13	14	15	Width
Thickness	0.243	0.258	0.246	2.122
Location	16	17	18	Width
Thickness	0.229	0.229	0.231	2.129
Location	19	20	21	Width
Thickness	0.232	0.232	0.232	2.137
Location	22	23	24	Width
Thickness	0.230	0.229	0.231	2.145
Location	25	26	27	Width
Thickness	0.239	0.237	0.234	2.149
Location	28	29	30	Width
Thickness	0.234	0.229	0.230	2.152
Location	31	32	33	Width
Thickness	0.229	0.231	0.232	2.164

Table 7. Sample C dimensions (in).

Location	1	2	3	Width
Thickness	0.271	0.271	0.270	2.186
Location	4	5	6	Width
Thickness	0.236	0.237	0.238	2.189
Location	7	8	9	Width
Thickness	0.230	0.232	0.233	2.188
Location	10	11	12	Width
Thickness	0.233	0.235	0.236	2.187
Location	13	14	15	Width
Thickness	0.239	0.261	0.238	2.184
Location	16	17	18	Width
Thickness	0.235	0.272	0.238	2.178
Location	19	20	21	Width
Thickness	0.236	0.257	0.235	2.186
Location	22	23	24	Width
Thickness	0.248	0.245	0.238	2.190
Location	25	26	27	Width
Thickness	0.240	0.243	0.242	2.196
Location	28	29	30	Width
Thickness	0.236	0.237	0.240	2.207
Location	31	32	33	Width
Thickness	0.236	0.235	0.235	2.211
Location	34	35	36	Width
Thickness	0.233	0.236	0.235	2.221

Table 8. Sample D dimensions (inch).

Location	1	2	3	Width
Thickness	0.226	0.232	0.238	2.334
Location	4	5	6	Width
Thickness	0.228	0.231	0.233	2.323
Location	7	8	9	Width
Thickness	0.232	0.234	0.241	2.309
Location	10	11	12	Width
Thickness	0.235	0.234	0.238	2.303
Location	13	14	15	Width
Thickness	0.238	0.248	0.239	2.296
Location	16	17	18	Width
Thickness	0.234	0.244	0.243	2.288

Location	19	20	21	Width
Thickness	0.240	0.260	0.234	2.274
Location	22	23	24	Width
Thickness	0.230	0.228	0.232	2.267
Location	25	26	27	Width
Thickness	0.230	0.239	0.232	2.257
Location	28	29	30	Width
Thickness	0.224	0.230	0.228	2.255
Location	31	32	33	Width
Thickness	0.228	0.232	0.233	2.256
Location	34	35	36	Width
Thickness	0.237	0.241	0.242	2.265

DSS fiber containing FBG's was woven into each sample in the weft direction (along the length of the sample). FBG active grids measured 5mm in length with the centers spaced at 1 cm intervals. In Samples A, B, and C, DSS fiber was woven into weft layer 2, looped around, and returned in weft layer 3, creating 2 DSS paths along the length of the sample. Sample D contained a second loop (layers 2 and 4) and, therefore, 4 DSS paths. In addition, surface optical fibers were mounted on the top and bottom surfaces of each sample.

### 9.2.2. Detection of Sensor Locations Using X-Radiography

X-radiography of each sample was performed to locate and determine the orientation of the DSS fiber paths. X-rays were taken at normal incidence and at an inclined incidence. Inclined incidence was used to estimate depth of the DSS fiber. The width of the sample was in excess of what could be penetrated by the X-ray source, preventing edge-wise views. X-ray examples are shown in Figures 39-42 (Sample A). Figure 39 shows the entire X-ray picture. The DSS fibers are visible along the approximate centerline of the sample. Enlargements of the left, center, and right portions of the sample (Figures 40 – 42, respectively) show the individual DSS fiber paths. The paths line-up (vertically through the sample) at various points along the length of the sample and separate at other points. The DSS fiber loop is visible at the right end of the sample (Figure 42). The inclined X-ray of Sample A were also taken and have been used to confirm Z coordinates of integrated optical fibers.

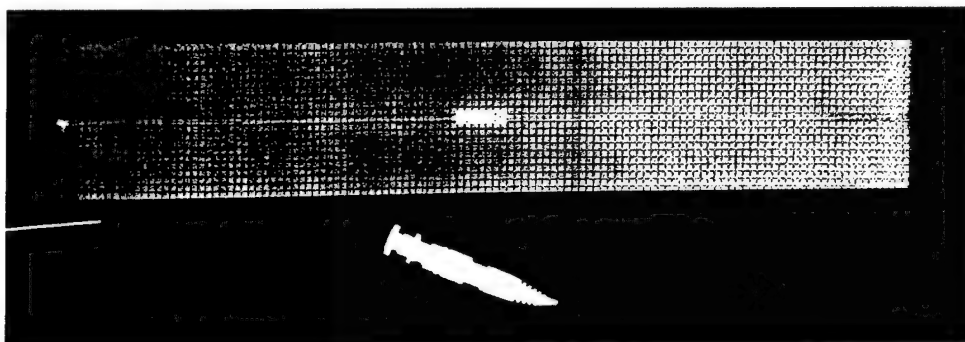


Figure 39. Sample "A" X-ray (normal view).

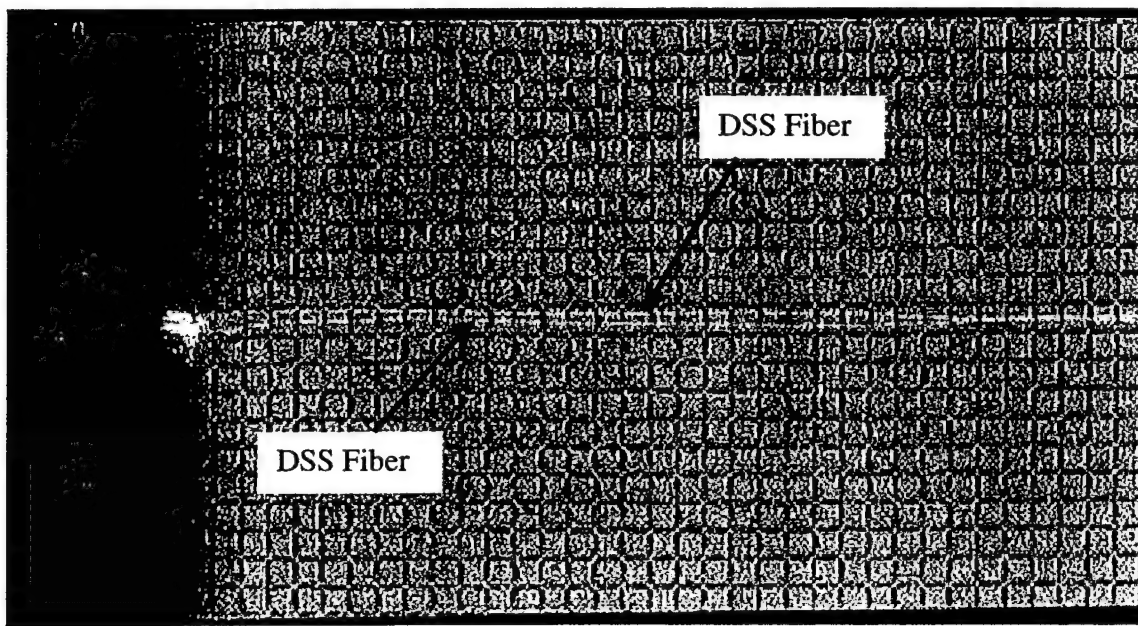


Figure 40. Sample "A" X-ray (normal view, left end enlarged).

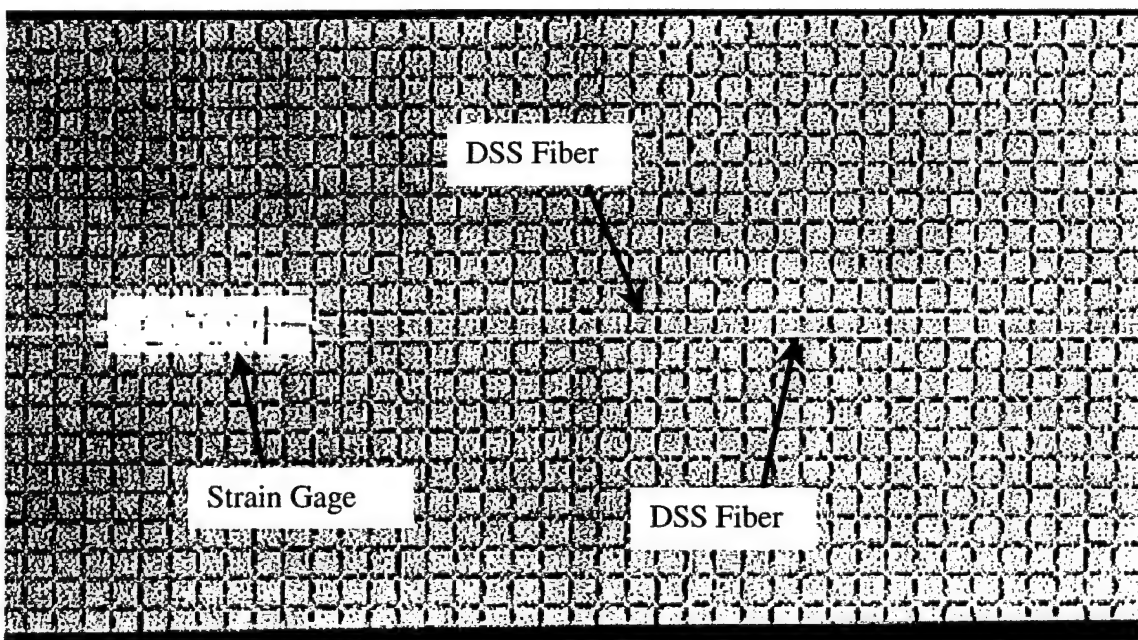


Figure 41. Sample "A" X-ray (normal view, center enlarged).

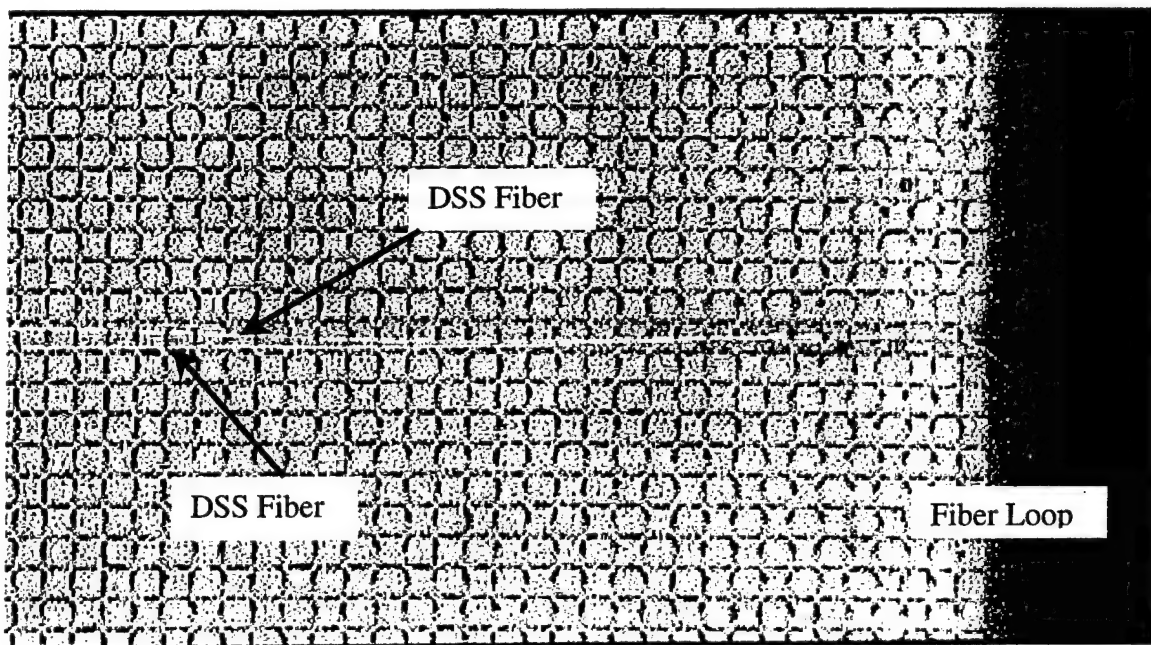


Figure 42. Sample "A" X-ray (normal view, right end enlarged).

### 9.2.3. Loading Configuration

The loading fixture was configured to provide an outer span of 11.0 inch and an inner load span of 5.50 inch for Samples A and C. The inner load span for Sample D was increased to 6.00 inch to avoid contact with surface mounted optical sensors. Figure 43 shows a photograph of the fixturing system with specimen installed. Optical fiber leads and the center displacement extensometer are visible.

Load was applied in machine-displacement control at a rate of 0.05 inch/min. to Sample A. The rate was increased to 0.1 inch/min. for Samples C and D to reduce the length of time required for a test. Both rates qualify as "quasi-static" rates since inertia effects of the loading were negligible. Each sample was loaded twice. The first included an extensometer rigged to the center portion of the sample to record center deflection. Peak loads in these tests were within the elastic range of the sample. In the second loading, samples were loaded until failure, or until further cross-head movement resulted in no additional (or decreasing) load.

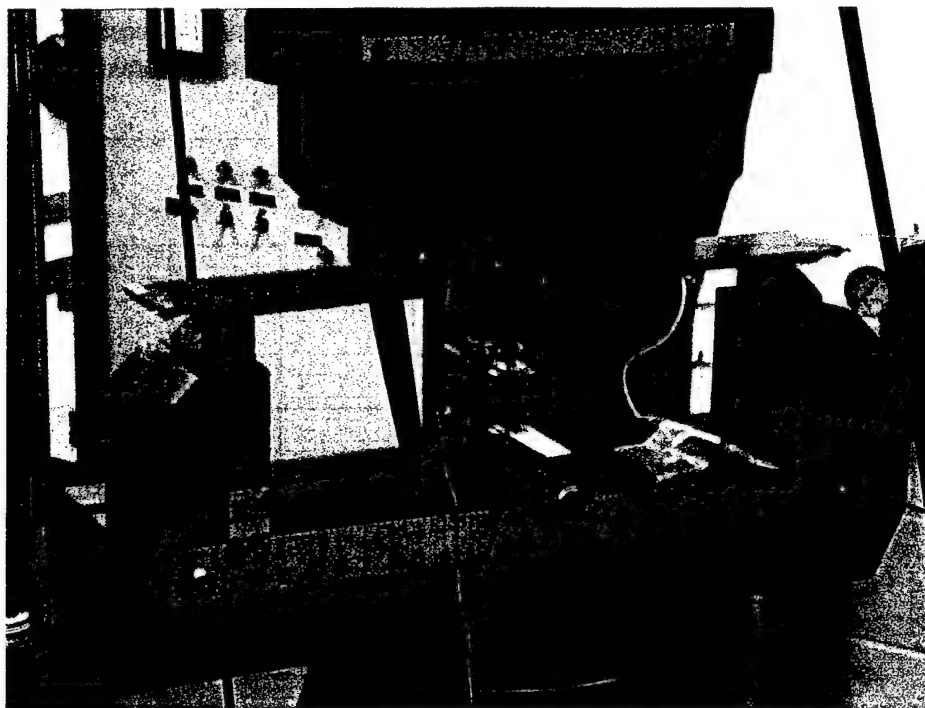


Figure 43. Four-point bend sample installed in load fixture.

#### 9.2.4. Data Acquisition

Optical data were collected by LUNA personnel using their patented DSS. Data were collected at a rate one scan per every 6 seconds (10 scans per minute). Data in terms of microstrain were logged to text files. Strain gage signals were conditioned using Vishay 2210 Signal Conditioning Amplifiers. Analog output from the conditioners was logged via PC and recorded in text format. Data from both sources were imported into Microsoft® Excel for manipulation and plotting.

In addition to strain gage data, the PC recorded analog voltage from the DSS instrumentation's scan indicator. These data served as "markers" in the strain gage data file for optical data scans. The strain gage data in one file could then be correlated with the optical data collected by the DSS. Strain gage data were acquired at 5 samples per second.

### 9.3. Strain Monitoring Results in Four-Point Bending Tests

Significant amounts of data were collected for each sample, owed to integration between 24 and 101 Bragg grating sensors carried by each optical fiber. Spatial strain distributions at fixed load are discussed below for all DSS fibers.

#### 9.3.1. Sample A

Test data for Sample A are shown in Figure 44 through Figure 48. These data are from Loading #1 (linear-elastic loading), since the number of data points in Loading #2 (up to failure loading) exceeded the capacity of the PC's logging software. Figure 44 shows clear linearity in the foil

gage response. Using a strength-of-materials approach, the macroscopic flexural stiffness of Sample A was obtained as 10.4Msi in tension and 10.2Msi in compression.

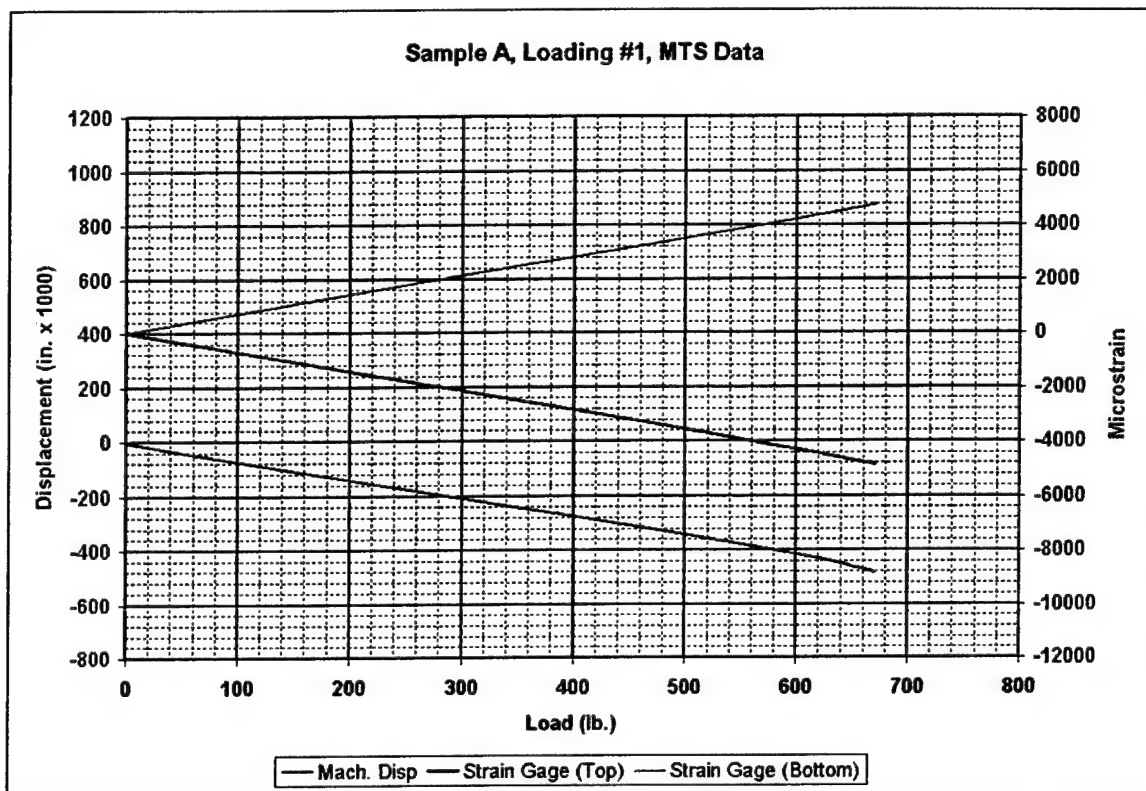


Figure 44. Foil strain data and machine displacement, Sample A.

Figure 45 compares foil and optical strain data for several load levels. The physical location of the foil gages relative to the optical gages is  $\pm 1$  sensor. Foil gages read consistently lower strain than optical gages, and the difference increases with load level. The difference may be related to the position of the optical fiber relative to the fiber tows. As shown in Figure 46, the surface optical fiber lies between fiber tows, resulting in somewhat higher strain for equivalent loading (low-stiffness resin occupies the space between tows). Figure 47 shows internal optical strain data at the same load levels as in Figure 45. The sensor response clearly shows the area between the load noses (a region of constant axial stress), as well as the area outside the outer supports. Deviations from uniform strain between the load noses are repeatable at the various load levels, and are attributed to slight differences in actual physical location within the internal tow. The second pass of the optical fiber through the test section results in a lower response magnitude due to the fiber's position closer to the neutral axis of the samples and due to slight attenuation as the signal passes through the loop at the sample end.

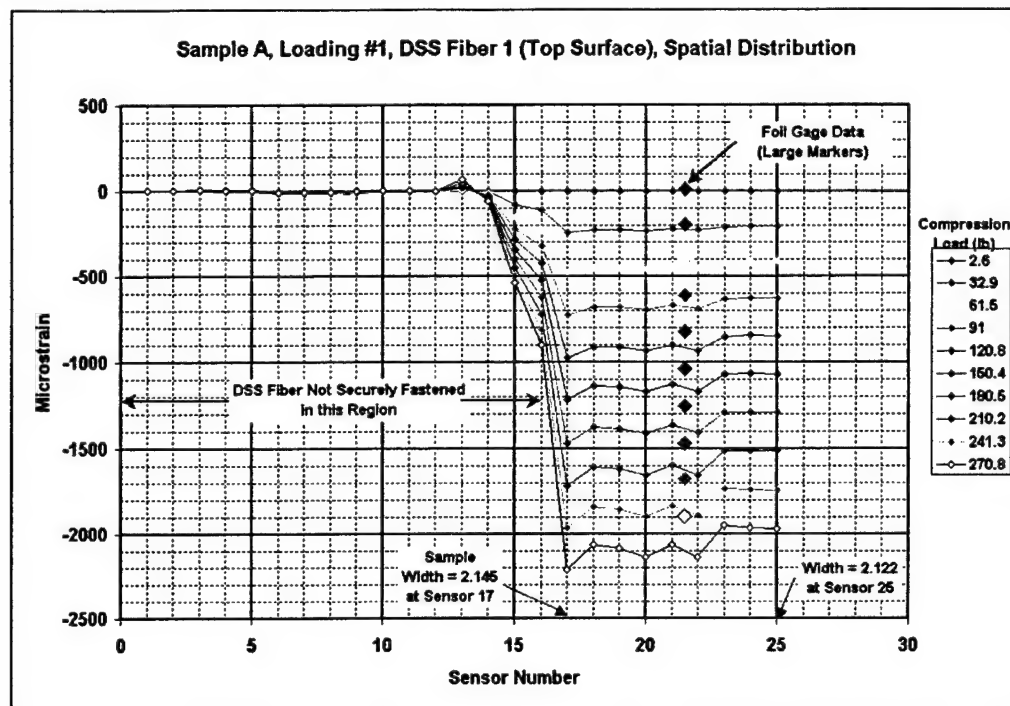


Figure 45. DSS Fiber 1 strain data, top surface of Sample A.

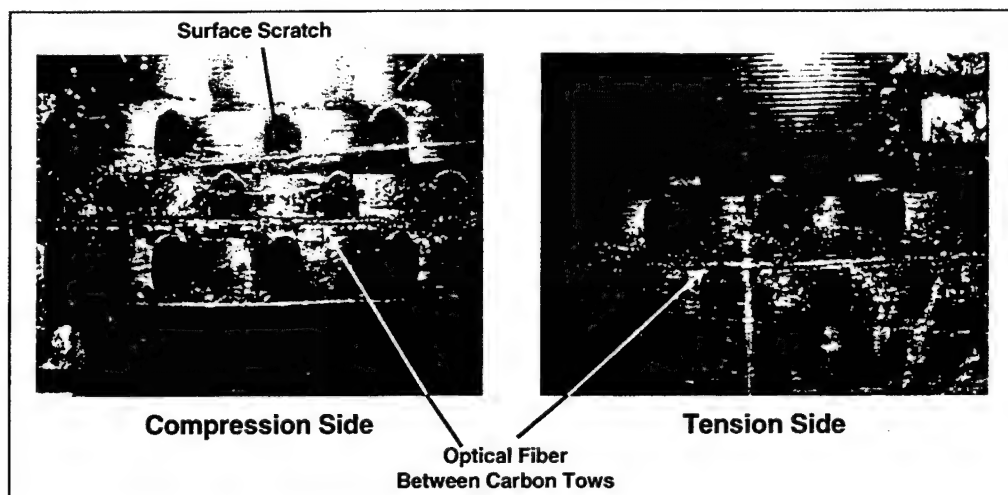


Figure 46. Closeup of surface optical fibers near strain gage.

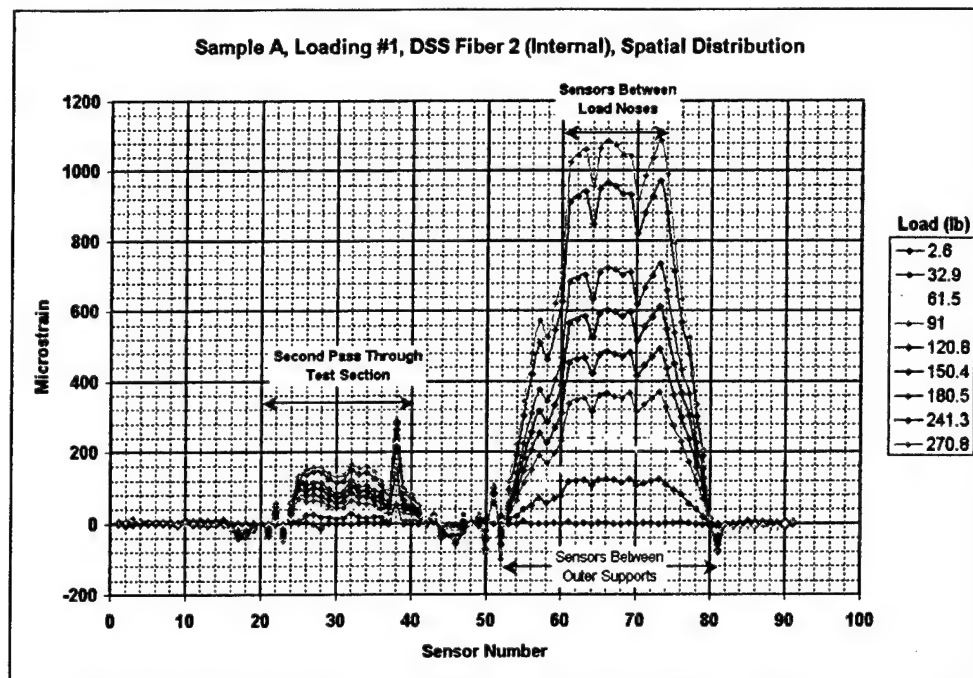


Figure 47. DSS Fiber 2 strain data, internal for Sample A.

Figure 48 shows optical fiber response on the bottom (tension) surface of the sample. As with the top surface gage, the foil gage data is consistently lower than the optical gage for specific load levels. Note that the DSS fiber appears to fail between 120 lb and 150 lb as the sense changes from tensile to compressive. The tensile surface of the sample is not damaged.

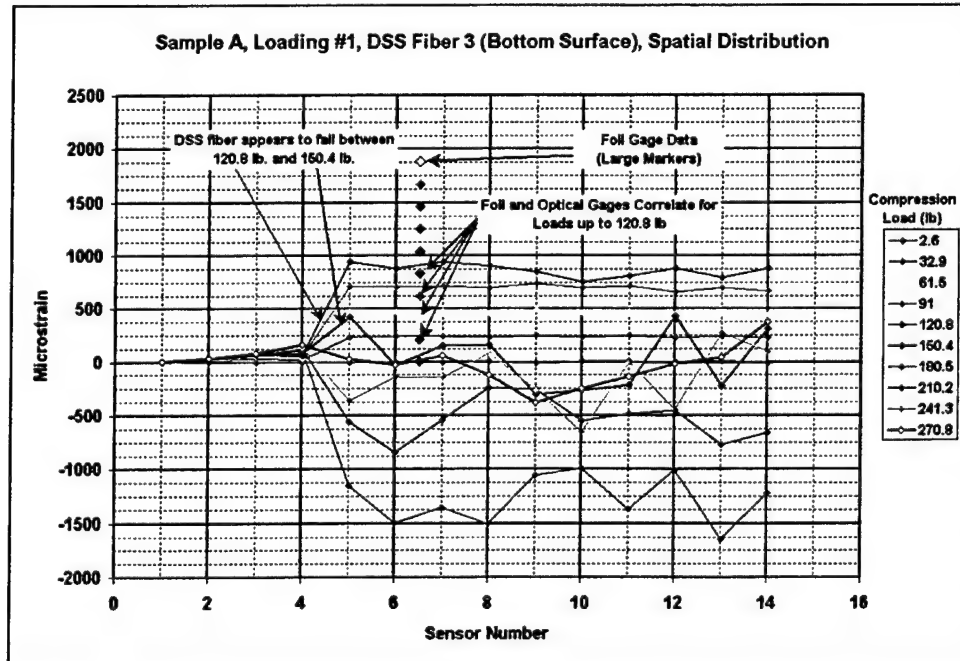


Figure 48. DSS Fiber 3 strain data, bottom surface of Sample A.

### 9.3.2. Sample C

Figure 49 indicates linear strain and displacement response for Sample C up to approximately 620 lbf. Using a strength-of-materials approach, the flexural moduli of this sample are obtained as 9.86Msi in tension and 9.83Msi in compression. Figure 50 compares foil gage and optical sensor strain monitoring results.

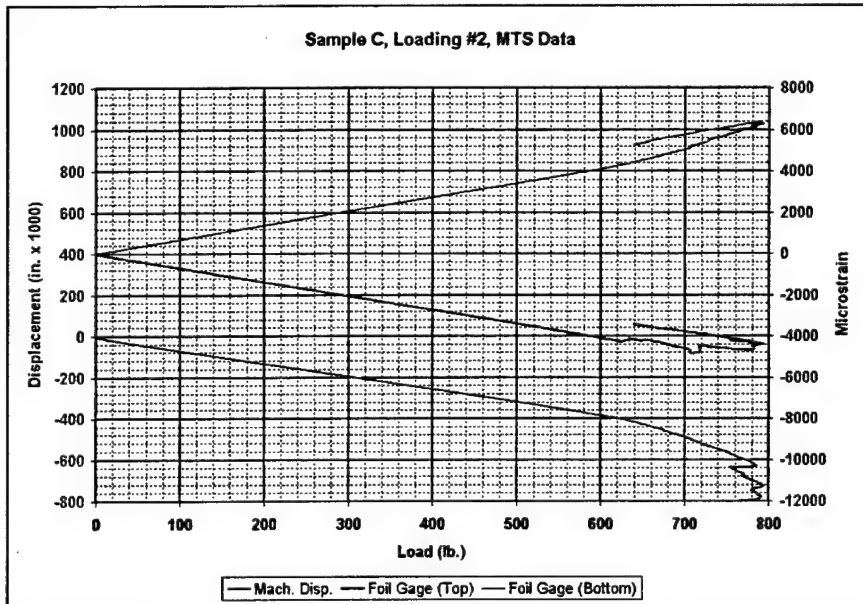


Figure 49. Foil gage strain data and machine displacement, Loading #2 of Sample C.

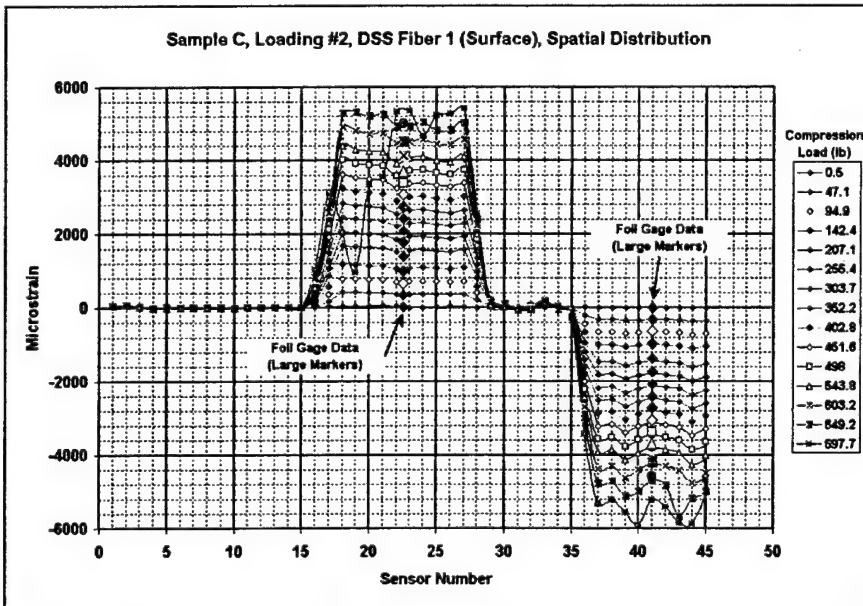


Figure 50. DSS Fiber 1 strain data, surface of Sample C, for several load levels.

The physical location of the foil gages relative to the optical gages is  $\pm 1$  sensor. Foil gages read somewhat lower than optical gages in tension, although the foil gage is positioned near an apparent "valley" in the optical data. Foil gages match nicely to optical gage data in compression, up to about 600 lbf. Optical gages on both surfaces show uniform strain change with load up to the interval 603 – 649 lbf. This range correlates to development of damage in the sample as indicated by the foil compression gage at about 620 lbf (Figure 49).

Figure 51 shows internal strain distribution for the optical sensors placed in Layers 2 and 3 of the sample. Features indicating the location of the load and support spans are clearly visible. The return-path of the optical fiber varies slightly above and below the neutral axis, resulting in regions of positive and negative strain data. The large spikes in the data at the load noses indicate the presence of large sub-surface contact stresses beneath the load noses.

### 9.3.3. Sample D

Sample D was loaded within its linear range during Loading #1. Two 0.5 inch – radius cutouts were then machined into the edges of the sample, creating two "open-hole" conditions at the location of the strain gage (Figure 52). The optical fibers running down the center of the sample were near the edges of the cutouts (as would be optical fibers running along the edge of a sample with a centered hole), thus allowing the optical fibers to sense a stress concentration. The sample was reloaded in bending. In each of the following comparisons, the first data set represents bending response of the sample *without* the cutouts, the second represents bending response *with* the cutouts.

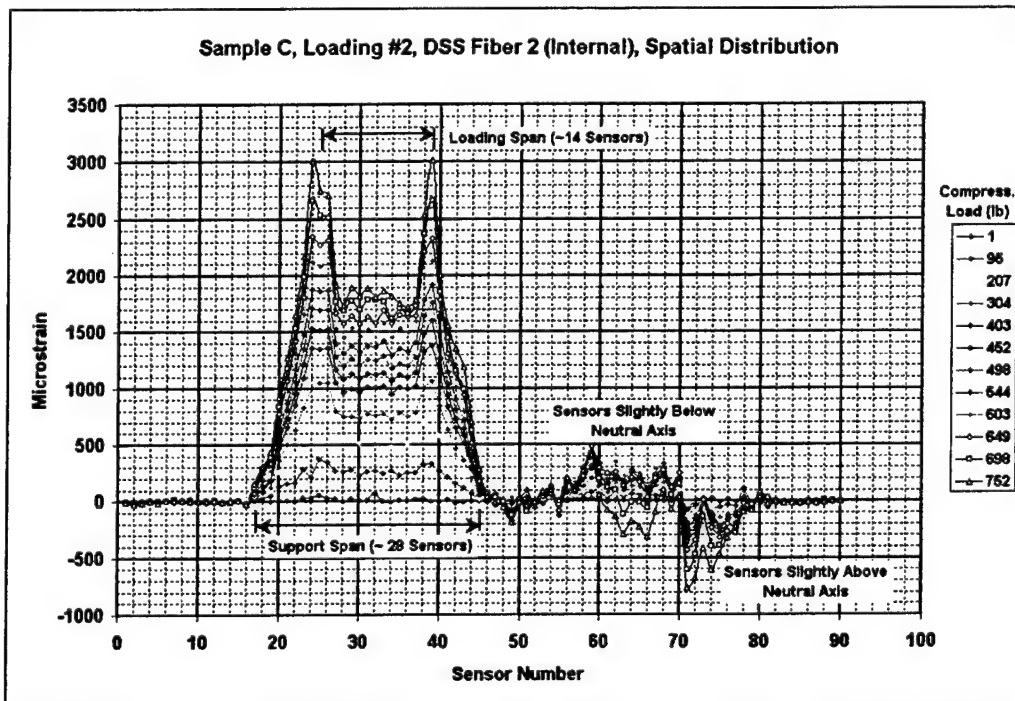


Figure 51. DSS Fiber 2 strain data, internal Sample C.

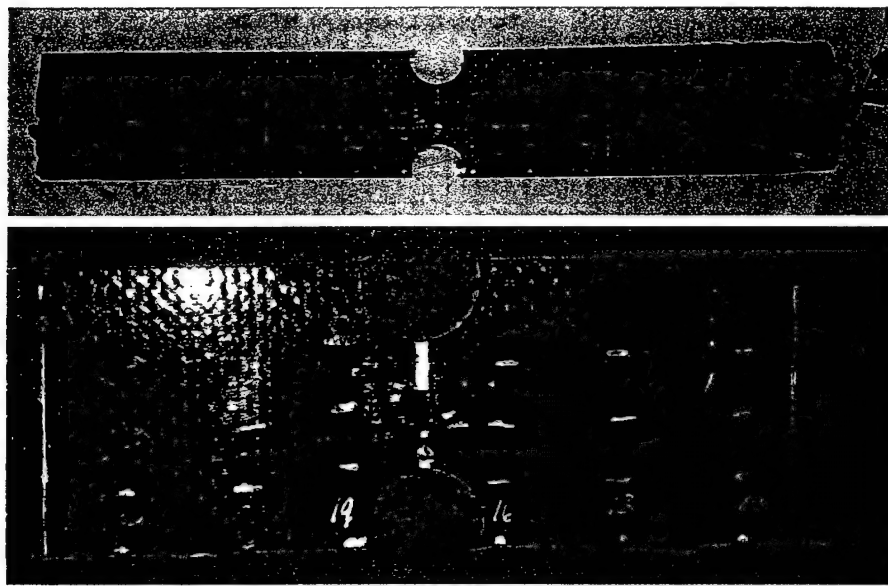


Figure 52. Edge cutouts in Sample D.

Figure 53 indicates linear strain and displacement response for Sample D up to approximately 325 lbf, which was the upper load limit of the test. Using a strength-of-materials approach, the flexural modulus of this sample was obtained as 9.95Msi in tension and 9.69Msi in compression. Figure 54 shows the "softer" response of Sample D with the cutouts. The response remains linear up to about 365 lbf.

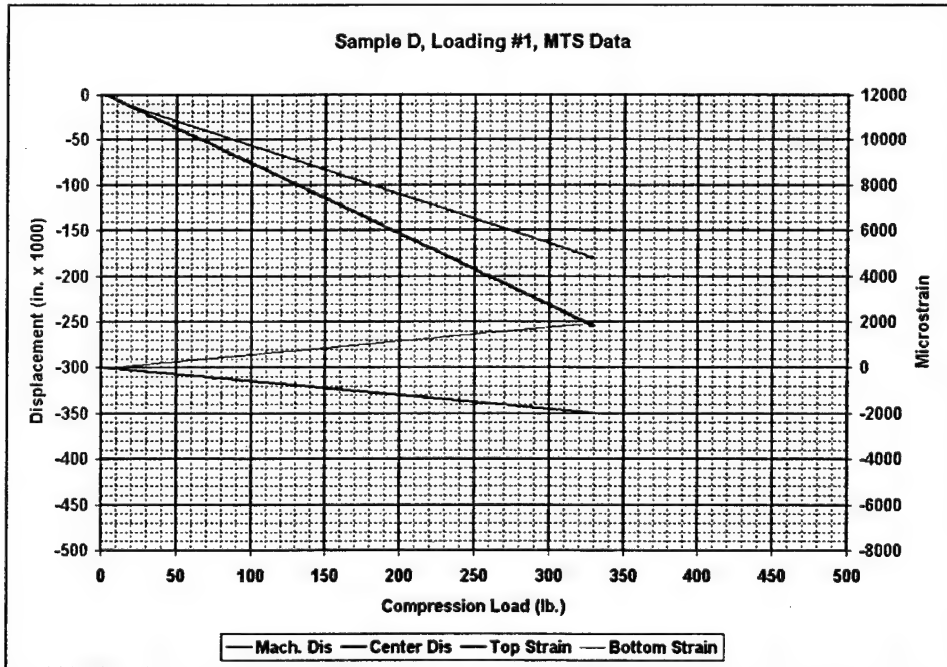


Figure 53. Sample D foil strain gage data and machine displacement, Loading #1.

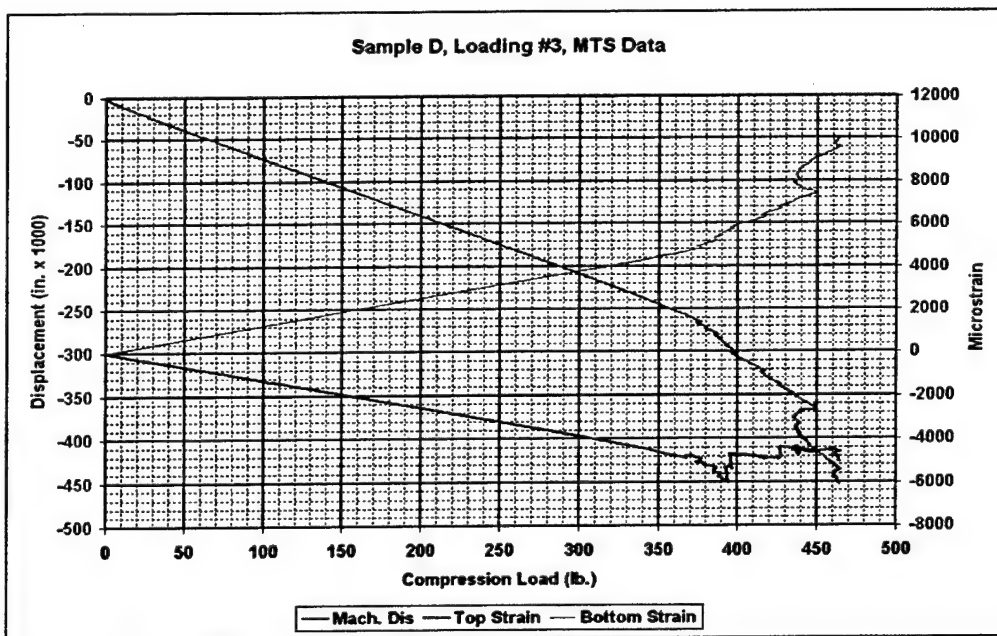


Figure 54. Sample D foil strain gage data and machine displacement, Loading #3 (sample with edge cutouts).

Figure 55 and Figure 56 compare foil and optical strain data for several load levels from the top and bottom surfaces of Sample D before and after the cutouts were made, respectively. Both the optical and foil gauges were applied externally to the completed coupons. The accuracy of the physical location plotted for the foil gages relative to the optical gages is  $\pm 1$  sensor.

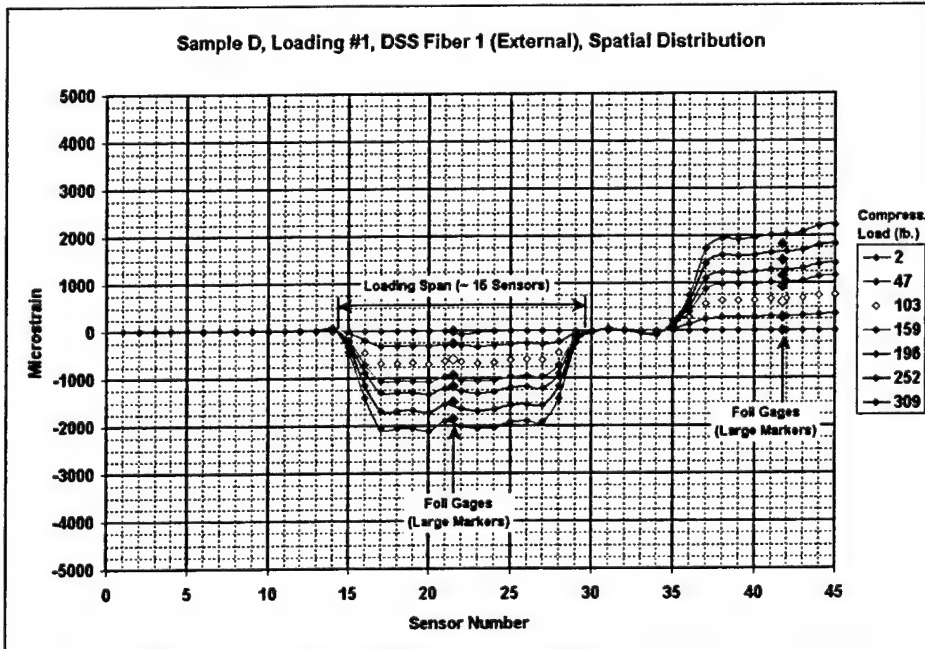


Figure 55. Sample D surface strain data (DSS Fiber 1), Loading #1.

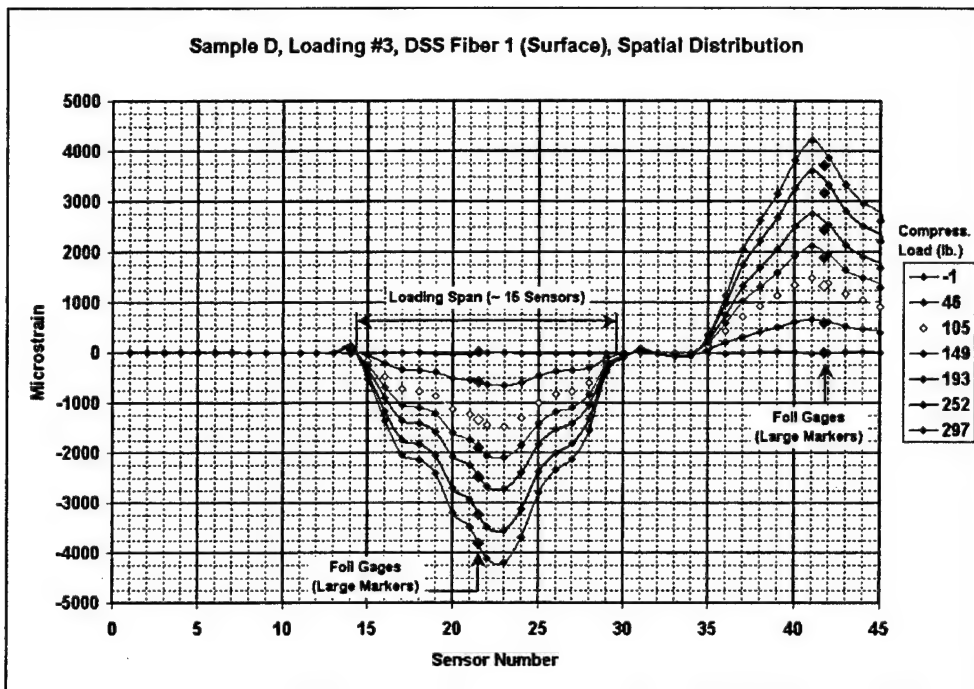


Figure 56. Sample D surface data (DSS Fiber 1), Loading #3 (with edge cutouts).

The uniform (inside the loading span) and antisymmetric (in the tensed and compressed sides of the specimen) strain response is clearly seen in Figure 55. The foil gage and optical gage data agree well. Comparing the two figures, it is obvious that both the foil gages and optical gages respond to the reduction in cross-section area and the stress concentration due to the cutouts. The stress concentration is clearly affecting the results, as the area reduction would affect only one or two sensors to either side of the strain peak (center of the cutouts).

Figure 57 and Figure 58 show optical strain data for internal woven-in sensor strands in weft Layers 2 and 4 (span direction), along the centerline of Sample D with and without cutouts, respectively. The difference in peak positive and peak negative response for specific load levels is attributed to the Z-position of each optical fiber relative to the neutral axis of the sample.

Variable location of each optical fiber within its host yarn places the gratings closer to or farther from the specimen mid-plane, which is expected to return the respective changes in the in-plane strains. If the optical fiber is located closer to the bottom of the host yarn in which it is integrated in Layer 2 (under compression), it will be closer to the mid-plane than the optical fiber integrated in Layer 4 (under tension), what should result in a larger tensile strain. The strains indicated here are actually lower than those nearer the edges even before the cutouts were made.

The presence of the cutouts is clearly seen when comparing Figures 57 and 58. As with the external gages, the effect of the cutouts extends well past the region inside which the cross-sectional area is reduced.

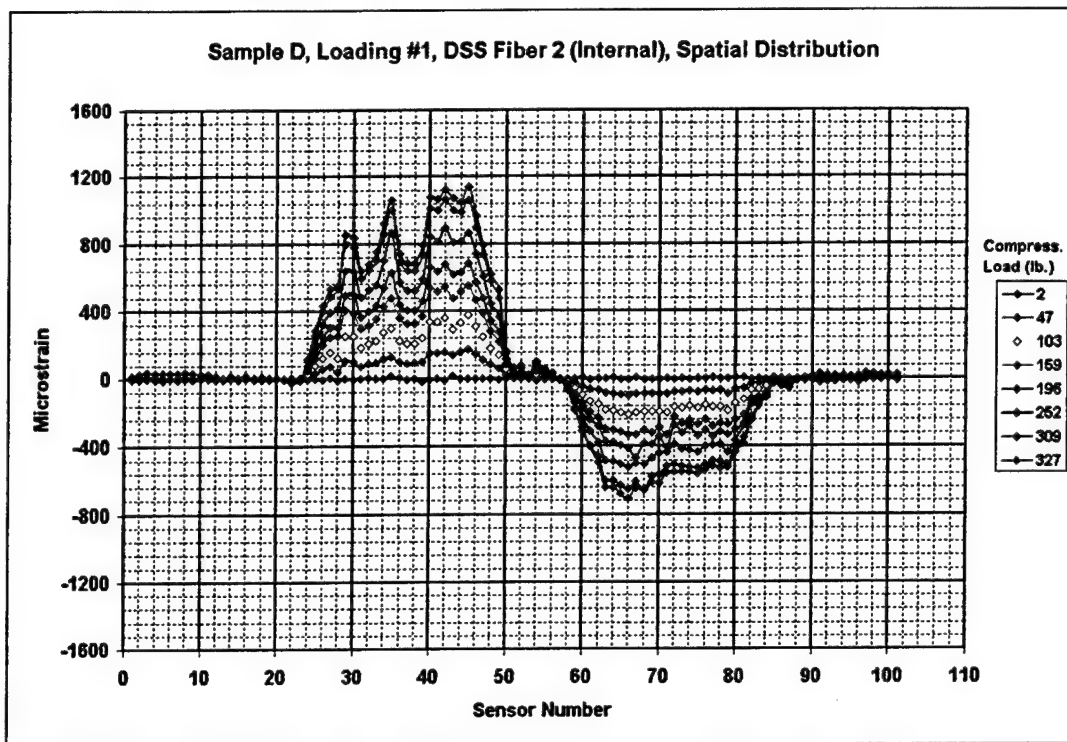


Figure 57. Sample D internal strain data (DSS Fiber 2), Loading #1.

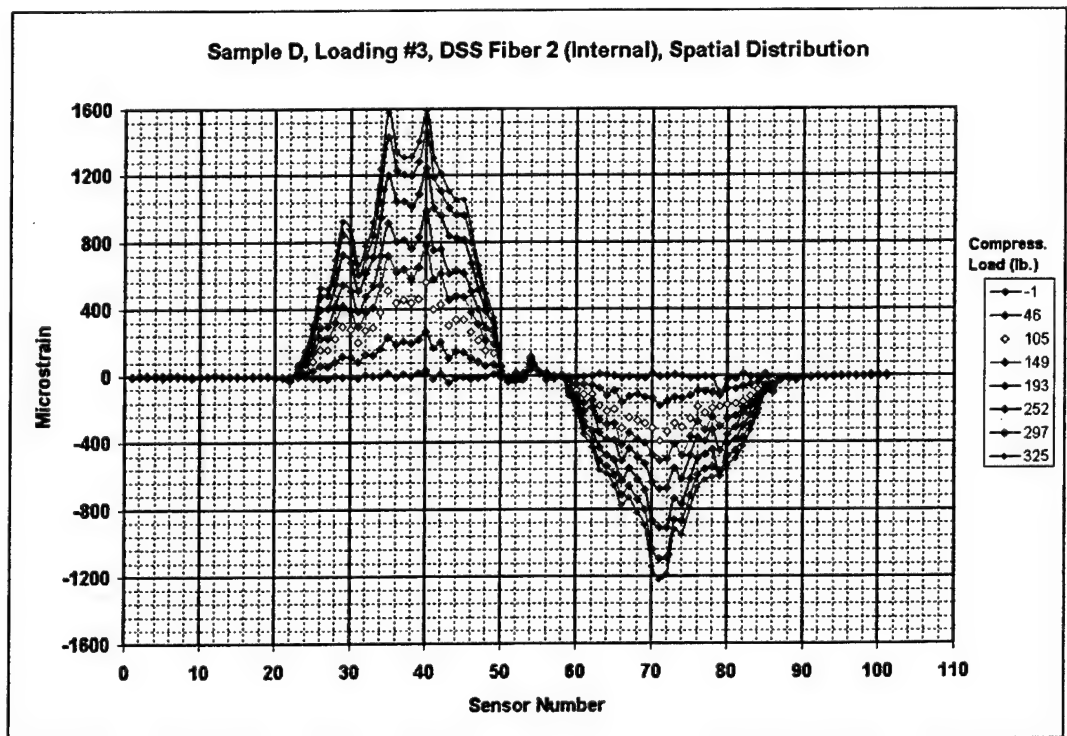


Figure 58. Sample D internal strain (DSS Fiber 2), Loading #3 (with edge cutouts).

Figure 59 and Figure 60 show optical strain data for internal sensors in weft (span axis) Layers 2 and 3, off-center, nearer the edges (and later the cutouts) in Sample D before and after cutouts were made, respectively.

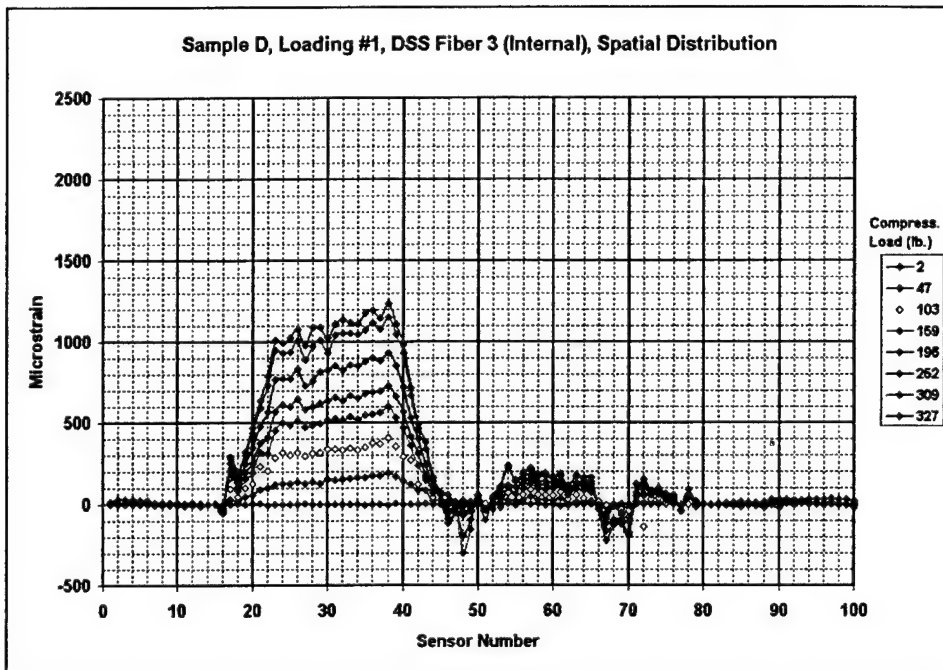


Figure 59. Sample D internal strain (DSS Fiber 3), Loading #1.

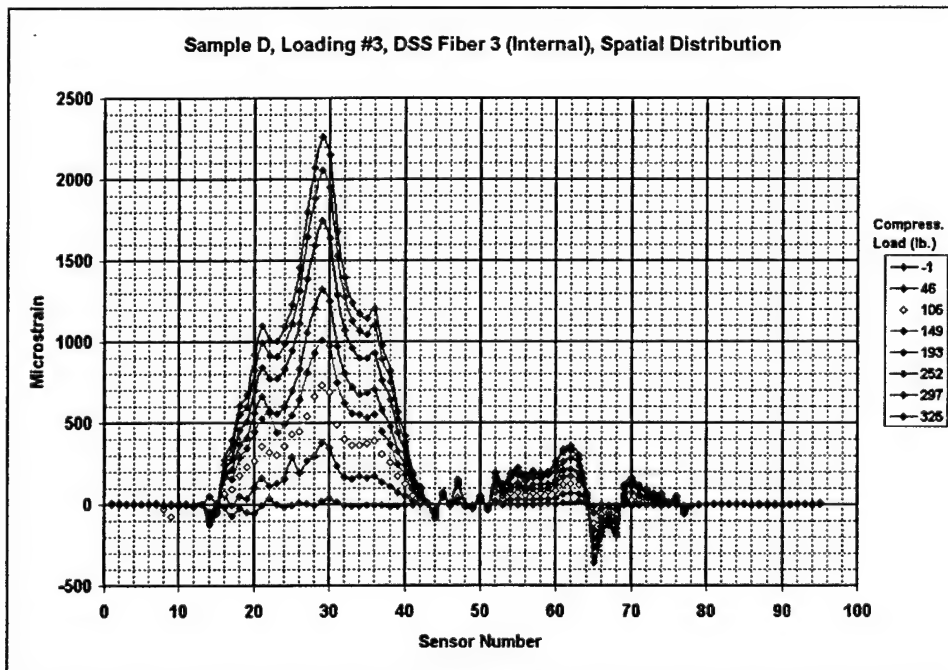


Figure 60. Sample D internal strain (DSS Fiber 3), Loading #3 (with edge cutouts).

The response in Layer 3 is very low due to its position centered at the mid-plane. This sensor strand was off center (closer to the edge of one cutout than the other), while the other strand of internal sensors was centered between the long edges of the specimen (and the two cutouts). As one might expect the sensors closer to the hole (Figure 59 and Figure 60) exhibit larger response. The sensors centered between the cutouts exhibit lower strains for equivalent loads. This illustrates the effects of the stress concentrations around the cutouts.

#### 9.4. Summary and Conclusions from Bend Testing

3Weave™ samples containing integrated optical fibers with Fiber Bragg Grating sensors were successfully tested in 4-point bending. Strain data were collected for up to 101 sensors along a single optical fiber. Strain data from foil gages compared well with data from optical gages when differences in gage length and sensor position were taken into account. The presence of cutouts near the optical gages demonstrated the ability of the FBG sensors to detect gradients extending beyond the physical position of the cutouts.

### 10. DOUBLE-LAP BONDED JOINT WITH INTEGRATED SENSORS

To further validate capabilities and in-situ performance of optical sensors integrated in composite structural elements in regions of high strain gradients, a bonded double-lap joint sample was fabricated with sensor strands entering at one end of the adherend and terminating at the other end. BGF optical strain sensors were integrated into 3Weave™ carbon fiber preform prior to resin infusion, so that strain response could be monitored along the respective warp, weft or Z yarns. The test series consisted of tensile testing of a double-lap bonded joint made of 3TEX material. Twenty-two Bragg grating sensor strands were integrated into the adherend portions of the sample, resulting in a total of approximately 320 sensors actively reading strain inside the sample.

#### 10.1. Experimental Sample Configuration

The fabricated test sample was constructed from the preform, which schematic fiber architecture is shown in Figure 61. In this figure, blue yarns are fill-directional and run along the length of the sample. Red yarns are warp-directional; they run the width direction of the sample. Yellow yarns are Z-directional. Details of the 3Weave™ preform used in the sample are given in Table 9.

Optical fibers with Bragg sensor gratings measuring 5mm long on 1 cm centers were integrated into the preform in the warp, fill, and Z-directions. The preform was infused with Derakane vinyl ester resin at 3TEX. Cross-sections of the infused preform are shown schematically in Figure 62, where the yarns take on rectangular shape during consolidation. The sample was constructed by adhesively joining composite strips cut from the consolidated composite panel. The strips were cut in the fill direction of reinforcement and adhesively bonded into the double-lap joint specimen configuration using Epon 828 resin and cured according to manufacturer's recommended schedule.

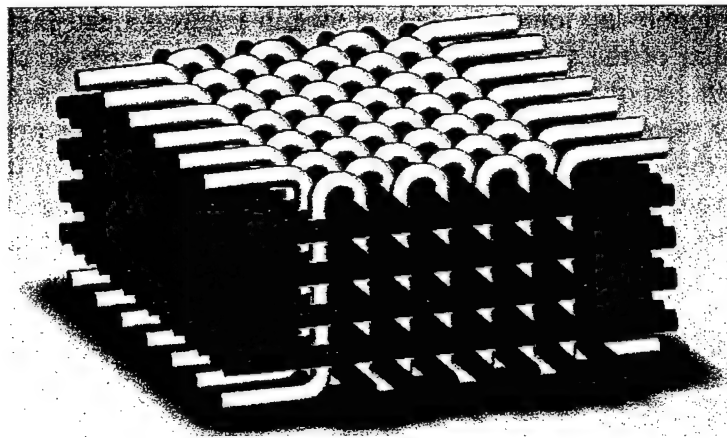


Figure 61. Schematic of 3Weave™ preform architecture.

Table 9. 3Weave® preform details.

	Fiber Type	Tow Size	Sizing (%)	Fill Yarn Rows	5
Warp (0°)	PAN T700	24K	1.1	Warp Yarn Rows	4
Fill (90°)	PAN T700	12K	1.1	Fill Yarn Columns	7
Z (Thickness)	PAN T300	3K	1		
Average Dimensions (Consolidated)	Sample X	Sample Y	Sample Z		
Warp	XX		XX		
Fill		XX	XX		
Z	XX	XX			

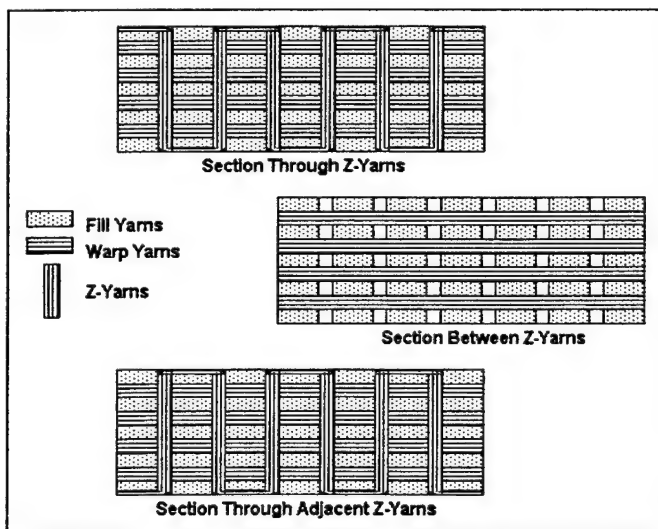


Figure 62. Cross sections of consolidated preform.

The resulting double-lap joint sample is shown in Figure 63 and Figure 64. Sensors entered the adherend portion of the sample at the right side of the sample as depicted in Figure 64 (right photo). The left end of the adherend (left side of Figure 64) was machined to square. The optical sensor strands were terminated at that point. Sensors were not present in the center section ("tongue") of the sample. Dimensions of the sample are shown in the schematic of Figure 65. Strain gages were mounted to the sample for previous tests, but were not used in this test series. Lettering on the right side of Figure 65 refer to labels of the optical sensor strands (see below for details on the sensors).

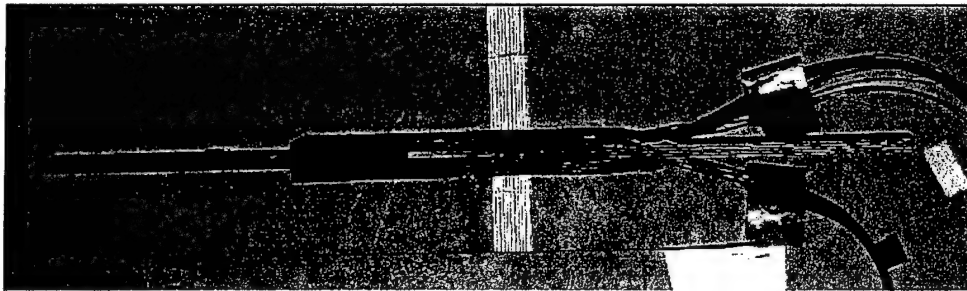


Figure 63. Double- lap bonded joint sample with integrated BGF optical sensors.

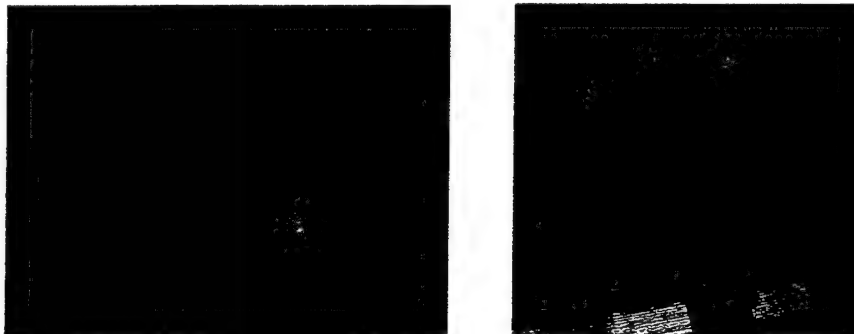


Figure 64. End views of double-lap bonded joint sample.

## 10.2. Optical Sensor Location and Positions

The positions of the optical fibers (carrying Bragg grating sensors) in the consolidated adherend cross-section are shown in Figure 66 (top side) and Figure 67 (bottom side). The columns of fill-tows have been labelled "1" through "5." The rows of fill-tows have been labelled "A" through "D," beginning at the bottom (bondline) side of the adherend. Individual optical fibers are referenced by their column and row: "A3," "B2," etc. Some strands on side "B" were not labeled according to their row and column designation; those strands are indicated in Figure 65. "F" (for Fill) precedes the column/row label on side A, but was omitted in the labelling of side B. The "side" label precedes the "F" label on side A and the column/row label on side B. For example, strand AFA2 runs along side A, row A, column 2. Strand BB3 runs along side B, row B, column 3. With the addition of a sensor strand to the bondline of side B during assembly, a total of 22 strands actively monitored strains in the sample.

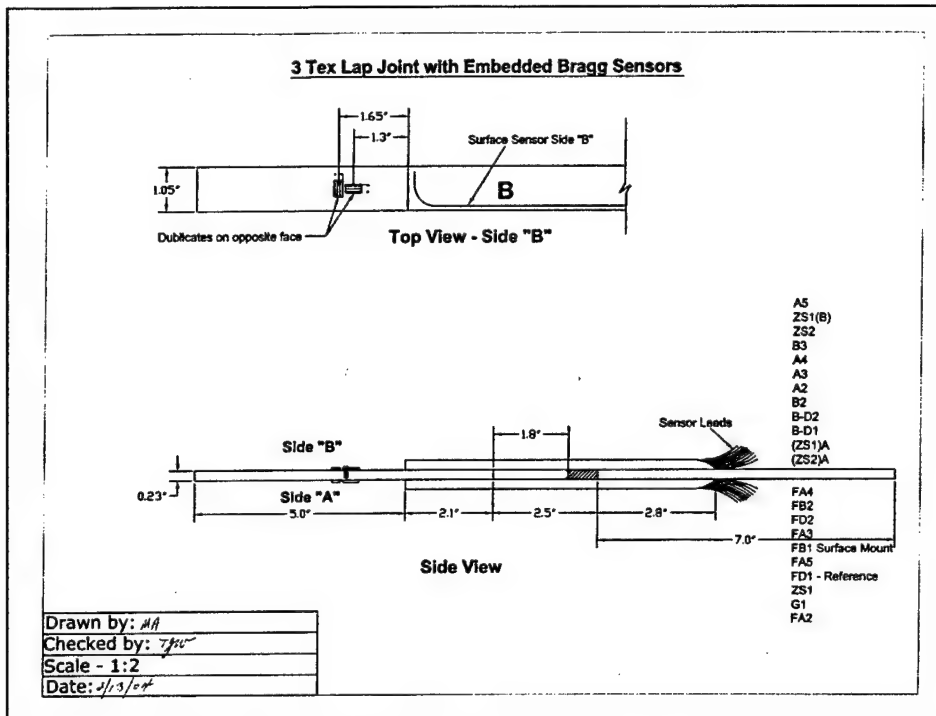


Figure 65. Schematic of double-lap bonded joint sample.

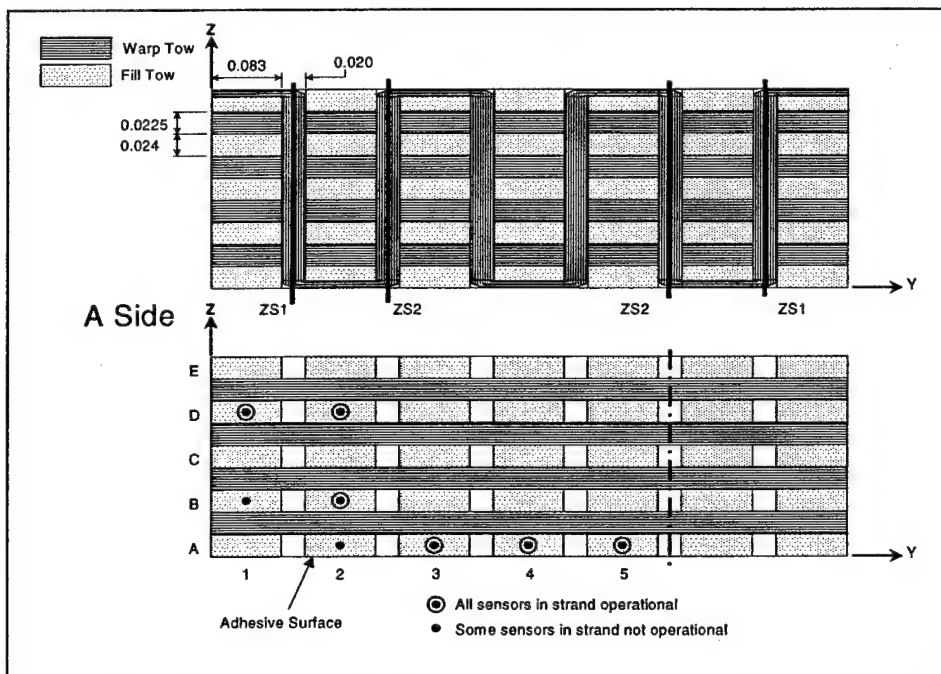


Figure 66. Optical sensor strand positions, sample top (A) side.

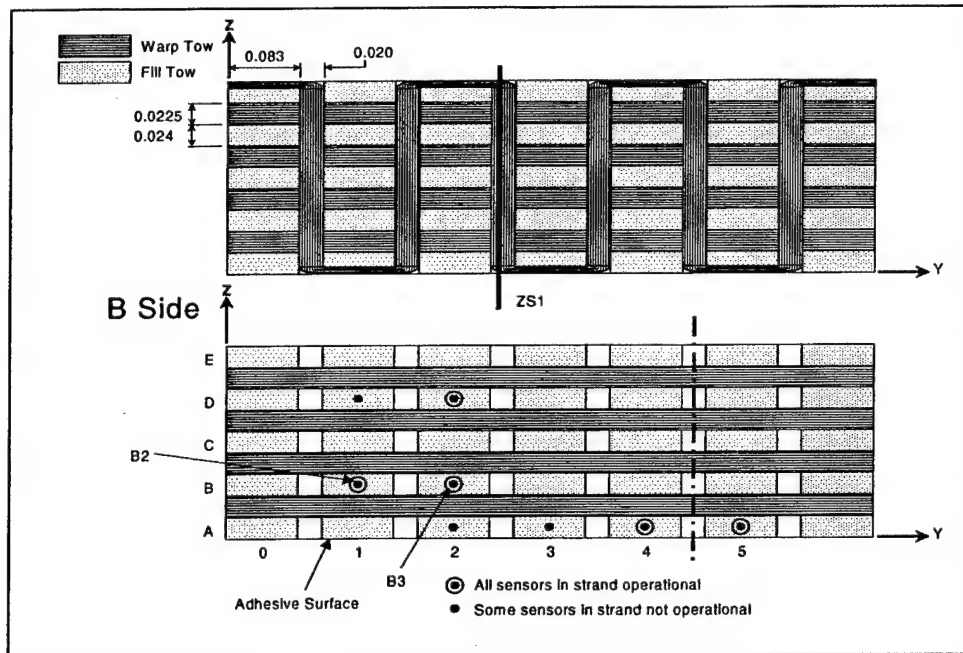


Figure 67. Optical sensor strand positions, sample bottom (B) side.

Optical fiber strands were also run through the Z-corridors as illustrated in Figures 66 and 67. The positions of these strands in relation to the fill yarns is indicated there.

While it was known *a priori* into which yarn each optical fiber strand was placed, it was not possible to know how the strand was positioned within the yarn, or how that position may have changed with location along the sample length. Besides, any slight variation from an exactly longitudinal orientation of the sensor could not be determined. X-rays could not effectively distinguish individual optical fiber strands within this particular sample. As a result, individual sensor locations, as identified by the coordinates of the center of the 5mm-long sensor, were assumed to lie at the center of the yarn.

Sensor locations along the sample length were estimated based on the sensor response: the first sensor showing non-zero strain response was assumed to lie 1 cm inside the sample, as measured from the entry point of the optical strand. It is acknowledged that this approach to locating the sensors results in uncertainty of  $\pm 5\text{mm}$  (0.20 in.) longitudinally (X-direction),  $\pm 0.30\text{ mm}$  (0.012 in.) vertically (Z-direction), and  $\pm 1.05\text{ mm}$  (0.041 in.) horizontally (Y-direction).

### 10.3. Foil Strain Gage Location and Functionality

Foil strain gages were also mounted to the surface of the sample per Figure 65. Characteristics of the foil gages are detailed in Table 10. The set of gages included longitudinal and transverse ones on each adherend surface, as well as a gage mounted in the through-thickness direction on the specimen edge. Load, stroke, and strain gage data were collected using a PC-based data acquisition system distinct from the optical fiber DSS system.

Table 10. Foil strain gage details.

	Top Surface	Edge
Gage Type	CEA-06-250-UW-350	
Manufacturer	Measurements Group, Inc.	Measurements Group, Inc.
Gage Factor	2.1	2.0
Grid Length	0.50 in.	
Grid Width	0.15 in.	
Adhesive	MBOND® 200	MBOND® 200
Bridge-Type	Quarter-bridge	Quarter-bridge
Instrumentation	Measurements Group Model 2210 Amplifier	Measurements Group Model 2210 Amplifier

To synchronize the two systems, voltage levels from the DSS indicator light were recorded by the PC-based system recording load, stroke, and foil data. During the DSS sweep, the indicator voltage level would change, creating a "marker" in the PC data file. The MTS data associated with the first marker was matched to the first DSS sweep, the second marker's data to the second sweep, and so on. Data were acquired by the PC at a rate of 0.5 Hz (2 samples per second). Typically, two consecutive "markers" appeared in the PC data, indicating the DSS sweep of all sensors required between 0.5 and 1.5 seconds. For analysis purposes, all DSS data in a given sweep were assumed to be taken at the same instant and matched to the PC data associated with the first of the two consecutive markers. Based on the load rates below, this assumption led to an uncertainty of  $\pm 16$  psi nominal stress ( $\pm 0.75s \times 5\text{lb/s} \div 0.23 \text{ in}^2$  nominal area) for any given strain data point.

#### 10.4. Test Procedure

The coupon was tested quasi-statically in an MTS servo-hydraulic load frame using a 5500 lb./6-in. stroke actuator and 5000 lb.-capacity load cell (Figure 68). Optical fiber connections were mounted to backing board on the left and right side of the sample. Because the DSS instrumentation was limited to three channels, and 22 optical sensor strands were integrated into the sample, it was necessary to repeatedly load, unload, and reload the sample, thus interrogating different sensor strands during each reload. Table 11 shows the order in which sensor strands were interrogated. Note that sensor strand AFD1 served as a "witness" strand and was interrogated during each reload to assure the loadings were repeatable. During each load "cycle", the coupon was loaded twice, per the data shown in Figure 69. The displacement rate was 0.04 in/s, resulting in an effective load rate of approximately 5 lb/s. Peak load in all cycles and repetitions was 1000 lb.

Table 11. Sensor strand interrogation order and number of sensors.

Loading Number	Channel 1 Strand	# of Sensors*	Channel 2 Strand	# of Sensors*	Channel 3 Strand	# of Sensors*
1	AFD1	70/16	AFA5	58/18	AFA2	62/4
2	AFD1	70/16	AG1	34/7	AFB1	50/17
3	AFD1	70/16	AFA3	68/11	AFD2	70/17
4	AFD1	70/16	AZS1	56	AFB2	71/19
5	AFD1	70/16	AFA4	65/19	BZS2a	85
6	AFD1	70/16	BZS1a	84	BD1	81/6
7	AFD1	70/16	BD2	91/18	BB2	78/18
8	AFD1	70/16	BA2	74/4	BA3	80/3
9	AFD1	70/16	BA4	82/17	BB3	87/16
10	AFD1	70/16	BZS2b	74	BZS1b	60
11	AFD1	70/16	BA5	95/18		

\*Total sensors interrogated/Number of sensors showing nonzero strain

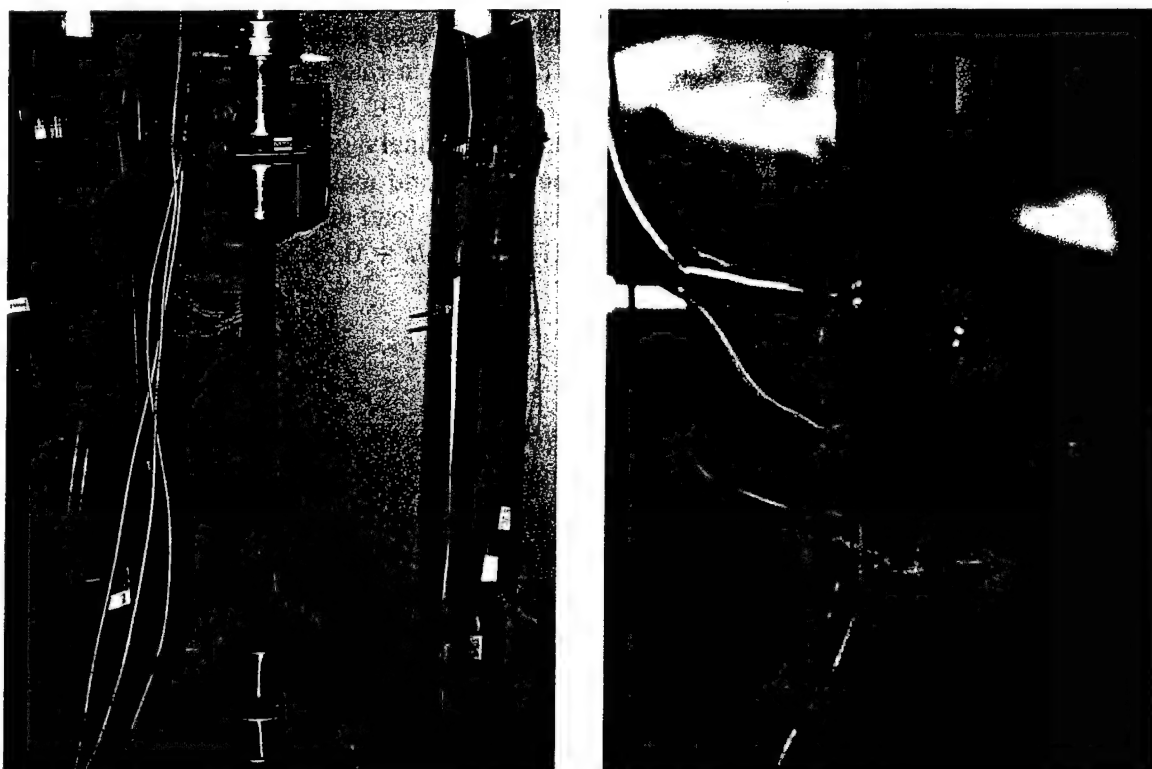


Figure 68. Double-lap bonded joint sample mounted in MTS frame and closeup of foil gages.

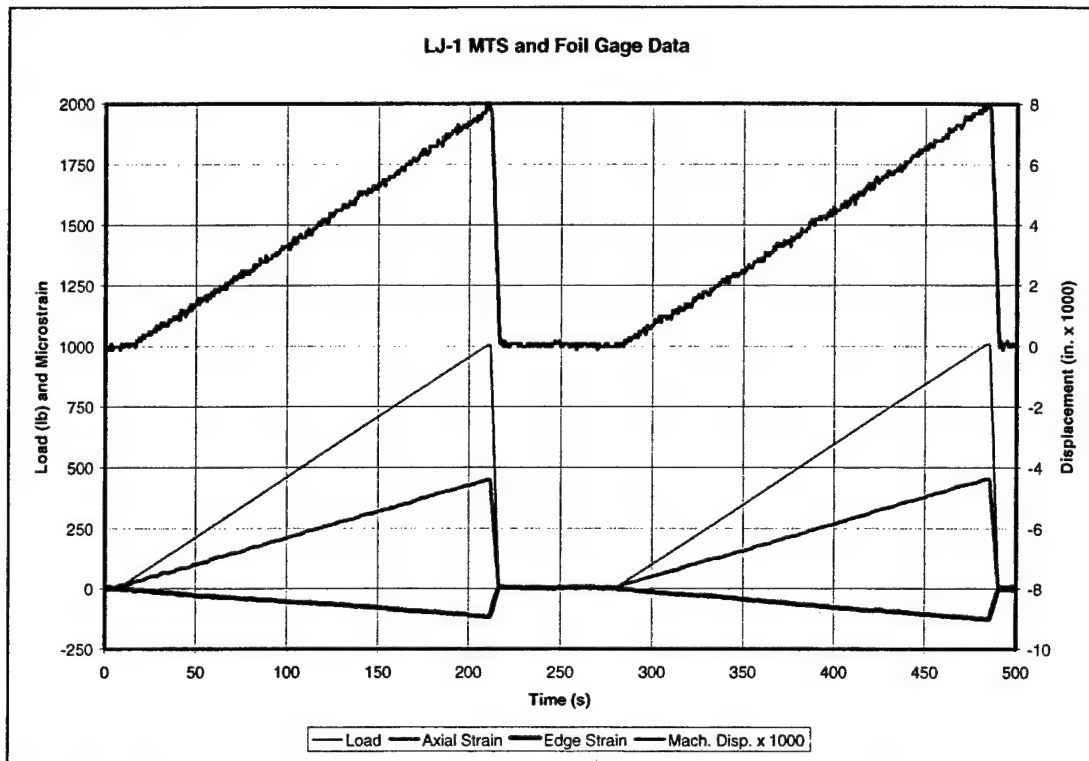


Figure 69. Representative MTS and foil gage data.

## 10.5. Experimental Results Provided by Optical Sensors and Their Discussion

Recall that the objective of the test was to validate the functionality of optical sensors in more complex geometric structures than flat coupons, and near a higher stress/strain gradient (in this case, the joint step and bondline). With this in mind, the analysis of the data sought to demonstrate:

- Linearity of strain data with loading, to ensure that deformation was elastic.
- Repeatability of sensor strand AFD1, to ensure that strain data under the same load level but from different cycles could be compared.
- Comparison of monitored strain values with nominal strain, to demonstrate the functioning of the optical sensors.
- Indication of the strain changes near the end of the overlap, to demonstrate sensing of the stress/strain gradients.

### 10.5.1. Linearity and Interpolation

Figure 70 shows strain vs. load variations for sensors #57, #60, #63 and #66 in strand AFD1 during Run #5, first load cycle. With the coupon oriented as in Figure 70, these sensors are located at the approximate positions shown in the figure. While there is some “noise” associated with the data, the data show overall linear strain response with applied load. The other sensors in the coupon showed similar variability around a linear response for this magnitude of strain. Higher magnitudes had lower relative variability.

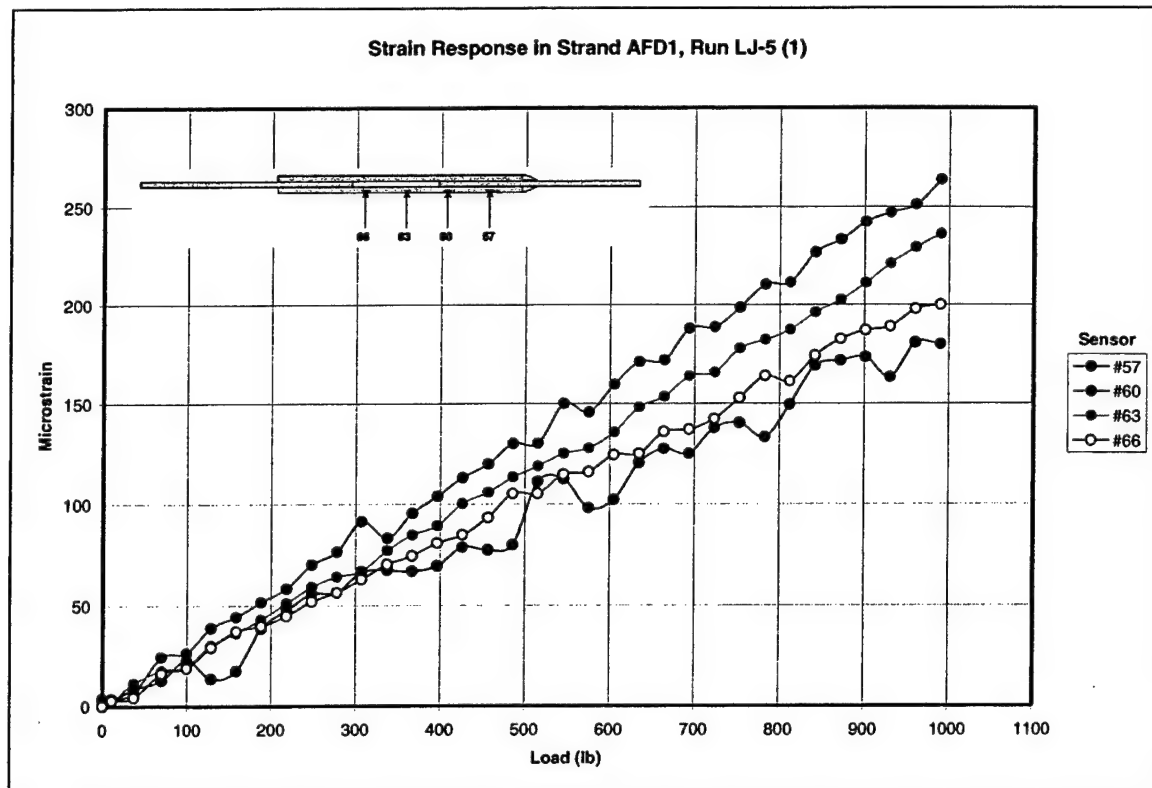


Figure 70. Linearity of optical strain response.

For further data analysis and comparison, the data were smoothed by fitting a least-squares linear interpolation to the load-strain data. Linear interpolation permitted the construction of strain profiles along each sensor strand at increments of 100 lb. (due to the test was displacement-controlled and the optical data acquisition rate was relatively slow, data was not necessarily collected at increments of 100 lb.). Interpolation also enabled easier identification of specific features in the data, such as stress concentrations and the occurrence of damage.

#### 10.5.2. Repeatability of Strand AFD1

To assess repeatability, interpolated strain data from sensor #60 in strand AFD1 were plotted as a function of load for the first cycles of runs LJ-1 through LJ-8. These data are shown in Figure 71. Note that these data represent linear interpolation over the entire load range (0 to 1000 lb.). The data demonstrate fairly good repeatability as the lines fall nearly on top of one another. The variation for any given load, 1000 lb. for example, appear random and not indicative of hysteresis or viscoelastic response.

Figure 72 shows strain variation vs. time at load level 1000 lb. after the first loading (LJ-1, first cycle). There appears to be no correlation between the strain value and time at which the data were recorded.

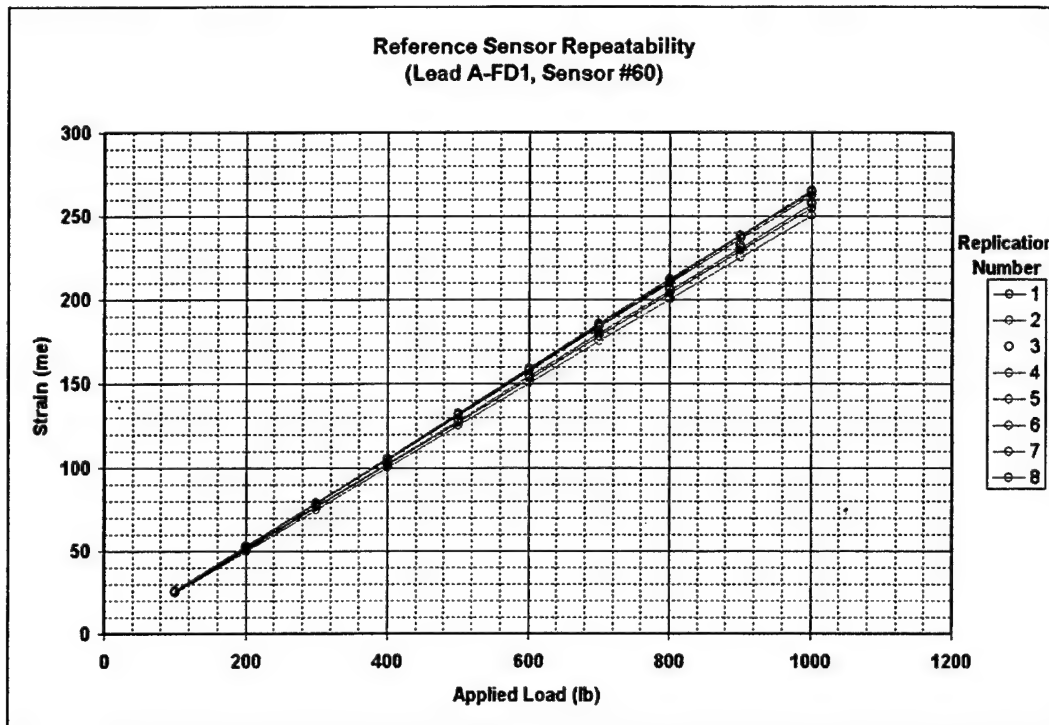


Figure 71. Repeatability of reference sensor readings.

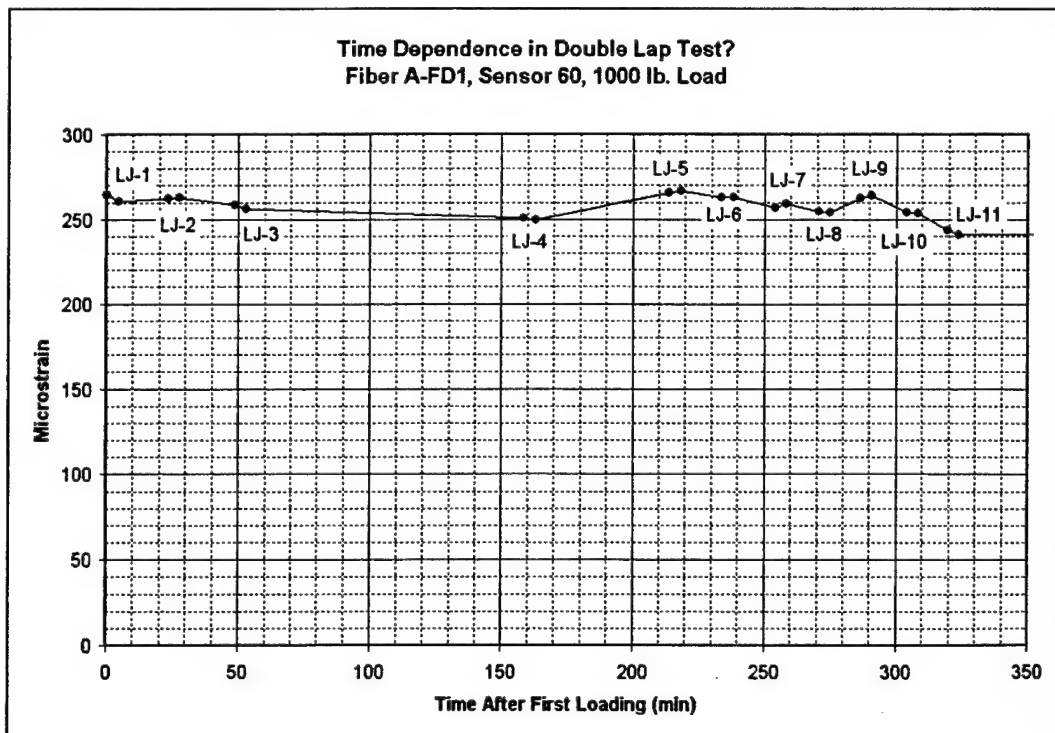


Figure 72. No apparent hysteresis or viscoelastic effects observed in strain response.

### 10.5.3. Comparisons of Theoretical and Experimental Strain Results

To calculate nominal stress for comparison to optical strain measurements, a first-order displacement-based linear finite element analysis was conducted using the geometry of the sample and homogenized effective elastic properties. A uniaxial load of 1000 lb. was applied to the model and strains were calculated and compared to the experimental data.

The finite element mesh is shown in Figure 73. Note that as a first approximation, the resin-rich region through which the optical fibers enter the sample have not been modeled (the end was simply squared off). Further, it was assumed that the adherends (Side A and Side B) were identical, meaning strains in this model would be symmetric about the mid-plane of the sample. The bondline was not explicitly modeled. PATRAN 2003 was used for pre- and post- processing and ABAQUS® was used to perform the analysis. The properties used in the analysis are shown in Table 12.

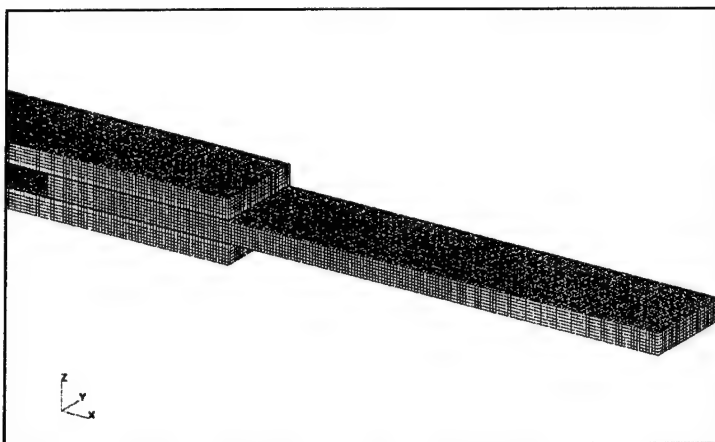


Figure 73. Finite element model of bonded lap joint.

Table 12. Material properties used in FEA of double-lap bonded joint.

Material Property	Value (english)	Value (metric)
$E_{11}$	10.1 Msi	69.7 GPa
$E_{22}$	8.41 Msi	58.0 GPa
$E_{33}$	2.23 Msi	15.4 GPa
$v_{13}$	0.037	0.037
$v_{23}$	0.113	0.113
$v_{12}$	0.113	0.113
$G_{12}$	0.940 Msi	6.48 GPa
$G_{13}$	0.283 Msi	1.95 GPa
$G_{23}$	0.226 Msi	1.56 GPa

The left end of the model was constrained in all three directions, and 1000 lb. load was applied to the right end. The longitudinal (X-direction) strains resulting from the load are shown graphically in Figure 74 and Figure 75.

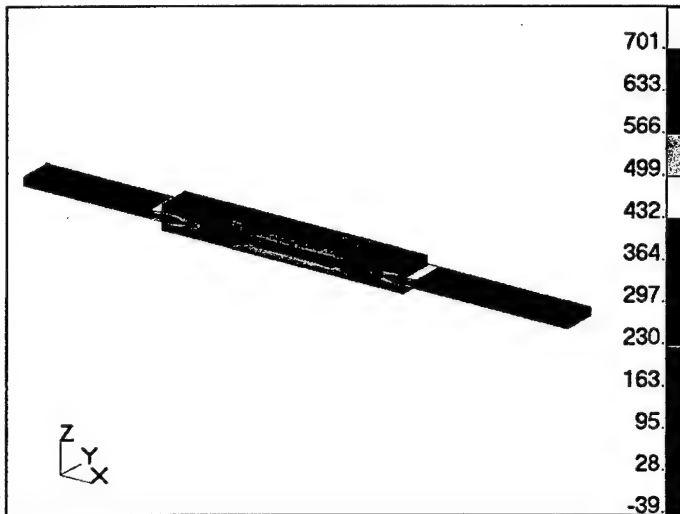


Figure 74. FEA-computed longitudinal strain under 1000 lb. axial load.

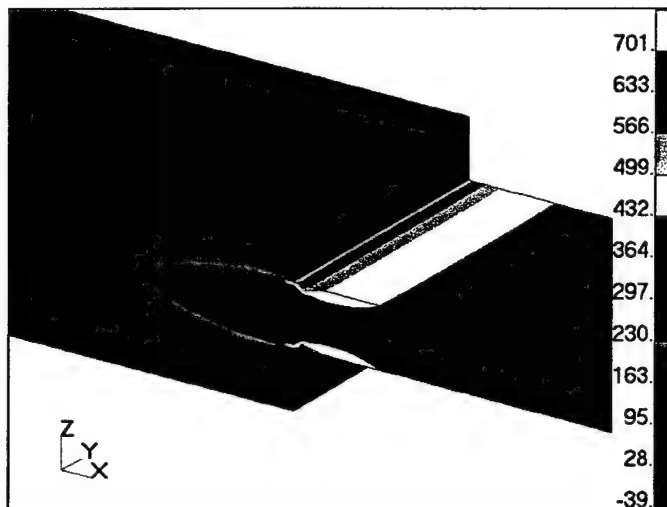


Figure 75. Closeup of FEA results highlighting the machined step region.

Figure 76 shows the strains occurring at the location corresponding to the center of the fill yarns containing the optical fibers. Note again that the individual yarns have not been discretely modeled, but the elastic properties homogenized ("smeared") over the volume of the sample. Figure 76 demonstrates how the strain profile varies with the distance from the bondline. It is also seen that the locations are sufficiently far from the lateral edges of the sample, so there is no difference between the strains corresponding to different columns (e.g., strains in strands D1 and D2 are identical).

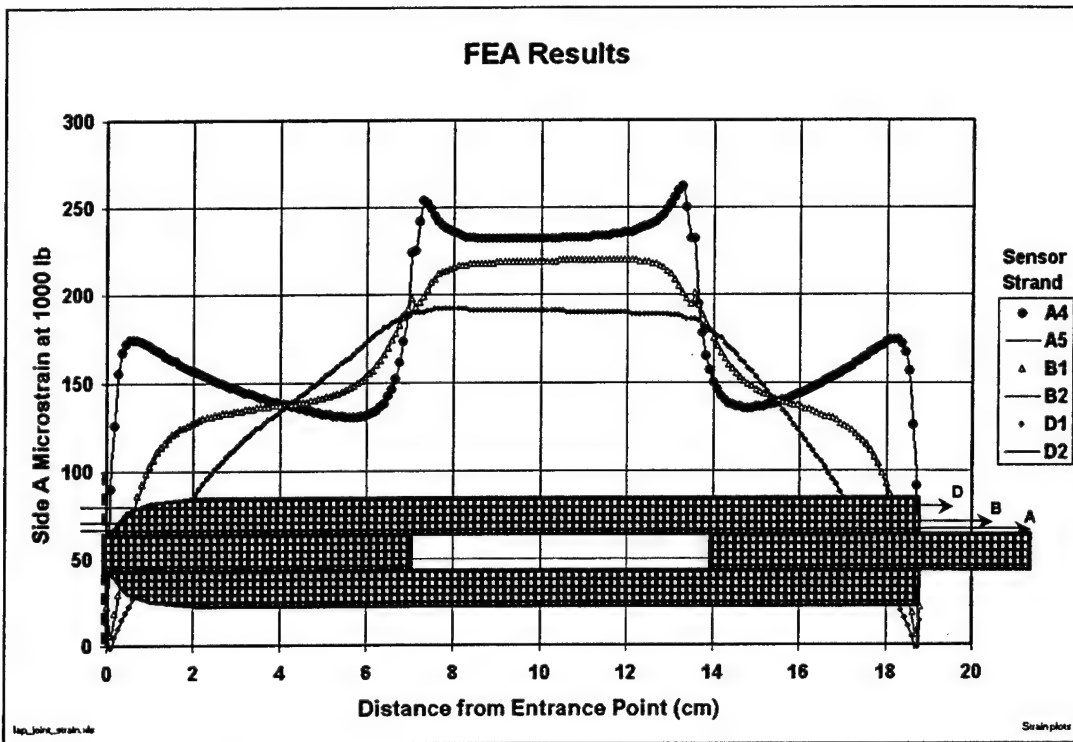


Figure 76. FEA-computed strains along fill yarns containing optical fibers.

Figures 77 through 82 compare the strains computed by finite element analysis and those measured by the optical fibers. In general, the obtained theoretical results capture correct trends. However, the measured strains are consistently higher than those computed by FEA. Three possible explanations for the differences come to mind immediately: (1) the homogenized elastic properties and lack of discrete tow detail in the analytical model produced artificially high stiffness and low computed strain; (2) the optical fibers were located in a region of low stiffness (such as the resin) and, given equivalent load distribution, were subjected to higher strain; (3) there are geometric variations in the sample that were not accounted for in the model. The first explanation seems the most reasonable, since homogenized properties do not account for the actual stress/strain variations between very stiff fiber tows and very compliant matrix. More sophisticated computational models are required to assess the effects of homogenization and other possible reasons of the detected discrepancy between theoretical and experimental results. Application of 3TEX's in-house 3D MOSAIC model and computer code [14,15] earlier used for stress/strain and crack propagation in double-lap adhesive bonded joints [15,16,17] and patch repairs [18] is underway. Analogously to the micromechanics analysis developed in [19,20], this model will allow predicting local stress/strain variations within individual resin-impregnated yarns and resin pockets between them for the tested double-lap joint element. Due to a high complexity and computational expense of such micromechanics model, sufficient numerical results were not obtained by the end of this project. However, this computational work is in progress and its results will be reported in future journal articles and conference presentations. Another possible approach is to use hierarchical capabilities of 3-D FEA available in ABAQUS

package. A comprehensive 3-D FEA analysis of stress/strain fields in double-lap composite bonded joint using ABAQUS "submodeling" approach has been reported in [21].

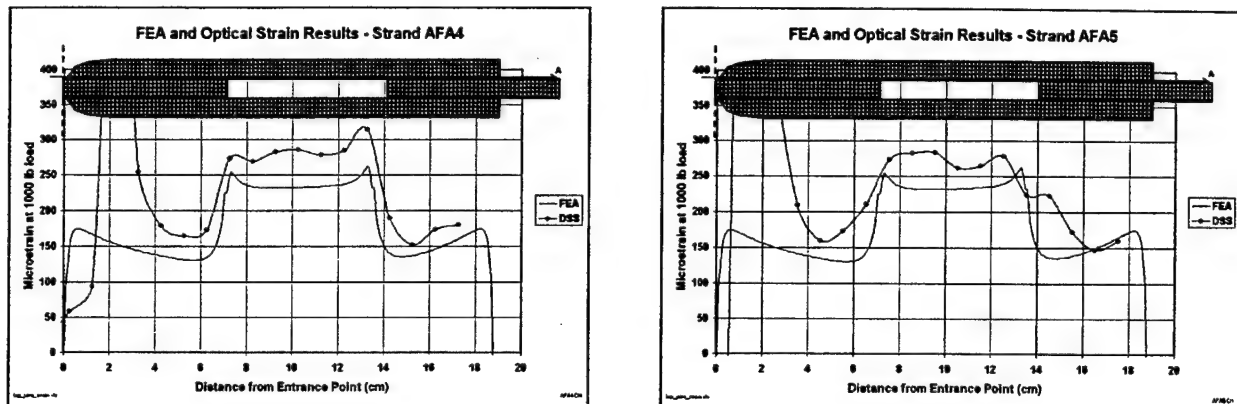


Figure 77. FEA and experimental strains in Fill Row A, Side A.

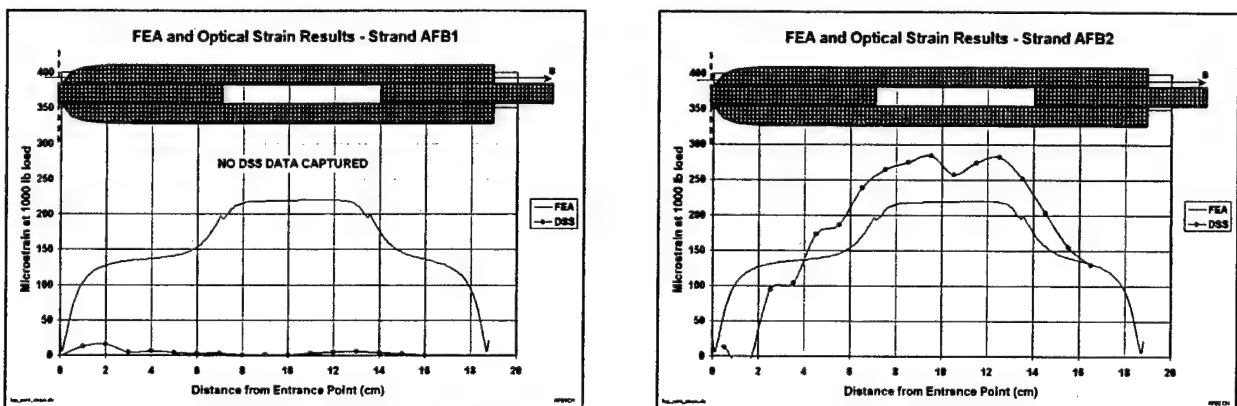


Figure 78. FEA and experimental strains in Fill Row B, Side A.

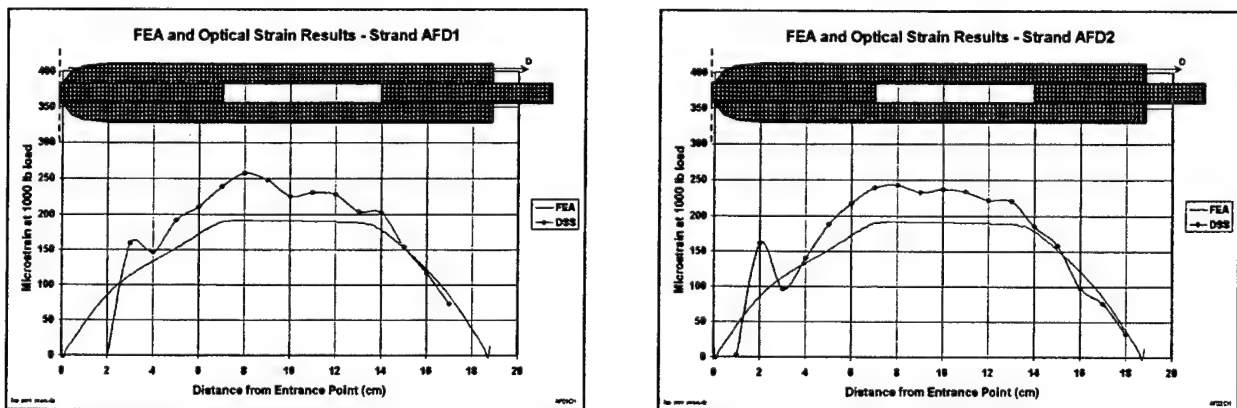


Figure 79. FEA and experimental strains in Fill Row D, Side A.

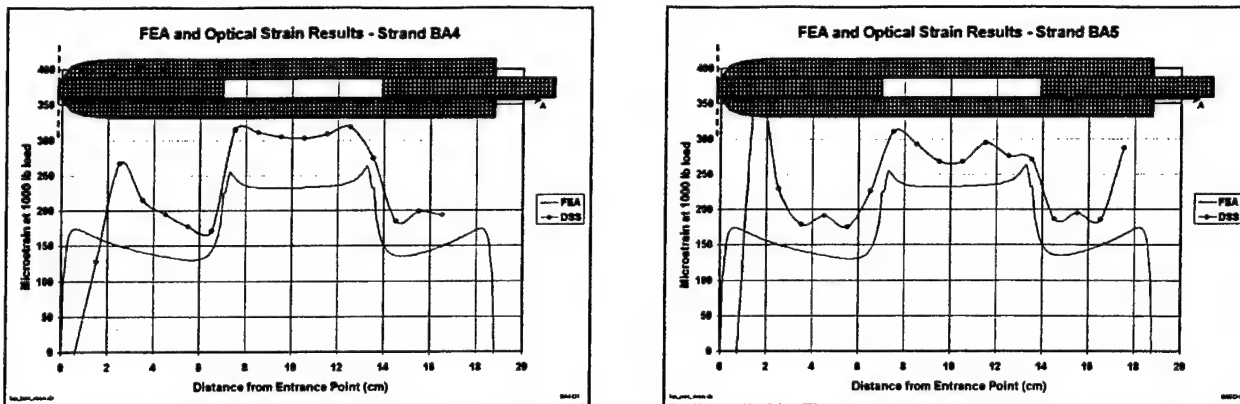


Figure 80. FEA and experimental strains in Fill Row A, Side B.

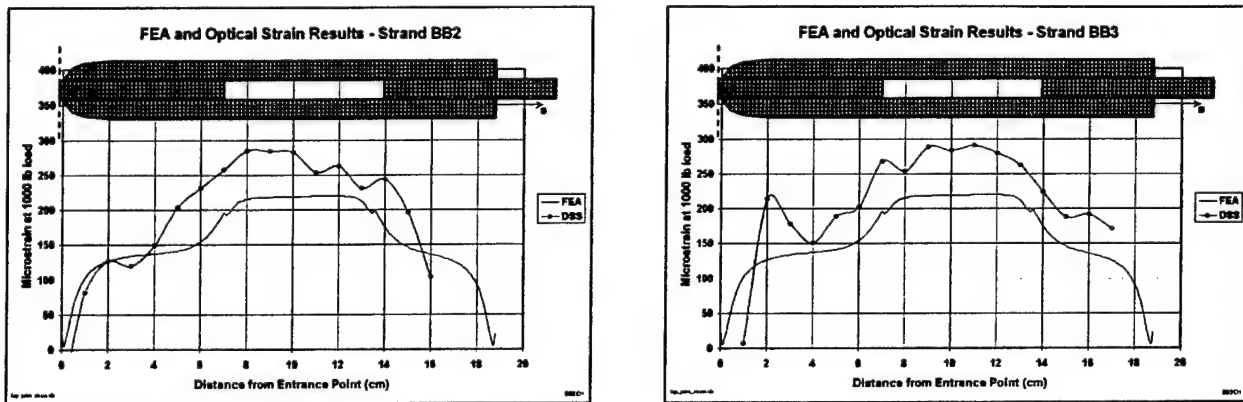


Figure 81. FEA and experimental strains in Fill Row B, Side B.

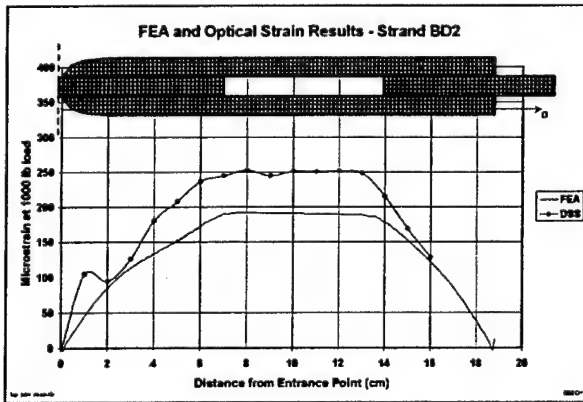


Figure 82. FEA and experimental strains in Fill Row D, Side B.

Note that the MTS and foil gage data presented in Figure 83 consistently show longitudinal strain of about  $450\mu\epsilon$  at 1000 lb. Since the gage was mounted to the sample tongue (which is half as thick as the combined thickness of two adherends), one would expect about twice larger strain in the foil gage as in the center portion of the optical sensors. Comparing  $225\mu\epsilon$  (half of  $450\mu\epsilon$ )

to the strain levels in Figure 79 and Figure 82 (row D near the surface), the analysis is still predicting less strain than what is measured by the foil gages. At the same time, in comparison of the optical sensor data from rows A, B, and D, it is clearly seen that the optical sensor data are trending toward approximately  $225\mu\epsilon$  at the surface.

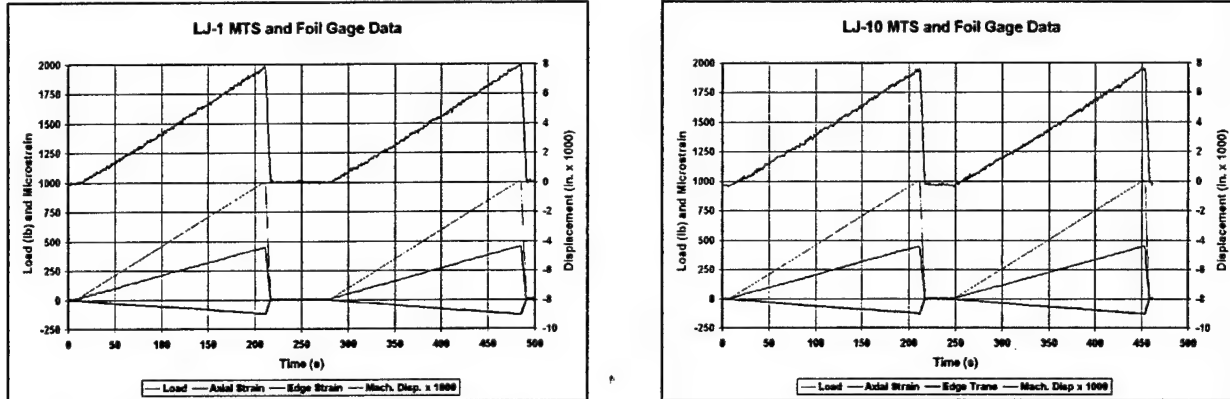


Figure 83. MTS and foil gage data from double-lap bonded joint loadings LJ-01 and LJ-12.

#### 10.5.4. Summary and Conclusions

A double-lap joint specimen consisting of 3Weave™ material with integrated fiber optic strain sensors and glued surface foil strain gages was successfully tested in repeated tension loading cycles. Optical sensors showed good linearity, considering the small magnitude of strain induced in the sample. Little or no hysteresis and good repeatability was observed in repeated loading. A 3-D first-order finite element analysis was performed using homogenized orthotropic properties of the 3-D woven composite. Analysis results were compared with the measured strains. The comparison showed that the numerical results captured major trends of the strain variations, although the experimental strain magnitudes were consistently higher than the analytical ones. Since the optical strain values tended toward those recorded on the surface with foil gages, it was concluded that inaccuracies introduced by homogenization of the material properties and the lack of geometric detail in the finite element model were, most likely, responsible for the discrepancies between theoretical and experimental results. Accordingly, a more sophisticated 3-D stress/strain analysis approach, which would capture the essential microstructural features of the material and bonded joint construction, should be exercised. Such analysis shall also account for exact location of integrated optical sensors within respective yarns in order to achieve a closer agreement between experimental and theoretical strain results.

### 10.6. Double-Lap Bonded Joint with Moiré Grating

#### 10.6.1. Full-Field Surface Strain Measurement Approach

Although comparison with nominal strains recorded by surface-mounted foil gages is useful, a more detailed full-field strain distribution picture would be much more informative for the purpose of validating the developed integrated fiber optic sensor technology. Since no other method of internal strain monitoring is available, a Moiré grid was placed on one side of the

previously tested double-lap joint sample to produce full-field surface strain data. While more complicated to implement, the full-field strain data obtained in the Moiré technique provide better resolution and improved likelihood of capturing damage initiation. Repeated loadings to approximately 1000 lbs. were performed, and three different Bragg grating sensor strands were interrogated during each load cycle. Moiré data were also collected at 500 lb. and 1000 lb. load levels. Strain data recorded by UDRI were reduced, analyzed and transferred electronically to 3TEX.

The double-lap bonded joint sample was used in the MTS testing for generating Moiré data. With the exception of a lateral through-hole, introduced in the second part of the Moiré test sequence (see below), the sample configuration was identical to that used for tensile MTS testing described Section 10.1.

#### 10.6.2. Sensors, Instrumentation, and Test Equipment

A Moiré interferometry grid was mounted on one side of the sample as shown in Figure 84. Moiré interferometry is a full-field optical technique that measures in-plane displacements on a surface. A microscopic grating of reflective material is adhesively bonded to the test surface. Laser light impinging on the sample is diffracted according to the grating frequency, laser wavelength, and the angle of incidence, as illustrated in Figure 85. When the grating deforms, the interference between the two beams creates a pattern that is a contour map of the in-plane displacements. The Moiré interferometer in which this work was performed has a displacement sensitivity of 0.417mm per fringe contour. The sensitivity can be improved by a factor of two through manual interpolation and by at least a factor of 10 through digital phase shifting.

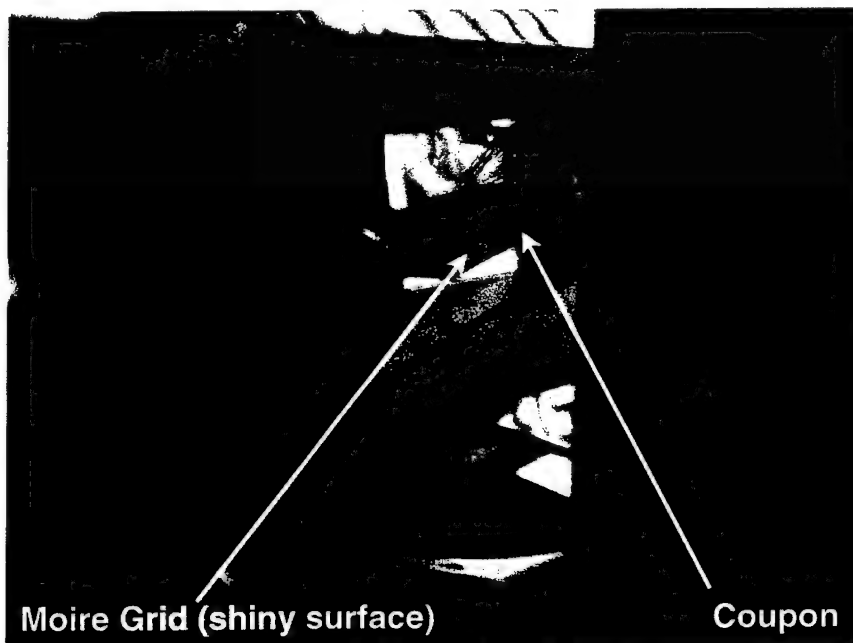


Figure 84. Double-Lap bonded joint sample with reflective Moiré grating.

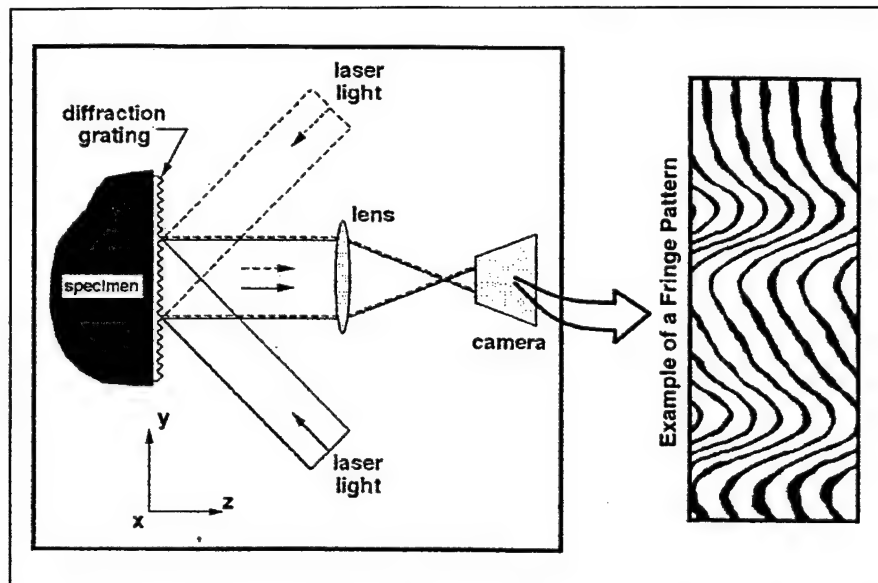


Figure 85. Schematic of Moiré interferometry.

The Moiré instrumentation and load frame are shown in Figure 86. The load frame resides behind the laser, mirror, and beam splitter assembly. A rotating disk of frosted glass serves to stabilize the image. A computer-controlled CCD camera captures the Moiré image for processing and conversion of displacement fringes to strain. Figure 87 and Figure 88 show the left side of the rig and a closeup of the right side, respectively, highlighting the grips used to load the sample. Figure 87 also highlights the nut turned to apply load to the sample. The grip slides within a keyway that prevents rotation.

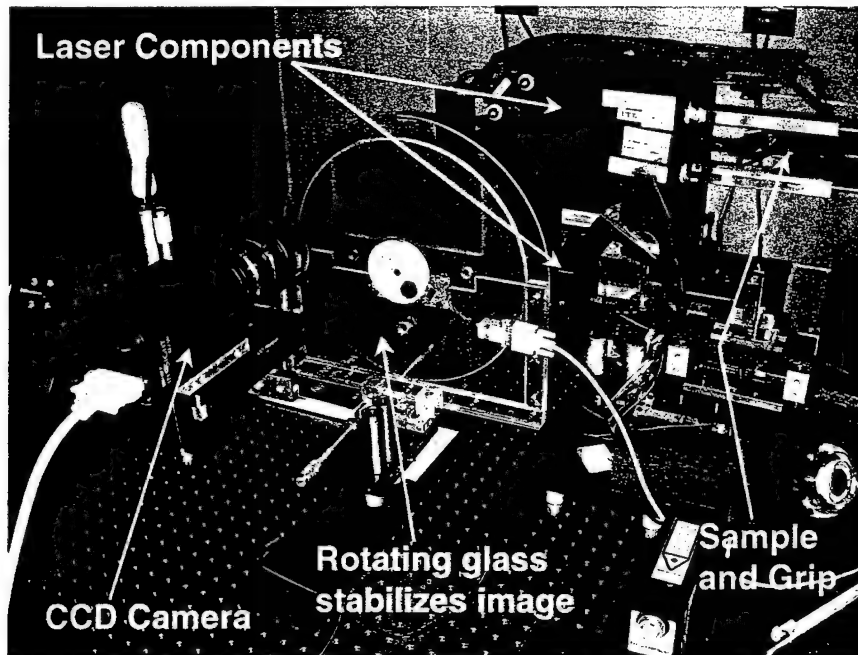


Figure 86. Moiré instrumentation and load frame.

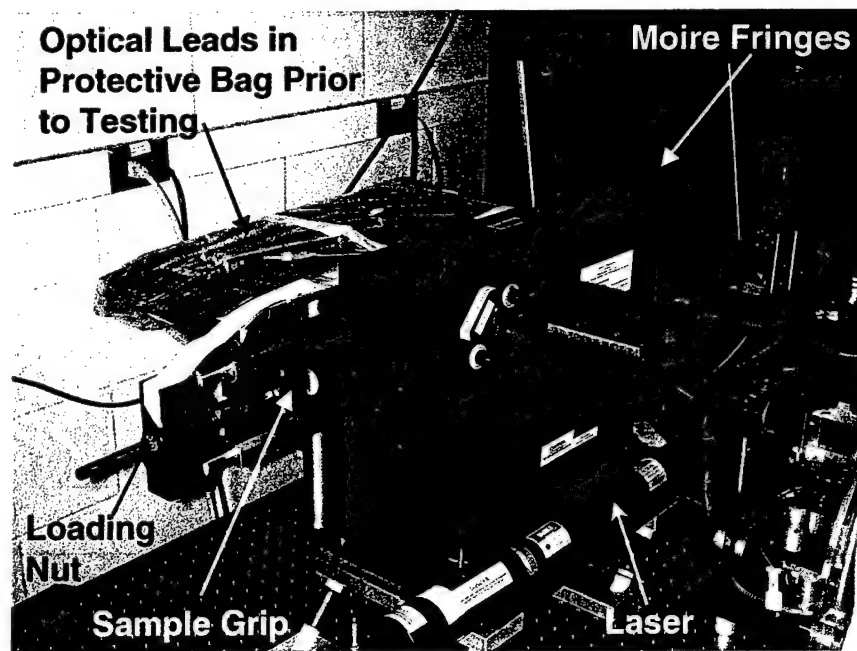


Figure 87. Left side of load fixture showing loading nut and grip.

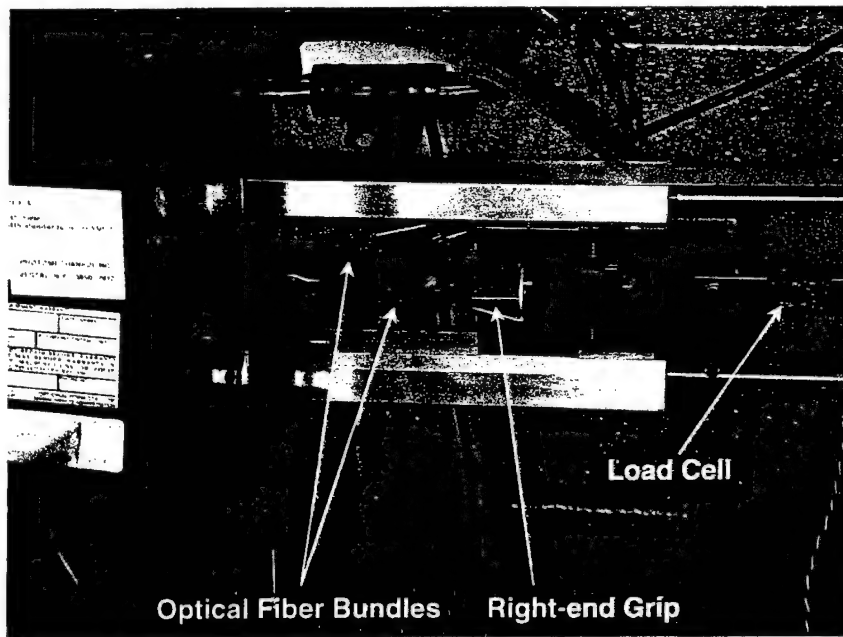


Figure 88. Right side of load fixture showing grip and egress of optical sensor fiber.

### 10.6.3. Test Procedure

The loading nut was manually turned slowly until 1000 lb. was applied to the sample, as determined by the load cell integral to the Moiré table load fixture. Moiré displacement data were captured digitally, filtered appropriately for locations at which the grid integrity was

suspect, and converted to strain by numerically computing derivatives. Bragg grating strain data were then collected using a repeated load-unload-reload sequence. As in the MTS testing, the DSS instrumentation was limited to three channels. Since 22 strands were available in the sample, it was necessary to repeatedly load, unload, and reload the sample, interrogating different sensor strands during each reload. The order in which sensor strands were interrogated was the same as previously described for the MTS tensile testing (see Table 11). Again, sensor strand AFD1 served as a "witness" strand and was interrogated during each reload to assure the loadings were repeatable.

At each reload interval, the loading nut was manually turned slowly until approximately 1030 lb. was applied to the sample, per the load cell readout (the coarse threads on the nut made it difficult to achieve precisely 1000 lb). Between 28 and 31 readings were then made on each of the three fiber strands at the fastest rate possible on the DSS instrumentation (0.5 to 1.0 seconds per reading). The load was removed and the next two optical strands were connected to the DSS instrumentation and all three channels zeroed for the next load cycle.

After eleven load cycles were completed, the load frame, with the sample still installed, was removed from the optical table and placed on a milling machine. Using a carbide-tipped end mill, a 0.25 in. diameter hole was machined laterally through the "tongue" of the sample, see Figure 89. The center of the hole was located 0.75 in. from the machined edge and was located within the interior of the Moiré grid. The loading frame was reinstalled on the Moiré table and the load-unload-reload cycles were then repeated in the exact sequence of the previous tests, with all optical strands being interrogated at 500 lb. A third set of load-unload-reload cycles was then conducted at 1000 lb.



Figure 89. Milling a 0.25 in. hole in the double-lap bonded joint sample.

After the completion of the third set, three sensor strands were selected for interrogation as the load on the sample was "ramped" to various load levels. The sensor strands were continuously monitored during the ramp to develop elementary load-strain curves. Ramps to 1000 lb., 1500 lb., 2000 lb., and 2700 lb. were developed. The load was released and the sensors re-zeroed between each ramp. Moiré displacement data were also collected at the 1000 lb., 1500 lb., and 2000 lb. load levels. The final ramp to 2700 lb. represented the maximum load achievable with the load frame on the Moiré table.

#### 10.6.4. Optical Strain Sensor Results and Discussion

Strain data are presented and analyzed first for the data collected at the three discreet load levels: 1000 lb. without hole, 500 lb. with hole, and 1000 lb. without hole. Repeatability, comparison to Moiré data, and strain field comparison along the bondline for the cases with and without hole, were investigated. These data were then used to "calibrate" the bridging section of the adherend so that load vs. strain data could be generated for the "ramp" loadings. These data were analyzed for appearances of nonlinearity or other signs of damage occurring in the sample.

Figure 90 and Figure 91 show strain data for sensor strand AFD1, the "witness" strand, for the three loading cases. These plots show average strain and  $\pm 2\%$  standard deviations about the mean, where each point represents the mean of the 11 loadings required to collect data for all the sensor strands. Note that for most sensors, the standard deviation is low and the error bars are very tight, indicating good repeatability between loading cycles. Some sensors, notably sensors 66, 67 and 68, show higher degree of instability.

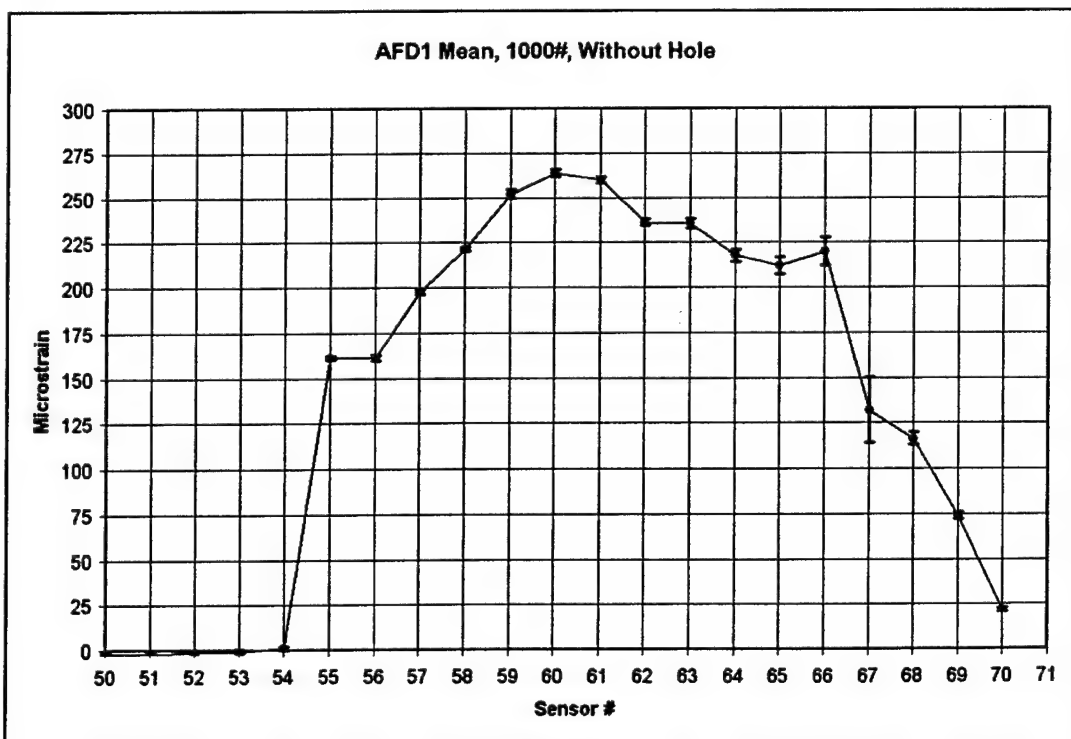


Figure 90. Repeatability in witness strand AFD1, without hole, 1000 lb.

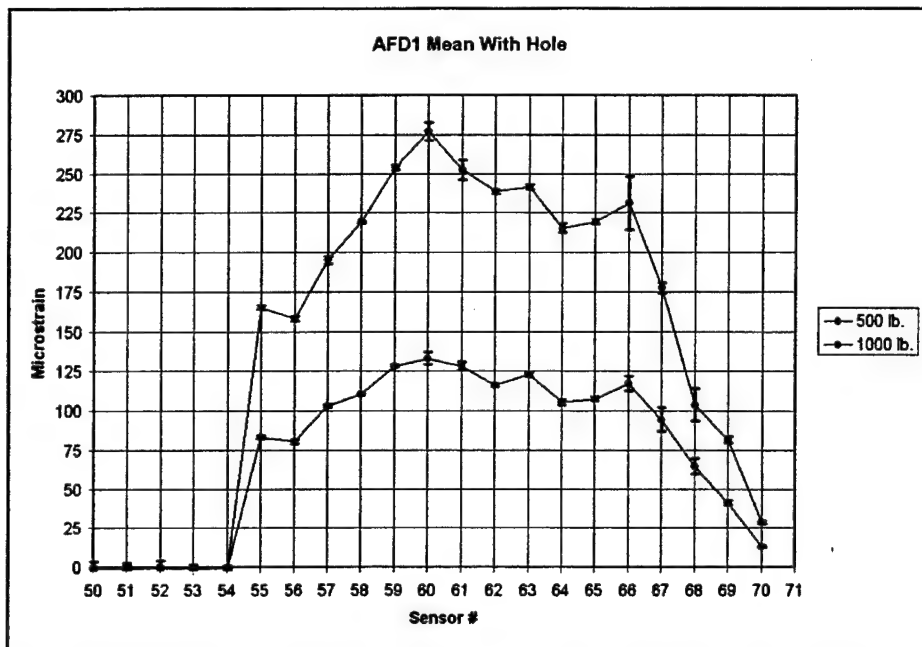


Figure 91. Repeatability in witness strand AFD1, with hole, at 500 lb. and 1000 lb. loads.

Figure 92 compares strains in strand AFD1 due to loading on the MTS machine and on the Moiré table. As the figure shows, the comparison is very good for all but two or three sensors. These are the same sensors showing larger scatter in Figure 90 and Figure 91. Note that during testing on the Moiré table, an additional active sensor was detected along the strand, providing an additional data point near the machined edge of the coupon.

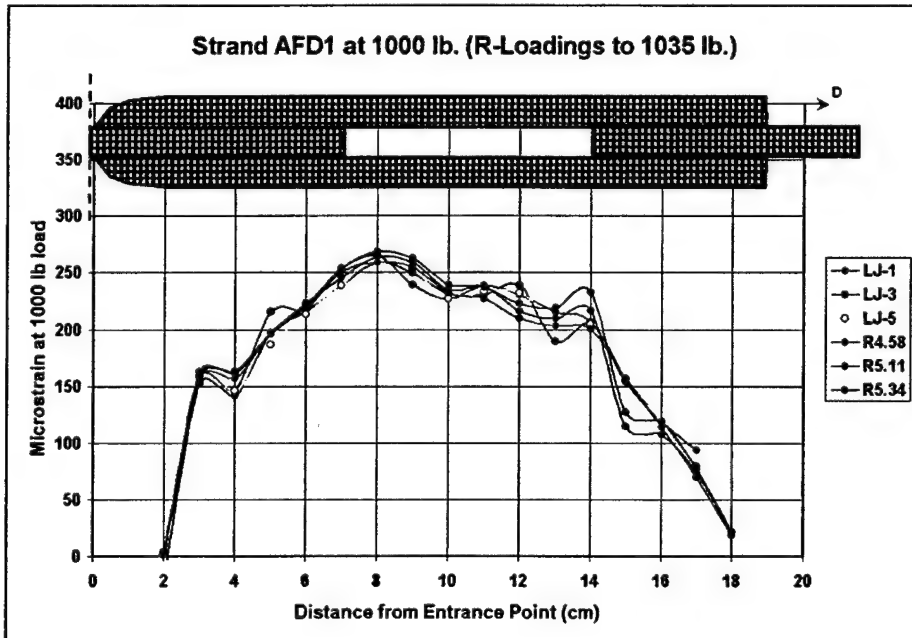


Figure 92. Comparison of Strand AFD1 for MTS (LJ series) and Moiré-table (R series) loadings.

Representative comparisons between loadings at 1000 lb. without hole, 500 lb. with hole, and 1000 lb. with hole, for Rows A, B, and D, are shown in Figure 93 through Figure 95. Comparing the data at 1000 lb., without and with hole (red and blue lines, respectively, in the figures), it is obvious that integrated optical sensors are reflecting the presence of the hole. The data with the hole are, in general, larger in magnitude than in the case without the hole for a given location, and the strain distributions have changed significantly. The effect is greater in Row A and Row B (near the hole edge), then in Row D (away from the hole edge).

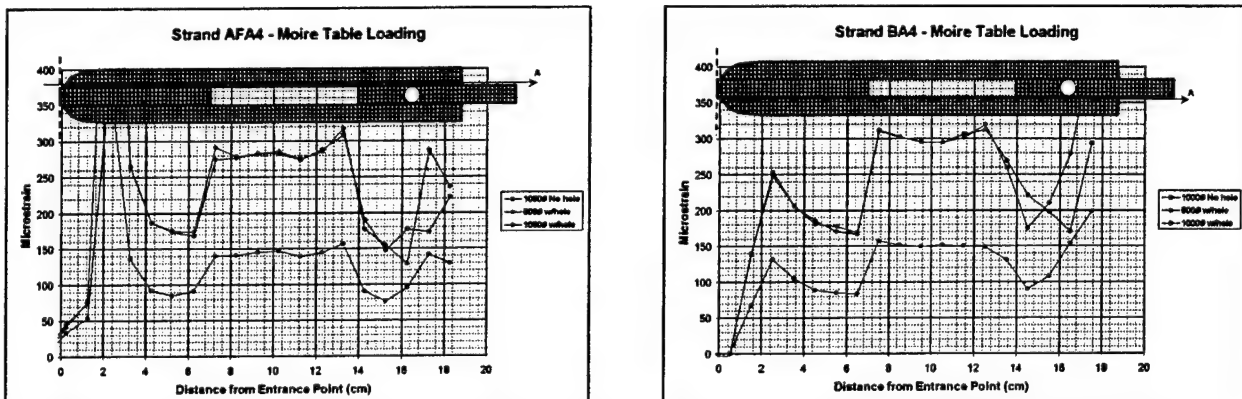


Figure 93. Comparison of optical strain sensor results with and without hole; Fill Row A.

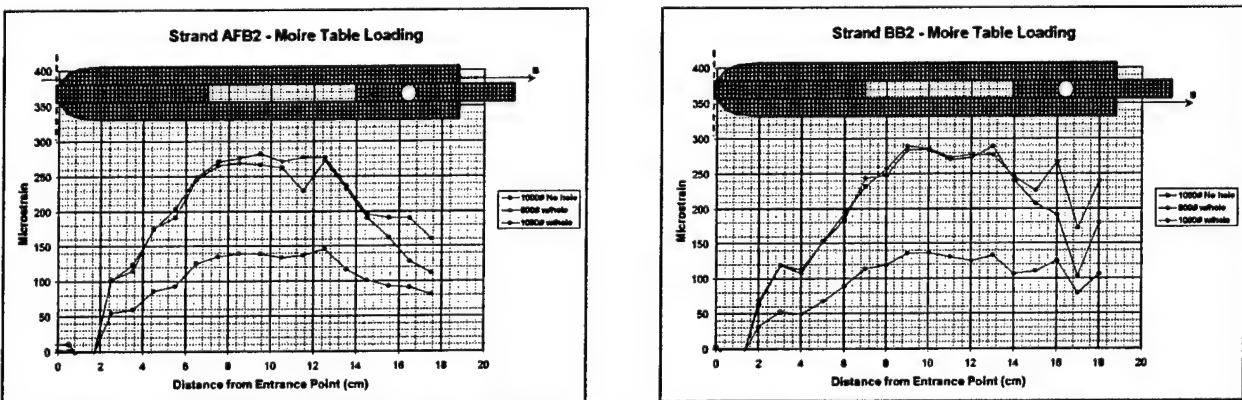


Figure 94. Comparison of optical strain sensor results with and without a hole; Fill Row B.

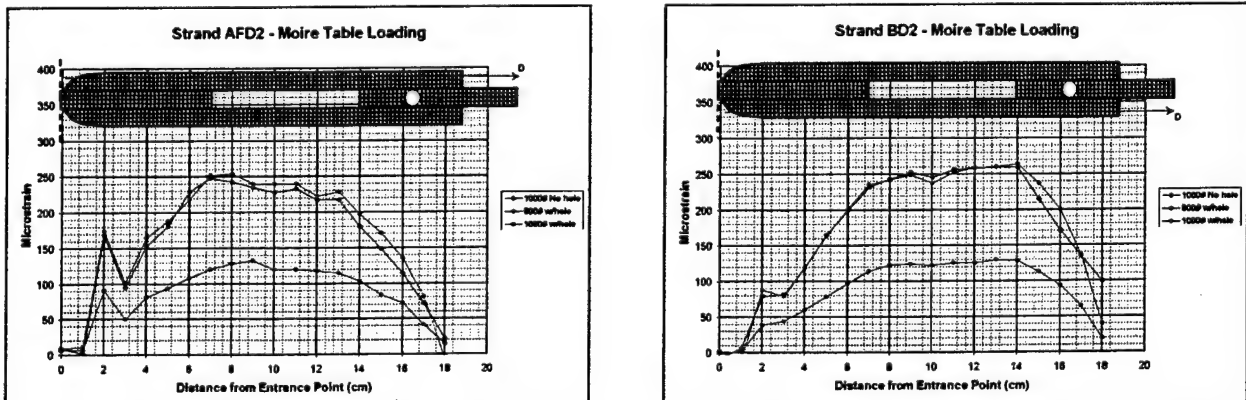


Figure 95. Comparison of optical strain sensor results with and without a hole; Fill Row D.

### 10.6.5. Moiré Full-Strain Field Results

Moiré data were collected from a region of the sample surrounding the hole. Data were collected before and after the hole was milled into the sample. Figure 96 shows a micrograph of the sample indicating the area over which data were collected. Note that all details of the reinforcement architecture are clearly visible in the micrograph. The portions of the reinforcement removed by milling the hole can also be identified in the micrograph.

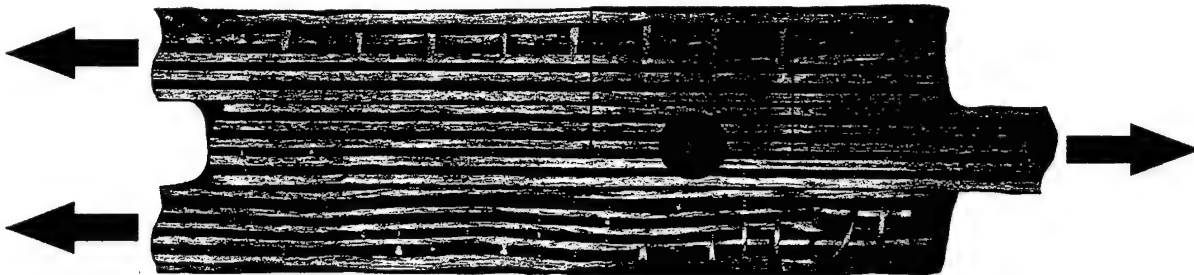


Figure 96. Sample micrograph showing Moiré strain data region, fiber architecture and hole location.

The following figures beginning with Figure 97 and through Figure 100 show axial strain ( $\epsilon_{xx}$ ) field for 1000 lb. load without hole and for 1000 lb., 1500 lb. and 2000 lb. loads with hole. The data have been scaled for the applied load to provide the best resolution in each figure. Black square areas contain no data. Note the data in Figure 98 were collected without hole; the hole is shown for reference purpose only. The data show the anticipated strain concentration occurring at the top edge of the hole, following a fill yarn. The large red region in Figure 99 has exceeded the strain range selected in the instrumentation, and this is, therefore, an artifact.

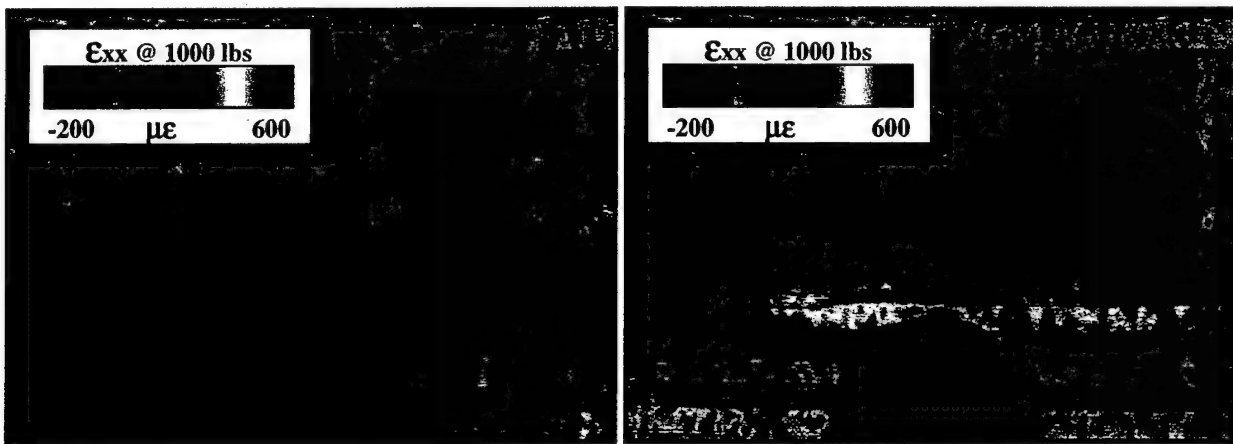


Figure 97. Axial strain at 1000 lb. without hole. Figure 98. Axial strain at 1000 lb. with hole.

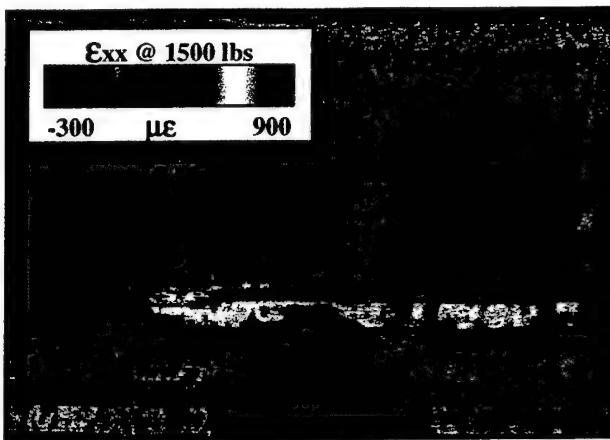


Figure 99. Axial strain at 1500 lb. with hole.

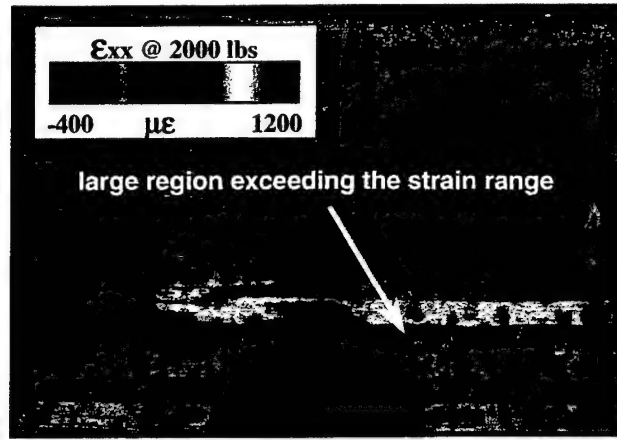


Figure 100. Axial strain at 2000 lb. with hole.

Figure 101 through Figure 104 show transverse strain ( $\epsilon_{yy}$ ) field for 1000 lb. without hole and for 1000 lb., 1500 lb. and 2000 lb., with the hole. Again, the data have been scaled for the applied load and black square areas contain no data. The presence of the hole has created anticipated compressive strain near the front and rear of the hole. Tensile strain had developed at the top of the hole, away from the hole surface. For a homogeneous isotropic material the peak tensile strain would be reached at a distance of  $1.414r$  from the edge of the hole ( $r$  = hole radius). However, in the present situation the material is neither homogeneous nor isotropic, and the tensile strain is not uniformly distributed. Rather, it is associated with warp yarns (those coming "out of the page") and peaks at a distance less than  $1.414r$  from the hole edge. Two areas in which the strain has exceeded the range are apparent at the 2000 lb. level.

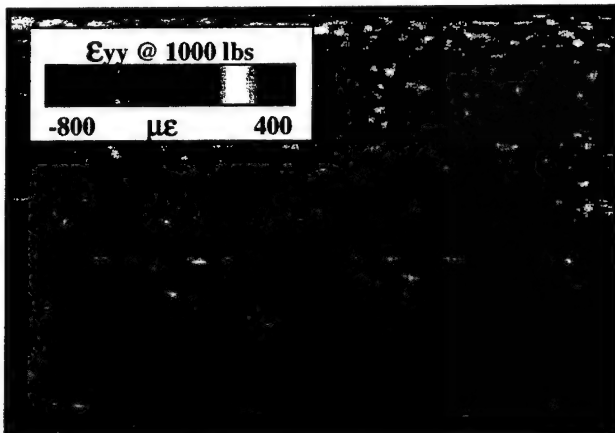


Figure 101. Transverse strain at 1000 lb. without hole.

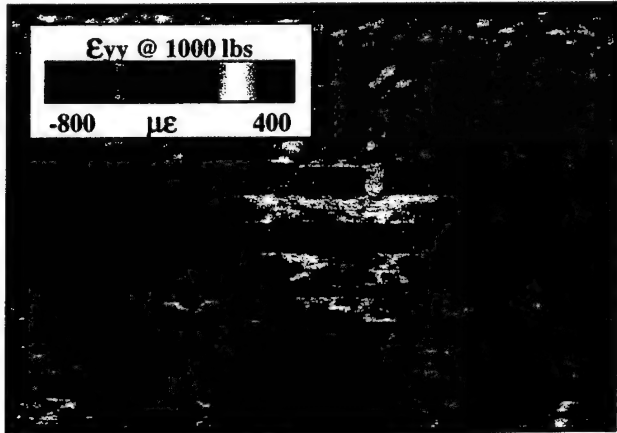


Figure 102. Transverse strain at 1000 lb. with hole.

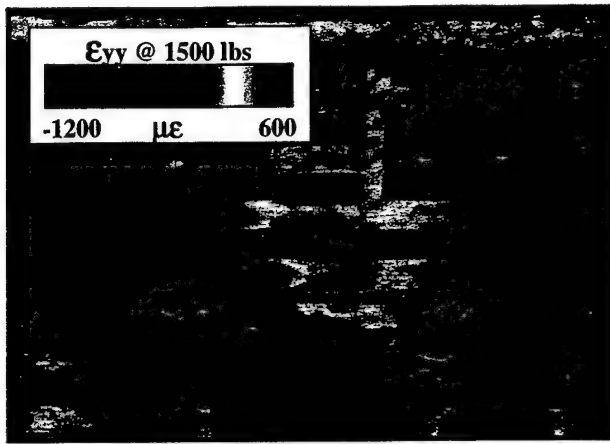


Figure 103. Transverse strain at 1500 lb.  
with hole.

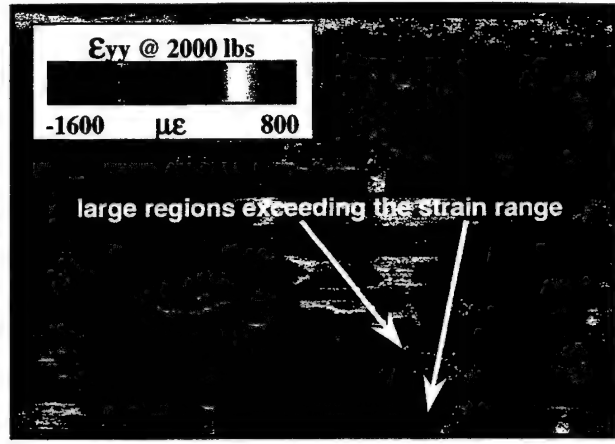


Figure 104. Transverse strain at 2000 lb.  
with hole.

Figure 105 through Figure 108 show shear strain ( $\gamma_{xy}$ ) fields for 1000 lb. without hole and for 1000 lb., 1500 lb. and 2000 lb., with the hole. The data have been scaled for the applied load and black square areas contain no data. As anticipated, positive and negative shear strain appears to the left and to the right of the hole, respectively. Higher strain magnitudes are associated with warp yarns. Peaks are on a trajectory originating at the hole center and extending at an angle of 45° from horizontal.

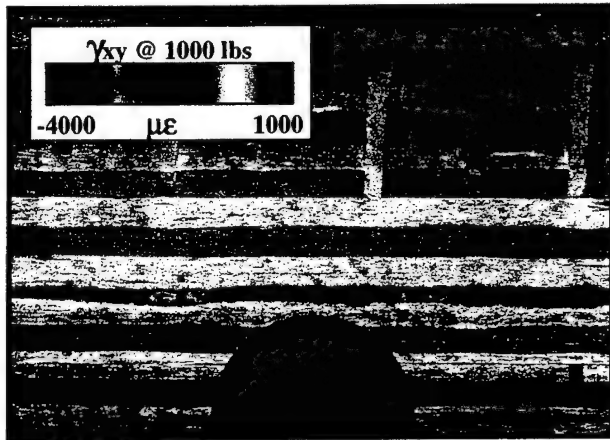
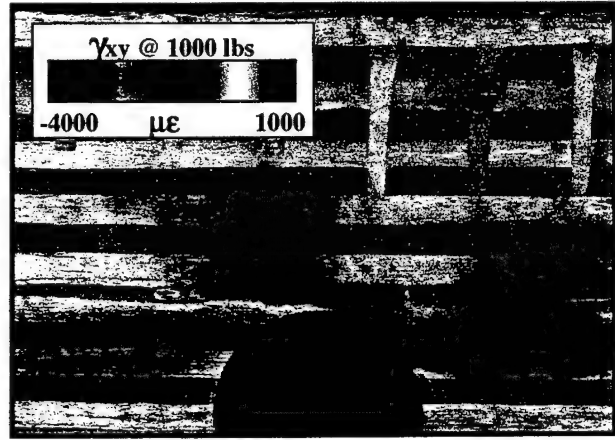


Figure 105. Shear strain at 1000 lb. without hole. Figure 106. Shear strain at 1000 lb. with hole.



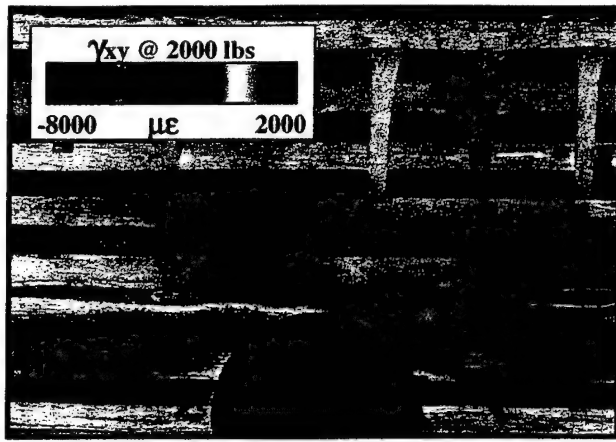
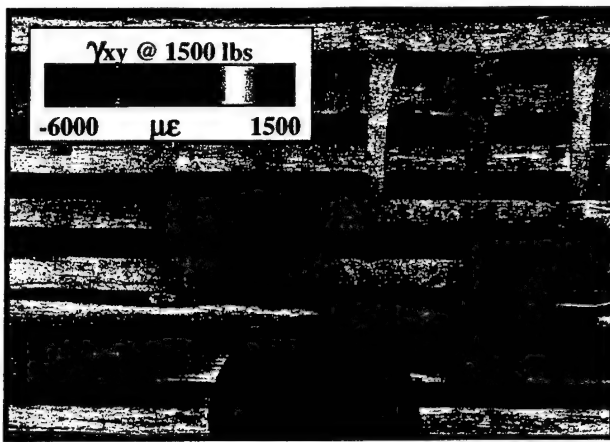


Figure 107. Shear strain at 1500 lb. with hole. Figure 108. Shear strain at 2000 lb. with hole.

## 10.7. Nonlinearity/Damage Detection

Local nonlinearities in strain response can be interpreted as yielding, or damage initiation. In the optical strain gages, changes in slope can be easily detected by plotting strain at uniform increments for all sensors, or strain against load for individual sensors. Figure 109 shows the strain data for each sensor in strand AFD2 for each of the "Ramp" loads (AFD2 was the only strand monitored containing complete strain data along the length of the coupon). The uniformity of the data at regular load intervals can be observed qualitatively for all sensors, with the exception of Sensor #16 near the hole. This sensor shows smaller strain increase when the load increases past 1500 lb., thus indicating the initiation of damage at some load between 1500 lb. and 2000 lb.

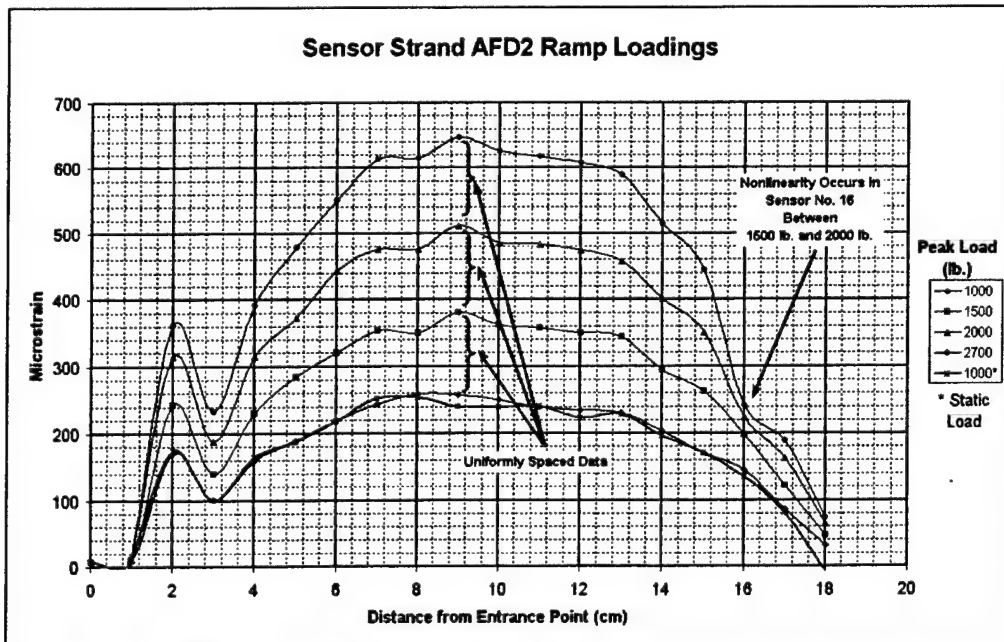


Figure 109. Linearity comparison for strand AFD2 during "ramp" loading.

Figure 110 shows the load-strain response from the ramp loading to 2700 lb. for Sensors #10-18. While the data are somewhat noisy due to manual loading of the coupon, the slope of the data for Sensor #16 appears to change at around 1600 lb., while the slopes of the other sensors remain relatively constant. These changes are attributed to damage developing in the coupon.

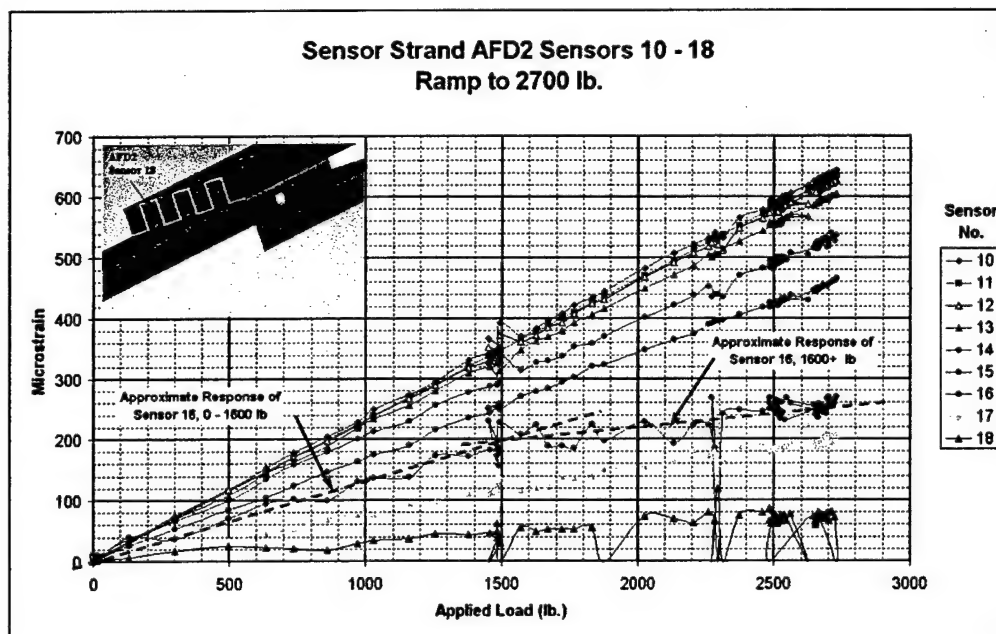


Figure 110. Change in slope at ~1600 lb for Sensor #16.

Nonlinearity in Moiré data is detected by subtracting linearly scaled data strain results for a low load from the data for a higher load. The difference will be zero if nonlinearities do not appear. For example, subtracting twice the data at 500 lb. from the data at 1000 lb. will result in a net of zero if the data are truly linear. Figure 111 shows the results of this test for axial strain data. The field is uniform when twice the 500 lb. data is subtracted from the 1000 lb. data and when 1.5 times the 1000 lb. data is subtracted from the 1500 lb. data. However, subtracting 1.33 times the 1500 lb. data from the 2000 lb. data produces a "hotspot" near the upper right corner of the hole. The conclusion is that damage has been initiated at a load magnitude between 1500 and 2000 lbs. Damage location corresponds to the warp yarn. The most likely damage mode is cracking between fibers within the yarn.

Damage in this load range also is seen in the linearity analysis of transverse strain (Figure 112) and shear strain (Figure 113). Nonzero difference is clearly observed at the same location when 1.33 times the 1500 lb. data is subtracted from the 2000 lb. data. Additional nonlinear behavior is observed in shear when 1.5 times the 1000 lb data is subtracted from the 1500 lb. data. The area of nonlinear shear behavior corresponds to the bondline between the coupon's upper lap and "tongue." Possible adhesive yielding at the bondline could occur between 1000 lb. and 1500 lb. load levels.

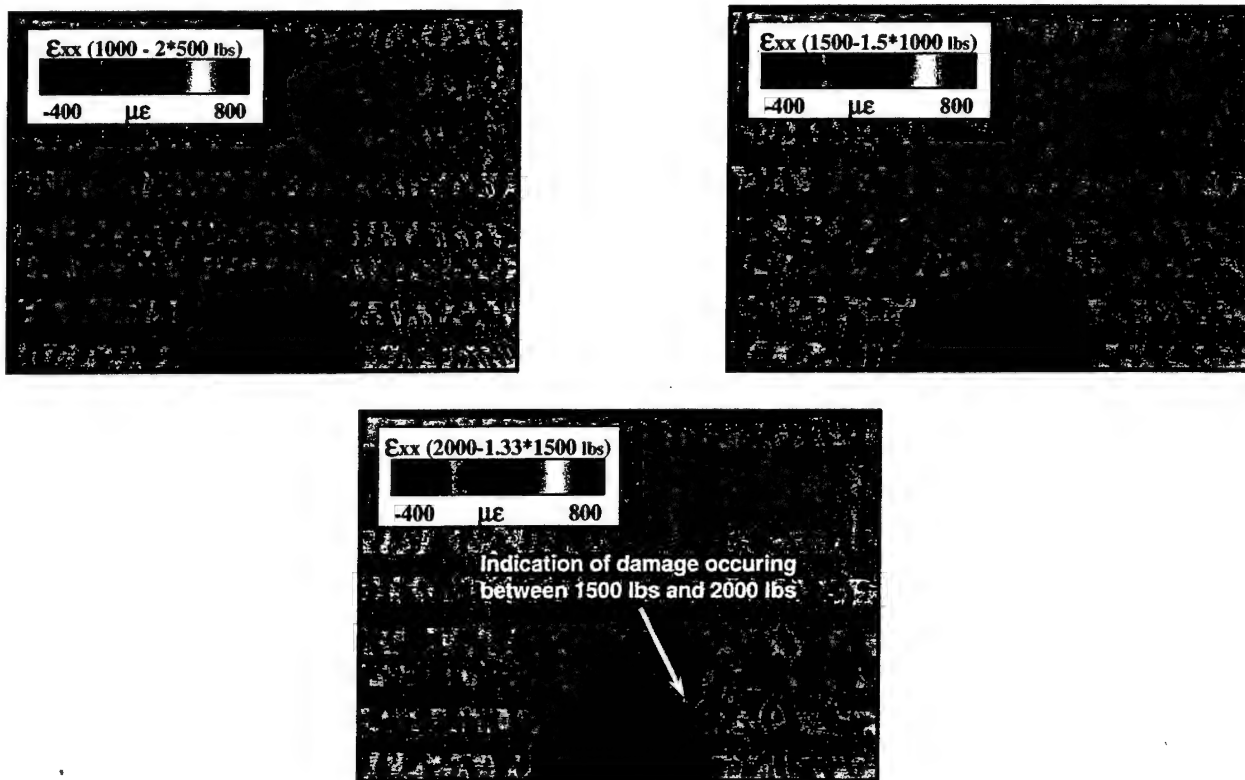


Figure 111. Evidence of longitudinal strain nonlinearity at 1000 lb., 1500 lb. and 2000 lb. loads.

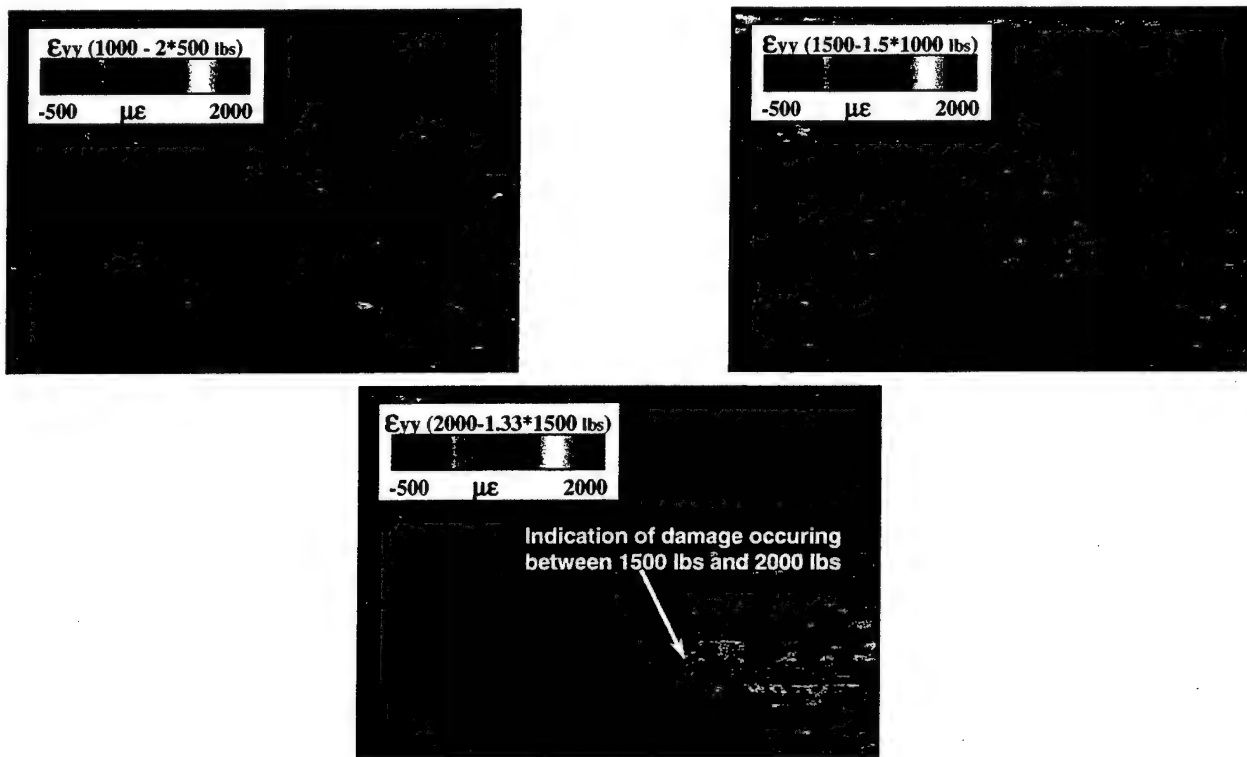


Figure 112. Evidence of transverse strain nonlinearity at 1000 lb., 1500 lb. and 2000 lb. loads.

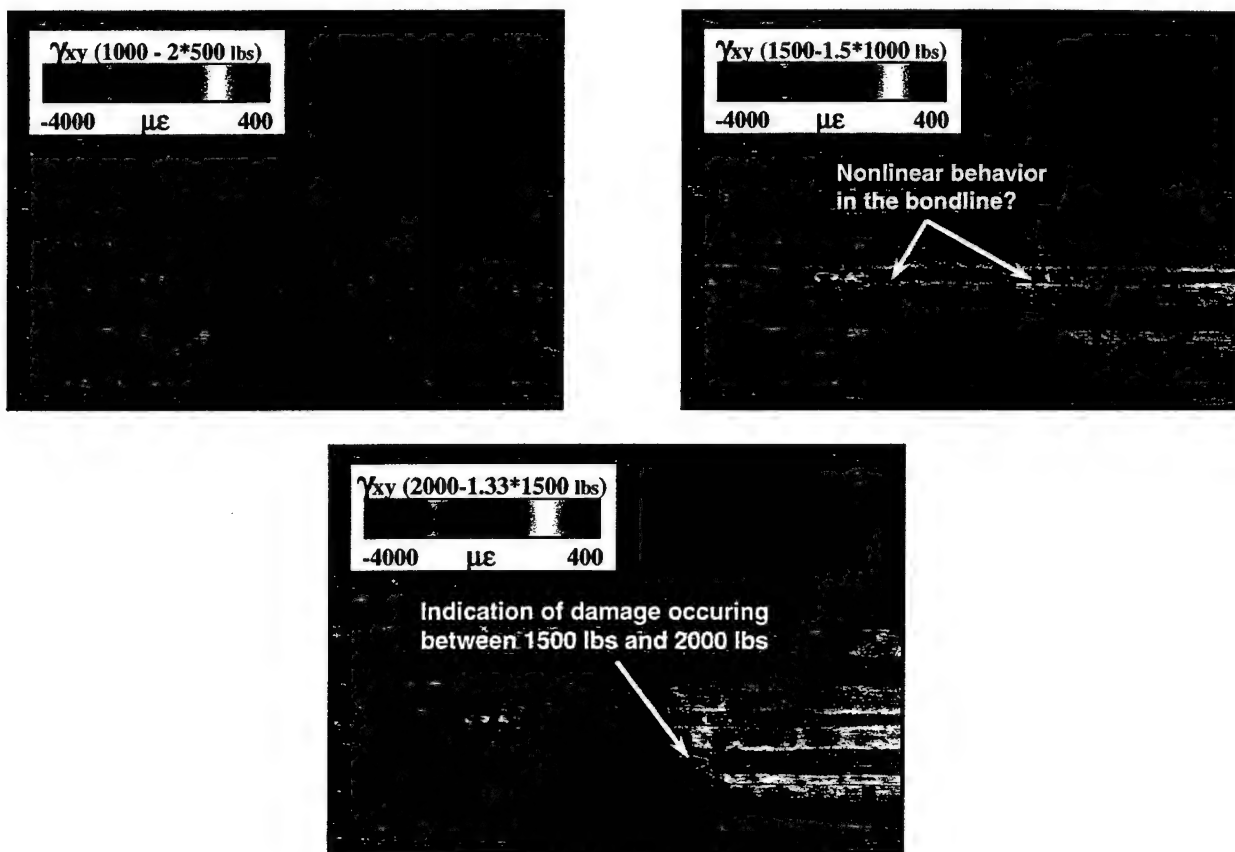


Figure 113. Evidence of shear strain nonlinearity at 1000 lb., 1500 lb. and 2000 lb. loads.

## 10.8. Summary and Conclusions

The optical sensor instrumented double-lap bonded joint was tested in tension in an MTS servo-hydraulic load frame, and then was re-tested on a Moiré interferometry table so that additional experimental data could be collected for comparison to the integrated optical sensor strain data. Keeping in mind that internal strain data were averaged over the length of the optical sensors (5 mm), one can expect that those data would differ somewhat from surface mounted foil gage strain data. The Moiré strain data and optical sensor strain data agree fairly well for constant load levels of 1000 lb., 1500 lb., and 2000 lb.

After initial loadings, a transverse hole was drilled in the "tongue" portion of the coupon to create significant strain concentration. Optical strain sensors were clearly capable of detecting the hole. The anticipated strain gradients around the hole also were observed in the Moiré data. Linearity analyses of both optical gage and Moiré data had detected the presence of nonlinearity or damage near the hole at a load level between 1500 lb. and 2000 lb. Linearity analysis of the Moiré shear strain data indicated damage or yielding along the specimen bondline between 1000 lb. and 1500 lb. load levels.

## 11. DOUBLE-LAP BOLTED JOINT WITH INTEGRATED FBG SENSORS

Composites joined with mechanical fasteners see frequent use in aerospace applications and present another structural problem in which significant stress and strain gradients occur. The objective of series of tests described in this section was to evaluate the use of integrated fiber optic (Bragg) sensors to detect strain gradients in the presence of a bolted joint. The test series was conducted on a double-lap bonded joint sample similar to the one described and tested in Section 10, with addition of mechanical fasteners joining the adherends to the tongue. Quasi-static tensile tests were conducted.

### 11.1. Sample Configuration

A drawing of the sample is shown in Figure 114. The overlap is approximately 1.5 in. (3.81cm) in length. Two 0.3 in. (0.762 cm) diameter holes were machined into the sample to accept 0.25 in. (0.635 cm) diameter bolts. The top, bottom and middle adherends were manufactured from the same material as in the previously studied bonded joint sample. A 2.0 in. (5.08 cm) spacer was used to grip the sample at the sample end with the two adherends.

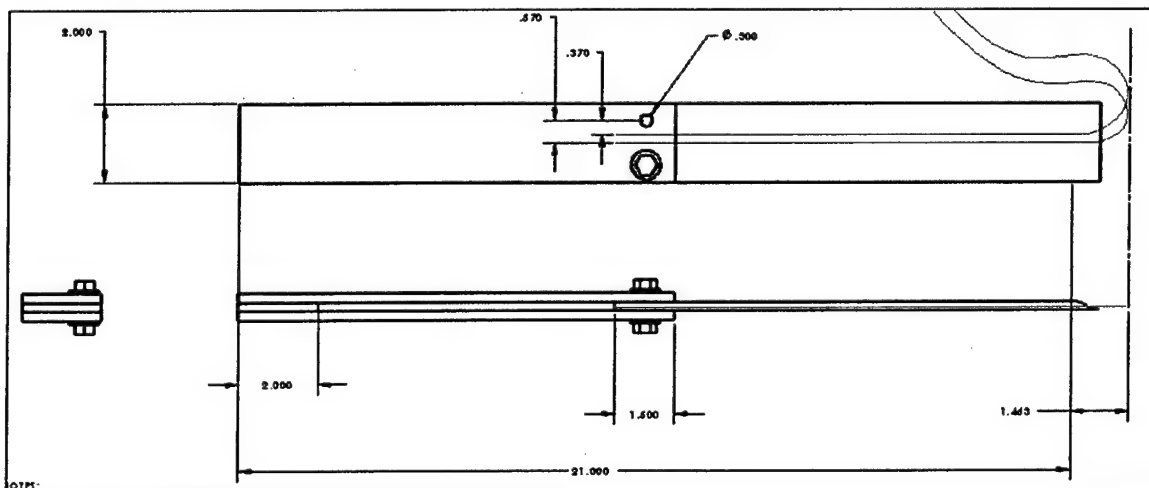


Figure 114. Schematic of double-lap bolted joint specimen.

### 11.2. Sensors, Instrumentation and Test Equipment

A total of four Bragg grating sensor strands were integrated into the middle adherend (as opposed to the top and bottom adherends as in the bonded joint sample). The sensors were positioned and stacked as shown in Figure 114 and Figure 115. The length of the tongue allows for a maximum of 30 active sensors in each strand. The sensors were monitored using the same DSS system used in the bonded joint testing. The coupon was loaded quasi-statically in an MTS servo-hydraulic load frame. Load, displacement, and strain (from longitudinal gages mounted front and rear on the tongue) were recorded digitally on the MTS computer system. The coupon is shown mounted in the test fixture in Figure 116.

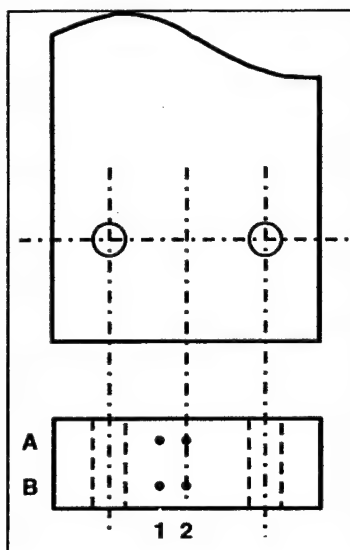


Figure 115. Location and nomenclature for optical sensor strands in bolted lap joint sample.



Figure 116. Bolted lap joint coupon mounted in MTS load frame.

### 11.3. Test Procedure

A total of six quasi-static loadings of the bolted lap joint sample were conducted. Test details are summarized in Table 13. The first loading was conducted to 5000 lb. only to assess elastic response and avoid damage, so that the fourth sensor strand could be interrogated in a second loading. This second loading was conducted at a slightly faster (though still quasi-static) rate with audible cracking/popping occurring at approximately 5300 lb. Unfortunately, the DSS data acquisition failed at approximately 7200 lb. The sample was unloaded, optical sensors and foil

gages re-zeroed, and the loading repeated (Load #3) after re-boot of the DSS system. The system again crashed at approximately 7200 lb. A fourth loading after DSS system re-configuration resulted in cracking/popping at approximately 8000 lb. load, then the test was halted after the sample could no longer support the increasing load. Sample inspection after the test revealed a shear-out failure of material between the bolt holes and the end of the sample.

Two additional loading sets were conducted on a new sample, fabricated by cutting off the failed portion of the original sample (~2.25 in.) and machining new holes centered 1.0 in. from the machined end. Loading #5 was conducted to assess elastic response and avoid damage so that optical strand B1 could be interrogated during an additional loading. This loading (#6) was conducted to failure (again, shear-out of the bolt holes).

Table 13. Bolted double-lap joint test details.

Loading →	#1	#2	#3	#4	#5	#6
Control	Displacement	Displacement	Displacement	Displacement	Displacement	Displacement
Load Rate (in/min)	0.01	0.05	0.05	0.05	0.01	0.05
Load Limit (lbs.)	5000	7300*	7200*	Failure	3000	Failure
DAQ Rate (samples/s)	10	5	5	5	5	2
Optical Fibers Interrogated	A1, A2, B1	A1, A2, B2	A1, A2, B2	A1, A2, B2	A1, A2, B2	A1, A2, B1
Bolt Torque (in-lb)	50	50	50	50	150	150
Notes	(1) A2 re-zeroed after clamping sample in MTS (2) Unload at 5000 lb. to determine elastic response	(1) All channels rezeroed after clamping in MTS; (2) Cracking heard at 5200-5300 lb (3) DSS System crash at 7300 lb.	(1) Restart after unload of Loading #2 (2) DSS System crash at 7200 lb.	(1) Restart after unload of Loading #3 (2) Cracking heard around 8000 lb. (3) Test halted – sample unable to hold increased load (4) Bolts req'd 200 in-lb to release (5) Shear-out failure of upper and lower layers.	(1) Sample length reduced to ~15.8 in. (2) Center portion of sample remachined. (3) New holes made 1.00 in. in from new cut end. (4) Unload at 3000 lb. to determine elastic response.	(1) Test halted – sample unable to hold increased load (2) Shear-out failure of upper and lower layers.

## 11.4. Results of Double-Lap Bolted Joint Tests

Additional tests with bolted joints were conducted with two optical fibers carrying dozens of sensors integrated between two bolts in the middle material, as shown in Figure 117. For the bolted double-lap joint, the fiber optic sensors demonstrated the ability to determine internal strain states, namely the increase of strain due to the presence of a bolt. Figure 118 shows the actual tested bolted joint specimen.

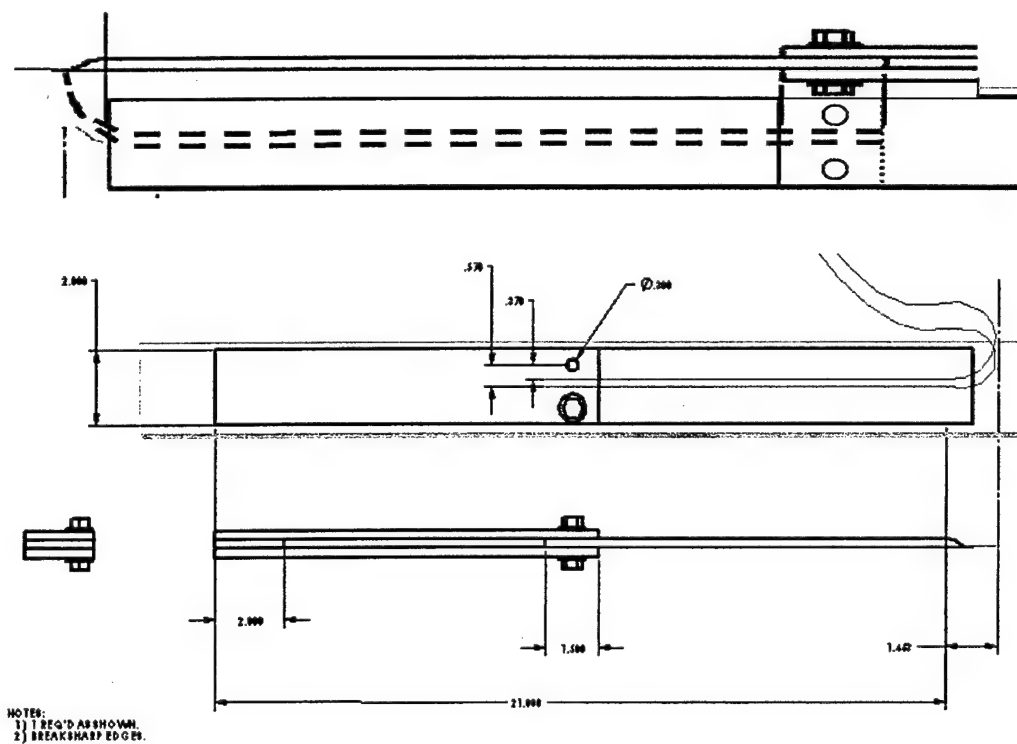


Figure 117. Schematic of double-lap bolted joint test specimen and location of integrated optical fibers with Bragg grating sensors.



Figure 118. Double-lap bolted joint test specimen with integrated fiber optic sensors.

The optical fiber nearest to the bolt (B1, the blue line) shows in Figure 119 an increase in strain as the sensor position nears the bolt itself. The optical fiber placed farther from the bolt (A2, the green line) shows in Figure 120 a considerable strain increase, but that is much less significant than the one monitored by optical fiber B1. The load was increased up to failure of the joint that occurred at 13009 lb. load. The data for B1 began to increase nonlinearly as early as at 9000 lb.

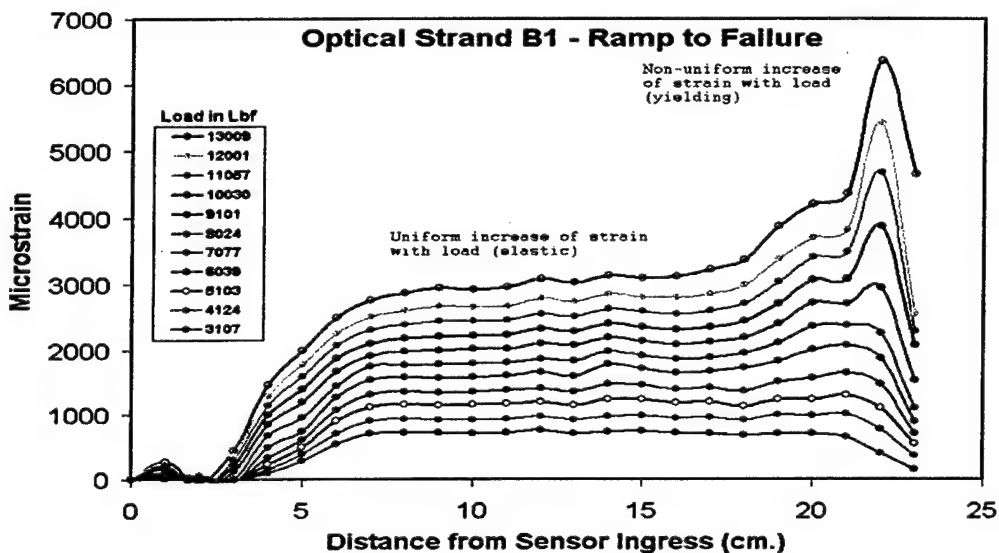


Figure 119. Longitudinal strains in double-lap bolted joint specimen recorded by optical fiber B1 sensors at different load levels.

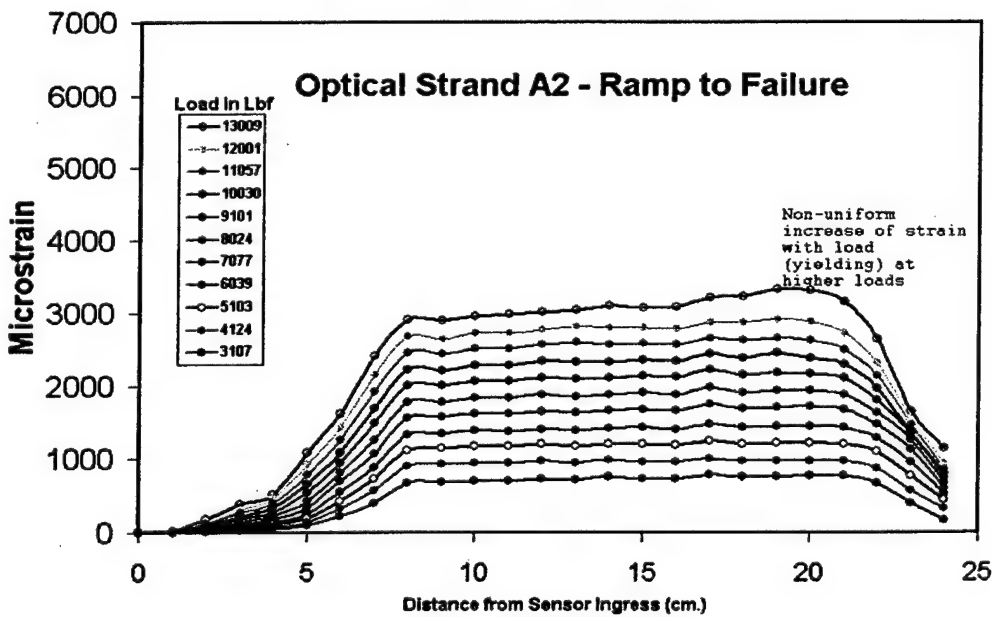


Figure 120. Longitudinal strains in double-lap bolted joint specimen recorded by optical fiber A2 sensors at different load levels.

The composite region around the bolt, shown in Figure 121, has been substantially deformed longitudinally (in the horizontal, loading direction), then the joint failed in shear. The structure around the holes stayed largely intact, and the optical fibers near the holes remained functional. Strain data continued to be taken from the sensors despite the severe and extended damage nearby.

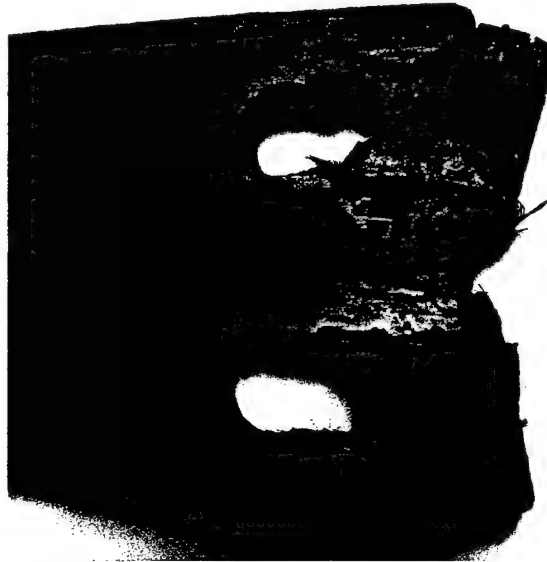


Figure 121. The failed fragment of bolted joint specimen.

## 12. ADDITIONAL TESTING AND MODELING OF 3Weave<sup>TM</sup> COMPOSITE MATERIAL

The mechanical tests of 3Weave<sup>TM</sup> materials in four-point bending, reported in the previous sections, produced data which did not correlate as well as expected with the theoretical results obtained from 3-D stress/strain analysis using 3D MOSAIC code. In addition, Phase I data from foil gages showed nonlinear trends that were not anticipated, particularly in the direction transverse to loading. The use of inaccurate material property data (fiber volume fraction and modulus, in particular) in the computational models was thought to be the most probable cause for the discrepancies between predictive analysis and actual mechanical test results. A brief additional test program was proposed to verify this suggestion. The plan included extraction of test coupons from the same panel which was used for original coupons, so that the data generated could be used directly in the computational model. Fabricating additional bending samples was intended to compliment tensile coupons, in order to provide additional data to which theoretical results could be compared.

### 12.1. Objectives, Scope and Summary of Test Results

The objectives of these additional tests were to (1) measure tensile properties (modulus and Poisson's ratio) in the warp and fill directions of a vinyl-ester-infused 3Weave<sup>TM</sup> carbon fiber

preform; (2) collect displacement and strain data during flexural tests of the 3-D woven composite; (3) perform fiber volume fraction measurements of samples extracted from the coupons after testing.

Strain data were collected from front- and rear- mounted axial foil gages, a transverse foil gage, and for the bending coupons, additional axial gages mounted outside the support span. Coupons were fabricated from the same panel from which previous coupons were extracted, despite any curvature or surface waviness that might have existed in the panel. A judgment was made that any error introduced by such imperfections would be overshadowed by the need to test the same panel from which previous coupons had been extracted (and to which theoretical models have been compared).

Tensile and four-point bending test data were generated for the 3Weave<sup>TM</sup> carbon fiber/vinyl ester matrix composite in both the warp and fill directions. Tensile data contained more scatter than expected, likely due to slight curvature in the samples. Bending data contained less scatter than tensile data and the slopes (moduli) showed improved repeatability.

## 12.2. 3-D Modeling and Predictive Analysis of 3-D Woven Composite

One of the objectives of the Phase II effort was to validate advanced 3-D stress/strain analysis tools by means of integrated fiber optic sensors. 3TEX has performed modeling of the carbon fiber/epoxy matrix 3-D woven composite material, which was studied experimentally in this project, and predicted its elastic properties using in-house 3D MOSAIC code. The 3-D stress/strain analysis approach is based on the displacement field approximation in terms of triple series with Bernstein polynomial basis functions, see [14], and applying suitable variational procedures. The related computational procedures with example of application to 3-D woven composite Unit Cell and prediction of effective elastic property prediction can be found in [19].

Further attempt was made to simulate 4-point bending tests using "Layered" and "Homogenized" models [20] of the same 3-D woven carbon/epoxy composite. The experimental results were described in detail in the Phase II Year 1 annual report. However, theoretical results obtained in that first attempt showed significant discrepancy with the experimental data for both transverse displacement ( central deflection) and longitudinal strains recorded on the 3-D woven composite specimen. Details are included below in this section. Among several possible reasons that can explain the observed discrepancy, the most probable are:

1. The developed geometric Unit Cell model of the actual material is not sufficiently accurate; specifically, the total fiber volume fraction in experimentally studied composite may be considerably lower than that obtained from the design model.
2. Visible in-plane fiber undulations, seen in the experimental specimen micrographs, were not accounted in the model.
3. Individual thickness and location of the warp- and fill-reinforced layers in experimental composite were not exactly the same as in the "Layered" composite model.
4. Considerable curvature caused by residual thermal stresses was observed on the experimental composite panel, though it was not accounted in the analysis.

Investigation of the above and some other possible causes of the observed discrepancies continues. Also, stress/strain analysis of the experimentally studied double-lap bonded joint is in progress. Results of that work, in comparison with strain data provided by integrated arrays of Bragg grating sensors, foil gages, and by Moiré interferometry, will be also be analyzed and reported in the future journal articles and conference papers.

Next we briefly report results of the modeling of the microstructure of 3-D woven carbon/epoxy composite under investigation, and the Unit Cell model development. Further, two models of the 3-D woven composite (called "Homogenized" and "Layered"), which were used in 3-D elastic simulation of 4-point bending tests, are presented.

Figure 122 shows a representative microstructure of the carbon/epoxy 3-D woven composite described in experimental section of this report. The photograph was taken at the cut edge of composite panel. One can recognize 4 warp, 5 fill yarn layers and continuous Z-yarn making periodic  $\Omega$ -type loops around the fill yarns. It is seen that the major length of Z-yarn goes in through-thickness direction, though there are also considerable segments oriented in warp-direction.



Figure 122. Edge view of the experimental carbon/epoxy 3-D woven composite.

A smaller fragment of composite edge (side views in the fill and warp directions are shown next to each other) can be viewed in Figure 123 along with the computational 3D MOSAIC model of the composite Unit Cell. The latter one was generated by using the design data (e.g., specific weaving machine set up parameters), together with some direct measurements taken on the produced preform and fabricated composite panel.

The Unit Cell model shown in Figure 123 has been used first for predicting orthotropic elastic properties of the 3-D woven composite. It was assumed in the model that total fiber volume fraction is 55%, with fiber volume content of warp direction 42.3%, in fill direction 52.3% and in Z direction 5.4%. This exactly corresponds to the fabric design parameters. The predicted properties were compared with tensile test data obtained by UDRI for five warp-directional specimens (1FTW thru 5FTW) and five fill-directional specimens (1WTW thru 5WTW). Numerical results are summarized in Table 14.

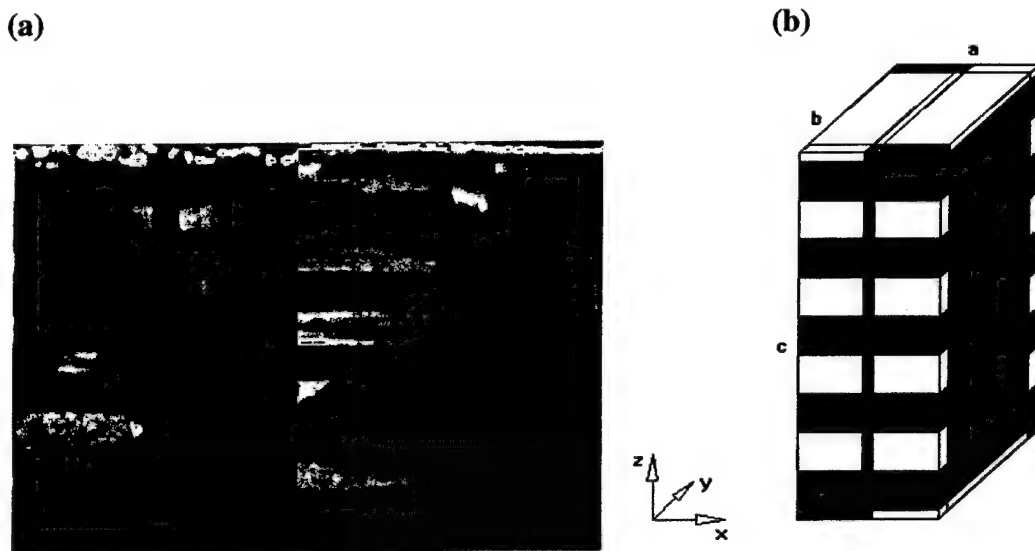


Figure 123. Edge views of two fragments of experimental carbon/epoxy 3-D woven composite (a) and 3-D Mosaic model of the composite Unit Cell (b).

Table 14. Experimental and theoretical elastic moduli in warp and fill directions.

Specimen ID	Loading Direction	$E^{front}$ , GPa	$E^{rear}$ , GPa	$E^{average}$ , GPa	$E^{theor}$ , GPa
1FTW	Warp	61.23	64.74	62.98	60.26
2FTW	Warp	61.92	69.64	65.78	
3FTW	Warp	63.30	64.67	63.98	
4FTW	Warp	62.05	50.95	56.50	
5FTW	Warp	58.40	56.95	57.67	
Average	Warp	61.38	61.40	61.39	
1WTW	Fill	75.84	77.22	76.53	71.23
2WTW	Fill	71.02	N/A	71.02	
3WTW	Fill	72.40	76.53	74.46	
4WTW	Fill	71.02	71.02	71.02	
5WTW	Fill	73.78	68.95	71.36	
Average	Fill	72.81	72.95	72.88	

Two distinct columns in Table 14, showing  $E^{front}$  and  $E^{rear}$ , correspond to elastic moduli processed from the strain data recorded at the center of each of the two faces of experimental specimen. It is seen that the average elastic modulus for five warp-directional specimens, namely 61.39 GPa, and for five fill-directional specimens, namely 72.88 GPa, are in a very good agreement with the theoretical predictions, which are 60.26 GPa and 71.23 GPa, respectively.

The obtained set of predicted effective elastic properties of the 3-D woven composite was then used in computer simulations of the 4-point bending test, where test specimen material was treated as homogeneous and orthotropic. The respective analysis model is called "Homogenized" Model, see Figure 124.

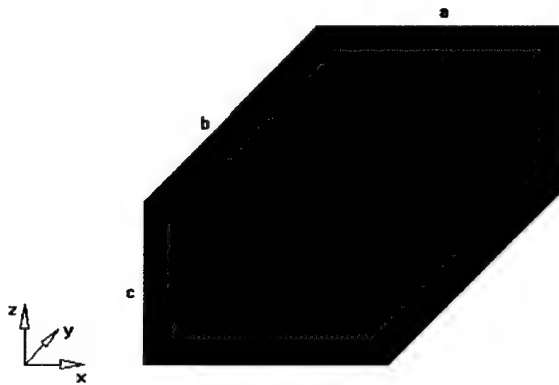


Figure 124. "Homogenized" Model of 3-D woven composite, ignoring actual through-thickness positions of warp and fill fiber layers.

The principal drawback of Homogenized Model is that it does not account for distinct positions of warp and fill yarn layers through the thickness of a 3-D woven composite. This effect is not important in modeling tensile test, but one can anticipate that such model may not be accurate in modeling bending tests. And this was, actually, demonstrated in one of the previous studies presented in [20] on the example of 3-point bending test simulation of 3-D woven S-2 glass/vinyl ester composite material.

In order to improve accuracy of bending problem simulation, a Layered Model shown in Figure 125 has been introduced. In this model, there are 9 homogenized layers: four "warp" layers containing warp yarns, vertical segments of Z yarns and matrix blocks; three inner "fill" layers containing vertical segments of Z yarns and matrix blocks; two outer "fill" layers contain fill yarns, vertical and horizontal segments of Z yarns and matrix blocks. Effective elastic orthotropic properties of each type of layers can be computed considering respective parts of the Unit Cell model (see Figure 123b) and using the same 3D MOSAIC analysis approach that was applied to the whole Unit Cell. Alternatively, those properties can be computed using Orientational Averaging Approach, see [19].

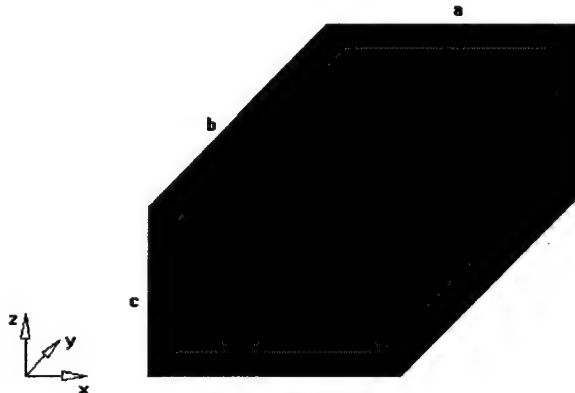


Figure 125. "Layered" Model of 3-D woven composite distinguishing actual through-thickness positions of warp and fill fiber layers.

### 12.3. Comparison of Theoretical and Experimental Results

A comparison of theoretical predictions obtained with Layered Model and experimental results showed excellent agreement for the case of 3-D woven S-2 glass fiber/vinyl ester resin composite [20]. That success encouraged us to expect that for 3-D woven carbon fiber/epoxy resin composite studied here, modeling 4-point bending test will be also accurate. Specifically, that theoretical predictions obtained with Layered Model will be closer to experimental results than their counterparts obtained with Homogenized Model. However, such an expectation was not realized in the initial 4-point bending test simulations.

In the initial effort to simulate 4-point bending problems for warp- and fill-directional 3-D woven composite specimens, it was assumed that all homogenized "warp" layers have 54% fiber volume fraction, while all homogenized "fill" layers have 52.3% fiber volume fraction. This percentage exactly corresponds to the ratio of fiber volume content of warp to fill fibers in the manufactured preform (43.2% vs. 52.3%). This percentage also yields the following "effective" moduli of the 9-layer model: 60.0 GPa in warp direction and 71.20 in fill direction, which are very close to experimental tensile moduli (see Table 14).

Results obtained for central transverse displacement (deflection)  $u_3^c$ , for loading nose transverse displacement  $u_3^n$ , for longitudinal strain at the center of the upper (compressed) side of the specimen  $-\varepsilon_1^{fc}$ , and for longitudinal strain at the center of the bottom (tensed) side of the specimen  $\varepsilon_1^{rc}$ , are all presented in Table 15 for one representative warp-directional specimen and in Table 16 for one representative fill-directional specimen. These results show that for warp-directional specimen all experimental characteristics are very close to theoretical predictions provided by Homogenized Model. At the same time, the experimental results are in unreasonably large discrepancy with theoretical predictions provided by Layered Model. This is unexpected, and we have no definitive explanation of such effect now. One can also notice in Table 15 that the displacements and strains predicted by Layered Model are significantly below their counterparts predicted by Homogenized Model.

Table 15. Comparison of experimental and theoretical results for warp-directional specimen 5WTWFL.

Characteristic	$u_3^c$ (mm) at 100 lb <sub>f</sub> load	$u_3^n$ (mm) at 100 lb <sub>f</sub> load	$-\varepsilon_1^{fc}$ ( $\mu$ strain) at 100 lb <sub>f</sub> load	$\varepsilon_1^{rc}$ ( $\mu$ strain) at 100 lb <sub>f</sub> load
Experimental	0.7573	0.5982	800.7	802.3
Layered	0.6574	0.4845	695.7	695.7
Homogenized	0.7712	0.5664	821.0	821.0

When analyzing results in Table 16, the opposite effects are seen. In the case of fill-directional specimen, the displacements and strains predicted by Layered Model are substantially above the respective values predicted by Homogenized Model. At the same time, experimental strains are

much closer to the values predicted by Layered Model, contrary to the effect seen in Table 15 for warp-directional specimen.

Table 16. Comparison of experimental and theoretical data for fill-directional specimen SFTWFLA.

Characteristic	$u_3^c$ (mm) at 100 lb <sub>f</sub> load	$u_3^n$ (mm) at 100 lb <sub>f</sub> load	$-\varepsilon_1^{fc}$ ( $\mu$ strain) at 100 lb <sub>f</sub> load	$\varepsilon_1^{rc}$ ( $\mu$ strain) at 100 lb <sub>f</sub> load
Experimental			1368	1306
Layered	1.162	0.8516	1244	1244
Homogenized	0.9076	0.6651	970.7	970.7

In the continuing effort, which can not be conclusively reported here, the large set of experimental data from earlier performed 4-point bending tests, provided by integrated fiber optic sensors and foil gages, will be closely studied and compared to computational results obtained from various 3-D woven composite models. Analysis of the test specimen response to bending and tension will be revised to take account of the modified material properties and also some additional effect not accounted before.

## 13. DEVELOPMENT OF CAP OPTICAL CONNECTION METHODS

### 13.1. Engineering Challenge

One of the hurdles a fiber optic sensor system must clear is the practical manufacture of composite parts from the fiber preforms. A challenge here is the development of a method to enable practical connections from the optical fibers to the data acquisition system. Current techniques are heavily burdened by the extraordinary efforts required to care for the delicate leads. Manufacture of practical, and serviceable components would be quite difficult and expensive due to the delicate nature of the leads and connectors, see Figure 126.

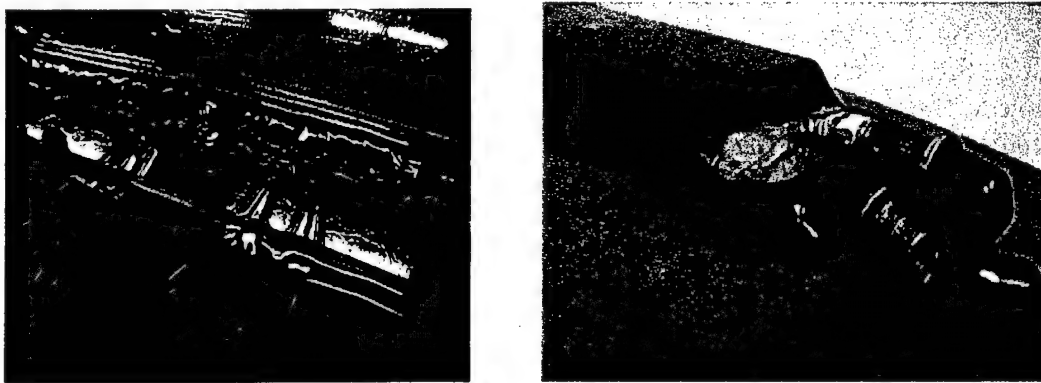


Figure 126. Delicate lead egress vs. robust embedded connectors developed in Phase I.

If a procedure were devised by which any lead end exposed by cutting could be accessed by polishing of that lead's exposed end, then this would entirely eliminate the need for protection of

the delicate leads after weaving. In this case, a preform would be woven with sensors being regularly pulled into the preform by the rapiers. After that the preforms can be cut to size (severing many leads) molded (encasing the leads entirely), and then machining of the parts or portions of them would expose bitter ends of the sensors in a grid pattern within. At that point, the ends would be located (by X-ray, optically, or by visual markers), and the end would be polished as is now in commercial practice with standard connectors. This could be done along with counter boring and threading of the adjacent material as in Figure 127, or subsequent bonding of a specialized connector to the polished surface which is aligned with the wave guide in the part as shown in Figure 128.

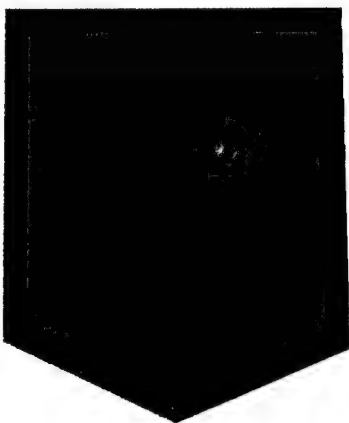


Figure 127. Machining/polishing of mechanical interface for robust connections.

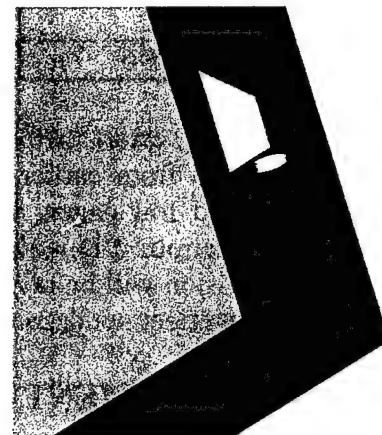


Figure 128. Bonding of surf connector to polished lead end.

In Year 1 of the Phase II effort, literature searches, and preliminary experiments involving connections made to fibers within epoxy castings pointed the way to developing a Cut And Polish (CAP) method. The goal is a method by which any lead end exposed by cutting could be accessed by polishing of that lead's exposed end, thus eliminating the need for protection of the delicate leads after weaving. The preform would be woven with sensors being regularly pulled into the preform by the rapiers. After the remaining manufacturing steps to make the part (molding, cutting, final machining) were complete, the severed fiber ends would be located, and then polished. Subsequent counter boring and threading of the adjacent material, then bonding of a specialized connector to the polished surface would complete the connection.

In Year 2 of the Phase II effort, LUNA has successfully established CAP connections, albeit with relatively high optical losses. LUNA's work has centered on ways to optimize the "one-way" CAP approach. In the "one-way" approach, the CAP connection serves to either deliver light into the embedded fiber or receive the sensor modulated light from the embedded fiber. LUNA has demonstrated the ability to transmit and receive light through two ruggedized CAP connections with a composite-embedded optical fiber.

The focus of this task was to develop the practical CAP connection technique. Each of the following sections review the critical steps that enabled LUNA to successfully develop and demonstrate the CAP connection approach.

### 13.2. Literature Search on Fiber Optics Connectors

The first step in developing the CAP technique was to conduct a literature search to investigate approaches toward positioning optical fibers. The search was broken into three categories: Patent Literature, Scientific Literature and Trade Literature. Based on available products for aligning optical fibers and the allowable losses in the DSS system, connecting one fiber to another fiber embedded in a composite material appears to be a tractable problem. Progress on the CAP connector feasibility study included making a polishing puck that would hold an epoxy block containing a single mode fiber and purchasing a small UV lamp to cure index matched UV adhesive.

A literature search was conducted on positioning optical fibers in optoelectrical devices and splices. Aligning optical fibers with edge emitting diodes or surface emitting diodes is similar to the CAP approach of connecting an optical fiber to an embedded Bragg grating. The literature search was divided into patent literature, scientific literature and product literature. The search explained many of the problems associated with aligning and attaching optical fibers in optoelectrical components. Optomechanical equipment and assembly techniques were also reviewed. The article [22] gives an overview of the tools and methods for obtaining precision fiber alignments. It will be used as a guide to organize the findings of the literature review.

An important step in the assembly of many optoelectronic devices involves the careful and precise alignment of components. Fibers, fiber arrays, lenses, diodes and other such components must be aligned properly to insure maximum light propagation. Likewise, mating an embedded optical fiber to another fiber will also require precise alignment. Alignments typically require minute nanometer scale motions with multiple axis stages. The methods to obtain and maintain precise alignments vary throughout the industry and upon the application but are inherently based upon basic optomechanical principles. Table 17 below compares the requirements of aligning optical fibers to optoelectric devices and the anticipated requirements of aligning optical fibers to DSS fiber embedded in textile composites.

Table 17. Suggested target specifications for a CAP connector system.

Requirement	Fiber to device	CAP Connection
Target loss	0.02 dB Fiber to Fiber 50-80 coupling efficiency	<4 dB
Assembly environment	Clean	Dirty
Alignment precision	0.3 micron	1 micron
Part Access	Good	Potentially bad
Control feedback	Transmitted power	Reflected power
Alignment type	Passive or Active	Active
Fiber end face preparation	Lensed	Polished
Device or DSS preparation	Not required	Polished
Degrees of Freedom	6	3 or 4
Initial alignment, "first light"	Image analysis, well known device placement	Very difficult

When operating the DSS power losses of greater than 8dB start affecting the instruments ability to measure the grating spectra. Therefore, the target loss for the CAP connection was set (somewhat arbitrarily) at 4 dB which would require a lateral alignment precision of roughly 1 micron. The losses through a fiber-to-fiber splice or a connector are around 0.02 dB requiring a lateral alignment precision of roughly 0.3 micron. A measure of the amount of optical power emitted from a source that can be coupled into a fiber is usually given by the coupling efficiency,  $\eta$ , defined as the ratio of power coupled into the fiber to the power emitted from the light source [23]. The coupling efficiency can be up to 80% when connecting to a surface emitting or edge emitting diode, but is often closer to 50%.

When connecting fibers to fiber arrays, lenses, diodes and other components the working environment is clean compared to what is expected for embedded sensor applications. Connections to the embedded DSS sensors would be at some point during the manufacture of the part. Presumably, in an aircraft structure, the connection would be made during assembly of the major airframe piece. Therefore, access to the DSS fiber may be space limited or dirty, which will influence the techniques used to make the CAP connection. A dirty environment may limit the choice of alignment stages. Space requirements will limit the size of alignment stages and any type of control instrumentation may need to be remote from the alignment stage.

When aligning optical devices with optical fibers, the control instrumentation measures the transmitted light and moves the stage to maximize the transmitted light. The exception would be in cases that use passive [24-27] alignment. During passive alignment, the source location is well known and dimensional tolerances are small enough to place the optical fiber in a prefabricated notch or groove obtaining the required coupling efficiency. When aligning embedded DSS fiber with optical fiber, the control instrumentation will measure reflected light from the Bragg gratings. The alignment stage would be moved to maximize the amplitude of the reflected grating. Passive alignment would not be possible in the CAP application since the position of the embedded fiber is not known with high enough precision.

Even though the position of a diode light source can be known with great precision, the size of the source can be small and elliptical compared to the receiving fiber. Many patent citations describe lens schemes used to optimize the coupling of light from a source to a fiber [27-32]. Scientific literature also contains many references to lens schemes [33-37]. A function of the microlens is to magnify the emitting area of the source to match exactly the core area of the fiber end face. Several possible lensing schemes include a rounded-end fiber, a non-imaging glass sphere, larger imaging glass spheres, cylindrical lens, tapered-end fibers, elliptic fiber ends, spot size converting the wave guides and tapered wave guides. Although these lenses can improve the source-to-fiber coupling efficiency, they can also create additional complexities such as fabrication and handling problems associated with their small sizes [23]. The DSS core diameter is slightly smaller, 7 microns, than a typical single mode fiber, 9 microns. This difference in core size does not justify the use of micro lenses for coupling optical fiber to DSS fiber embedded in a composite. Coupling to an embedded DSS fiber more closely resembles fiber-to-fiber coupling. Alignment losses associated with fiber-to-fiber coupling are well characterized in the literature [38-44]. End separation, lateral misalignment and angular misalignment are the primary sources of optical power loss. In single mode, fiber lateral misalignments are the largest source of optical power

loss. One significant difficulty in coupling to an embedded DSS fiber will be fiber end face preparation. When making a splice or a connector, the optical fiber is cleaved to form a smooth, flat and perpendicular end face, which prevents the light from being deflected or scattered at the joint. Any additional polishing can be accomplished in the field after the fiber is inserted into a ceramic ferrule and connector. With the embedded DSS fiber, polishing the end face and surrounding material must prepare a smooth, flat and perpendicular end face. Precise polishing in the field will be a challenge in part because the DSS fiber may not be perpendicular to the edge. Fixtures to maintain a flat surface will need to be secured in place and polishing fluids may need to be recovered. Two examples of portable polishing equipment are shown in Figure 129 and Figure 130. These instruments are used for field inspection of metal parts requiring microscopic surface examination.

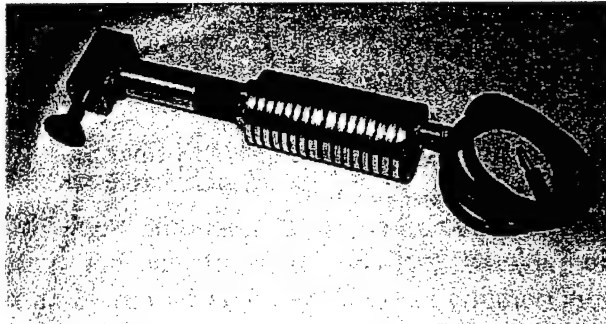


Figure 129. A portable grinder polisher from Metallography Equipment Manufacturers is suitable for preparing metallographic quality surfaces.

(<http://www.metequip.net/index.htm>)

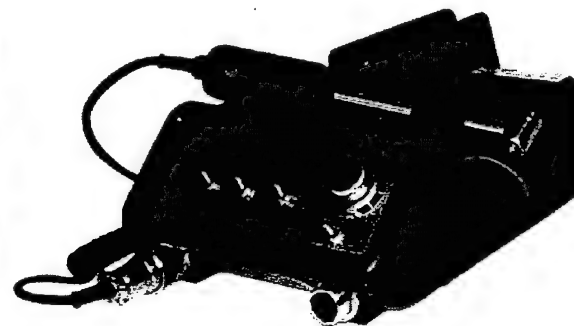


Figure 130. The Saphir 300 from Clemex is a portable polishure featuring variable speeds for varying applications.

(<http://www.clemex-metallography.com/>)

Once the DSS fiber is polished at the surface of the part, the mating optical fiber will be aligned and secured to the part with an index matching UV adhesive. Alignment stages can have up to 6 degrees of freedom—translation in X, Y and Z, and rotation about each of the three axes. Figure 131 is a sketch illustrating the orientation of the different axes. In the DSS application, rotation around the Z axis or the axis of the fiber is not necessary, because polarization-maintaining fiber is not involved. The X-Y plane is polished perpendicular to the DSS fiber. In practice, the optical fiber is not guaranteed to be perpendicular to the machined edge of the part. Therefore, the polishing process would need to produce a polished face perpendicular to the fiber axis. Assuming that the part is a thin plate, the angle the fiber makes in the XZ plane can be seen in an X-ray, but the angle the fiber makes in the YZ plane remains unverified. Angular misalignments are unavoidable [45], but for now the optical fibers are assumed to be perpendicular to the polished face and the alignment stage is mounted to hold the mating fiber perpendicular to the polished face. Rotation around the X and Y-axis could be included in an alignment stage. However, the added complexity will influence the size of the stage and the ability to mount it to a part containing the DSS fiber.

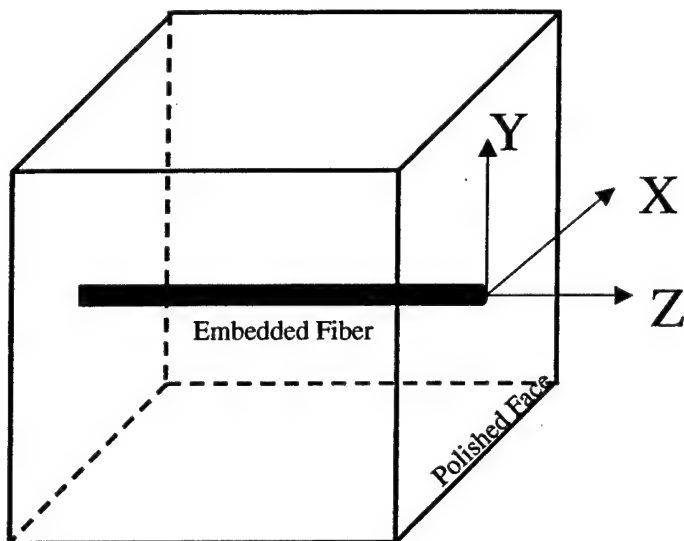


Figure 131. Coordinate system describing the location of the embedded DSS fiber.

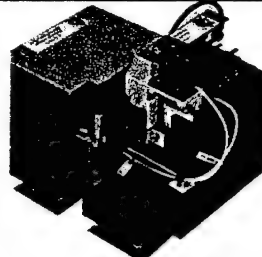
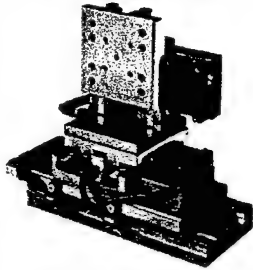
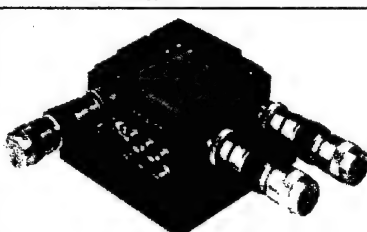
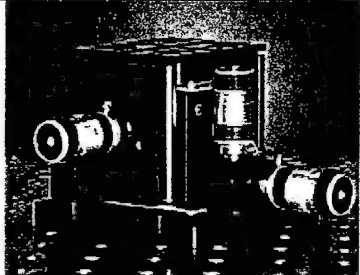
A variety of manufacturers offer optical stages with three degrees of freedom. Some of the manufacturer and representative stages are shown in Table 18. A slightly different stage configuration is described in [46]. The stage has all three actuators pointing in the same direction providing space savings and easy access that would prove useful in a CAP connection scheme. A complete CAP connector system would include the mechanical stage, the actuator, feedback control including a DSS system, fixtures to attach the stage to the part and an adhesive dispensing unit. Similar systems are available for assembling optical fibers to diodes [47,48]. Mechanical stages are either based on roller or ball bearing stages or on flexure stages. A frictionless mechanical bending action moves the flexure stage. Flexure stages have very high resolution but the range of motion can be limited. The lack of bearing in the flexure stage may make it more suitable for the manufacturing environment of the CAP Connector. The actuators that move the stages can be a DC motor, a stepper motor, a piezo motor or a piezo actuator.

The process of aligning the two fibers consists of two steps: Step 1 is a prealignment or “first light” search and the second is the fine alignment of the fibers. The first light search is complicated by the fact that the embedded DSS fiber is not clearly visible. The DSS fiber, however, is bigger than the surrounding structural fibers and its location could be pinpointed with the aid of a microscope. Both ends of the DSS fiber may not be accessible; therefore, first light and the feedback to the control system may be reflected light rather than optical power from transmitted light. The alignment control system and alignment algorithm would need to be designed accordingly. Alignment speed will not be a major factor in the alignment algorithm for the CAP connector since the number of connections made will be small compared to assembly of optoelectronic devices.

The summary from [22] applies very well to the case of the CAP connector and is quoted here: “Through careful studies analyzing all critical parameters of the alignment process and individual components involved, it is possible to determine an efficient alignment algorithm. The choice of prealignment tools, stages, and actuators is critical in aligning optics that require these levels of precision. The most difficult task is to select the best possible prealignment method and scan algorithm for the application being considered. Once these are selected, the integration of the proper

tools into the process can begin. Examples were cited in this discussion to some different tools. . . . that can be used as a starting point, but each application is different and may require new methods and tools that were not previously considered for fiber optic alignment applications."

Table 18. Listing of alignment stage manufacturers and representative products.

<p><b>Adept Technology Inc.</b> NanoStage L1P2 is a three-axis (XYZ) auto-alignment system with integrated closed-loop piezo (X-Y axes) and precision motor stage (Z-axis) actuators that provide precise alignment of fiber optic components.</p> <p><a href="http://www.adept.com/main/index.html">http://www.adept.com/main/index.html</a></p>	
<p><b>Bayside Motion Group.</b> Precision linear and rotary stages combine crossed roller bearings in a small stage cross section with a high resolution linear encoder and a piezo motor or brushless DC linear servo motors. The piezo motor combines the ability to achieve resolutions below 50nm, with absolute position stability.</p> <p><a href="http://www.baysidemotion.com/">http://www.baysidemotion.com/</a></p>	
<p><b>Edmund Industrial Optics.</b> Very common stage but does not have the require precision. Actuator is a micrometer with 0.01mm graduations (0.5mm per rotation). Two bracket options are available for x-y-z configurations.</p> <p><a href="http://www.edmundoptics.com/">http://www.edmundoptics.com/</a></p>	
<p><b>Melles Griot NanoMax™</b> 3-axis stage with parallel flexure design virtually eliminates friction, stiction, and backlash. Modular drives can be interchanged or replaced without removing the stage or disturbing the system alignment.</p> <p><a href="http://www.mellesgriot.com/">http://www.mellesgriot.com/</a></p>	
<p><b>EXFO</b> The TSE-820 Positioning System combines Burleigh's patented Inchworm® motor, a precision translation stage and an integral 20 nm linear encoder.</p> <p><a href="http://www.exfo.com">http://www.exfo.com</a></p>	
<p><b>Thorlabs Inc.</b> The MDT-Series Flexure Stages are designed to provide 2mm of travel and accept motorized drives, piezo stacks and micrometer heads.</p> <p><a href="http://www.thorlabs.com">http://www.thorlabs.com</a></p>	

### 13.3. Polishing Technique

The dual layer-CPC® buffer coating on the SMF-28 fiber provides a unique polishing situation on the end-face of the coupon/fiber. Softer materials (CPC® coating) grind/polish faster than harder ones (glass), this creates a recess between the glass core/cladding and the epoxy coupon. The recess leaves the edges of the core/cladding more prone to chipping during the polishing process, which results in light dispersion at the end of the fiber. The DSS fiber has the same core/cladding diameters as the SMF-28 fiber. DSS fiber also has a polyimide buffer coating instead of the dual layer-CPC® and may polish differently. This effect will be examined in future testing.

Polishing and aligning the fiber end-faces perpendicular to the fiber axis is also a challenge. The coupons mounted on the microscope translation stages can only move in the X, Y and Z directions. At this time, LUNA does not have stages that adjust pitch and/or yaw. It is possible the end-face of the fibers may not be exactly parallel to each other, resulting in a power loss. In addition, the smallest division on the micrometer-driven stages is 10  $\mu\text{m}$ ; it is difficult to optimize the alignment when the core is only 9  $\mu\text{m}$  in diameter.

### 13.4. Fiber-Fiber Alignment Experiments

The next step in the process was to determine the requirements and feasibility of a CAP connector system. Experiments were conducted to measure losses between optical fibers in space and between optical fibers embedded in epoxy blocks.

The test setup is shown in Figure 132. A light source, 1550 nm for the single mode fiber and 820 nm for multimode, was introduced into the fiber through an FC connector and allowed to pass across a gap filled with air or index matching gel. The 1550 nm source was built in-house with a laser diode. The 820 source was from a LUNA Fiber Pro system. The power meter was a Noyes mode OPM 4. The alignment stage consists of a single actuators fixed to move in the Z-direction and a group of three actuators arranged to move in the X, Y and Z directions. The alignment stages are manufactured by Parker automation (Model 4002M). The smallest measuring division on the manual drive is 10 micron.

Power loss between the two fibers was measured with the optical power meter and the reference power was measured with a patch cord connecting the source and meter directly. The fiber ends were prepared by either cleaving the end or by casting the fiber in a  $\frac{1}{4}$ " by  $\frac{1}{2}$ " by 1  $\frac{1}{2}$ " epoxy block (Buehler Epoxicure® Resin and Hardener). One end of the block containing the optical fiber was polished on a standard disk polisher to a 1-micron grit aluminum oxide finish. The cleaved ends of the fiber were taped to the alignment stage while the fibers cast in epoxy were secured on the alignment stage using set screws. Once the fibers were secured, the light source and power meter were turned on. While monitoring the power meter the stage was adjusted until the fibers were aligned visually. In the case of both bare fiber and fiber cast in epoxy, the fibers were visible and, therefore, could be aligned visually. The stage was adjusted manually until first light was detected. Then the stage was systematically adjusted until the power loss was minimized. The minimum power loss was recorded. Then the stage was moved in incremental steps to produce a lateral misalignment and the loss was recorded at each step for both single mode and multimode fibers.

Losses were similarly measured while separating the fiber in the axial direction. The experiment was repeated with index matching fluid between the two fibers.

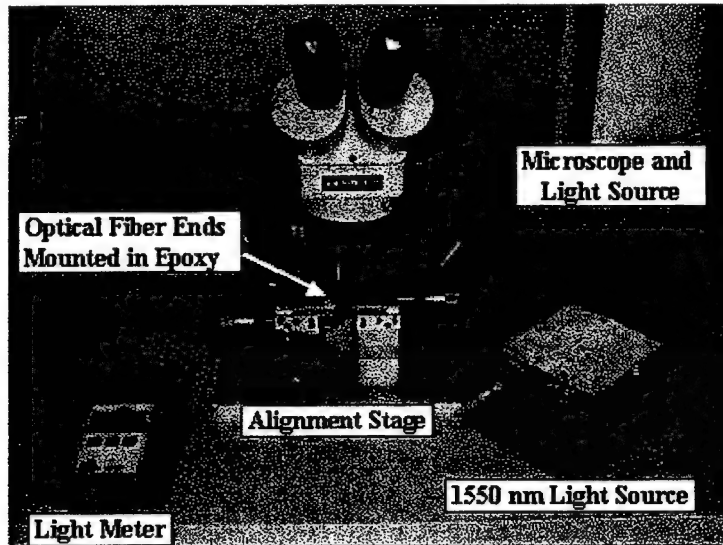


Figure 132. A 1550 nm light source shines light through a single mode fiber across a gap to a second single mode fiber attached to a power meter. The power loss is referenced against a patch cord connected directly from the source to the meter. The loss is minimized by adjusting the alignment stage in the X, Y and Z directions.

Matching gel was used to couple the end of a bare fiber to another fiber imbedded in epoxy. The same misalignment experiment was not performed because the gel would move the end of the free fiber. The fibers were first aligned without the gel. Then they were axially separated and a small amount of index matching gel was applied to the end of the free fiber. Then the two fiber ends were brought back together.

During the alignment loss experiments both fiber ends were visible making the initial or "first light" capture very easy compared to the case of a fiber imbedded in a composite where only the fiber face is visible. Once the first light is captured, minimizing the power loss with fine adjustment is a matter of minimizing the loss by moving the stage in one direction until a minimum is reached then moving the stage in a second orthogonal direction until a minimum is reached again. The process could then be repeated if the alignment stage had enough resolution. In practice an X-ray of a marked fiber embedded in a composite would locate the fiber in-plane leaving the depth of the fiber known to a lesser degree depending on which ply the fiber was located. These experiments address losses associated with lateral misalignment and longitudinal separation. Angular misalignment was not addressed but was a factor since the fibers embedded in the epoxy were not absolutely perpendicular to the edge of epoxy.

Lateral offset was the largest source of power loss in these experiments, which is expected based on the literature information [23]. The smallest increment of measure on the alignment stage was 10 microns. For the multimode fiber, with a core diameter of 50 microns, the stage could move the fiber over a considerable distance and generate an offset and subsequent loss. The single mode fiber has a 6-micron core diameter and the smallest movement of the stage caused a loss of nearly

10 dB that would make strain measurements with the DSS nearly impossible. Finer adjustment and angular adjustment on the stage may improve the ability to align the fibers to minimize the original loss. The literature review points to several existing methods for aligning fibers on a micron and sub-micron level.

The experiment compared bare fiber to bare fiber losses, embedded fiber to bare fiber losses, and embedded fiber to embedded fiber losses. Higher losses (33.05 dB) occurred when both fibers are embedded in epoxy compared to 6.6 dB, when one fiber is embedded in epoxy and versus 2.5dB, when two bare fibers are aligned. The two bare fibers do not have an appreciable amount of angular misalignment and their cleaved ends may provide a better end face in which to couple light. The embedded fibers are not perfectly aligned in the cast epoxy, resulting in an angular misalignment when the cured billet is mounted in the alignment stand. In a composite part, angular misalignment will be an issue when the fiber is not perpendicular to the part edge.

Index gel reduces the losses between two fibers when they are close together. Theoretically, if an optical adhesive with an index of refraction of 1.56 were used with a fiber that has a core index of refraction of 1.6, the losses due to Fresnel reflections from perpendicular end faces would be reduced from 0.2 dB in air to 0.0007 dB with index matching between the two fibers. The experimental results above gave only one order of magnitude loss reduction between the two fibers, which means more than Fresnel reflection losses were involved. Other sources of optical power loss would include lens effects from polishing, angled end faces, angled fibers or inadequate polishing.

Following the initial round of alignment testing, LUNA determined that additional fixtures needed to be designed and fabricated. A new mold fixture was fabricated to ensure the proper alignment of the fibers. In addition, a custom polishing puck was fabricated to assist in polishing the end-face of the coupons perpendicular to the body of the coupon. This next set of tests evaluated the repeatability of aligning two embedded fiber coupons and the performance of UV-cure optical epoxy in fixing the coupons together.

Single mode fiber (SMF-28) was embedded in epoxy coupons using a custom-made mold fixture. The epoxy coupons were then mounted in a polishing puck and the end-face was ground with 600-grit paper. It was then polished successively with 1 micron, 0.3 micron, and 0.05 micron slurry on metallographic polishing machines. The end result is shown in Figure 133. The fiber lead of each coupon was terminated with a standard FC-style connector.

The 1550 nm source was initially referenced on a NOYES optical power meter using a SMF-28 patch cord. The power meter was configured to measure the optical power loss due to misalignment of the coupon samples. Next, two embedded fiber coupons were placed on a stereo microscope stage and configured as shown previously. The two coupons were aligned visually at first, and then adjusted using the micrometer-driven X, Y, Z translation stages. Adjustments were made until power loss was minimized.

Optically clear UV-cure epoxy was used to bridge the air-gap, fastening the coupons together as shown in Figure 134. Optical loss measurements (dB) were taken prior to and after the epoxy application and cure. To check the repeatability of the power loss measurements, the epoxy

coupons were broken apart and the surface was prepared again. The coupons were run through the abovementioned polishing process, to ensure they had completely new end-faces.

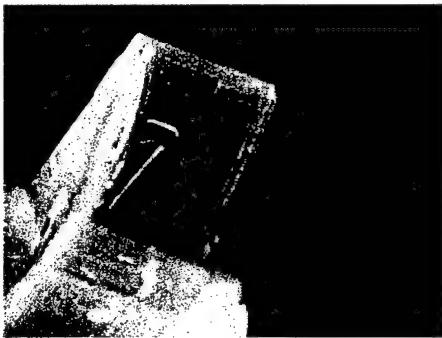


Figure 133. Polished end-face of epoxy coupon with embedded fiber (SMF-28).

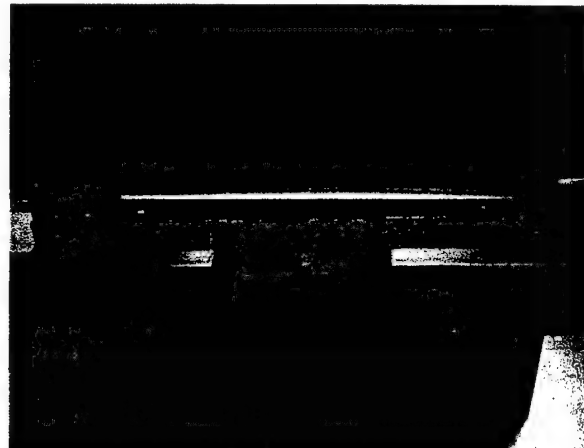


Figure 134. UV-cure epoxy was used to bridge the air-gap and fasten the coupons together.

A summary of the results from the loss readings is shown below in Table 19. Trial 1 readings were taken with coupons embedded with Lucent 1550 nm fiber, but were initially referenced in the same manner as mentioned in the experimentation setup section. Trial 1 is not necessarily representative of the performance of SMF-28 fiber, but was tested due to the availability of the samples at the time. Trial 2 used SMF-28 embedded fibers and resulted in a very low power loss. After Trial 2, one of the coupons was damaged and an additional coupon was fabricated in the same way. Trials 3 and 4 had losses far greater than those obtained in Trials 1 and 2. There is a large variation in the readings recorded. The values shown in Table 19 represent the lowest loss achieved in each case. Possible sources of variation are described in the discussion section.

Table 19. The optical loss readings recorded during the UV-cure performance testing.

	Trial 1*	Trial 2 (SMF-28)	Trial 3 (SMF-28)	Trial 4 (SMF-28)
Before epoxy	3.67 (dB)	3.56	20.24	19.44
After UV-cure	4.20	1.99	20.80	19.19

\*Lucent 1550 nm fiber

The results show a large discrepancy in the power loss readings obtained during the testing. Trials 3 and 4 had losses too large for any potential distributed-strain-sensing (DSS) fiber to be interrogated, since the maximum allowable loss for the DSS system is approximately 9dB. There are likely physical phenomena occurring during the curing and/or polishing processes that are contributing to the large variability.

### 13.5. Fiber-Composite Alignment Experiments

The next step was to prepare the sample of SMF-28 fiber embedded in a carbon fiber composite piece for alignment testing as described previously. LUNA was not able to visually align the

optical fiber embedded in carbon fiber composite. Therefore, this was a much more time-intensive process as the stages are swept through a grid-like pattern to locate the fiber with an optical power measurement. Additional fixtures were also fabricated to aid in the preparation of the composite piece as shown in Figure 135.

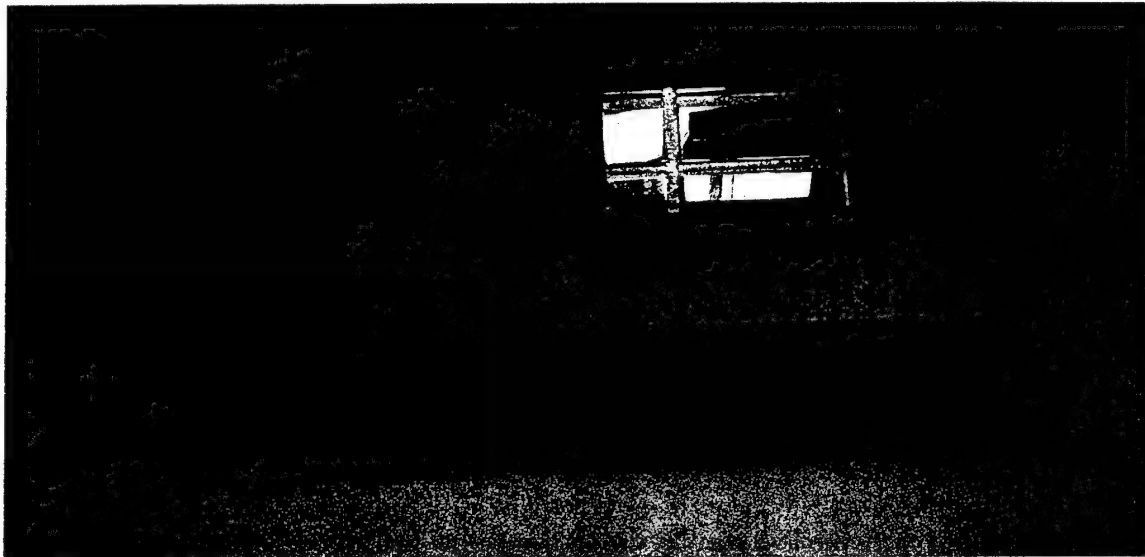


Figure 135. Composite polishing fixture.

To identify the location of the embedded optical fiber in reflection, an epoxy coupon with an embedded fiber was connected to the optical setup shown in Figure 136 to monitor reflected power. The epoxy coupon was then placed in a positioner, approximately aligned to the composite coupon. The setup is shown in Figure 137. The embedded fiber was then identified by sweeping the epoxy coupon through a grid-like pattern and monitoring the changes in reflected power. When the composite and epoxy embedded optical fibers are aligned, reflected power will decrease due to the increase in coupled or transmitted power.

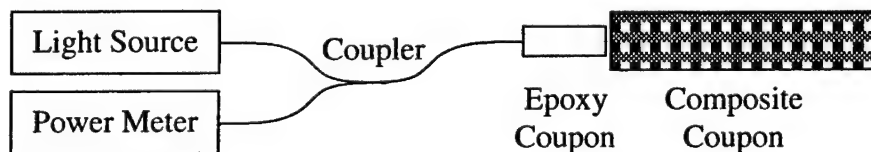


Figure 136. Optical test setup.

The next step was to investigate the ability to align the composite and epoxy coupons given one known end protruding from the composite coupon.

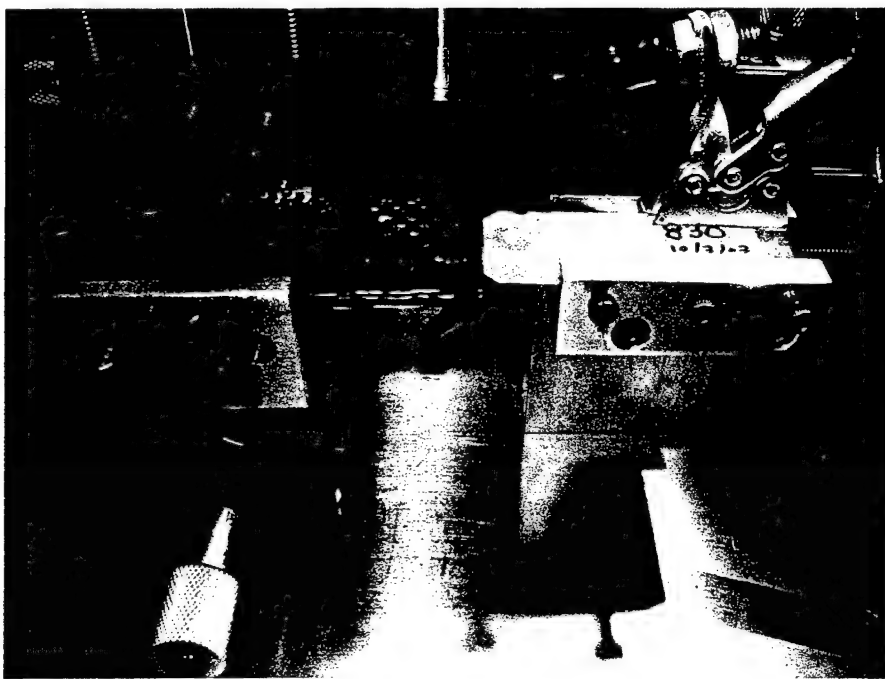


Figure 137. Alignment setup.

A LED light source was connected to the epoxy coupon fiber exiting composite coupon and a power meter was attached to the composite coupon. To align the coupons, it was necessary to obtain one fixed axis in the Z-Y sweep scan. A small red laser was used to sight the fiber in the composite coupon. With the red laser illuminating the polished fiber end in the composite coupon, it was now possible to position the Y-axis of the composite fiber adjacent to the source fiber in the epoxy coupon using the staged microscope. With the alignment of the two fibers in the Y-axis fixed visually, the X-axis could then be manipulated to obtain an approximately 25 micron gap between the two coupons using LUNA's Fiber Pro optical measurement system. With the Y- and the X-axis in approximately correct position, the Z-axis was swept while monitoring the power meter to look for some positive activity. The stage was moved up and down with fine movements until a small positive recording noticed on the power meter. Once transmission was established, the Z and Y stages were moved in very small increments to obtain a peak power reading. Optical coupling gel was then applied to minimize loss. Typical power measurements were 6.397  $\mu\text{W}$  given an input power of 12.45  $\mu\text{W}$ , equating to a loss of 2.89 dB.

### 13.6. Fiber-Composite Embedded EFPI Alignment Experiments

The focus of this effort was to align an optical fiber to a cut and polished composite coupon with embedded EFPI sensors. A diamond saw was used to cut the composite coupon at as near a right angle as possible. The cut surface was then polished using various grit wet-paper's with the final polish using 0.3 micron slurry. A figure of the polishing setup is shown in Figure 138.

The initial diamond saw cut was taken two inches from the terminator end. After polishing, the embedded fibers were clearly visible due to the protective Teflon sleeve. Initial attempts were made to couple the sectioned coupon to the epoxy pucks (used in the previous trials with the  $\frac{1}{4}$ "

thick composite coupon). Because of the extra coupon depth, it proved impossible to make a good alignment with the epoxy puck. Several attempts were made to optimize the alignment, re-polishing the epoxy puck to get closer angular alignment, etc. Because of the difficulty of successfully aligning the embedded fiber with the epoxy puck, it was decided to try directly coupling an individual optical fiber to the coupon.

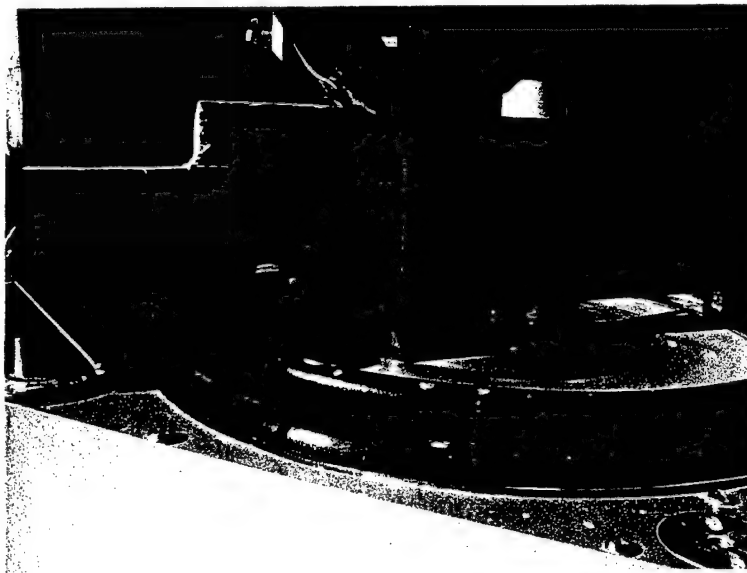


Figure 138. Final polish of composite coupon with 0.3 micron polishing slurry.

A cleaved single mode 830nm fiber was used to detect the embedded EFPI sensor. Although it is possible to get good depth perspective using the stereo microscope, it was extremely difficult to couple the two fibers in a way that gave optical continuity between the embedded sensor and the optical fiber, see Figure 139 below.

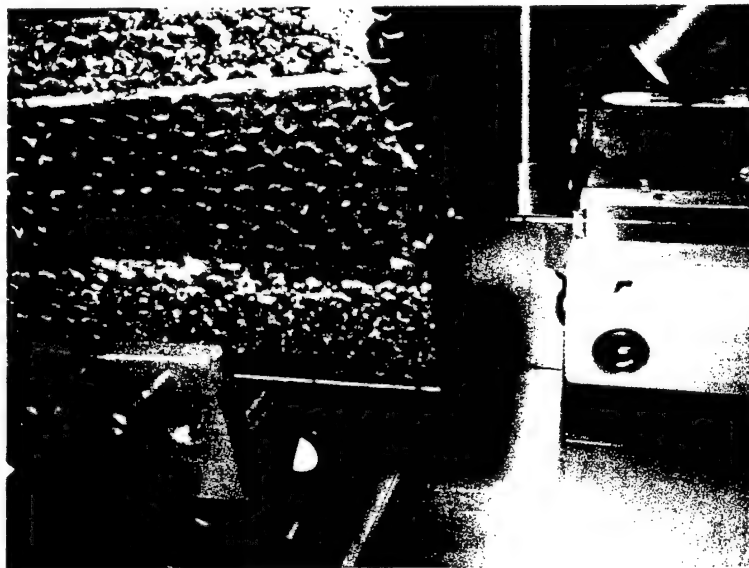


Figure 139. Cleaved fiber being aligned with the embedded sensor.

A connector was installed on the free end of the fiber, so that the LUNA Fiber Pro could be used to detect the embedded EFPI sensor as shown in Figure 140. After many attempts, the two fibers lined up and the EFPI fringe pattern from the embedded sensor was visible on the system, as shown in Figure 141.

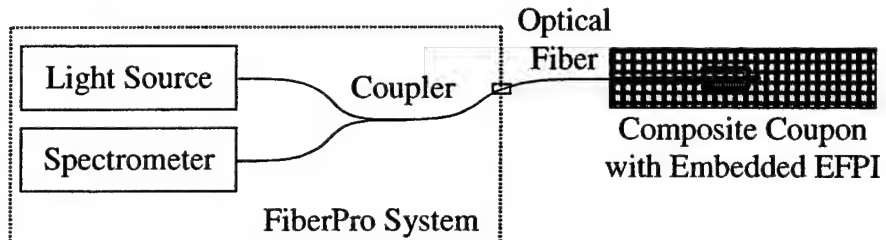


Figure 140. Fiber Pro testing setup.

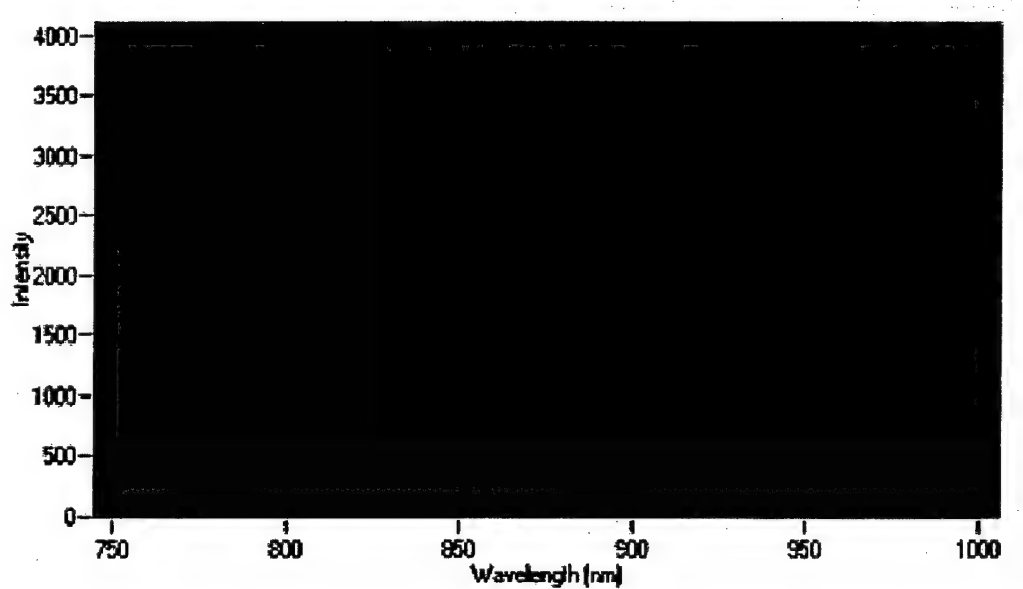


Figure 141. Fiber Pro display with EFPI embedded fiber aligned.

After the EFPI was detected, the stage holding the composite coupon was moved very slightly to try to maximize sensor response. The stage proved to be incredibly sensitive to any stress imposed on it. After several attempts to get a maximum peak, the two fibers were joined with the UV adhesive. The joint was allowed to cure for one hour under UV light.

Inspection of the joint using the Fiber Pro revealed that the joint was extremely sensitive to any movement induced on the exiting fiber. Just touching the exiting fiber caused the amplitude of the signal to vary significantly.

The next step was attempting to align the optical fiber to an embedded sensor without the Teflon sleeve. A second diamond saw section was made, this time 4 inches from the terminator end. The fibers that were presented after this section had no Teflon sleeve around the fiber. The intent was to evaluate if not having the Teflon sleeve made it significantly more difficult to align. Finding the fibers proved to be quite a straightforward task.

The composite coupon was clamped between the two moving stages of the stereo microscope, and then the cross section of the coupon was visually scanned across the middle area. Once the position of the three fibers had been located using the stereo microscope, small tape markers were applied directly to the composite polished end, helping to assist in future identification of the fibers.

LUNA continued to attempt connecting to these embedded sensors. Repeated attempts were made and although visually the embedded fiber and the cleaved fiber appeared under the microscope to have coupled perfectly, it was not possible to successfully couple to the EFPI sensor.

Next, LUNA evaluated direct alignment between an input/output optical fiber connected to a Fiber Pro optical support system and a second optical containing an EFPI sensor. Multiple scenarios have been investigated, as shown in Figure 142.

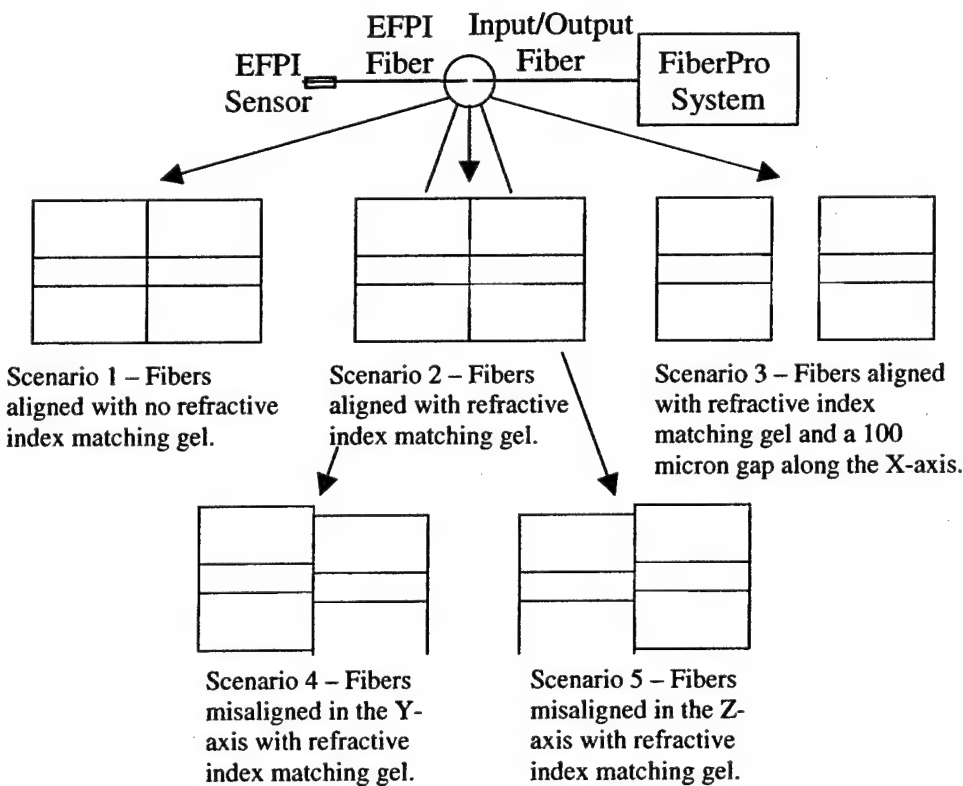


Figure 142. Alignment scenarios for coupling light in/out of a fiber containing an EFPI sensor. A Fiber Pro system was used to monitor the coupled response of the EFPI sensor.

In Scenario 1, the input/output fiber and EFPI fiber were each mounted to independent multiple-axis positioners and aligned under a microscope. The resulting spectrum is shown in Figure 143. The spectrum is a composite of two interferometric signals – one is the spectrum associated with the EFPI sensor and the second signal is due to a very small gap between the input/output and EFPI fibers. This gap is on the order of microns and highly unstable – leading to dramatic fluctuations in the shape and strength of the signal. While this small gap can be “filtered” out with signal processing, it consumes a significant amount of optical power, resulting in a “weaker” measured EFPI spectrum.

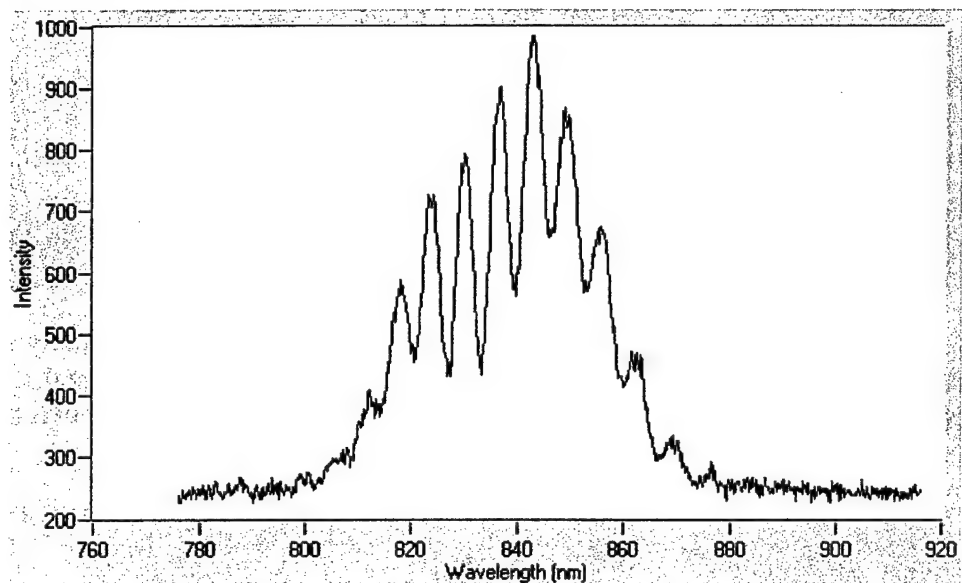


Figure 143. Scenario 1 – The EFPI optical fiber and input/output fiber are optimally aligned with no refractive index (RI) matching gel. The resulting spectrum is a composite of the actual EFPI signal and a second gap created between the two fibers on the order of microns.

Refractive-index (RI) matching gel was used in Scenario 2 to eliminate the effect of this second signal. The coupled spectrum, as shown in Figure 144, directly matches the expected/actual spectrum of the EFPI sensor.

The next scenario (Scenario 3) involved moving the input/output fiber away from the EFPI fiber and monitoring the change in coupled spectrum. The coupled spectrum at a gap of 100 microns is shown in Figure 145. As expected, the coupled spectrum gets “weaker” as the input/output fiber is moved away from the EFPI fiber. “Weaker” is defined by a decrease in the overall power level and fringe depth of the spectrum. However, a “weaker” spectrum alone does not result in greater measurement noise due to the interferometric nature of the sensors.

Scenarios 4 and 5 focused on slight misalignments of the input/output and EFPI fibers along the Y and Z axes. The resulting spectrums are shown in Figure 146 and Figure 147. The misalignments were very slight, within a few microns, and well below the precision of the multiple-axis positioners. Any adjustment beyond a few microns resulted in no coupled EFPI response. A similar response was seen when this experiment was attempted with a gap between the input/output and EFPI fibers. Again the fibers were extremely sensitive to misalignment.

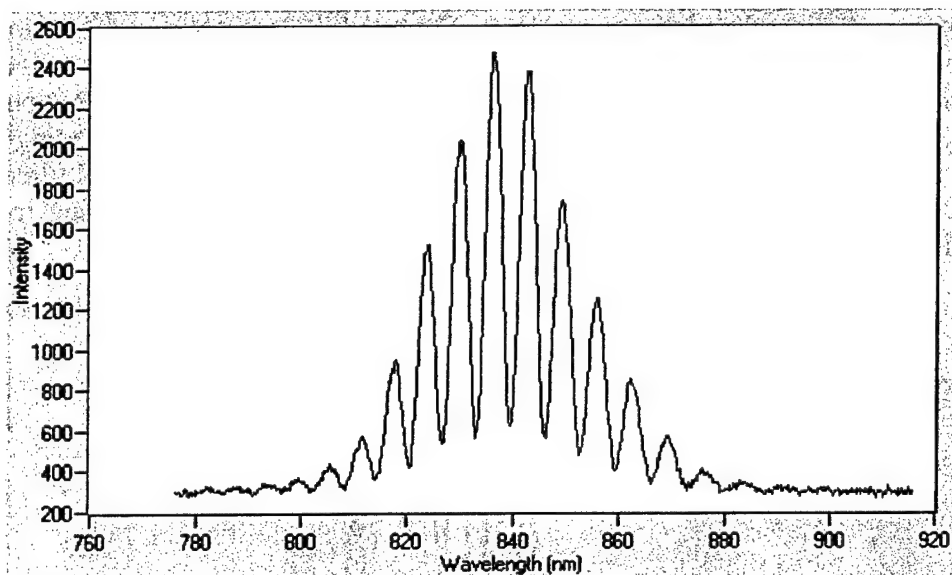


Figure 144. Scenario 2 – The EFPI optical fiber and input/output fiber are optimally aligned with RI matching gel. The resulting spectrum is the spectrum of the actual EFPI signal. The second signal, as seen in Scenario 1 due to the sub-micron gap created between the two fibers, is eliminated with the addition of RI matching gel.

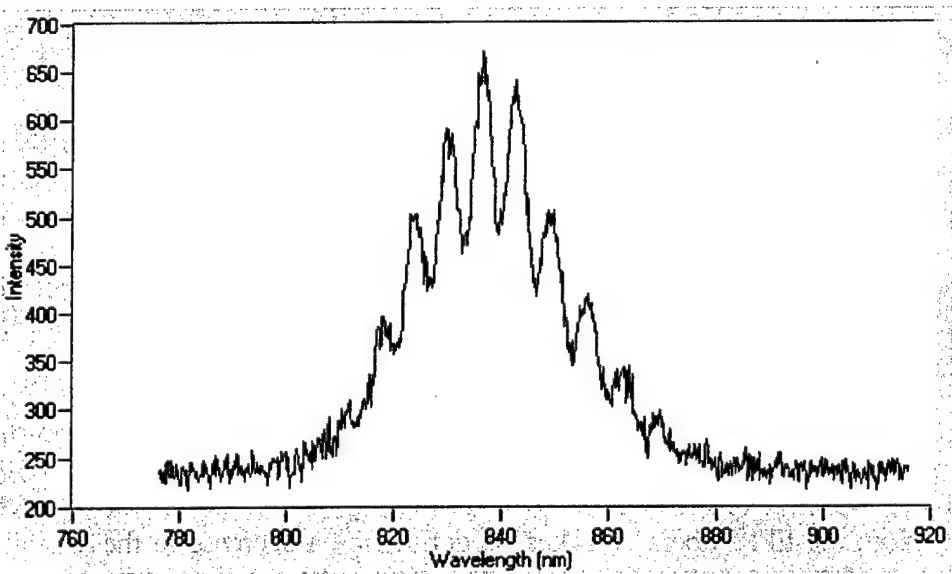


Figure 145. Scenario 3 – The EFPI optical fiber and input/output fiber are aligned with a 100 micron gap along the X-axis between the two fibers. RI matching gel filled the 100 micron gap. The resulting spectrum is a “weaker” version of the actual EFPI spectrum. However, due to the interferometric nature of the signal processing, a “weaker” spectrum does not correlate to greater noise in the measured signal.

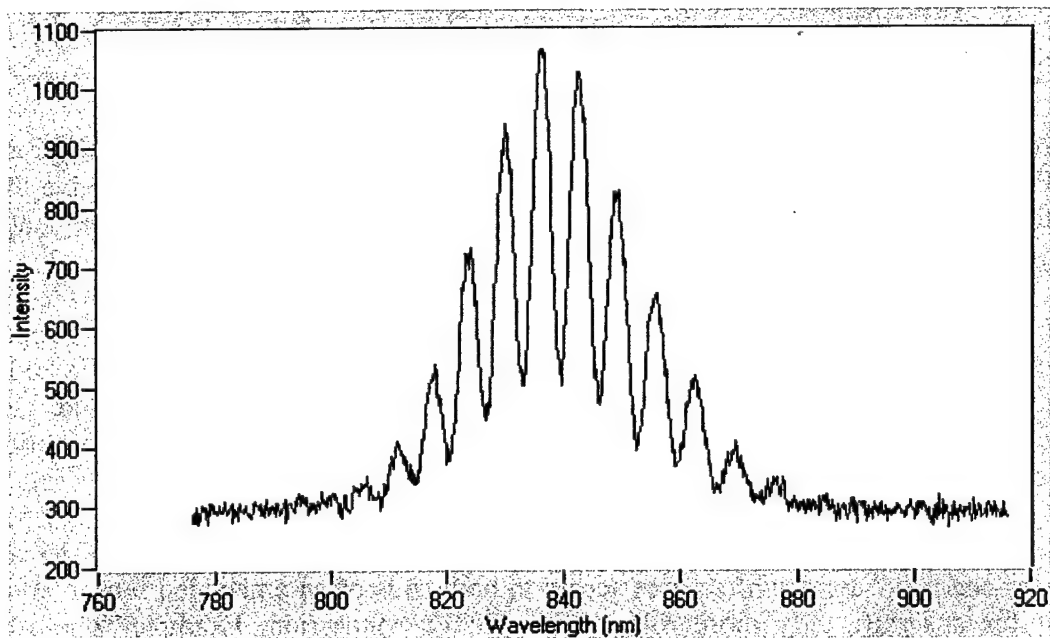


Figure 146. Scenario 4 – The EFPI optical fiber and input/output fiber are misaligned along the Y-axis with RI matching gel. The resulting spectrum is a “weaker” version of the actual EFPI spectrum. The misalignment was on the order of a couple micron offset.

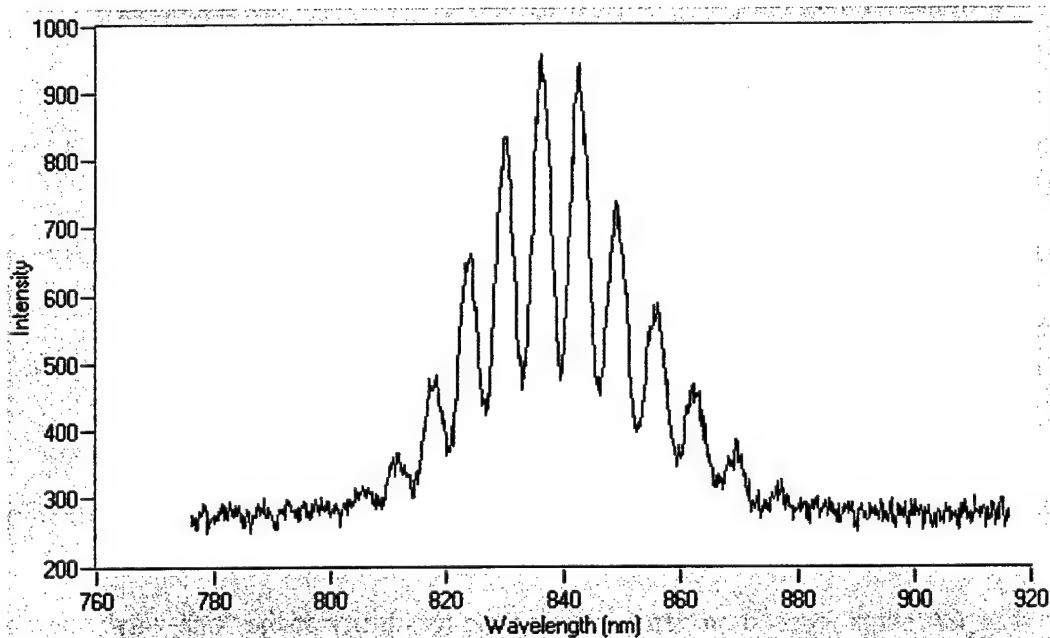


Figure 147. Scenario 5 – The EFPI optical fiber and input/output fiber are misaligned along the Z-axis with RI matching gel. The resulting spectrum is a “weaker” version of the actual EFPI spectrum. The misalignment was on the order of a couple micron offset.

### 13.7. Cut and Polish Approach

There are two different CAP approaches, “one-way” and “two-way”. In the “one-way” approach, the CAP connection serves to either deliver light into the embedded fiber or receive the sensor modulated light from the embedded fiber. In the “two-way” CAP approach, single CAP connection provides both input and output to the embedded optical fiber.

Initially, LUNA focused on the “two-way” CAP approach, however this approach is exponentially more sensitive to alignment than the “one-way” technique. To reduce this alignment sensitivity, different lensing/collimator prototypes were fabricated. However, preliminary testing showed no improvement in alignment sensitivity with the use of the lensing/collimator prototypes.

From discussions with 3TEX, it was determined to shift focus to the “one-way” CAP approach. While the “one-way” approach requires access to both ends of an embedded sensor, it offers the potential for a significantly more robust and reliable connection. Example “one-way” CAP approaches are shown in Figure 148.

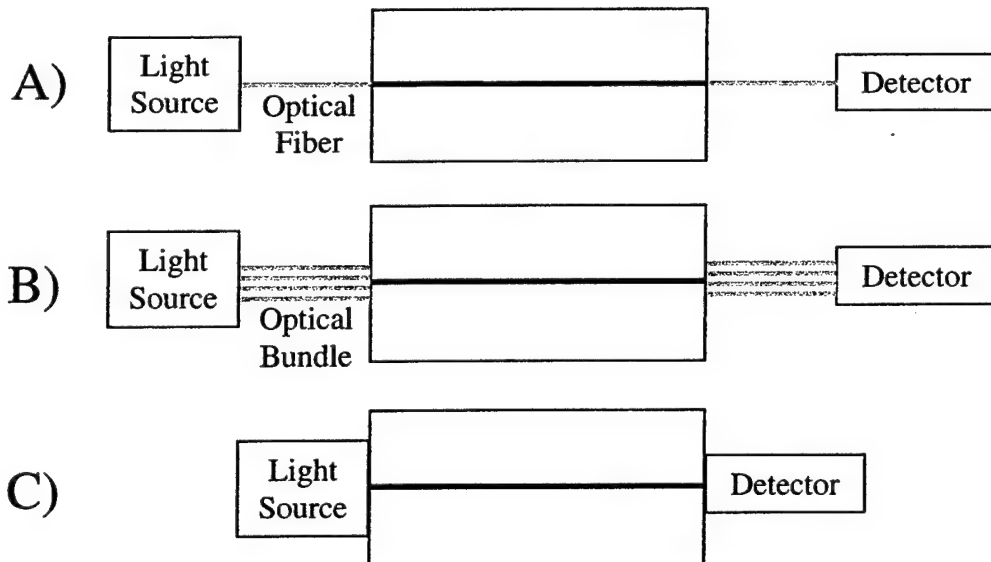


Figure 148. “One-way” CAP approaches using A) single optical fiber, B) a bundle of optical fibers, and C) direct connection.

The initial experiments focused on demonstrating the feasibility of the “one-way” approach using both individual optical fibers and an embedded optical fiber. A laser system producing 1300 nm wavelength light with a measured power of 2865  $\mu$ W was used as a light source. The power of the coupled light source was measured using an optical power meter (Noyes model OPM 4). A stereomicroscope was used to carefully mate the cleaved ends of each fiber type with the fiber end of the light source using a micrometer stage with controlled X, Y and Z positions. The optical power was recorded once it had reached a stable value on the meter.

Small sections of both single-mode and multi-mode fiber, approximately four inches in length, were cleaved at both ends with a Sumitomo fiber cleaver model FCP-22L. In proof of concept experiments, each of these fibers was mated on one end with the laser fiber and mated on the opposite end with the optical power meter. Both the fiber and fiber end of the light source were taped to the micrometer stage to prevent movement during the experiment. Initially, a connectorized multi-mode fiber was used because it has a larger diameter core compared to a single-mode fiber. Alignment of the multi-mode fiber and the light source was easily achieved, and the measured power of the 1300 nm light through the fiber was 2600  $\mu$ W. Alignment was eventually achieved with a connectorized single-mode fiber as well, which produced light output at approximately 2000  $\mu$ W.

With the aid of the stereomicroscope, the fiber was aligned with the laser fiber. Once the two fibers were touching, the single-mode or multi-mode fiber was carefully moved in the Y and Z-directions until the optical power meter showed a significant increase in power output from the opposite end of the fiber. The optical power was recorded when the fibers were mated with and without the laser source turned on. The connection between the cleaved fiber end and the optical power meter was open to stray light during the experiment. Power readings were recorded at certain intervals of time to determine the reproducibility of measurement.

For example, two separate tests were conducted on the 4-inch long section of single-mode fiber to determine the reproducibility of the power reading using the current setup. The power output was maximized upon fiber alignment, and power values were recorded at different time intervals over 20 minutes. Because the connection between the fiber end and the power meter was open to stray light, an original baseline reading was recorded and subtracted from all measured readings. Two trials were run on separate days, and the corrected power readings are shown in Table 20.

Table 20. The power readings obtained on two trials ran on separate days.

Time	Reading 1 ( $\mu$ W)	Reading 2 ( $\mu$ W)
0 sec	0.4500	1.770
30 sec	0.4189	2.064
1 min	0.4298	2.049
1.5 min	0.4127	2.121
2 min	0.4031	2.266
5 min	0.3726	2.319
10 min	0.3973	2.579
20 min	0.4120	2.655
Baseline reading	0.15	0.23

A similar procedure was used to mate the embedded fiber in the composite coupon with both the laser fiber and the power meter. The approximate position of the embedded fiber was marked with tape that could easily be seen through the microscope. The connection between the opposite end of the coupon and the power meter was not open to stray light.

Successful alignment of the embedded fiber with both the laser fiber and the power meter produced drifting power values. A maximum 6-7  $\mu$ W was recorded at one point. Originally, a

stable reading was recorded at  $0.125 \mu\text{W}$ . However, after approximately ten minutes, this reading had drifted down to  $0.0129 \mu\text{W}$ .

Several observations have been made from this collection of experiments. The steps of the CAP technique are summarized in Table 21.

Table 21. Principal steps of Cut And Polish technique.

	Embed optical fiber sensors within composite sample.
	Cut and polish the composite sample perpendicular to the axis of the embedded optical fiber. Repeat procedure for the opposite end of the embedded optical fiber.
	Mount cut composite sample to a rigid, stable surface that is accessible by the 3-axis micrometer. Mount a cleaved optical fiber in the 3-axis micrometer.
	Align a white light source to one end of the embedded fiber to shine through the composite sample such that visible light is emitted from opposite end of the embedded fiber.
	Align a cleaved optical fiber with to the embedded optical fiber in the coupon using the emitted light as a target.
	Bond optical fiber in place.

Clearly, light can be coupled through the embedded fiber based on a sudden increased output of power associated with a certain position on the coupon. In addition, this was confirmed by shutting off the power source when the power had been maximized through the fiber. Without the

laser power, the power reduced to the baseline value of 0.0004  $\mu$ W. A large drift, both to increasing and decreasing values, was observed. Some of this drift can be attributed to vibrations from the equipment on the bench top. In addition, the laser light was taped to the stage, but it was not completely prevented from rolling slightly on the stage during measurement.

### 13.8. Fiber-Composite Embedded Optical Fiber Cut and Polish Demonstration

The first step of the CAP procedure is to cut the face of the composite/fiber with a diamond saw. Two sample images are shown in Figure 149 and Figure 150. Figure 149 shows the cut composite and embedded optical fiber surrounded by a Teflon tube. Figure 150 shows the cut composite and an embedded optical fiber. The face is then cleaned and polished as necessary. The next step is to repeat this procedure with the opposite face of the composite/fiber. White light is then shined through one end, and an optical fiber is aligned to the opposite end using a translation stage. The alignment of the fiber is optimized and bonded using a UV cure epoxy. This process is then repeated for the opposite side of the composite/fiber. Figure 151 shows the setup for aligning optical fibers to a composite-embedded fiber using the CAP approach.



Figure 149. Image of cut composite end and optical fiber in Teflon tube.

Once the fibers were successfully bonded to the coupon, as shown in Figure 152, the loss through the system was evaluated. Given a source power of around 1.2mW, the detected power through 2 CAP connections was about 22 $\mu$ W. In a second iteration of the CAP approach on the same coupon, the detected power was about 7 $\mu$ W.

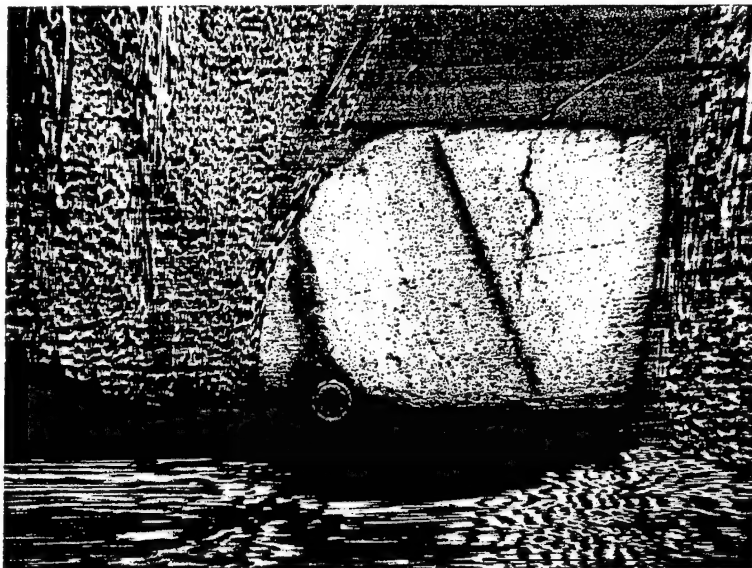


Figure 150. Image of cut composite end and optical fiber.

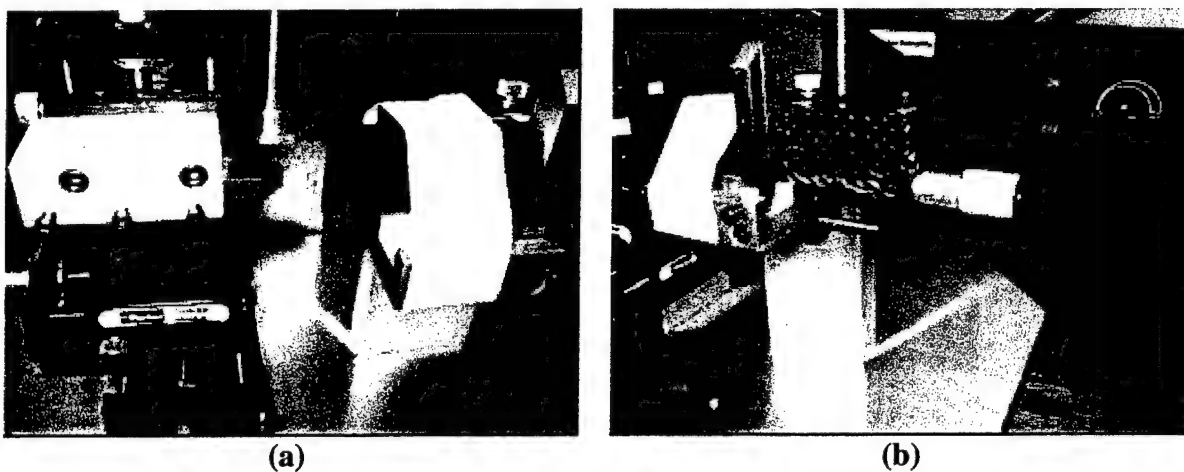


Figure 151. Cut and polish alignment setup. a) Detection fiber aligned and bonded to CAP end face of composite-embedded fiber. b) Source fiber aligned.

### 13.9. Fiber-Composite Integrated DSS Cut And Polish Demonstration

While the effort to optimized the “one-way” cut and polish (CAP) approach continued, it became possible to improve the amount of power transmitted through two ruggedized cut and polish connections with a composite-integrated DSS optical fiber from around  $5 \mu\text{W}$  to more than  $60 \mu\text{W}$ , given a source power of about  $1.4 \text{ mW}$ . While still a reasonably lossy connection, it is believed this connection should be efficient enough to interrogate the integrated DSS sensors.

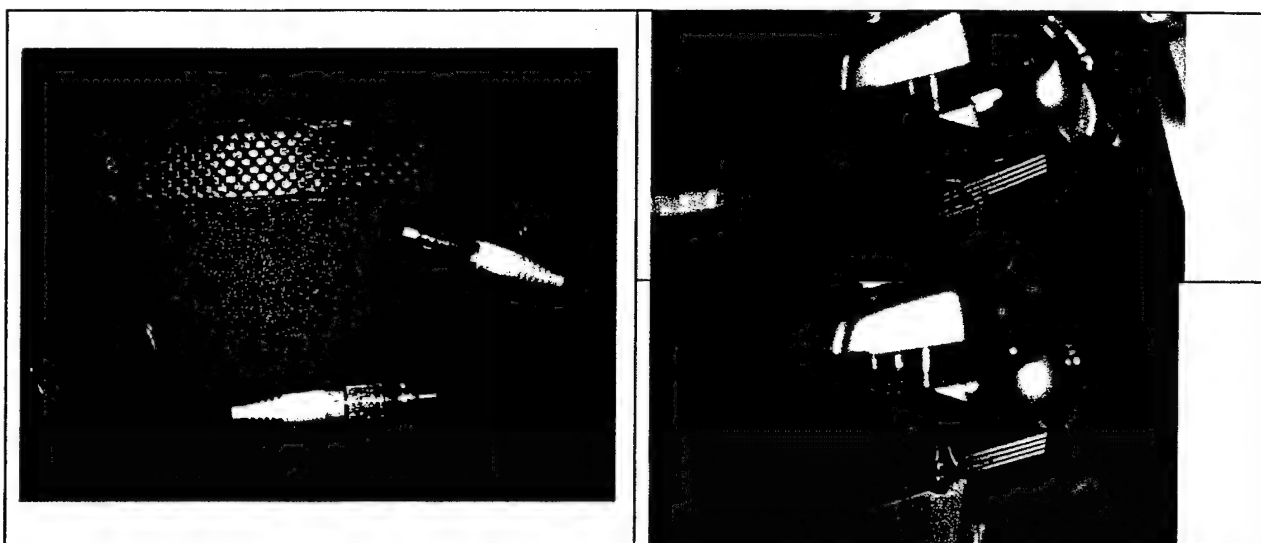


Figure 152. Optical fibers connected to a composite-integrated optical fiber through the CAP approach. Close-ups of a composite sample after being cut and polished and with an optical fiber aligned and bonded to one end.

While it has been believed that only a “one-way” CAP approach would provide sufficient signal, LUNA attempted to monitor the integrated sensors using the “two-way” approach. In the “two-way” approach, a single fiber is used to as the source and detector for the integrated sensors. A single fiber was used to connect one of the CAP connections to the DSS system. The DSS system, as shown in Figure 153, successfully interrogated each of the sensors integrated within the panel. The experiment was then repeated using the CAP connection on the opposite end of the coupon. These results are shown in Figure 154. As shown in these figures, while one CAP connection was stronger than the other, both connections were strong enough to interrogate the multiplexed sensors.



Figure 153. Screen capture from DSS system showing Bragg gratings integrated within 3-D woven composite sample connected via one of the CAP connections.

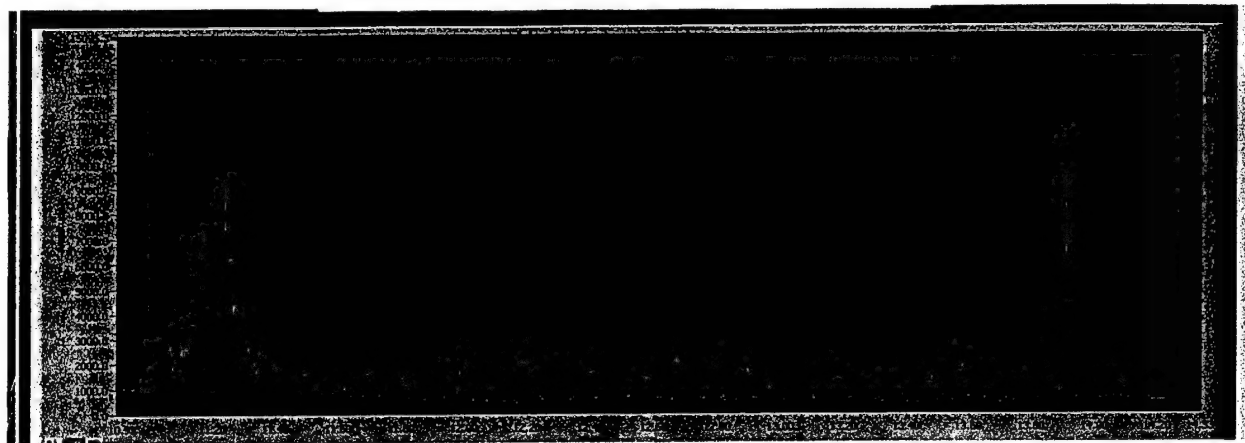


Figure 154. Screen capture from DSS system showing Bragg gratings integrated within 3-D woven composite sample connected via the opposite CAP connection.

### 13.10. Fiber-Composite Integrated DSS Panel Cut and Polish Attempt

The next step was to attempt a CAP connection to a DSS optical fiber embedded within a large composite panel. The integrated DSS sensors were multiplexed along a single optical fiber woven in a serpentine path within the panel. The fiber was woven such that the fiber would enter and exit the panel along the same side. A schematic of the panel is shown in Figure 155. The two optical fiber egress/ingress points are labeled as #1 and #2, respectively.

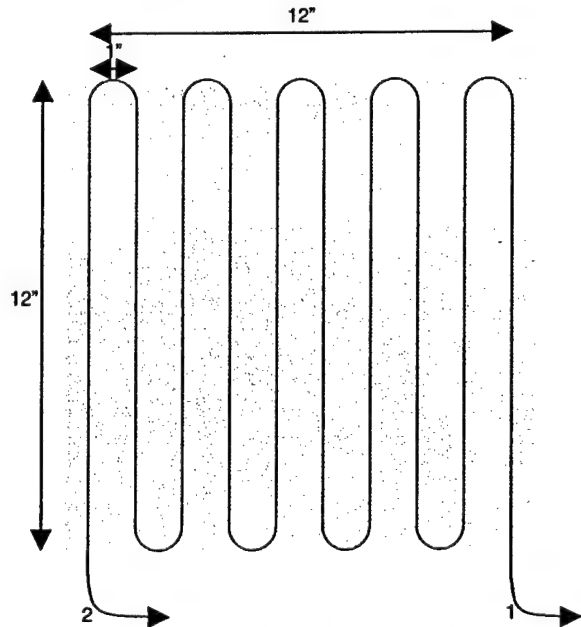


Figure 155. Schematic of composite panel as received.

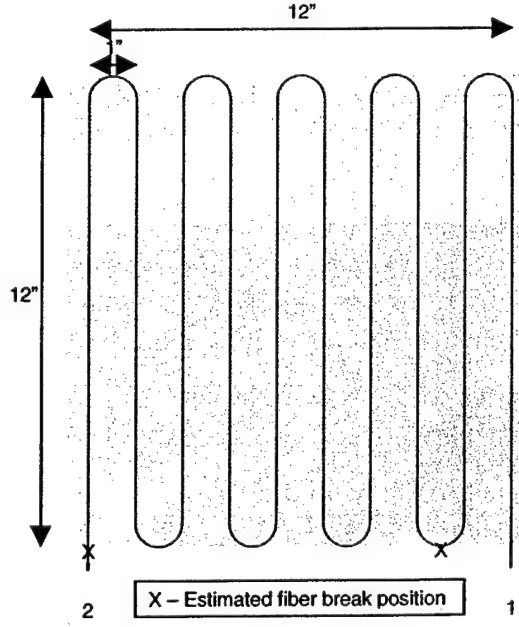


Figure 156. Schematic of the optical fiber breaks in the as received composite panel.

Each end of the optical fiber was connected to a DSS system to verify the functionality of the integrated optical sensors. First, connection to fiber #1 was made, and 126 sensors were found (Figure 157) between the connector and some point within the composite. Then, connection was made to fiber #2, and 67 sensors were found (Figure 158) between the connector and another point within the composite. These results revealed that the optical fiber was broken at least in two positions within the composite. Based on the sensor spacing and the length of the optical fiber leads, it was possible to determine the position of the break in the optical fibers, see Figure 156.

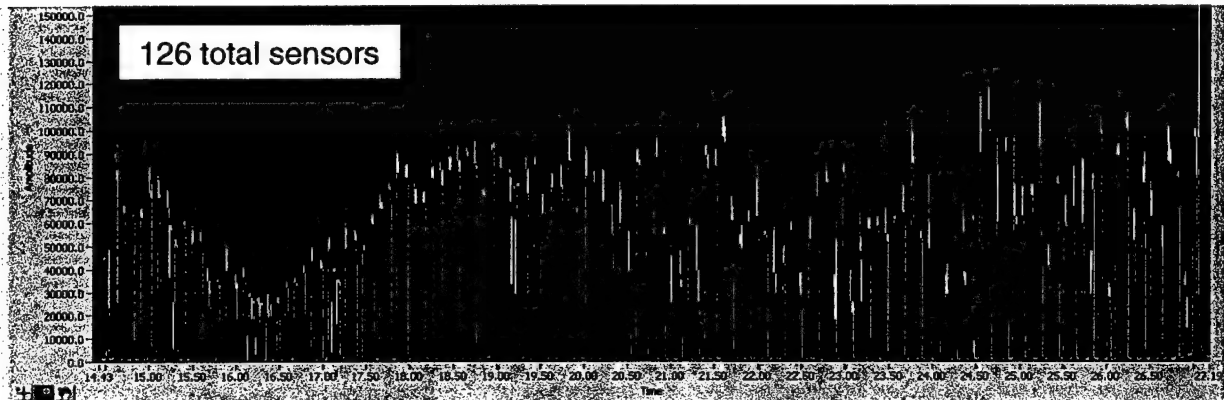


Figure 157. Response from DSS fiber at position #1.

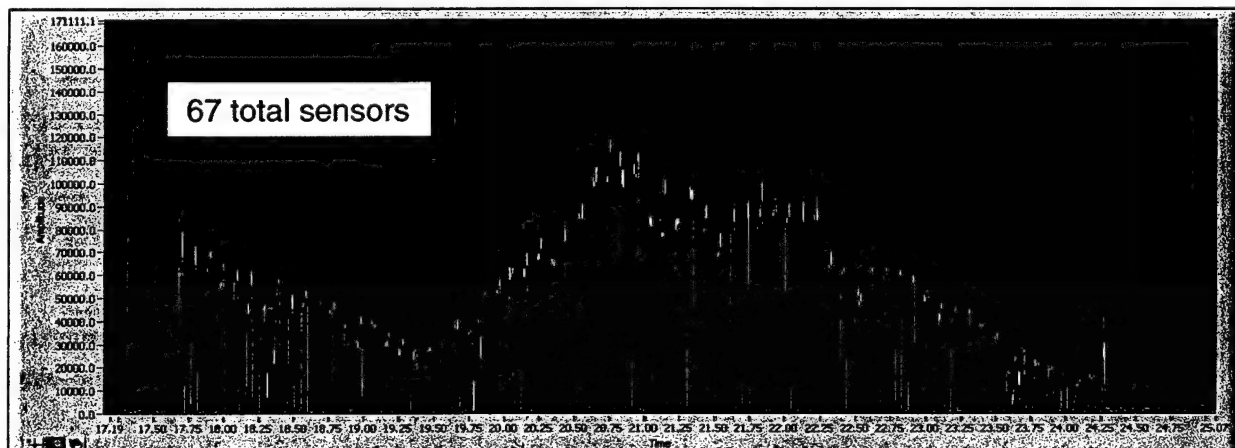


Figure 158. Response from DSS fiber at position #2.

Despite the broken optical fibers, an attempt was undertaken to make a CAP connection to the composite panel. The panel was cut and polished as shown in Figure 159. White light was shown into the side of the panel at the positions noted by the checked green boxes, but no light could be transmitted through the fiber, suggesting an additional break point. Then, the panel was cut and polished again, as shown in Figure 160. White light was successfully shown into each CAP end (noted by a green box) and observed out of the corresponding opposite end. It was then attempted to make a CAP connection to one of the CAP ends, but has yet been unsuccessful.

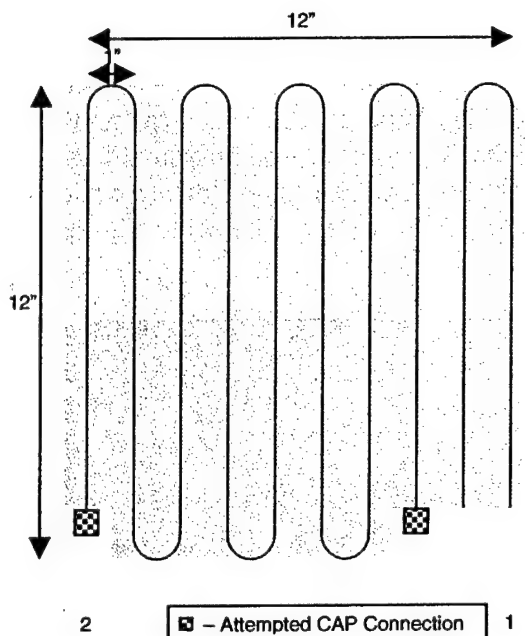


Figure 159. Schematic of first CAP connection attempt.

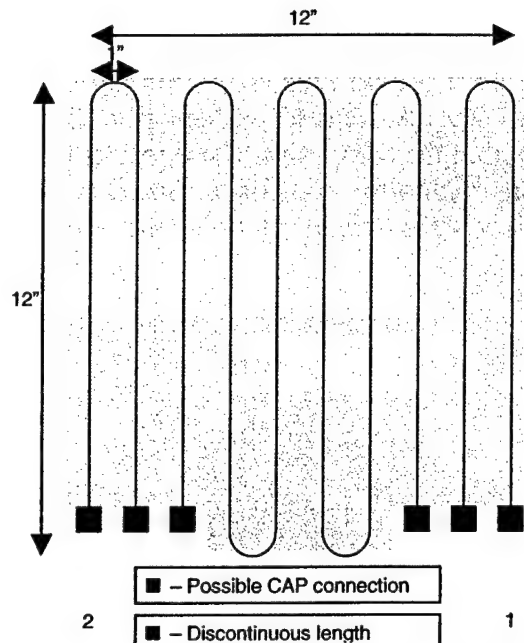


Figure 160. Schematic of second CAP connection attempt.

## 14. GENERAL CONCLUSIONS

Significant progress has been made toward scientific understanding, engineering means and practical experience of automated manufacture of a multi-functional material, where fiber optic sensors are integrated directly into yarns before 3-D weaving, then used as integral part of 3TEX 3-D weaving process, successfully pass through VARTM composite fabrication process and, as the final result, enable continuous in-situ strain monitoring within manufactured composite material or structural component. The principal highlights of the performed work follow:

- Automated integration of optical fibers into 3-D woven preforms during fabric formation was demonstrated with no damage to the fibers and with excellent transmission along the warp and weft weaving directions.
- Bragg grating fiber optic sensors were integrated into a single specimen with more than 400 gratings spread over the composite sample, which required only 16 connections. Used in conjunction with LUNA's Distributed Sensor System, these sensors demonstrated real-time measurement of strains during loading of the samples.
- Strain data from fiber optic sensors showed good agreement with foil strain gauge readings in 4-point bend tests and with Moiré interferometry data in bonded joint specimen tests. In each case, the fiber optic sensors could detect internal strain gradients not measurable by the other methods.
- Integrated fiber optic sensors detected changes in the linearity of the response of the material (in some cases at rather low load levels) in the regions of high strain gradients. This opens the possibility of an early, in-situ, damage detection and timely prevention in a composite structure.

- Test data from the fiber optic sensors has been shown to be repeatable.
- Initial effort has been made to directly compare internal strains recorded by integrated arrays of fiber optic sensors in 4-point bend specimen and surface strains recorded by foil gages to theoretical predictions obtained with 3TEX's in-house 3D MOSAIC predictive analysis tool, based on the Unit Cell micromechanics model of 3-D woven fabric composite. The observed discrepancy between theoretical and experimental results, which is likely caused by the composite manufacturing flaws and imperfections, is under close investigation.
- Numerical results provided by the first order 3-D ABAQUS finite element analysis for 3-D woven composite bonded joint with fully homogenized adherends, showed generally correct trends, though significant quantitative discrepancies with experimental strain values. This result suggests that more sophisticated material models, as a minimum distinguishing between the warp-and fill-reinforcement layers and their through thickness positions, has to be applied for a higher predictive analysis accuracy.
- A new method, Cut And Polish (CAP), has been proposed and elaborated to make the connections from the fiber optic sensors integrated in composite part and the data acquisition system. Initial results show great promise. Connections have been successfully made and repaired. Optical losses were held to levels that would allow measurements by existing equipment. Improvements could be made to further reduce the optical losses. The new CAP method is patentable and 3TEX and Luna intend to pursue joint IP to protect it.

## 15. PRACTICAL VALUE OF THE DEVELOPED METHODOLOGY

The profile of the strain variation along a sensing fiber (illustrated again in Figure 161) in a composite structural component, structural joint, etc., loaded in a known fashion, was shown to linearly scale with that load and retain its shape "signature" in any "acceptable" service situation (e.g., in essentially elastic regime), while losing such signature linearity when approaching to some catastrophic situation.

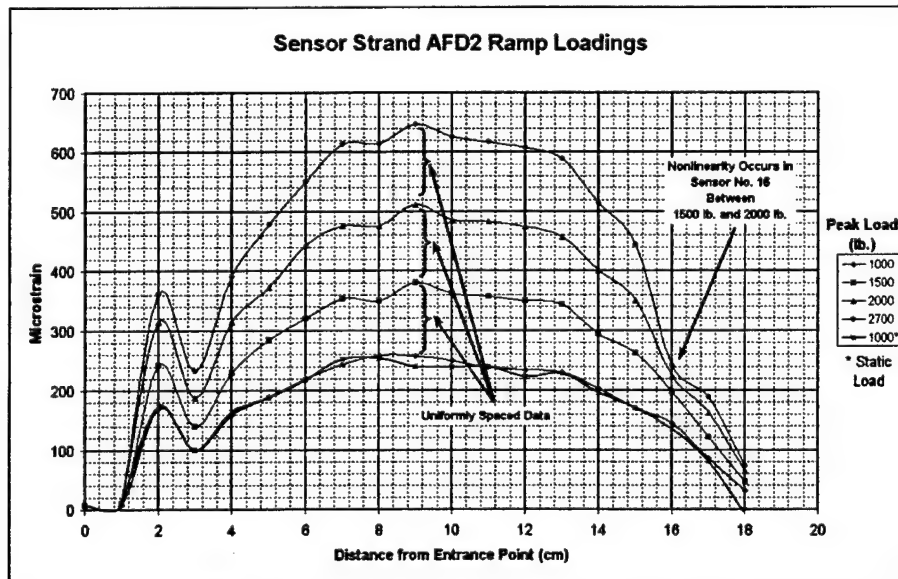


Figure 161. Illustration of a linear ("normal") and nonlinear ("abnormal") scaling of the integrated Bragg grating strain sensor readings with increasing load level.

Any deviation from a linear "load-strain" scaling should be immediately considered as a strong indication of some kind "abnormality", which may be due to significant yield, crack or damage development, debond, delamination, or other type local material malfunction proximal to that sensor. Failure of or mechanical rejection of adjacent structures or devices would affect this profile as well.

Image recognition, or neural net like methods may well allow detection of a change in the aforementioned strain variation profile, thus identifying significant increase in the compliance of the structure, hence, triggering inspection, or even adjustment of flight parameters to mitigate damage, i.e. "limping".

A simple beam or ligament specimen in fatigue might serve well to allow refinement of such software. Later extension to structures with multiple strands could follow.

In possible continuation of this research and development, 3-D Braided stiffeners should be produced having integrated sensing and/or data strands tested to validate possibility of providing both sensing and data transmission functions along entire fuselage. Monitoring the strain distribution "signature" along integrated fiber optic sensor strands within several stringers and ribs could allow monitoring of the representative strain field within entire fuselage, or wing. If the "signature" were to change along several fuselage stringers near the same ring or bulkhead, inspection might be triggered well before catastrophic failure, such as occurred with Aloha Flight 243, see Figure 162.

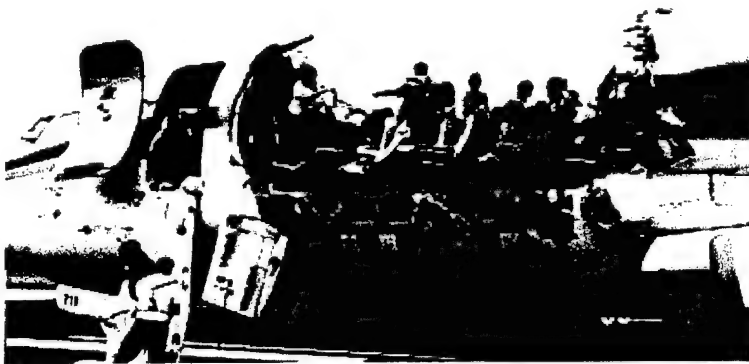


Figure 162. Failure... ALOHA Airlines, Flight 243, Boeing 737-200, N7371I, Maui, Hawaii, April 28, 1988.

Tapping into an optical strand without actually contacting it may be feasible with powerful light sources, and sensitive detectors. Injection of, and detection of light may be done through the side wall of the optical fiber. These things may be more feasible for data than for interrogating FBGs, but a long stringer or wing box having sensing fiber along its entire length might be tapped in this fashion to allow other data to be passed along it without opening or cutting. Thus, the sensing fiber could serve dual functions.

CAP connection to optical fibers of all types, in composites of any type, looks very promising. Continued refinement of standardized components (connectors etc.) and tools (alignment jigs, CCD detector patches, clamp-on stages etc.) should be pursued to provide for easy to use kits for the field implementation of the CAP method. Bond-on Laser diodes and CCD detectors may make alignment nearly trivial in CAP. CAP methods should be further investigated, developed, and extended to allow boring into parts perpendicular to the optical fiber at any point and tapping into it. This would allow much more flexibility of using integrated networks of fiber optic sensors.

## 16. REFERENCES

1. Roy, A.K., "In Situ Damage Observation and Failure in Model Laminates Containing Planar Yarn Crimping of Woven Composites," Mechanics of Composite Materials and Structures, 1996.
2. Mohamed, M.H. and Zhang, Z.-H., "Method of Forming Variable Cross-Sectional Shaped Three Dimensional Fabrics," U.S. Patent No. 5,085,252, issued February 4, 1992.
3. Mohamed, M.H., "Weaving for Composites," Proc. Textiles Used in Structural Composites, Symp. Sponsored by SAMPE and the Industrial Fabrics Association, March 1996.
4. Dickinson, L.C. and Mohamed, M.H., "Recent Advances in 3-D Weaving for Textile Preforming," Proc. of the ASME Aerospace Division, Book No. H01214, 2000, pp. 3-8.
5. Mohamed, M.H., Bogdanovich, A.E., Dickinson, L.C., Singletary, J.N., and Lienhart, R.B., "A New Generation of 3-D Woven Fabric Preforms and Composites," SAMPE Journal, 2001, Vol. 37, No. 3, pp. 8-17.
6. Udd, E., Schulz, W., and Seim, J., "Measurement of Multidimensional Strain Fields Using Fiber Grating Sensors for Structural Monitoring," SPIE Vol. 3860, Fiber Optic Sensor Technologies and Applications, December 1999, pp. 24-34.
7. Froggatt, M., "Distributed Measurement of the Complex Modulation of a Photoinduced Bragg Grating in an Optical Fiber", Appl. Opt., Vol. 35, No. 25, 1996, pp. 5162-5164.
8. Froggatt, M. and Moore, J., "Distributed Measurement of Static Strain in an Optical Fiber with Multiple Bragg Gratings at Nominally Equal Wavelengths", Appl. Opt., Vol. 37, No. 10, April 1998.
9. Childers, B.A., Froggatt, M.E., Allison, S.G., Moore, T.C., Hare, D.A., Batten, C.F., and Jegley, D.C., "Use of 3000 Bragg Grating Strain Sensors Distributed on Four Eight-meter Optical Fibers During Static Load Tests of a Composite Structure," Smart Structures and Materials Conference, SPIE Vol. 4332, 4-8 March 2001.
10. Hagemann, V., Trutzel, M.N., Staudigel, L., Rothhardt, M., Muller, H.R. and Krumpholz, O., "Mechanical Resistance of Draw-tower-Bragg-grating Sensors", Elec. Lett., Vol. 34, No. 2, January 1998.
11. Askins, C.G., Putnam, M.A., Patrick, H.J. and Friebel, E.J., "Fibre Strength Unaffected by On-line Writing of Single-pulse Bragg Gratings", Elec. Lett., Vol. 33, No. 15, July 1997.
12. Bogdanovich, A.E., Wigent, D.E. III, and Whitney, T.J., "Fabrication of 3-D Woven Preforms and Composites with Integrated Fiber Optic Sensors," Proc. of 48<sup>th</sup> Int. SAMPE Symposium and Exhibition, May 11-15, 2003, Long Beach, CA. SAMPE Publ., pp. 1357-1371. Also in SAMPE Journal, Vol. 39, No. 4, July/August 2003, pp. 6-15.

13. Wigent, D.E. III, Bogdanovich, A.E., and Whitney, T.J., "Strain Monitoring of 3-D Woven Composites Using Integrated Bragg Grating Sensor Arrays," Proc. of 49<sup>th</sup> Int. SAMPE Symposium and Exhibition, May 16-20, 2004, Long Beach, CA, SAMPE CD publication.
14. Bogdanovich, A.E., "Three-Dimensional Variational Theory of Laminated Composite Plates and Its Implementation with Bernstein Basis Functions", Computer Methods in Applied Mechanics and Engineering, 2000, Vol. 185, No. 2-4, pp. 279-304.
15. Bogdanovich, A.E., "Three-Dimensional Variational Analysis of Composite Structures Using Bernstein Polynomial Approximations," Mechanics of Composite Materials, 2001, Vol. 37, Nos. 5/6. Part 1, pp. 525-538; Part 2, pp. 539-552.
16. Bogdanovich, A.E. and Yushanov, S.P., "3-D Progressive Failure Analysis of Bonded Composite Joints," Proc. of the 39th AIAA/ASME/ASCE/AHS/ASC Structures, Structural Dynamics and Materials Conf., Long Beach, CA, April 20-23, 1998, Pt. 3, AIAA Paper A98-25163, pp. 1616-1626.
17. Bogdanovich, A.E. and Yushanov, S.P., "Progressive Failure Analysis of Adhesive Bonded Joints with Laminated Composite Adherends," Journal of Reinforced Plastics and Composites, 1999, Vol. 18, No. 18, pp. 1689-1707.
18. Bogdanovich, A.E. and Yushanov, S.P., "Patch Repair of Damaged Structures: Predictive Analysis, Design and Practical Realization Using 3-D Woven Composites," Proc. of the 21<sup>st</sup> Int. Conf. SAMPE Europe, April 18-20, 2000, Paris, France. SAMPE Publ., pp. 547-558.
19. Bogdanovich, A.E., "Multiscale Predictive Analysis of 3-D Woven Composites," Proc. of 35<sup>th</sup> International SAMPE Technical Conference, Vol. 35, Dayton, OH, September 28-October 2, 2003.
20. Bogdanovich, A., "Structural Analysis Tools for Validating Mechanical test Methods and Experimental Results for 3-D Woven Composites," Proc. of the 25<sup>th</sup> Jubilee International SAMPE Europe Conference, Paris, France, March 30-April 1, 2004, pp. 393-398.
21. Bogdanovich, A.E. and Kizhakkethara, I., "Three-Dimensional Finite Element Analysis of Double-Lap Composite Adhesive Bonded Joint Using Submodeling Approach," Composites, Part B: Engineering, 1999, Vol. B30, pp. 537-551.
22. Eiklenborg, M., and Scott, J. "Tools and Methods for Obtaining Precision Fiber Alignments," IMAPS Advanced Technology Workshop on Optoelectronics Packaging, Radisson Hotel, Bethlehem, Oct. 11-14, 2001.
23. Keiser, Gerd, "Optical Fiber Communications, Second Edition", McGraw-Hill, New York, 1991.
24. Collins, J.V. and Lealman, I.F., "Passive Alignment of a Semiconductor Laser to Optical Fiber Utilizing a Silicon Micro-bench," IEE Colloquium on Microengineering Applications in Optoelectronics, 1996, pp. 5/1-3.
25. Craig, A., et.al., "Method for Passive Alignment of Diod Laser Arrays and Optical Fibers," US Patent Application 91111501, Filed July 1991.
26. Haugsjaa, P., Armiento, C., "Silicon Waferboard Alignment of Laser Arrays to Single-mode Optical Fiber for Analog Optoelectronic Module Applications," Proc. SPIE- Int. Soc. Opt. Eng., vol. 26310, pp. 150-158, October 1995.
27. Lam, Yee Loy, Tan, Peh Wei, "Optical Coupling Mount", US Patent Application 006752/10, Filed September 2001.
28. Mertz, Pierre H., Babic, Dubravko, "Integrated Coupling Modules for High-Bandwidth Fiber-Optic Systems"; US Patent Application 726370/09, Filed September 2001.

29. Jian, Benjamin Bin, "Multilayer Optical Fiber Coupler"; US Patent 06328482; issued December 2001.
30. Cho, Alfred Yi, "An Integrated Optical Package for Coupling Optical Fibers to Devices with Asymmetric Light Beams"; US Patent Application 93303235, Filed April 1993.
31. Saito, Masahiro et.al., "Optical Fiber Microlens, Optical Fiber and Method of Positioning Optical Fiber", US Patent Application 069868/10, Filed August 2002.
32. Lee, Yong Hee, Ju, Young Gu, and Lee, Myung Lae, "Optical Interconnection Structure for Enlarging Alignment Tolerance"; US Patent 06253004, June 2001.
33. Nicia, A., "Lens Coupling in Fiber-Optic devices: Efficiency Limits," Appl. Opt., Vol. 20, pp. 3136-3145, Sept. 1981.
34. Kawasaki, B.S. and Johnson, D.C., "Bulb-ended Fiber Coupling to LED Sources," Opt. Quantum Electron., Vol. 7; pp. 281-288; 1975.
35. Ackenhusen, J.G., "Microlenses to Improve LED-to-Optical Fiber Coupling and Alignment Tolerance," Appl. Opt., Vol. 18, pp. 3694-3699, Nov. 1979.
36. Sumida, M. and Takamoto, K., "Lens Coupling of Laser Diodes to Single-mode Fibers," J. Lightwave Tech., vol. LT-2, pp. 305-311, June 1984.
37. Hasegawa, O., Namazu, R., Abe, M., and Toyoura, Y., "Coupling of Spherical-Surfaced LED, and Spherical-ended Fiber," J. Appl. Phys., Vol. 51, pp. 30-36, Jan. 1980.
38. Novikov, L.V., "Analysis of the Accuracy of Different Methods for Aligning Single-mode Optical Fibers"; Sov. J. Opt. Technol., Vol. 58, No. 6, pp. 326-329, June 1991.
39. Novikov, L.V., "Taking Alignment Error Into Account in Evaluating the Adjustment Accuracy of Single-mode Optical Fibers," Sov. J. Opt. Technol., Vol. 59, No. 2, pp. 77-79, February 1992.
40. DiVita, P. and Rossi, U., "Realistic Evaluation of Coupling Loss Between Different Optical Fibers," J. Opt. Commun., Vol. 1, pp. 26-32, Sept. 1980.
41. DiVita, P. and Rossi, U., "Evaluation of Splice Losses Induced by Mismatch in Fibre Parameters," Opt. Quantum Electron., Vol. 13, pp. 91-94, Jan. 1981.
42. Gloge, D., "Offset and Tilt Loss in Optical Fiber Splices," Bel. Sys. Tech. J., Vol. 55, pp. 905-916, Sept. 1976.
43. Chu, T.C. and McCormick, A.R., "Measurement of Loss Due to Offset, End Separation, and Angular Misalignment in Graded Index Fibers Excited by an Incoherent Source," Bel. Sys. Tech. J., Vol. 57, pp. 595-602, Mar. 1978.
44. Wang, L.A. and Su, C.D., "Tolerance Analysis of Aligning an Astigmatic Laser Diode with a Single-Mode Optical Fiber," J. Lightwave Technol., Vol. 14, No. 12, pp. 2757-2762, Dec. 1996.
45. Tang, Z, Zhang, R., and Shi, F.G., "Effects of Angular Misalignments on Fiber-optic Alignment Automation", Opt. Commun., Vol. 196, pp. 173-180, September 2001.
46. Harman, M.R., "Positioning Device Especially for Assembling Optical Components," US Patent No. 6498862, December 2002.
47. Witham, C.R., Beranek, M.W., et. al., "Fiber-optic Pigtail Assembly and Attachment Alignment Shift Using a Low-cost Robotic Platform," Proceedings. 50<sup>th</sup> Electronic Components and Technology Conference, pp. 21-25, May 2000.
48. Bondarev, T.I. and Kryazhev, A.S., "Apparatus for the Alignment of Single-mode Optical Fibers," Meas. Tech., Vol. 38, No. 8, pp. 888-889, August 1995.

## 17. PERSONNEL SUPPORTED

The following personnel have provided technical support billed directly or indirectly during the Phase II work period in the capacities specified. Other personnel in each institution have provided administrative or clerical support not directly billed and as such are not listed.

Professional personnel supported by the research effort:

Dr. Alexander Bogdanovich (Principal Investigator), Vice President, R&D, 3TEX, Inc.

Mr. Donald Wigent (Leading Research Engineer), Product Development Engineer, 3TEX, Inc.

Dr. Thomas J. Whitney, Senior Research Engineer, University of Dayton Research Institute.

Mr. Thomas Wavering, Research Scientist, Luna Innovations, Inc.

Dr. Keith Furrow, Research Scientist, Luna Innovations, Inc.

Personnel Providing Technical Support in Sub-Tasks

3TEX, Inc.:

Mr. Patrick Duke, Product Development Engineer

Luna Innovations, Inc.:

Mr. Roger Duncan

Mr. David Broaddus

Mr. David Slusher

Mr. Jason Chevalier

Mr. Kevin Burris

Mr. Larry Vicari

University of Dayton Research Institute:

UDRI supervision was provided by Michael P. Bouchard, Head, Aerospace Mechanics Division, and Daniel R. Bowman, Head, Structures Group. Messrs. John Camping and Ron Esterline for sample preparation and testing; Dr. David Mollenhauer, AFRL/MLBC, for Moiré interferometry; and Messrs. Doug Wolf and Ed Porter for X-ray evaluation.

## 18. PUBLICATIONS

1. A.E. Bogdanovich, D.E. Wigent III, and T.J. Whitney, "Fabrication of 3-D Woven Preforms and Composites with Integrated Fiber Optic Sensors," SAMPE Journal, Vol. 39, No. 4, July/August, 2003, pp. 6-15.
2. A. Bogdanovich, D. Wigent, T.J. Whitney, and P.A. Clark, "3-D Woven Composites Instrumented with EFPI Fiber Optic Sensors," CD Proceedings of IMECE'02, ASME International Mechanical Engineering Congress & Exposition, New Orleans, November 17-22, 2002.

3. A.E. Bogdanovich, D.E. Wigent III, and T.J. Whitney, "Fabrication of 3-D Woven Preforms and Composites with Integrated Fiber Optic Sensors," Proceedings of the 48<sup>th</sup> Int. SAMPE Symposium and Exhibition, May 11-15, 2003, Long Beach, CA, SAMPE Publ., pp. 1357-1371.
4. T.J. Whitney, A.E. Bogdanovich, and D.E. Wigent III, "In-Situ Strain Monitoring of 3-D Woven Composites Using Integrated Fiber Optic Sensors," CD Proceedings of ICCM-14, the 14<sup>th</sup> Int. Conf. on Composite Materials, July 14-18, 2003, San Diego, CA, Paper #1343.
5. D.E. Wigent III, A.E. Bogdanovich, and T.J. Whitney, "Strain Monitoring of 3-D Woven Composites Using Integrated Bragg Grating Sensor Arrays," CD Proceedings of 49<sup>th</sup> Int. SAMPE Symposium and Exhibition, May 16-20, 2004, Long Beach, CA.

## **19. INTERACTIONS/TRANSITIONS**

### **Participation/presentations at meetings, conferences, seminars, etc.**

Researchers contributed to this research project have participated in conferences, seminars and meetings or made presentations associated with the research conducted under this project at the following:

1. Four conference presentations in 2002-2004, see list of published papers in Section 18 above.
2. Dr. Bogdanovich presented reports on this project at the Annual AFOSR Aerospace and Materials Programs Contractor's Review Meetings, in 2001, 2002, 2003 and 2004.
3. Regular meetings and reviews of the project have been held with Air Force Research Laboratory personnel at WPAFB, Dayton, OH (Dr. Ajit Roy, Dr. Steven Donaldson, Dr. Ozden Ochoa, Dr. David Mollenhauer, Dr. Greg Schoeppner participated).
4. Dr. Bogdanovich presented some results of this project at the 1<sup>st</sup> Air Force Workshop on Multifunctional Aerospace Materials, held at Purdue University, West Lafayette, IN, October 23-24, 2002.
5. Dr. Bogdanovich presented some results of this work at the seminar held at ESM Department, Virginia Polytechnic Institute and State University, Blacksburg, VA, February 18, 2004.
6. Dr. Bogdanovich will present essential results of this project at the seminar to be held on February 7, 2005 at Boeing Commercial Airplanes (Advanced Structural Technologies and Manufacturing Research & Development Divisions), Seattle, WA.

### **Consultative and advisory functions to other laboratories and agencies**

Researchers have consulted with, or supported other agencies or contractors in matters associated with the research conducted under this project as follows:

Donald Wigent, performed consultation, contribution, and support of a proposal made by Eric Walliser of Boeing-Mesa toward US ARMY BAA DAAH10-03-R-0004 describing potential applications of similar technology in US army Rotorcraft Structural Elements.

2004 Force Phase II STTR proposal "*High Spatial Resolution Shape Sensing for Adaptive Aerospace Vehicles*" 03-1-A7.01-7035 LaRC was submitted (wherein 3TEX subcontracted to Luna Innovations Incorporated) to manufacture a "smart" wing structure by integration of new Luna fiber optic shape sensors. Contact Roger Duncan at 540-953-4274.

### **Transitions**

Discussions have begun with Boeing's multi-functional structures group toward the transfer of, and continued development of the described technologies for application in military vehicles.

Contacts have been made and information exchange initiated with Boeing Commercial Airplanes, Advanced Structural Technologies and Manufacturing Research & Development Divisions in Seattle, WA (Mr. Jeffery L. Marcoe and Mr. Robert G. Albers) on potential implementation of this technology in the future commercial Boeing aircraft.

Mr. Wigent and Dr. Bogdanovich presented review of technology for AFRL VAS Composite Structures Group Wright-Patterson AFB. Mr. Richard C. Holzwarth (Team Leader, Advanced Structural Concepts), Dr. Stephen B. Clay (Aerospace Engineer), Dr. Ronald J. Kerans (Ceramics Research Group Leader) and others participated and expressed high interest in 3TEX's integrated sensor technology.

Dr. Bogdanovich visited NextGen Aeronautics company, in Terrence, CA and had extensive technical information exchange and discussion with CEO Dr. Jay Kudla, Principal Engineer Dr. Shiv Joshi and others about possible collaboration on their DARPA BAA project aimed at integrated antenna development for Northrop Grumman Unmanned Aircraft.

Dr. Bogdanovich had contacts with Lockheed Martin's Senior Aeronautical Engineer Dr. Robert Taylor and Dr. Steven Engelstad and informed them on 3TEX's development of fiber optic sensor integration into composite materials and structures. Potential collaboration was discussed.

## **20. NEW DISCOVERIES, INVENTIONS**

3TEX, Inc. has filed in November 2003 U.S. patent application entitled "Three-Dimensional Woven and Braided Fabrics and Composites with Integrated Devices, Systems and Networks".

3TEX, Inc. and Luna Innovations, Inc. has jointly initiated the pursuit of intellectual property rights associated with innovation in CAP connection.

## **21. HONORS/AWARDS**

First Place Outstanding Technical Paper Award at SAMPE 2003/Long Beach Conference to Dr. Alexander Bogdanovich, Donald E. Wigent III and T.J. Whitney.